CLIC Drive Beam Phase Stabilisation

Alexander Gerbershagen
Keble College, Oxford

CERN-THESIS-2013-160
25/07/2013

Thesis submitted in fulfilment of the requirements for the degree of Doctor of Philosophy at the University of Oxford

Trinity Term, 2013

Abstract

The thesis presents phase stability studies for the Compact Linear Collider (CLIC) and focuses in particular on CLIC Drive Beam longitudinal phase stabilisation. This topic constitutes one of the main feasibility challenges for CLIC construction and is an essential component of the current CLIC stabilisation campaign. The studies are divided into two large interrelated sections: the simulation studies for the CLIC Drive Beam stability, and measurements, data analysis and simulations of the CLIC Test Facility (CTF3) Drive Beam phase errors.

A dedicated software tool has been developed for a step-by-step analysis of the error propagation through the CLIC Drive Beam. It uses realistic RF potential and beam loading amplitude functions for the Drive and Main Beam accelerating structures, complete models of the recombination scheme and compressor chicane as well as of further CLIC Drive Beam modules. The tool has been tested extensively and its functionality has been verified.

The phase error propagation at CLIC has been analysed and the critical phase error frequencies have been identified. The impact of planned error filtering and stabilisation systems for the Drive Beam bunch charge and longitudinal phase has been simulated and the optimal specifications for these systems, such as bandwidth and latency time, have been calculated and discussed. It has been found that a realistic feed-forward system could sufficiently reduce the longitudinal phase error of the Drive Beam, hence verifying that a satisfactory CLIC luminosity recovery system is possible to develop.

Alternative designs of the Drive Beam accelerator, the recombination scheme and the phase signal distribution system have also been analysed.

Measurements of the CTF3 Drive Beam phase have been performed. The source of the phase and energy errors at CTF3 has been determined. The performance of the phase feed-forward system prototype for CTF3 has been simulated. The prototype's specifications have been defined so that it will provide a sufficient test of the feed-forward correction principle. The prototype based on the defined specifications is currently in development and is to be installed at CTF3 in the second half of 2013.

This thesis is dedicated to my grandmother, Anastasia Fokina, who, with her practical wisdom, provided me with a great guidance for my future life.

Acknowledgements

Foremost, I would like to express my sincere gratitude to both of my thesis supervisors: Prof. Philip Burrows from University of Oxford, who provided me with the possibility of writing the thesis for the FONT group and was very helpful in shaping the content of my research, in applying for funding as well as with his fantastic overview of the field and an open ear for all possible questions. Dr. Daniel Schulte from CERN was an inspiring source of many ideas realised in the thesis. With his scientific excellence and extensive accelerator physics knowledge he has identified the most challenging issues of CLIC stabilisation and guided me towards the solutions, always finding time for meeting me despite his busy schedule.

My gratitude goes also to the CTF3 colleagues Emmanouil Ikarios, Tobias Persson and Piotr Skowronski, who patiently supported me in collecting and analysing the phase data at CTF3 as well as to Roberto Corsini, who supervised and guided us. Also CLIC simulation studies would not be possible without the results delivered by Rolf Wegner, Oleksiy Kononenko and Avni Aksoy. I would also like to express a special thanks to the members of the FONT group at University of Oxford, in particularly to Glenn Christian and Colin Perry, who have always provided an independent perspective and a good reality check for my measurement and simulations data.

A big thanks to my office colleagues Jochem Snuverink, Javier Barranco Garcia and Erik Adli, who have helped me a lot, especially in the beginning phase of the thesis, with their knowledge of accelerator physics, CLIC machine and computing. Jochem Snuverink together with Robert Apsimon were also so kind to read the present thesis and provide me with their comments and recommendations, for which I am very grateful. Furthermore I would like to thank my CERN colleagues and friends Yngve Inntjore Levinsen, Reidar Lillestol, Frank Stulle, Jose Abelleira Fernandez and Hector Garcia Morales, who helped a lot on an everyday basis, be it with IT-advice or with an occasional encouragement at afternoon coffee. I was lucky to have a great administrative assistance from the secretaries at Oxford and CERN: Kim Proudfoot, Sue Geddes, Alexia Augier and Delphine Rivoiron.

Last but not least, I would like to thank my mother Irina and my partner Márta, who stood behind me during the thesis time and whose support has motivated me to continue my work on accelerator physics in the future. And cheers to all my friends whom I could always count on, in particular Ilknur Colak, Vasileios Martos and Esa Paju in Switzerland, Dan Johnson and Adrian Lewis in the UK, and Andrej Nikonov, Ksenia and Alexander Yefremov, Hans Kessler, Wiebke Ohm, Marcel Ruhnke, Boris Friesen, Roman Bauer, Eugen Axt, Agnieszka Hyszka, Anna Koziel, Marc Scheele and Márta, József and Áron Varga in Germany. And to anyone whom I did not mention personally, but surely have in my memory.

Contents

1 Introduction **1**
- 1.1 Outline of the thesis . . . 1
- 1.2 Particle physics . . . 1
  - 1.2.1 History of particle physics . . . 1
  - 1.2.2 The Standard Model . . . 2
  - 1.2.3 Present research fields of particle physics . . . 5
- 1.3 Accelerators and colliders . . . 6
  - 1.3.1 Beam Dynamics . . . 7
  - 1.3.2 Fixed-target and two-beam colliders . . . 9
  - 1.3.3 Synchrotrons and linear colliders . . . 9
  - 1.3.4 LHC and the need for a future lepton collider . . . 10
- 1.4 Feedback On Nanosecond Timescale . . . 15
- 1.5 CERN . . . 18

2 CLIC **21**
- 2.1 Overall Design . . . 21
- 2.2 Drive Beam . . . 21
  - 2.2.1 Drive Beam accelerator . . . 22
  - 2.2.2 Recombination scheme . . . 26
- 2.3 PETS and Main Linac . . . 27
- 2.4 Interaction point and detectors . . . 30
  - 2.4.1 Interaction point . . . 30
  - 2.4.2 Detectors . . . 31
- 2.5 Stability requirements . . . 32
  - 2.5.1 Proposed Phase Feed-Forward System . . . 35
  - 2.5.2 Synchronisation system . . . 36
- 2.6 CTF3 . . . 37
  - 2.6.1 Beam stabilisation . . . 40

3 Software Tool for CLIC Drive Beam Error Analysis **41**
- 3.1 Simulation models . . . 42
  - 3.1.1 Simulated parameters and their interdependences . . . 42
  - 3.1.2 Drive beam accelerator . . . 46
  - 3.1.3 Compressor chicane . . . 51
  - 3.1.4 Recombination scheme . . . 52
  - 3.1.5 PETS and Main Linac . . . 55

3.2 Charge feedback model . . . 58
3.2.1 PID Controller . . . 58
3.2.2 Optimisation of feedback latency time t_l . . . 58
3.2.3 Feedback gain time t_g . . . 60
3.3 Phase feed-forward . . . 62
3.4 Summary . . . 64

4 Verification of software tool functionality 67
4.1 Drive Beam accelerator . . . 67
4.2 Compressor chicane . . . 69
4.3 Recombination scheme and bunch z-position . . . 69
4.4 Impact of Drive Beam errors on the Main Beam . . . 72
4.4.1 Single bunch error propagation . . . 72
4.4.2 Impact of constant parameter offset . . . 74
4.5 Conclusion of verification studies . . . 75

5 Simulation results for CLIC 76
5.1 Error filtering along the Drive Beam . . . 76
5.1.1 Error filtering in the recombination scheme and Main Beam acceleration structures . . . 77
5.1.2 Error filtering in the Drive Beam accelerating structures . . . 77
5.2 Drive Beam bunch charge feedback system . . . 82
5.3 Drive Beam phase feed-forward system . . . 87
5.3.1 Timing of feed-forward correction application . . . 88
5.3.2 Impact of the feed-forward bandwidth on the correction effectiveness 89
5.3.3 Specifications of the distributed timing system . . . 94
5.4 Modification of Drive Beam accelerating structure RF filling time . . . 98
5.5 Low Energy recombination modes . . . 103
5.5.1 Nominal 3 TeV operation mode . . . 105
5.5.2 Lower energy operation modes . . . 105
5.5.3 Consequences for the error propagation and correction . . . 107
5.6 Chapter summary . . . 108

6 CTF3 phase measurement, analysis and simulations 111
6.1 Phase measurement results along CTF3 . . . 111
6.2 Determination of phase error sources . . . 116
6.2.1 Possible source of additional phase error introduced in the stretching chicane . . . 118
6.2.2 Beam energy after the CTF3 linac . . . 120
6.2.3 Phase error in the linac . . . 122
6.2.4 Klystron amplitude and phase errors . . . 122
6.3 Phase stabilisation system prototype for CTF3 . . . 129
6.3.1 Performance simulation of phase feedback correction . . . 129
6.3.2 Performance simulation of CTF3 feed-forward phase correction system 131
6.4 Chapter summary . . . 134

7 Conclusions and suggested further work **136**
7.1 Phase stabilisation for CLIC 137
7.1.1 CLIC design 137
7.1.2 Methodology of Drive Beam error propagation simulation 137
7.1.3 Results of simulation studies for the CLIC Drive Beam tolerances . . 138
7.1.4 Impact of charge feedback system on Drive Beam tolerances 139
7.1.5 Impact of phase feed-forward system on Drive Beam tolerances 139
7.2 Phase stabilisation at CTF3 141

Bibliography **143**

List of Figures

1.1 Representation of the history of the matter structure investigation. 2
1.2 Table of fundamental particles of the Standard Model. 3
1.3 Representation of the Higgs mechanism. The symmetry in the centre is spontaneously broken when the particle moves to the minimum of the potential. . 4
1.4 The resonant peak of the Z boson. 6
1.5 Scheme and description of LHC accelerating cavity. 7
1.6 A fixed-target collider (left) and a two-beam collider (right). 9
1.7 Schematic layout of the Large Hadron Collider. 11
1.8 Parton distribution functions measured at H1 and ZEUS experiments (DESY, Hamburg). The probability densities for finding a gluon (xg), a virtual quark (xS) and a real up- or down-quarks (xu and xd respectively) are plotted as functions of momentum fraction x. Total momentum transfer is $Q^2 = 10$ GeV^2. 12
1.9 Schematic layout of the ILC for 500 GeV collision energy. 14
1.10 Amplitude of the ground motion as a function of motion frequency measured at different locations. 16
1.11 Correlation of the movement of two points in 100 m distance for different ground motion frequencies. 17
1.12 Layout and operating mode of the FONT system. 17
1.13 The operation of FONT2 measured by the beam position monitor at the NLC Test Accelerator. 18
1.14 Simulation of FONT operation impact on CLIC luminosity. 19
1.15 The twenty member states of CERN. 20

2.1 Layout of Compact Linear Collider at 3 TeV. 22
2.2 Layout of the CLIC Drive Beam. 23
2.3 Principle of fully loaded acceleration. 24
2.4 The optimal RF filling function vs. time after the RF wave enters the structure (left) and beam loading (right) along one Drive Beam accelerating structure. 24
2.5 The layout of the Drive Beam complex showing the position of the Drive Beam linac sections (DBL) and of the bunch compression and decompression chicanes (BC). 25
2.6 Compressor chicane position in the Drive Beam Linac. 26
2.7 Scheme of the Drive Beam compressor chicane. 26
2.8 CLIC Drive Beam combination principle on the example of the Delay Line. . 27
2.9 CLIC two-beam scheme: An RF wave is extracted from the Drive Beam and is fed through waveguides to the Main Beam. 28

2.10 Power Extraction and Transfer Structures - view of the assembled structures (left) and structure profile of one bar (right). 28
2.11 A snapshot of excited wakefelds at the time point of the bunch exiting the PETS. The red colour represents a strong propagating electromagnetic field, the yellow and green colours represent the weaker dissipating fields. 29
2.12 Left: the accelerating voltage for the optimized RF pulse in the Main Beam structures. Right: energy spread along the Main Beam train. The dotted blue line represents the relative energy error, the dashed green line represents the standard deviation of this energy error. 30
2.13 Horizontal and vertical normalised emittance values for the different existing (in red) and planned (in blue) accelerator facilities. 31
2.14 Scheme of CLIC interaction region with both detectors. 32
2.15 Relative peak luminosity within 1% of nominal beam energy E as a function of the energy offset $\delta_0 = \Delta E/E$. 33
2.16 Tolerances of different parameters along the CLIC Drive Beam. 34
2.17 Scheme of the feed-forward chicane for CLIC Drive Beam phase correction. . 35
2.18 Propagation of the reference signal based on the Main Beam (A) and chained distribution of master clock signal (B). 36
2.19 Layout of CLIC Main Linac at 3 TeV. 37
2.20 Layout of the CLIC Test Facility (CTF3). 38
2.21 Measurement of RF power input and output at CTF3. The linac is operating with full beam-loading. 39
2.22 Recombination with factor eight demonstrated at CTF3. 39

3.1 Simplified process diagram of operation of Drive Beam error tracking simulation tool. 42
3.2 The scheme of the Drive Beam complex showing the changes in the nominal bunch length. 45
3.3 Simulation result for beam loading amplitude (V) of CLIC Drive Beam cavities (in green) as a function of distance from the bunch (m). Two exponential approximations are indicated by the black solid and the dashed lines. The linear approximation is indicated by a red line. 48
3.4 Simulation result for RF filling potential (V) as a function of time (ns) for CLIC Drive Beam cavities. The linear approximation is indicated by the red lines. 49
3.5 The amplitude (in arbitrary units) of the RF wave entering the Drive Beam accelerating structure (top), amplitude of its reflection (middle) and the RF amplitude at the exit of the structure (bottom) as a function of time (s). . . 50
3.6 Drive Beam phase error at the compressor chicane (deg. at 1 GHz) vs. relative beam energy error (%) at linac entrance with different R_{56} values. 51
3.7 Relative bunch length error at the compressor chicane (%) vs. relative bunch charge error (%) with different R_{56} values. 52
3.8 Scheme of first several circulations in the first Combiner Ring. In step 4 the 1 GHz bunch frequency train is extracted without recombination. 54
3.9 Bunch z-position before and after passing Drive Beam recombination scheme. 54

3.10 Depiction of train errors' overlap. 55
3.11 Simulation result for beam loading amplitude (V/C) as a function of time for CLIC Main Beam cavities. The linear approximation is indicated by a red line. 56
3.12 Simulation result for RF filling potential (V) as a function of time (ns) for CLIC Main Beam cavities. The linear approximation is indicated by the red lines. 57
3.13 Illustration of the action of a feedback system resonant (top) and anti-resonant (bottom) to the dominant jitter frequency. The error in arbitrary parameter is plotted as a function of time. 59
3.14 Error amplitude as a function of jitter frequency for the impulse response of proportional (red) and differential (green) feedbacks. 60
3.15 Illustration of the feedback system simulation. A normalised error at bunch number two is introduced, the error of a system without feedback (in blue) and with feedback (in red) is plotted as a function of bunch number. 61
3.16 Illustration of the feed-forward simulation with $t_l = 0$ and $t_g = 5$. A normalised error at the bunch number eleven is introduced, the error without (blue) and with (red) feed-forward application is plotted as a function of bunch number. 62
3.17 Illustration of the feed-forward simulation with $t_l = -\frac{1}{2}t_g$ and $t_g = 5$. A normalised error at the bunch number eleven is introduced, the error without (blue) and with (red) feed-forward application is plotted as a function of bunch number. 63
3.18 The error without (blue) and with feed-forward application with $t_g = 5$ bunches (red) and $t_g = 11$ bunches (green) is plotted as a function of bunch number. A normalised error at the bunch number eleven is introduced. . . . 64

4.1 Drive Beam energy as a function of bunch number in the case that the Drive Beam accelerating RF amplitude has a 2 ns long relative error of 0.38%. . . 68
4.2 69
4.3 Drive Beam bunch z-position as a function of bunch number before the beam enters the Delay Line. 70
4.4 Drive Beam bunch z-position as a function of bunch number after the beam has passed the Delay Line. 71
4.5 Drive Beam bunch z-position as a function of bunch number after the beam has passed the first Combiner Ring. 71
4.6 Drive Beam bunch z-position as a function of bunch number after the beam has passed the second Combiner Ring. 72
4.7 Phase error of the Main Beam bunches relatively to the accelerating RF as a function of Main Beam z-position for a single Drive Beam bunch phase error. 74
4.8 Phase error of the Main Beam bunches relatively to the accelerating RF as a function of Main Beam z-position for a constant Drive Beam phase offset. . . 75

5.1 Phase error amplitude as a function of frequency after filtering by the recombination scheme and Main Beam acceleration structures. 78

5.2 Filtering factor of the ideal RF filling function for different RF amplitude or RF phase jitter frequencies. 79
5.3 Phase error, caused by different frequencies of RF amplitude or RF phase jitter, after the filtering by the recombination scheme and the ideal Drive Beam RF filling function. 80
5.4 Filtering factor of the ideal beam loading function for different bunch charge jitter frequencies. 81
5.5 Phase error, caused by the white noise jitter of the bunch charge, after the filtering by the recombination scheme and the ideal Drive Beam beam loading function for different jitter frequencies. 82
5.6 Phase error caused by 0.05% Drive Beam RF amplitude jitter at different frequencies, calculated with realistic RF filling function. 83
5.7 Phase error caused by 0.1% Drive Beam bunch charge jitter at different frequencies, calculated with realistic beam loading function. 84
5.8 Phase error caused by 0.1% bunch charge jitter without feedback (red) and after feedback with 110 ns latency and 10 ns gain duration (green). 85
5.9 Phase error caused by 0.1% bunch charge jitter without feedback (red) and after feedback with 200 ns latency and 40 ns gain duration (green). 86
5.10 Phase error at lower frequencies without feedback (red) and after feedback with 110 ns latency and 10 ns gain duration (green) and 200 ns latency and 40 ns gain duration (blue). 87
5.11 Total bunch charge error as a function of gain duration and latency time of the charge feedback system. A normalized white noise before the recombination scheme filtering and the feedback application is assumed. 88
5.12 Phase error as a function of jitter frequency with 20 ns gain duration feed-forward. The feed-forward correction application starts at the bunch with the measured error (red curve) and 10 ns earlier (green curve). 89
5.13 Phase error as a function of jitter frequency without feed-forward (red) and with 50 ns (green) and 10 ns (blue) gain duration feed-forward. The tolerance of 14 μm phase error resulting from the BDS energy bandwidth is indicated with a horizontal red line. 90
5.14 Normalized phase error generated by bunch charge errors (top) and Drive Beam RF phase errors (bottom) for different noise spectra. The error value is plotted before recombination (first entry on x-axis), after filtering by the recombination scheme (second entry on x-axis) and after feed-forward correction with different gain times (following entries on x-axis). 92
5.15 Tolerance improvement for the phase error generated by bunch charge (top) and Drive Beam RF phase (bottom) errors for different noise spectra, normalised to the tolerance value after the recombinations scheme. The tolerance improvement is plotted before recombination (first entry on x-axis), after filtering by the recombination scheme (second entry on x-axis) and after feed-forward correction with different gain times (following entries on x-axis). 93

5.16 Phase correction system based on the Main Beam phase measurement (A) and on the external master clock (B). The Main Beam is depicted in blue, the Drive Beam in black, the independent optical system in brown. The small arrows indicate the signal transmission. The red blocks represent the phase monitors and the larger light-blue boxes the feed-forward processor. The green blocks represent the signal of the distributed timing system. 95
5.17 Phase error caused by 0.05% jitter in the accelerator RF amplitude without feed-forward correction (solid red) and with 11.7 MHz bandwidth feed-forward correction (dashed blue). 99
5.18 Phase error caused by jitter in the accelerator RF amplitude for the nominal (dashed blue) and triple (solid yellow) RF filling time with a 11.7 MHz feed-forward correction (linear frequency scale). 99
5.19 Phase error caused by jitter in the accelerator RF amplitude for the nominal (dashed blue) and triple (solid yellow) RF filling time with a 11.7 MHz feed-forward correction (logarithmic frequency scale). 100
5.20 The ratio of the phase error (caused by jitter in the accelerator RF amplitude) filtered by the modified RF filling time structures to the one filtered by the nominal structure. The modified structures have an RF filling time of 0.8 (top), 1.4 (middle) and 2.0 (bottom) relative to the nominal structure. . . . 101
5.21 Total phase error caused by jitter in the accelerator RF amplitude as a function of the RF filling time of Drive Beam accelerating structures. The phase error is induced by white noise in the accelerator RF amplitude. 102
5.22 Total phase error caused by jitter in the accelerator RF amplitude as a function of jitter frequency for nominal (dashed blue) and triple (solid yellow) RF filling time of Drive Beam accelerating structures. The phase error is induced by white noise (top diagram), pink noise (middle) and red noise (bottom) in the accelerator RF amplitude. 103
5.23 Total phase error caused by jitter in the accelerator RF amplitude as a function of the RF filling time of Drive Beam accelerating structures. The phase error is induced by white noise (dashed blue curve), pink noise (dotted yellow curve) and red noise (solid green curve) in the accelerator RF amplitude. 104
5.24 The recombination scheme switching pattern of the nominal 3 TeV mode - 120 even and 120 odd buckets. 105
5.25 The recombination scheme switching pattern of the 2.25 TeV mode - even and odd trains come alternating in groups. 106
5.26 Bunch position after the recombination with the nominal 3 TeV mode switching pattern (top) and with the 2.25 TeV mode switching pattern (bottom). . 106
5.27 Main Beam RF phase error caused by 0.05% Drive Beam RF amplitude error for 2.25 TeV mode. 108

6.1 Layout of the CLIC Test Facility. The positions of the phase monitors are indicated by the blue arrows and the R_{56}-values (in meters) of the chicanes are highlighted by the red boxes. 112
6.2 Average phase of 383 subsequent trains at CTF3 plotted against the train number for all seven phase monitors. 114

6.3 Phase profile of CTF3 train, averaged over 383 subsequent trains. Each point on the x-axis represents a resolution point, full train length on the x-axis is about 1.2 μm. 116
6.4 Phase profile along the average train measured at CL475 monitor, divided in five equal intervals. 117
6.5 Average phase error measured at first four monitors at CTF3 with different R_{56} settings of the stretching chicane for the first and the second datasets. . 119
6.6 Plot of the CTF3 trains' RMS phase profile before (top) and after (bottom) the chicane for the second dataset with $R_{56} = 0.45$ m (left) and $R_{56} = 0.0$ m (right). 120
6.7 Scatter plot of the phase error change in the chicane vs. the dispersive energy measurement in the transfer line (BPI0608 monitor) for the first (top) and second (bottom) datasets with $R_{56} = 0.45$ m. 121
6.8 Scatter plot of the beam energy vs. the incoming phase error measured at CL475 monitor for the first (top) and second (bottom) datasets with $R_{56} =$ 0.45 m. 123
6.9 Scatter plot of the phase error change in the chicane vs. the incoming phase error measured at CL475 monitor for the first (top) and second (bottom) datasets with $R_{56} = 0.45$ m. 124
6.10 Correlation between phase error change in the chicane and klystron amplitude error for the first (top) and second (bottom) datasets with $R_{56} = 0.45$ m. . . 125
6.11 Correlation between phase error change in the chicane and klystron phase error for the first (top) and the second (bottom) datasets with $R_{56} = 0.45$ m. 127
6.12 Correlation between phase error before the stretching chicane (monitor CL475) and klystron phase error for the first (top) and the second (bottom) datasets with $R_{56} = 0.45$ m. 128
6.13 Train mean phase with and without feedback. 130
6.14 Scheme of phase feed-forward system modules. 131
6.15 Depiction of the beam trajectory in TL2 chicane bent by the feed-forward kickers. 132
6.16 Measured phase error at CT and CC monitors along the average train. Monitors are positioned next to TL1 and TL2 chicanes respectively. 133

List of Tables

1.1 Gauge groups and the corresponding fermions of the Standard Model. 4

2.1 Summary of CLIC parameters at the IP. 31

3.1 Matrix of CLIC Drive Beam parameter interdependences in linear approximation. The errors in the parameters of incoming bunches (columns) contribute in the compressor chicane to the errors in the parameters of the outgoing bunches (rows). 53

6.1 Correlation constants of the measured average phase error of the trains between the different monitors. 115

6.2 Phase standard deviation in degrees at 12 GHz. The train is divided into five equal intervals, each about 0.24 μs long, with interval 1 being at the tail and interval 5 at the head of the train. 117

6.3 The phase error at the monitors CL475 and CT (in deg at 12 GHz) depending on the R_{56} setting of the stretching chicane (in m). 119

6.4 Quadratic sums of correlation constants of the klystron phase and amplitude data with the phase error increase in the stretching chicane and the measured beam energy. 126

6.5 Standard deviation of the average train phase with and without feedback. . . 131

6.6 Standard deviation of bunch phase with and without feed-forward. 134

Chapter 1

Introduction

1.1 Outline of the thesis

The introduction chapter of the thesis is aimed at non-experts in the field of particle and accelerator physics. It will briefly introduce the subject and summarise the motivation for the construction of a next generation linear collider. The following chapters are more technically detailed. Chapter 2 describes the Compact Linear Collider (CLIC) and its components as well as the CTF3 facility. Chapters 3, 4, 5 and 6 present the author's original research contributions, if not stated otherwise. Chapter 7 summarises the study and presents a research outlook for the future of this topic.

1.2 Particle physics

1.2.1 History of particle physics

Particle physics deals with the study of the smallest building blocks of matter and matter's most fundamental properties. Its history in Europe began in Antiquity, when the Greek philosopher Democritus hypothesised that matter consists of smallest inseparable blocks, which he called atoms (from the Greek word $\alpha\tau o\mu o\varsigma$, which means indivisible) [1]. Later in the 19th century, when John Dalton and Amedeo Avogadro made the first experimental observation of the entities we call atoms today, they considered these entities to be indivisible, and hence gave them this name [2]. At the end of the 19th and beginning of the 20th centuries it became clear due to the discovery of the electron by Joseph John Thomson [3] and of the atomic nucleus by Hans Geiger and Ernest Rutherford, that atoms are divisible into smaller sub-particles [4]. It was shown that nuclei consist of protons and neutrons. Protons, being positively charged particles, define the placement of the element in the periodic table, neutrons on the other hand add mass to the nucleus. Elements with the same number of protons but different numbers of neutrons are called isotopes.

In the 1960s the discovery of a large number of particles (the so-called particle zoo) led

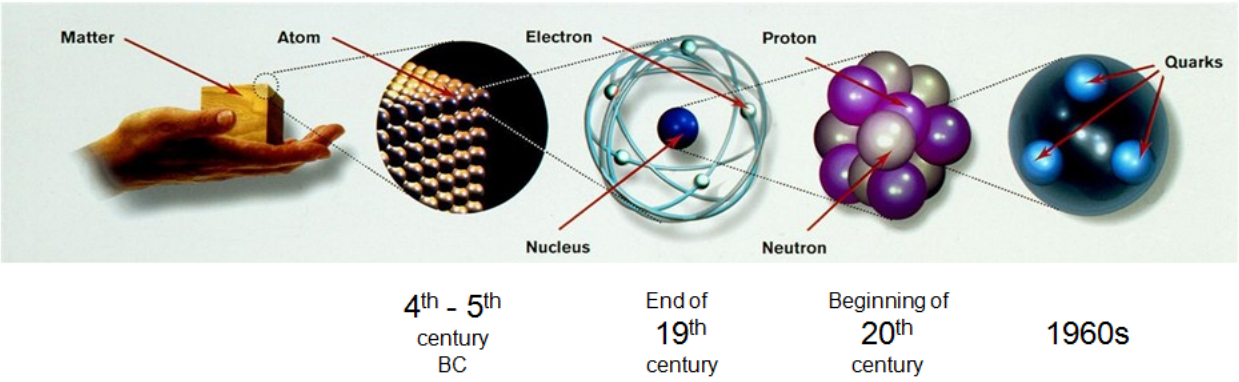

Figure 1.1: Representation of the history of the matter structure investigation.

to the hypothesis that they can be described as consisting of a smaller number of inseparable sub-particles called quarks. Experiments in which the particles were brought into collision by accelerators showed that the quarks are not only a theoretical concept for the description of the particles they form, but are physical objects [5].

In parallel with the investigation of particle composition at smaller and smaller scales, theories concerning the nature of the particles have changed during the 20th century. In the beginning of the century it was shown that the electrons' orbits can only have discrete energy values in the electromagnetic potential of the nucleus [6]. It was also shown that light is not a continuous stream of energy, but is separated in minimal portions called quanta [7]. With that Quantum Mechanics was born - the theory in which matter is described by a so-called quantum field of probability for a particle to be located at a given position.

Simultaneously with Quantum Mechanics another theory - Special Relativity - was developed by Albert Einstein [8]. The theory unified time and space in one single spacetime and changed our understanding of matter properties, in particular at velocities approaching the speed of light, which is postulated by Einstein as the maximal speed for any interaction. This theory has been merged with quantum mechanics to form Quantum Field Theory, a relativistic version of Quantum Mechanics. Quantum Field Theory describes the interaction between quanta as an exchange of other quanta, e.g. the electromagnetic repulsion of two electrons as an exchange of photons. So all charged particles and their interactions are described by the dynamic quantum fields.

1.2.2 The Standard Model

The Standard Model (SM) is a theory which systematises all known elementary particles and orders them by their properties [10] [11]. As one can see in Fig.1.2 the theory describes two types of matter - quarks and leptons [12], which are called fermions. SM fermions are particles with a spin value of 1/2, spin being a quantum quantity similar to the angular

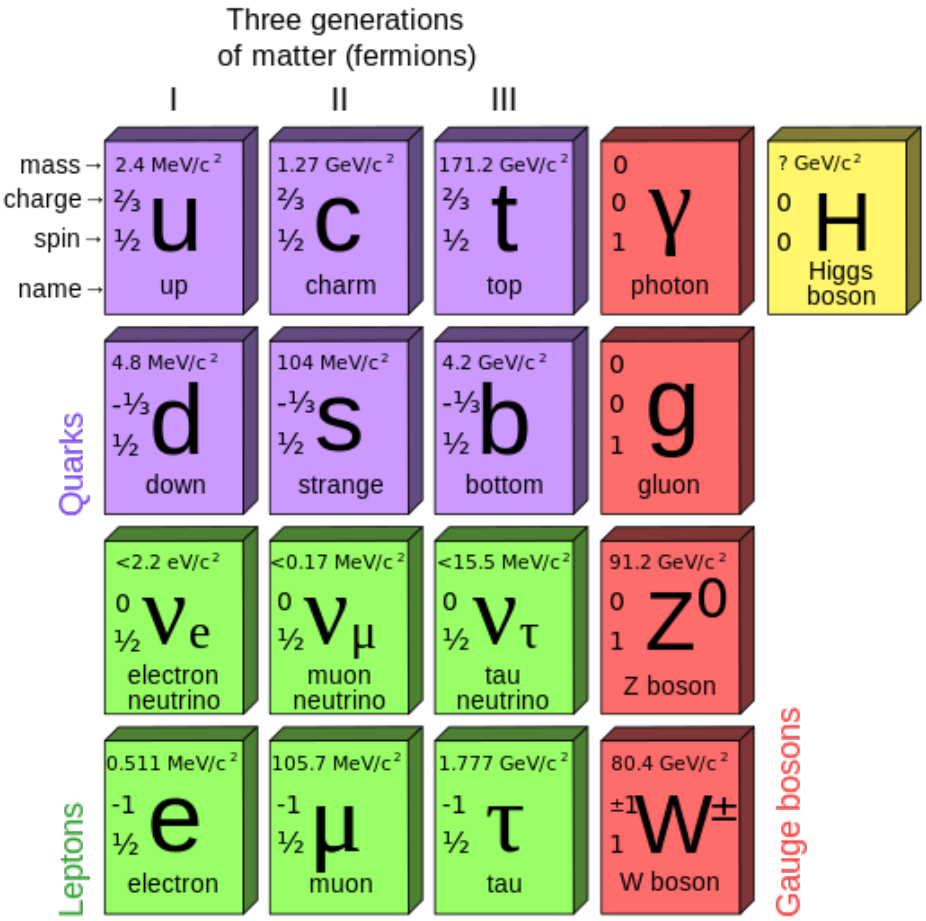

Figure 1.2: Table of fundamental particles of the Standard Model [9].

momentum in classical mechanics.

Quarks are particles which cannot be observed individually. The reason is that the energy needed to separate them is higher than the energy for creation of quark-antiquark pairs from the vacuum. Hence each time the quarks are pulled apart by some powerful interaction, a created quark and antiquark pair connects to the original separating quarks and so forms more complex particles again [13].

In the Standard Model the forces are transmitted by bosons, spin 1 particles. The SM includes three of four known interactions - the electromagnetic, weak and strong interactions. The gravitational interaction could not be implemented so far into the theory for mathematical reasons and is also too weak compared with the other three interactions in order to be tested experimentally in elementary particle physics experiments.

A mathematical description of the SM is provided by group theory [14]. The interactions between the particles can be described as symmetry transformations within a gauge group, meaning that the function describing the dynamics of the system, called the Lagrangian, stays invariant under certain local transformations. The Standard Model is based on a

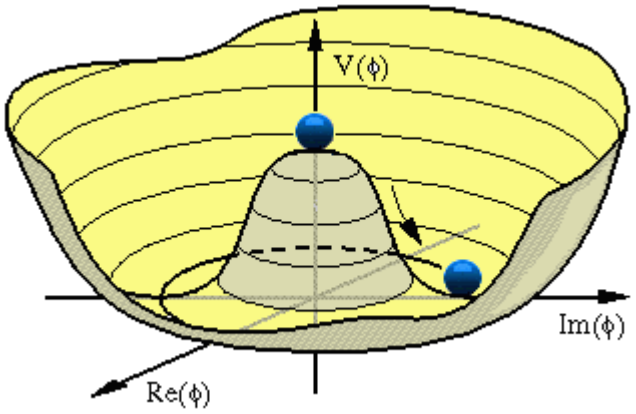

Figure 1.3: Representation of the Higgs mechanism. The symmetry in the centre is spontaneously broken when the particle moves to the minimum of the potential [17].

gauge group

$$G = SU(3)_C \times SU(2)_L \times U(1)_Y \tag{1.1}$$

where C, L and Y represent the gauge properties of the strong interaction charge called colour, and of the electroweak interaction's left-handed helicity and hypercharge respectively.

The fermions of the Standard Model can be represented by the elements of the gauge groups as shown in Tab. 1.1.

$L_L(1,2,-1/2)$	$Q_L(3,2,1/6)$	$E_R(1,1,-1)$	$U_R(3,1,2/3)$	$D_R(3,1,-1/3)$
$\begin{pmatrix} \nu_e \\ e \end{pmatrix}_L$	$\begin{pmatrix} u \\ d \end{pmatrix}_L$	e_R	u_R	d_R
$\begin{pmatrix} \nu_\mu \\ \mu \end{pmatrix}_L$	$\begin{pmatrix} c \\ s \end{pmatrix}_L$	μ_R	c_R	s_R
$\begin{pmatrix} \nu_\tau \\ \tau \end{pmatrix}_L$	$\begin{pmatrix} t \\ b \end{pmatrix}_L$	τ_R	t_R	b_R

Table 1.1: Gauge groups and the corresponding fermions of the Standard Model.

Higgs mechanism

The mass of the SM particles is assumed to be provided by the Higgs mechanism. The mechanism implies the existence of the Higgs field, to which all massive particles couple. The minimum of the Higgs field potential for the massive particles is not zero, and so when particles change to the minimal energy state via spontaneous symmetry breaking they receive their mass values (Fig. 1.3). The Higgs theory received a strong confirmation by the discovery of a Higgs-like boson at CERN in summer 2012, though the properties of the boson are still to be further investigated (status: spring 2013) [15], [16].

1.2.3 Present research fields of particle physics

The Standard Model, though being a broad theory, which describes all known elementary particles and three of four interaction forces, does not explain several essential aspects of modern physics. Hence, there is an intensive search for extensions of the SM or development of an underlying theory.

One of the aspects not described by the SM is the gravitational force. In classical Newtonian mechanics objects move along curved trajectories because of the attractive force of gravity. In modern physics gravity is described by General Relativity, which assumes that massive objects bend spacetime. Bodies move under the influence of gravity along straight trajectories, but in a bent spacetime, so that there is an impression of moving in a curve. This theory is applicable and well verified at cosmic scales for massive bodies like planets, stars, galaxies or galaxy clusters, but it is not clear how it can be brought into coherence with Quantum Field Theory, which is valid on the microscopic scale for small objects like elementary particles. The branch of theoretical physics that attempts to unify General Relativity and Quantum Field Theory is called Quantum Gravity.

Another important question arises from astrophysical observations that show that the baryonic matter (meaning matter consisting of baryons, particles composed of three quarks) that we can observe in the universe is only responsible for 4 % of its total energy and mass. 73 % of the total mass-energy is so-called dark energy, which accelerates the expansion of the universe. Another 23 % is dark matter, the unknown form of massive matter the existence of which is indicated by such factors as the rotational speeds of galaxies, gravitational lensing and the temperature distribution of the hot gas in galaxies.

One of the possible candidates for the dark matter is presented by supersymmetry, the theory that assumes that every fermion or boson has a supersymmetric partner, a boson or a fermion respectively [18] [19]. These supersymmetric particles are supposed to be more massive than their SM counterparts and so could be responsible for the unobserved mass in the universe. The search for these particles is one of the main challenges of accelerator physics. Additionally to presenting candidates for dark matter, supersymmetry could solve the so-called hierarchy problem, the large difference between the Planck energy (the energy at which gravity starts playing an important role in quantum interactions) and the mass of the Higgs boson and consequently of W and Z bosons.

Supersymmetry, despite some lack of a deeper explanatory power (supersymmetry has more free parameters than the SM and postulates many unobserved particles) is of particular interest for theoretical physics since, if verified, it could be a hint for the validity of string theory. String theory attempts to explain all existing particles as the vibration modes of elementary strings. String theory, though being partially based on speculative mathematical assumptions and not being experimentally validated, could be a good candidate for the "theory of everything", since it has a potential to explain Quantum Field Theory, General Relativity and the existence of particles by a simple concept of vibration modes of identical

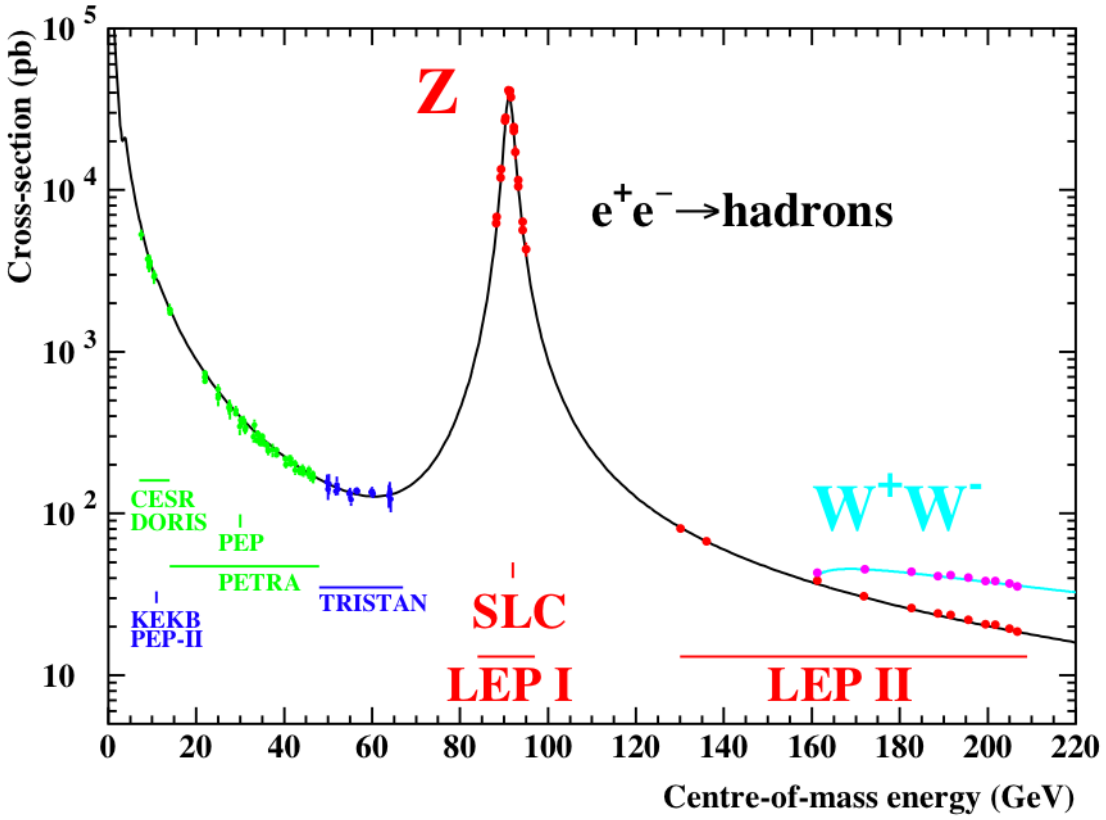

Figure 1.4: The resonant peak of the Z boson [20].

strings.

1.3 Accelerators and colliders

Accelerators and colliders have been the most successful way of studying particle physics in the last half century. In these machines charged particles such as protons or electrons are accelerated via an electromagnetic field to a high kinetic energy and are brought into collision in the middle of a detector. According to Quantum Field Theory different sorts of particles can be transformed into one another, so the result of the collision may include particles different for the ones which entered it. Special Relativity states that energy is equivalent to mass, $E = mc^2$, and hence the higher the kinetic energy of a collision, the higher is the mass of the particles which can be created in it. This fact prompted the progress of accelerator physics to reach higher and higher collision energies.

The new particles are discovered as the peaks of interaction probability at some energies. These peaks are called resonant peaks - an example of such a peak is shown in Fig. 1.4. From the width of the resonant peak (Γ) the lifetime of the particle (τ) can be calculated.

$$\Gamma = \frac{\hbar}{\tau} \tag{1.2}$$

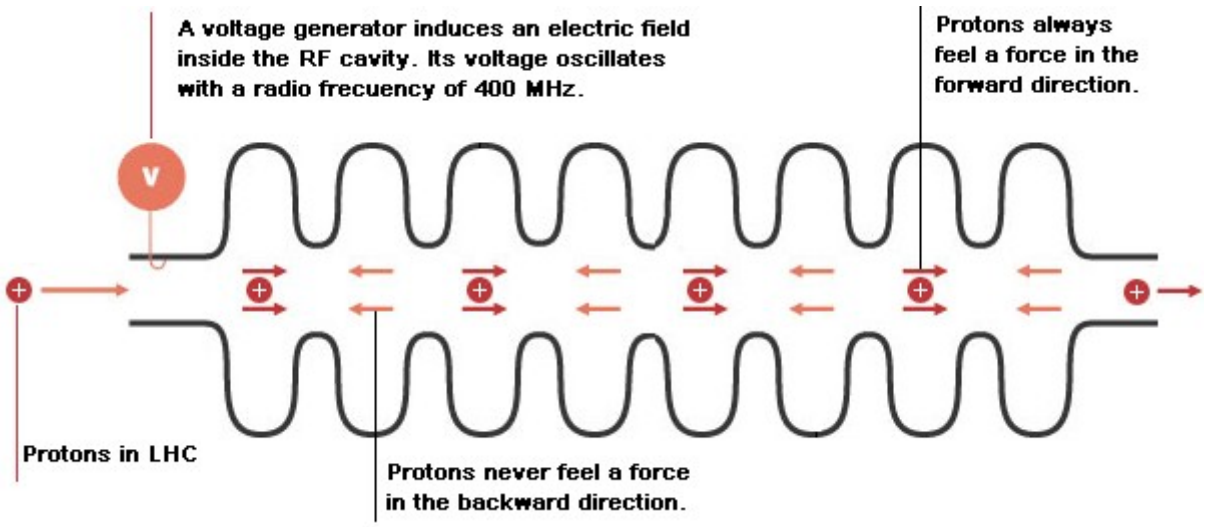

Figure 1.5: Scheme and description of LHC accelerating cavity [21].

with $\hbar$ being the reduced Planck constant.

A research frontier of particle colliders has been also the luminosity - the density of the particle flow in the interaction region. The higher the luminosity of an accelerator, the higher is the total number of interactions and the easier is the observation of new particles or phenomena, since the precision of the measurements performed in the collision experiment increases with the experiment's event rate. The luminosity is given by

$$\mathcal{L} = f_{rep} N_b \frac{N_1 N_2}{4\pi\sigma_x\sigma_y} \tag{1.3}$$

with f_{rep} being the repetition rate of the beam pulses, N_b the number of particle bunches per pulse, N_1 and N_2 the number of particles per bunch of both colliding beams and σ_x and σ_y the size of the interaction cross section in the horizontal and vertical planes respectively.

1.3.1 Beam Dynamics

The acceleration of particles in a collider is performed via a standing or travelling electric field wave in the accelerating modules, the so-called radio frequency (RF) cavities. When power is supplied to the cavities, the RF wave fills them and the particle bunches can be accelerated as shown in Fig. 1.5. The accelerating voltage integrated over the length of the structure is called the RF filling, the energy absorbed by the particle bunches is called beam loading.

The trajectory of the particles in a synchrotron is bent into a circle by dipole magnets. The beam is focused with the help of quadrupole magnets, which act like optical lenses on the beam, focusing it in one transverse dimension and defocusing it in the other. For that

reason the layout of the magnets is called the "optical lattice" in accelerator physics. The optical lattice is simulated and designed with the help of computer programs (e.g. MAD-X [22]). Directed by the quadrupole magnets particles perform an oscillation in the transverse dimensions, which is called betatron oscillation.

The position (x, y or z) and angle ($x^{'}$, $y^{'}$ or $z^{'}$) of a particle in one plane in the accelerator can be described as a two-dimensional vector. Hence, with two transverse and one longitudinal dimension the particle's state in the accelerator can be described with a 6-dimensional vector. The movement along the accelerator can be described by a transfer matrix, M (Eq. 1.4).

$$\begin{pmatrix} x_1 \\ x_1^{'} \\ y_1 \\ y_1^{'} \\ z_1 \\ z_1^{'} \end{pmatrix} = \begin{pmatrix} R_{11} & R_{12} & R_{13} & R_{14} & R_{15} & R_{16} \\ R_{21} & R_{22} & R_{23} & R_{24} & R_{25} & R_{26} \\ R_{31} & R_{32} & R_{33} & R_{34} & R_{35} & R_{36} \\ R_{41} & R_{42} & R_{43} & R_{44} & R_{45} & R_{46} \\ R_{51} & R_{52} & R_{53} & R_{54} & R_{55} & R_{56} \\ R_{61} & R_{62} & R_{63} & R_{64} & R_{65} & R_{66} \end{pmatrix} \begin{pmatrix} x_0 \\ x_0^{'} \\ y_0 \\ y_0^{'} \\ z_0 \\ z_0^{'} \end{pmatrix} \tag{1.4}$$

The longitudinal position of the bunches z can be expressed in terms of an angle of a sinusoidal RF wave. This angle is called the phase (ϕ).

A parametrisation of the transfer matrix can be performed with the help of the so-called Twiss parameters: β (transversal modulation function resulting from focusing properties of the lattice), α (change of β along the lattice) and μ (phase advance). Eq. 1.5 shows such a parametrisation in one dimension.

$$\mathbf{M} = \begin{pmatrix} \sqrt{\frac{\beta_1}{\beta_0}} \left[\cos\mu + \alpha_0 \sin\mu\right] & \sqrt{\beta_0\beta_1} \sin\mu \\ -\frac{1+\alpha_0\alpha_1}{\sqrt{\beta_0\beta_1}} \sin\mu + \frac{\alpha_0-\alpha_1}{\sqrt{\beta_0\beta_1}} \cos\mu & \sqrt{\frac{\beta_0}{\beta_1}} \left[\cos\mu - \alpha_1 \sin\mu\right] \end{pmatrix} \tag{1.5}$$

From the Twiss parameter β one can calculate the transverse size of the beam spot σ:

$$\sigma_{x,y,z} = \sqrt{\epsilon_{x,y,z}\beta_{x,y,z}} \tag{1.6}$$

with ϵ being the mean spread of particles in position-momentum phase space called the emittance. The emittance can be normalised so that it is a conserved quantity during the beam acceleration. This Lorentz invariant emittance ϵ^* can be expressed as

$$\epsilon^* = \beta\gamma\epsilon. \tag{1.7}$$

The luminosity of a collider is higher if the beam spot size at the interaction point is small, $\mathcal{L} \propto 1/\sigma$.

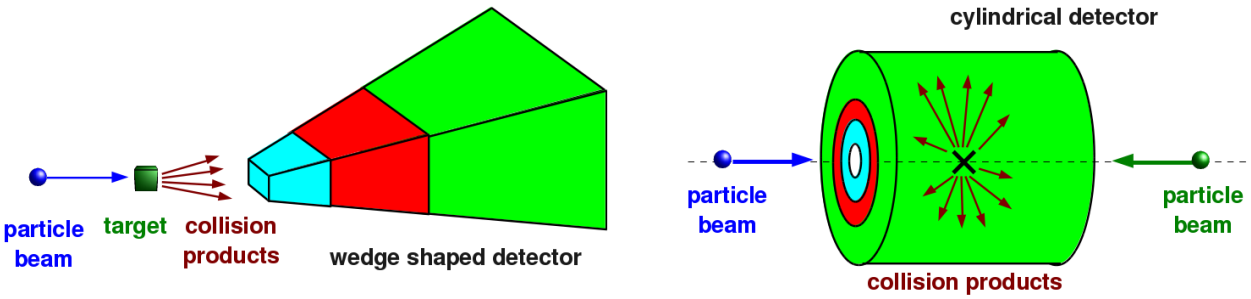

Figure 1.6: A fixed-target collider (left) and a two-beam collider (right) [23].

1.3.2 Fixed-target and two-beam colliders

The first particle collider experiments, starting with Rutherford's gold foil experiment, were fixed target experiments, where a beam is collided with a fixed piece of material (see Fig. 1.6, left). This type of experiment has the advantage that the fixed target is large and easy to hit with a beam, and hence the luminosity of the experiment is high. The total energy of the collision in the centre of mass system for such an experiment can be calculated with

$$E_{coll} = \sqrt{2m_0c^2E_p} \tag{1.8}$$

$$\Leftrightarrow E_p = \frac{E_{coll}^2}{2m_0c^2} \tag{1.9}$$

where E_{coll} is the collision energy in the centre-of-mass system, m_0 is the mass of the fixed-target particle at rest and E_p is the kinetic energy of the particles in the beam. This means the total collision energy scales with the square root of the beam energy.

Another type of collider is a two-beam collider, where two beams of particles are directed towards each other head-on under some small angle, so that they cross in the middle of a detector (see Fig. 1.6, right). This method requires higher beam intensities and beam stabilisation in order to achieve a significant luminosity, but the energy of such collisions is given by

$$E_{coll} = 2E_p \tag{1.10}$$

with both beams having the same energy E_p. So the collision energy scales linearly with the beam energy making two-beam colliders more suitable for modern high-energy physics purposes.

1.3.3 Synchrotrons and linear colliders

There are two versions of modern high-energy two-beam colliders - synchrotrons and linear colliders.

A synchrotron is a circular machine, where the beam is held in a closed circular trajectory by dipole magnets. This form of collider has the advantage that the same accelerating

modules can be used over and over each circuit the particles make in the machine. On the other hand, charged particles lose electromagnetic energy when their trajectory is bent at each dipole magnet via so-called synchrotron radiation. The power loss due to synchrotron radiation is given by

$$P = \frac{e^2 c \gamma^4}{6\pi\epsilon\rho^2} \tag{1.11}$$

where e is the electromagnetic charge, c is the speed of light, γ is the relativistic Lorentz factor, ϵ the vacuum permittivity and ρ the bending radius.

A linear collider is a machine in which the particles are accelerated along a straight line and then brought into collision. Since the particles make only one pass in the linear collider, these machines are composed for the most part of accelerating cavities in order to provide a strong acceleration. This form of collider has the advantage that there is no energy loss due to synchrotron radiation, but since the beams can be collided only once and have to be dumped afterwards, it is challenging to reach high luminosity.

There are two requirements for the particles used in the colliders. First, in order to be accelerated by an electromagnetic field the particles must have electric charge. Second, the particles must be stable for the time of the acceleration. In modern accelerators usually three types of particles are used - electrons, protons and ions. The electrons have about 2000 times smaller mass than the protons, so at the same energy their Lorentz factor γ is significantly higher. This means that the power loss due to the synchrotron radiation (Eq. 1.11) for high-energy electron machines is a factor 10^{13} higher than for proton machines. Consequently, the power loss is the limiting factor for the energy achievable in circular electron machines.

Circular proton and ion accelerators do not have a significant power loss due to synchrotron radiation, but the magnet strength required for keeping the particles in circular trajectory is much higher, setting the energy limitations.

For linear colliders the maximal energy is defined by the accelerating gradient of the machine multiplied by the total length of the accelerating structures. A too high accelerating gradient leads to electromagnetic breakdown in the accelerating cavities and the length of the machine is proportional to its costs, so the gradient and length are the energy limiting factors for linear colliders.

1.3.4 LHC and the need for a future lepton collider

The Large Hadron Collider (LHC) (see Fig. 1.7) in operation at CERN is at the moment the accelerator with the highest collision energy. It is 27 km long and is designed to collide two proton beams with energy of 7 TeV each, totalling 14 TeV of centre-of-mass collision energy (it had been operated at maximally 8 TeV collision energy by 2012). The accelerator

is built using superconducting technology, its magnets operating at a temperature of 1.9 K. There are four beam crossing points with corresponding detectors around them - ATLAS and CMS for general purposes, ALICE for the study of the quark-gluon plasma generated in heavy ion collisions and LHCb for the study of matter and antimatter.

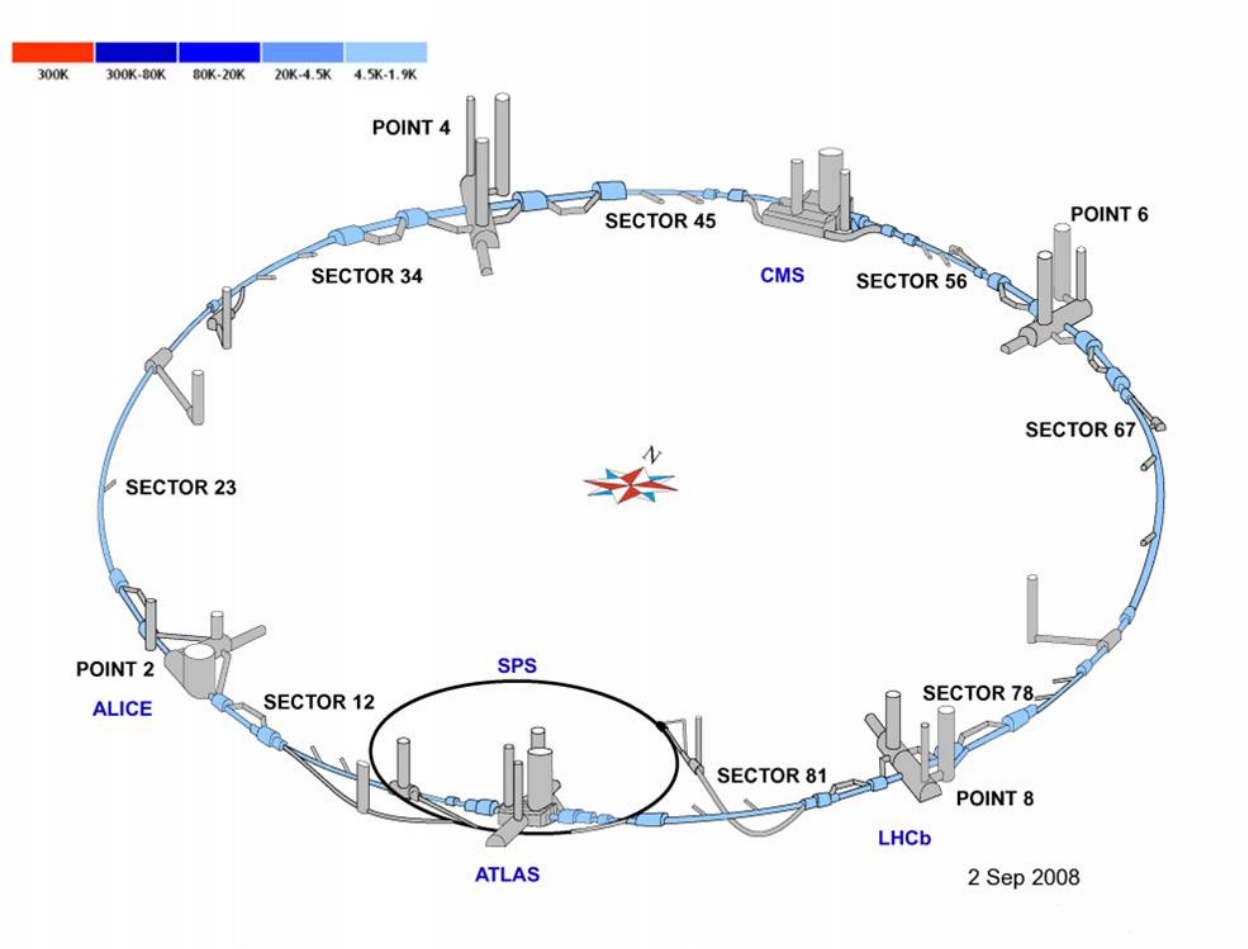

Figure 1.7: Schematic layout of the Large Hadron Collider [24].

Protons are not elementary particles but consist of quarks and gluons and these elementary particles each carry only a fraction of the collision energy of protons. The probability for proton sub-particles to carry a given fraction of a proton's energy is given by the parton distribution function (Fig. 1.8). This function is non-zero for most of the probability values, so the energy of the elementary particle collisions at LHC cannot be precisely pre-defined. This makes the analysis of LHC data very challenging and removes the possibility of energy scans in energy regions where new discoveries are possible. Leptons on the other hand are elementary particles and these problems do not occur for them - the kinematics of a lepton-lepton collision are clear, there are no underlying events and the energy of the collision can be set quite precisely. Additionally, the detector can be located much closer to the interaction point, which increases the measurement precision.

There are six known leptons, but electrons, being the lightest leptons, are good candidates

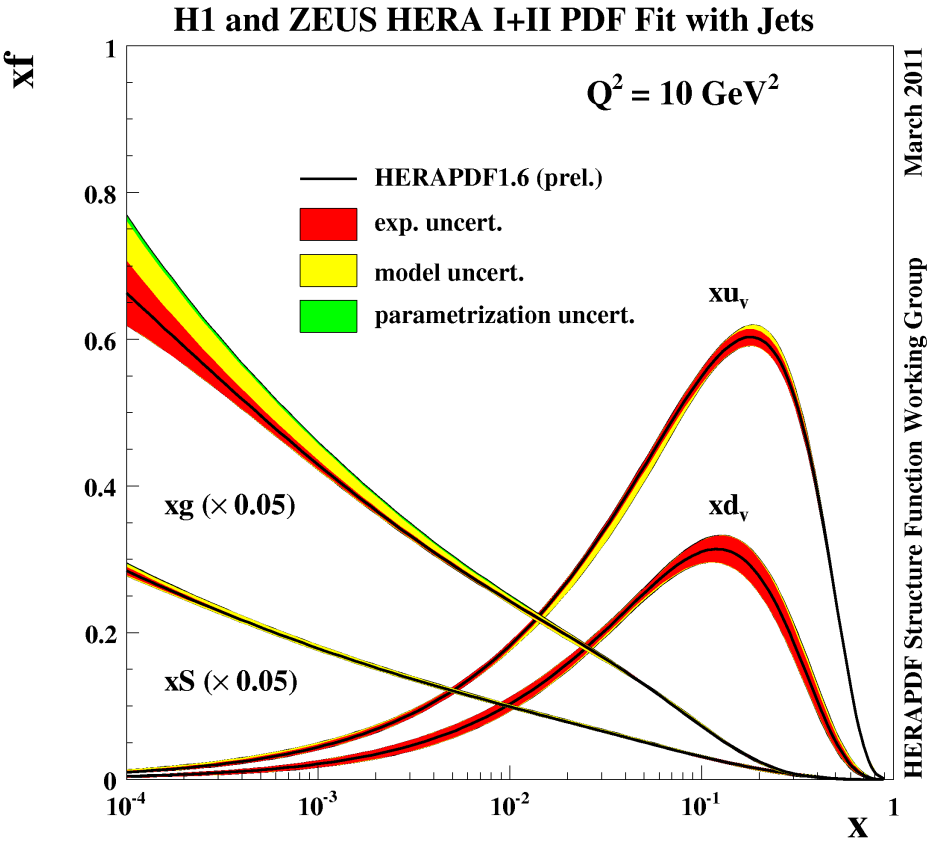

Figure 1.8: Parton distribution functions measured at H1 and ZEUS experiments (DESY, Hamburg). The probability densities for finding a gluon (xg), a virtual quark (xS) and a real up- or down-quarks (xu and xd respectively) are plotted as functions of momentum fraction x. Total momentum transfer is $Q^2 = 10$ GeV^2 [25].

for being used in an accelerator, since they are the only charged stable leptons. In a new high-energy collider they would be collided with their anti-particles, positrons, since these collisions result in the annihilation of the both electron and positron, so that the total energy of the collision can be transformed into new particles. However synchrotron radiation losses in circular high-energy electron colliders are large, e.g. the most powerful electron-positron collider, LEP2, which was in the same tunnel as used for LHC, had a length of 27 km and lost 3% of its 105 GeV beam energy each turn [26]. The energy loss via the synchrotron radiation is proportional to the fourth power of the relativistic factor γ, (see Eq. 1.11), which is proportional to beam energy, so for a collider at the TeV energy scale the losses would be significantly higher. Hence, at this energy scale a linear collider is more feasible.

There are two large design projects for a future high-energy linear e^+e^- collider - the International Linear Collider (ILC) and the Compact Linear Collider (CLIC).

International Linear Collider

The International Linear Collider (Fig. 1.9) is a proposed electron-positron collider, with a collision energy of 0.5 TeV, extendable to 1 TeV. The project emerged when the efforts for the design of the Next Linear Collider (NLC), the Global Linear Collider (GLC) and the Teraelectronvolt Energy Superconducting Linear Accelerator (TESLA) were combined in 2004. The collider is designed to use superconducting accelerating cavities operating at a temperature of 2 K with gradient of 31.5 MV/m [27]. The total length of the collider is planned to be ∼31 kilometers, in addition there are two damping rings each with a circumference of 6.7 kilometers. The beam size in the interaction region is $640{\times}6\ nm^2$ [28], which will allow ILC to have a peak luminosity of $2 \times 10^{34}\ \mathrm{cm}^{-2}s^{-1}$ [29]. The electron and positron beams are designed to have a polarisation of at least 80% and 30% respectively. It is possible to upgrade the system to achieve a positron beam polarisation of up to 60%.

Compact Linear Collider

The Compact Linear Collider (CLIC) is a project in development by CERN and 42 other institutions [31]. Different designs of the collider exist, with energies ranging from 0.5 to 3 TeV, with 3 TeV being the baseline design energy. CLIC is based on a two-beam-scheme and is designed to extract the RF energy from high-current low-energy Drive Beams and use this energy for acceleration of the low-current high-energy Main Beams. The Main Beams are then brought into collision [32]. Further technical details of CLIC and CTF3 can be found in Chapter 2.

Other future colliders

Additionally to the ILC and CLIC projects there are other possibilities for providing the basis for potential future lepton colliders.

One proposal is the LEP3 e^+e^- collider that would be situated in the LHC tunnel. With only small upgrades to LEP2 collider design one could increase the centre-of-mass energy to 250 GeV and hence produce Higgs bosons with large luminosity [33]. However, no large improvement of the collision energy would be possible at LEP3 because of the synchrotron radiation losses and hence it would not get close to the energy frontier of the LHC.

The Muon Collider [34] is a proposed machine for colliding muons, leptons similar to the electrons, which are heavier and unstable. This higher mass allows muons to be accelerated in synchrotrons without significant radiation losses and couples them more strongly to the Higgs field, hence allowing production of larger number of Higgs bosons in the collisions. However, the acceleration and collision have to be performed before the muons decay. Also muons cannot be found in ordinary matter and hence have to be produced first in particle collisions. After the collision the transverse emittance of the muon beam is extremely high and must be strongly reduced simultaneously with muon beam acceleration. The process of

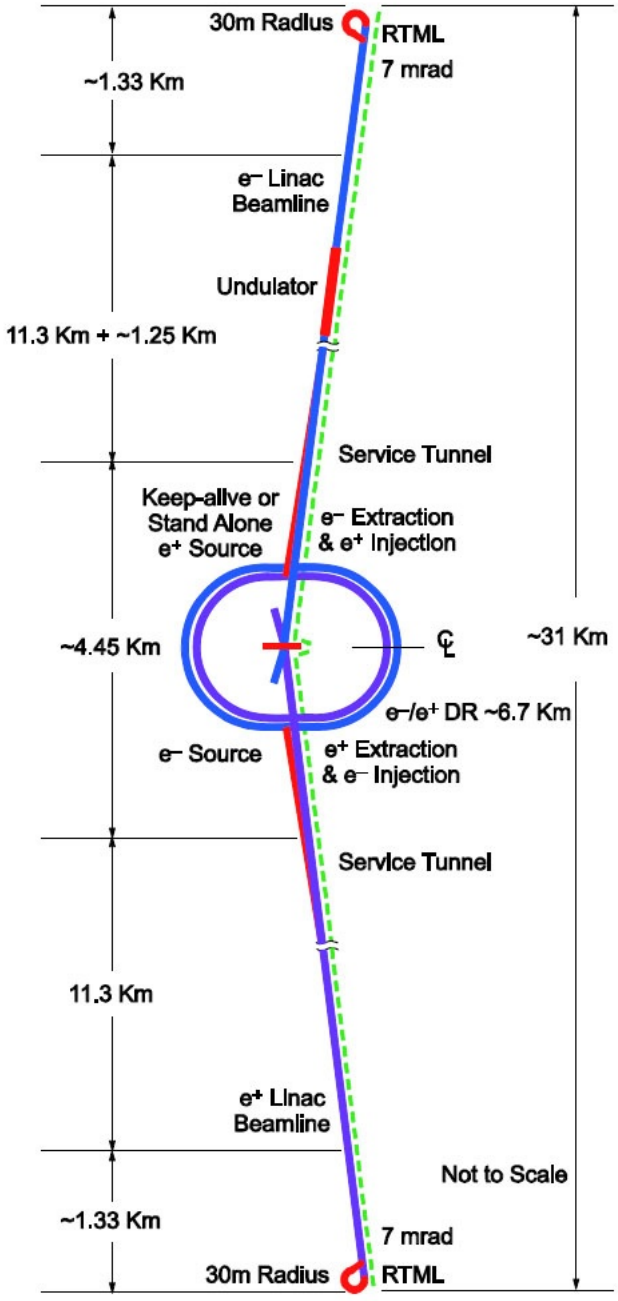

Figure 1.9: Schematic layout of the ILC for 500 GeV collision energy [30].

emittance reduction is refered to as muon cooling and it poses the main challenge for the Muon Collider design at the moment.

Alternative schemes of laser and plasma acceleration are also being developed. In these schemes the acceleration is provided not by the means of an RF wave in the accelerating cavities as in colliders nowadays (see section 1.3.1), but by a traveling electromagnetic field generated in a plasma, which is produced either by an electron beam or a laser pulse. These schemes could potentially produce a very high accelerating gradient, but are at the moment technically far from application at a real high-energy collider.

1.4 Feedback On Nanosecond Timescale

The luminosity of two-beam colliders can be strongly reduced if the beams have a relative offset at the interaction point. This offset can be caused by instabilities in the electrical supply to the collider lattice elements or by external vibrations.

Electrical noise in power supplies can lead to instabilities in the fields of the magnets and the electric field of the accelerating cavities. This can lead to a higher beam emittance and errors in the focusing by the so-called beam delivery system, which transports the beams from the exit of the accelerators to the interaction point (IP). These type of errors can be reduced by feedback or feed-forward systems for the different parameters of the machine.

The external vibrations can be caused by seismic activities, civilisation noise or even sea waves. Measurement of the ground vibration amplitude as a function of vibration frequency is presented in Fig. 1.10. Generally the vibration amplitude is proportional to $1/\omega^4$ (with ω being the frequency of the vibration), with some additional noise at the different locations due to the impact of civilisation, different ground structure etc. For all locations the high-frequency motion is not of a high importance, since its amplitude is low.

On the other hand, if the frequency of the ground motion is very low (and hence the wavelength is very large) all of the points of the collider move simultaneously. Hence, the beams are moved into the same direction and no luminosity loss occurs. Fig. 1.11 shows the correlation between the movement of two points 100 m apart, which is a typical lenth of the betatron oscillation, measured at SLAC. As one can recognise, the correlation of the movement of the points is nearly one for the low frequencies. Also, slow feedback systems can correct the low-frequency variation in beam parameters quite effectively.

From these considerations one can conclude that only vibrations in a window of frequencies from 0.1 Hz up to 100 Hz can cause a significant luminosity loss. It is crucial to stabilise the collider at the IP against these vibrations.

The Feedback on Nanosecond Timescale (FONT) group of the University of Oxford is developing fast responding feedback systems for performing such stabilisation. These function in the following way (see Fig. 1.12): if the bunches miss one another at the IP of a collider, they still interact electromagnetically (since they are electrically charged) and

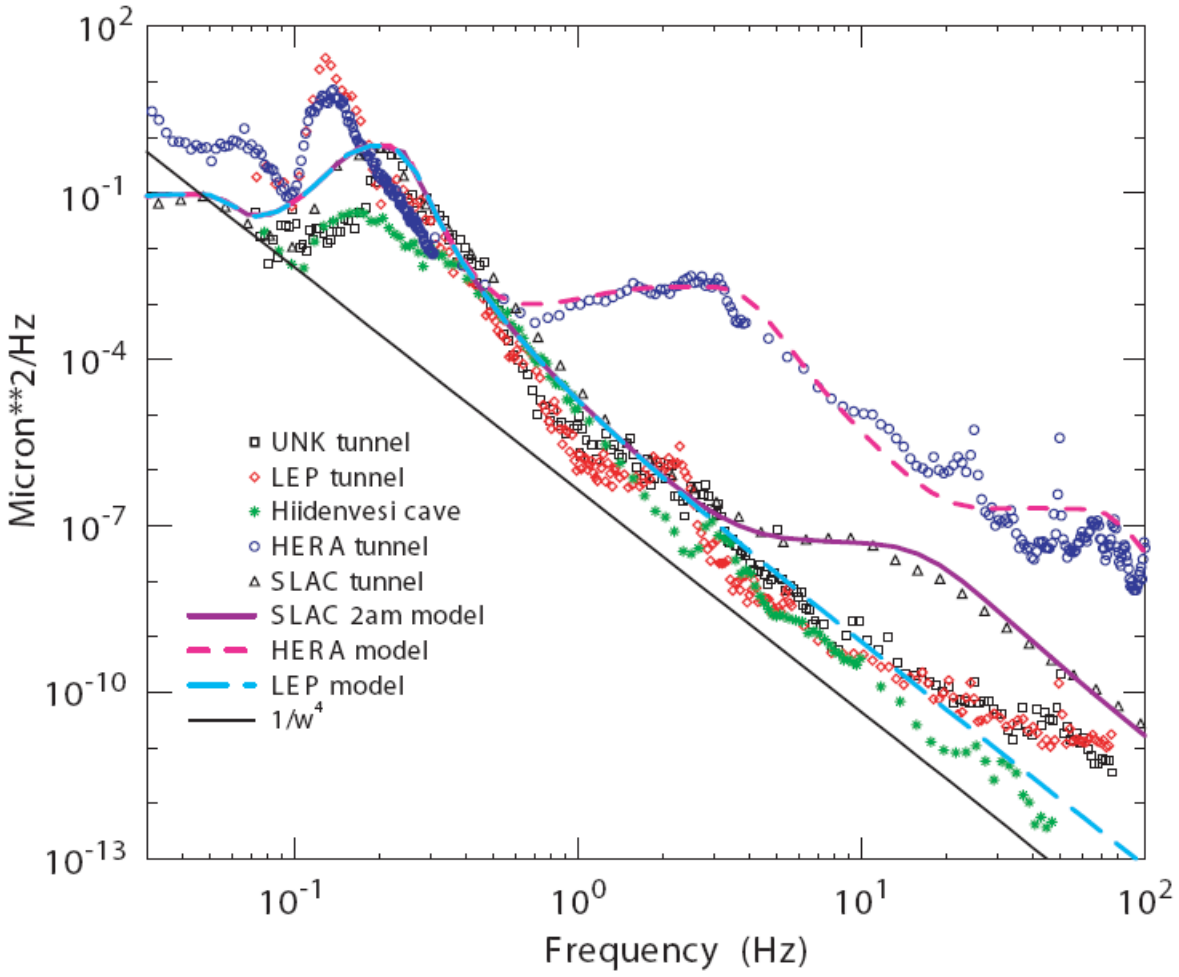

Figure 1.10: Amplitude of the ground motion as a function of motion frequency measured at different locations. [35].

deflect, changing their trajectory. This trajectory change can be measured by beam position monitors downstream of the beam. The signal of the measurement is amplified and sent to the electromagnetic kicker, which applies a voltage to change the trajectory of the next bunches in order to bring the beams back into collision.

The total process takes several tens of nanoseconds, depending on the position of the beam position monitors, kickers and the cabling of the system. The process must happen as fast as possible, since the train length of future colliders is only of the order of ms (for ILC) or even hundreds of ns (for CLIC). Also, a high degree of bunch-to-bunch position correlation along the train must be assured for successful correction; this can be reduced by high frequency instabilities.

Fig. 1.13 shows the impact of the FONT 2 system operation at the NLC Test Accelerator [38]. On the y-axis one can see the transverse beam position as a function of time. The first figure on top shows the offset, which was artificially induced in order to test the functionality of the correction by the FONT system. The second figure shows the effect of the beam flattener. The third figure shows the impact of the feedback system - the error is reduced

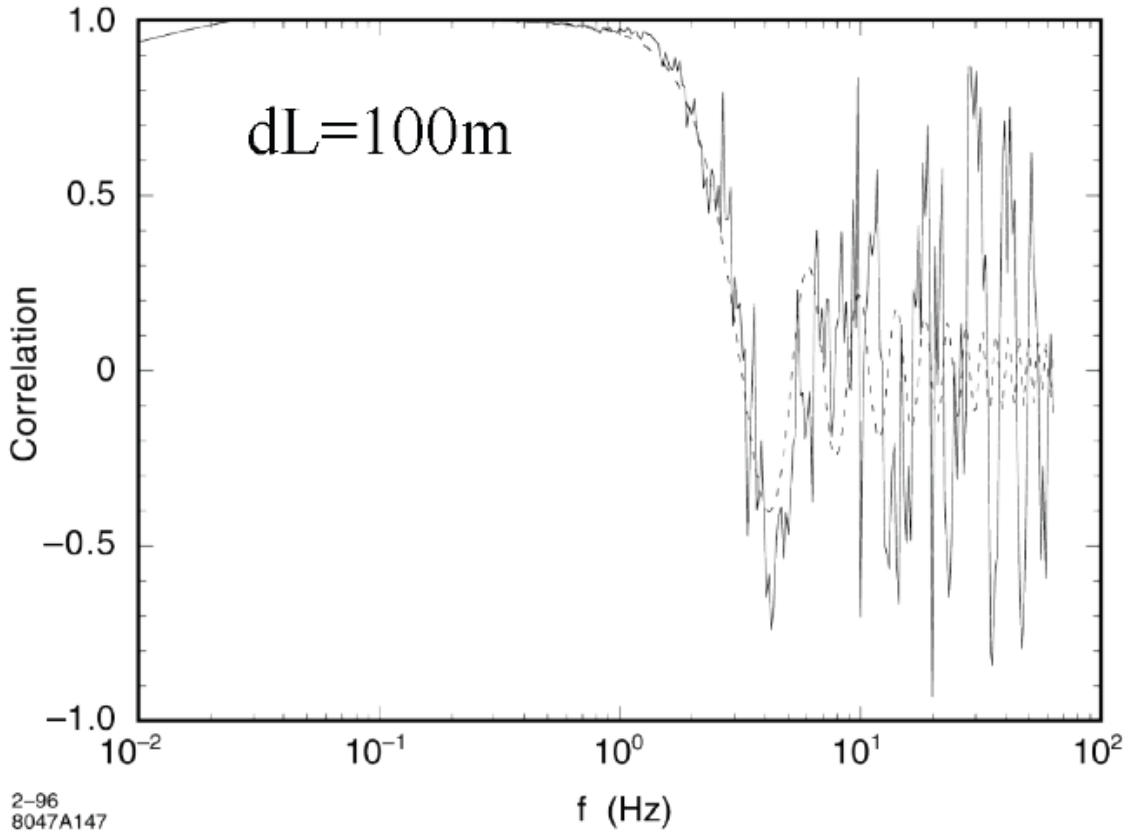

Figure 1.11: Correlation of the movement of two points in 100 m distance for different ground motion frequencies [36].

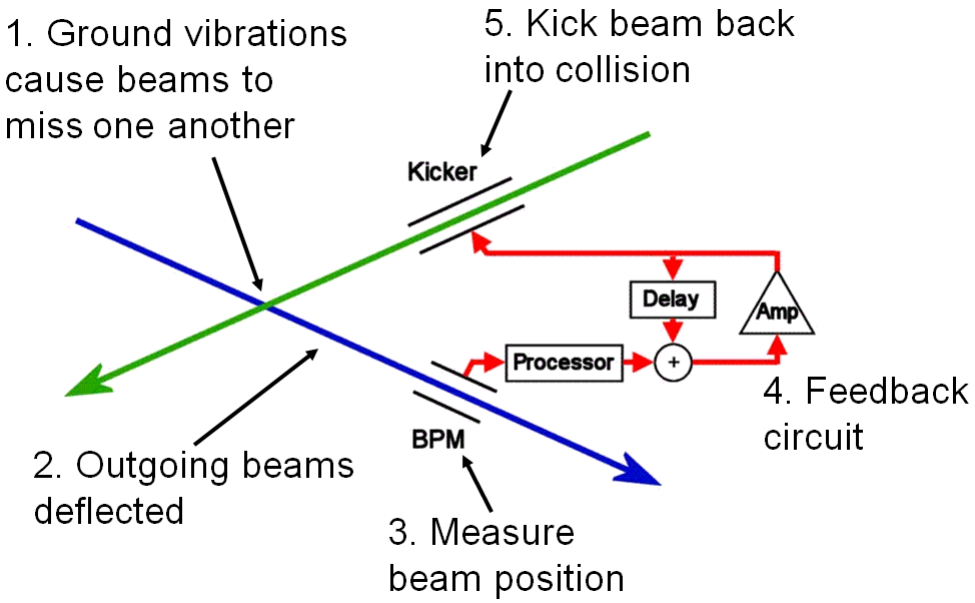

Figure 1.12: Layout and operating mode of the FONT system [37].

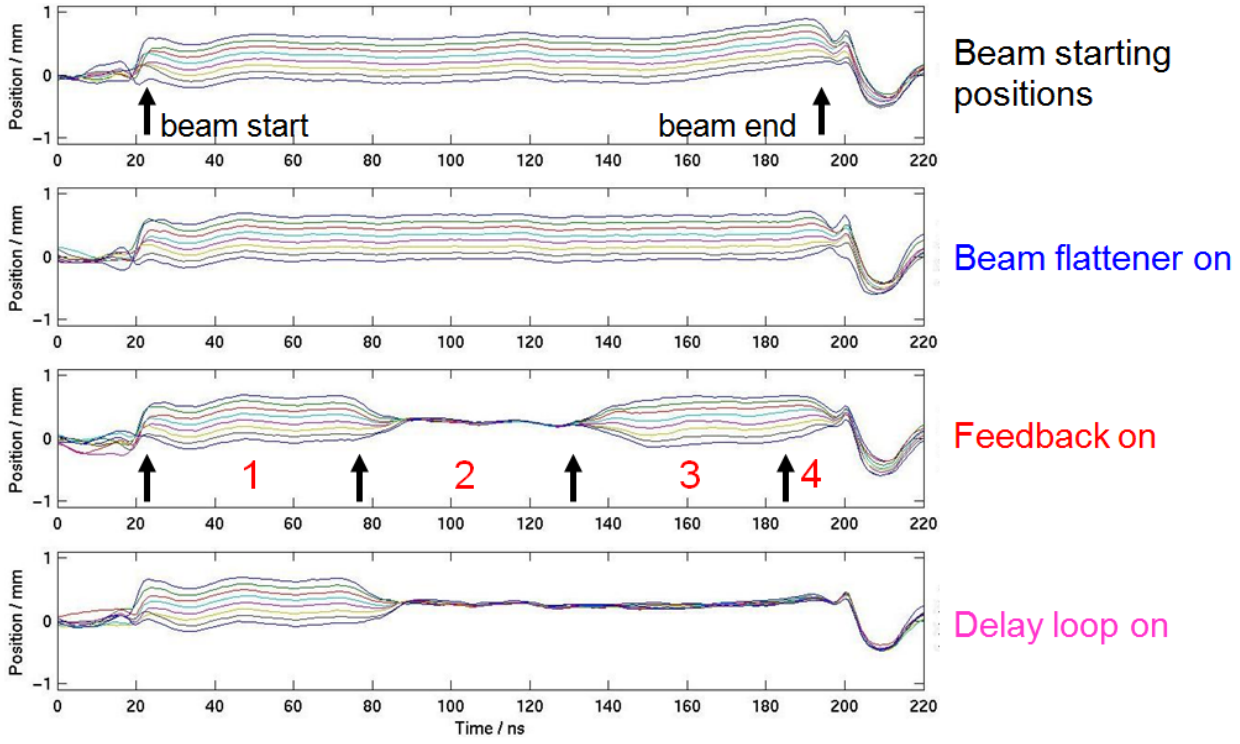

Figure 1.13: The operation of FONT2 measured by the beam position monitor at the NLC Test Accelerator [38].

after the interval marked as "1", which corresponds to the feedback latency time. In the interval "2" the error is low, but since the measurement shows the absence of the error, the amplifier sets the voltage on the correction kicker to zero again, hence in the interval "3" the large error value returns. This unwanted effect can be removed by use of the delay loop (fourth figure, on the bottom), which recognises the impact of the feedback system and keeps the previous kicker voltage in case that the correction is performed well and no error is measured.

The FONT team has developed five versions of system over the years in order for it to be applicable for the future colliders NLC and ILC. A system for CLIC is in development; a simulation of the effectiveness of the system is shown in Fig. 1.14. Additionally to the beam collision feedback, FONT amplifiers can be used in a feed-forward system for CLIC Drive Beam phase stabilisation. The investigation of such a system's specifications is the main topic of this thesis and is presented in full detail in Chapters 3, 4, 5 and 6.

1.5 CERN

The European Organization for Nuclear Research (CERN) is the world's largest laboratory for particle physics research. It is located at the Swiss-French border near Geneva and is a joint venture of 20 member states [40].

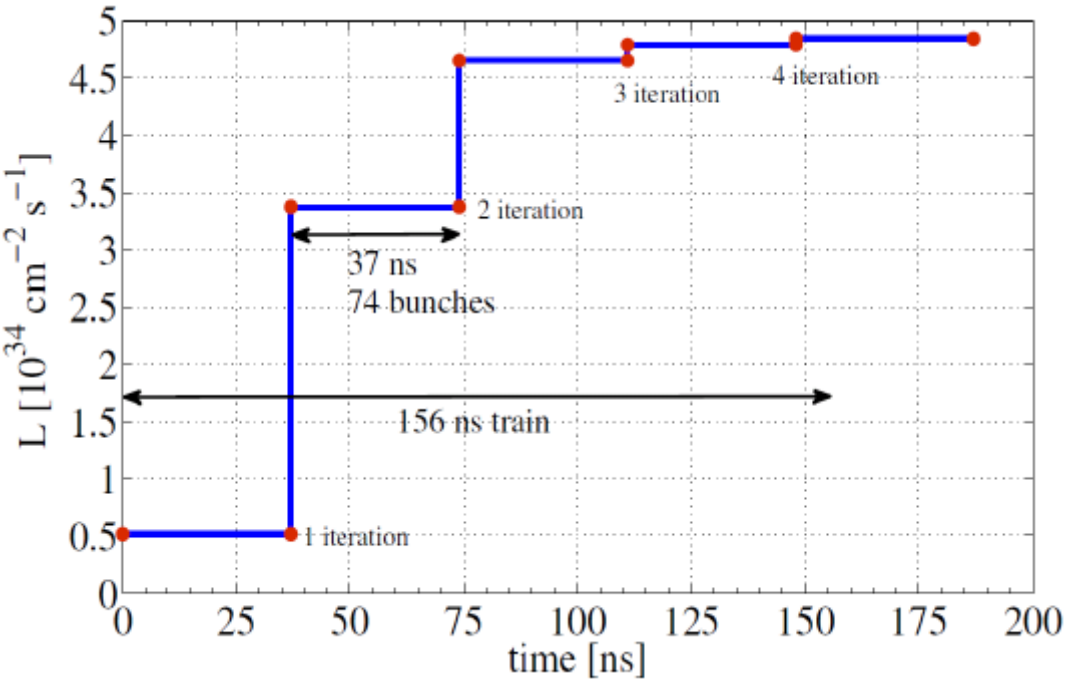

Figure 1.14: Simulation of FONT operation impact on CLIC luminosity [39].

The Conseil Europeen pour la Recherche Nucleaire, the council which gave CERN it's acronym, decided shortly after the Second World War to unite the European effort and funding for fundamental particle physics research. The organisation was founded in 1954 by 12 member states.

The organisation employs nowadays over 3000 staff members, postdoctoral researchers and students, having over 10 000 users at the CERN site. The users come from the academic institutions in order to participate in research activities and CERN's main task is to develop and maintain experiments and to provide infrastructure for the users.

The current accelerator complex of CERN includes two linear accelerators Linac 2 and 3 (for protons and ions respectively), the Proton Synchrotron Booster, the Proton Synchrotron, the Super Proton Synchrotron, the Large Hadron Collider and the test facility for the Compact Linear Collider as well as a number of smaller experimental facilities.

In the last 58 years several major discoveries have been made at CERN. These include the discovery of W and Z bosons, the number of neutrino families, CP violation (an asymmetry between matter and antimatter) and, most recently, a Higgs-like boson with a mass of 125 GeV. CERN was the first place where anti-hydrogen was created - after the Big Bang the antimatter must have dissipated before the temperatures decreased strongly enough for the stable anti-atoms to form and so it could not be created in this period.

Additionally to the break-throughs in fundamental research CERN has produced a number of technological spin-offs with wide practical applications, such as the development of the World Wide Web and proton cancer therapy.

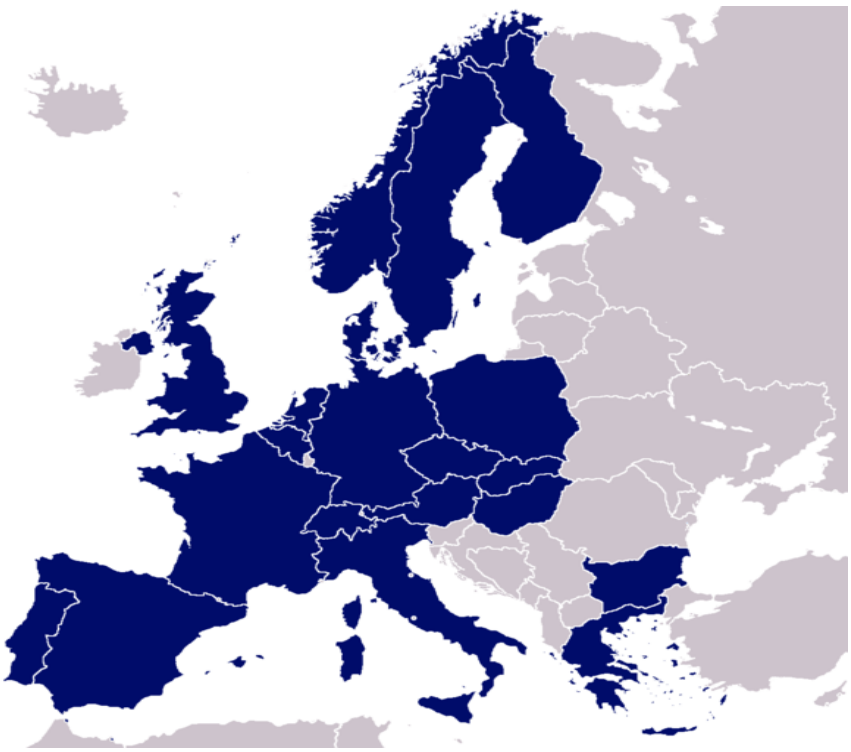

Figure 1.15: The twenty member states of CERN [41].

Although a large part of the analysis of data from CERN experiments is performed by the user institutions, two Nobel prizes have been awarded to CERN employees: in 1984 to Carlo Rubbia and Simon van der Meer for their contribution to the discovery of the W and Z bosons and in 1992 to Georges Charpak for his involvement in particle detector development.

Chapter 2

CLIC

2.1 Overall Design

The Compact Linear Collider (CLIC) is a proposed high-energy e^+e^- collider in development at CERN and the collaborating institutions. It is based on a unique two-beam acceleration scheme designed to reach an accelerating gradient of $E_{acc} = 100$ MV/m at the $f_{RF} = 12$ GHz RF frequency of the Main Linac accelerating structures (see Fig. 2.1). The previous designs of the machine included gradients of up to 150 MV/m at an RF frequency of 30 GHz [42], but in the process of cost optimisation the gradient and frequency have been set to the current values.

The electron and positron beams will be generated at the accelerator source and afterwards sent to the damping rings in order for their emittance to be reduced. Afterwards in the 42.16 km long Main Linacs they will be accelerated by the RF power extracted from the Drive Beam. The 156 ns long Main Beam trains will be focussed by the 2 × 2.75 km long beam delivery system and collided at 3 TeV collision energy with a bunch frequency of 2 GHz at the interaction point in the centre of the detector [43]. The overall length of the CLIC site is 48.4 km.

The present chapter describes the layout of CLIC and explains the basic concepts of its design. A particular focus is on the aspects needed for understanding the following chapters and in particular the Drive Beam phase stabilisation system, hence these aspects are depicted in greater detail.

2.2 Drive Beam

In order to achieve the design accelerating gradient of 100 MV/m the CLIC Main Linac cavities must operate at 12 GHz frequency and provide an accelerating power of 250 MW per metre. This adds up to a total power of 10^4 GW over the two 21 km long linacs [32].

It would not be feasible to achieve such an acceleration with klystrons, since many of them would be required - about 35 000, each providing a power of 50 MW with RF compression

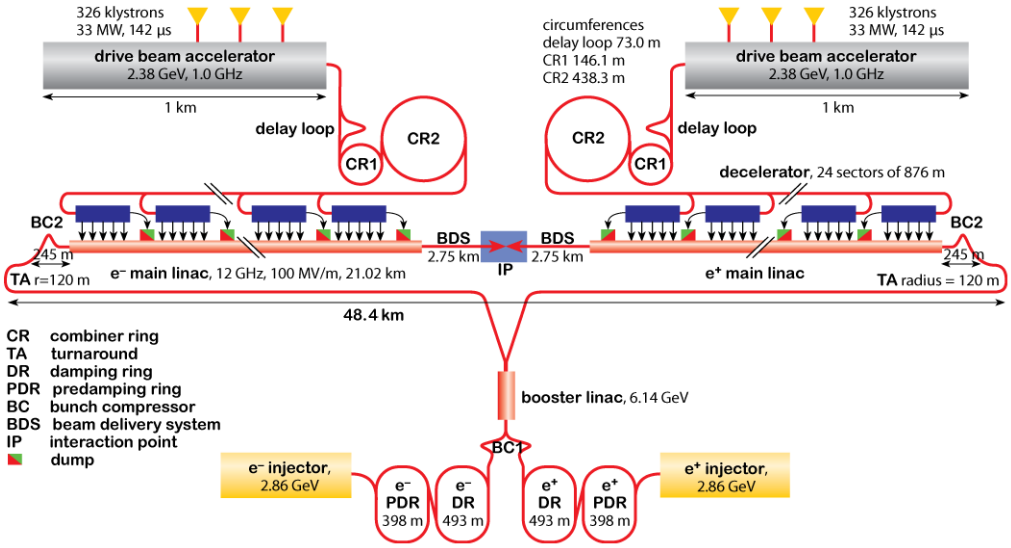

Figure 2.1: Layout of Compact Linear Collider at 3 TeV [32].

by a factor of five. The efficiency of the klystrons would also be comparably low - only ca. 40% considering the RF compression [1] [32].

Hence, another solution has been chosen: the RF power is provided by the Drive Beam, which is generated at the lower bunch frequency of 0.5 GHz and then compressed in the recombination scheme by a factor of 24 to the 12 GHz bunch frequency. The accelerating RF wave in the Main Beam structures must be longer than the Main Beam trains in order to fill the accelerating structures before the beam's arrival and to provide a flat, stable accelerating RF wave. So for the Main Beam with 156 ns train length, 244 ns long Drive Beam pulses at 12 GHz frequency are needed.

Fig. 2.2 shows the components of the Drive Beam complex - the accelerator on top left, the recombination scheme consisting of a Delay Line and two Combiner Rings, and the Power Extraction and Transfer Structures on the bottom, where the RF wave is extracted from the Drive Beam and the beam is decelerated and afterwards dumped. The following subsections describe each of these components in more detail.

2.2.1 Drive Beam accelerator

The Drive Beam accelerator is designed to accelerate the Drive Beam pulses of 142 μs length at a frequency of 50 Hz to 2.38 GeV energy [32]. The beam current in the Drive Beam linac is 4.2 A, with bunch charge of 8.4 nC and a bunch frequency of 0.5 GHz.

The Drive Beam electron pulse is generated at a 140 keV thermionic gun. The pulse is then bunched by three sub-harmonic bunchers, the pre-buncher and a buncher, at the end of which the electrons have a momentum of 4.2 MeV/c.

[1] Acceleration using klystrons is however considered as an alternative option for the low energy versions of CLIC.

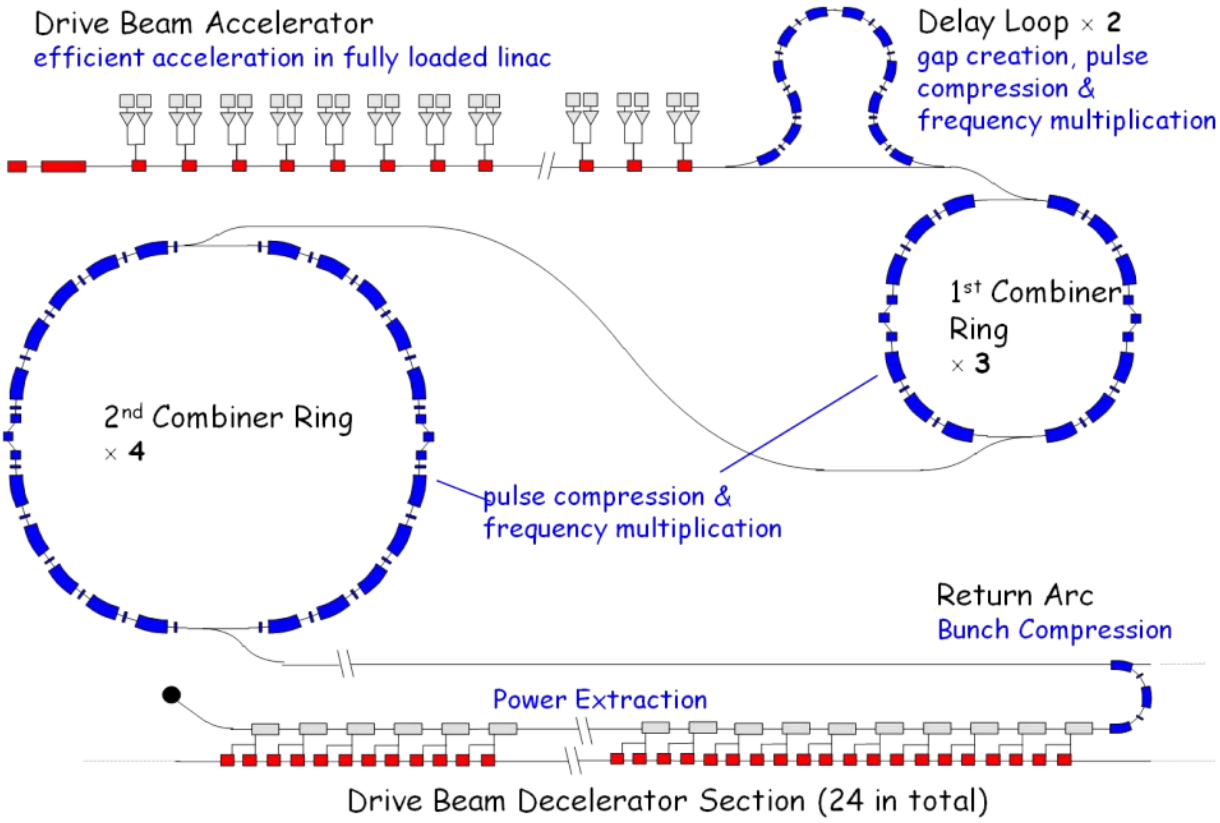

Figure 2.2: Layout of the CLIC Drive Beam [44].

The Drive Beam Linac 1 (DBL1) is used to accelerate the electrons up to an energy of 300 MeV. It is followed by the bunch compressor chicane (see further below) and the Drive Beam Linac 2 (DBL2), which accelerates the beam to its final energy of 2.38 GeV. The acceleration is performed with the help of conventional high-power klystrons operating at an RF phase of 27.5° in DBL1 and 18° in DBL2. The beam is focused by solenoid magnets in the section directly after the source and via a FODO cell lattice in DBL1 and DBL2. The total length of each of the two Drive Beam accelerator complexes is 2.6 km.

In order to obtain high efficiency the RF units have been designed to operate in the full beam loading mode (Fig. 2.3). In this mode the RF power from the structure is completely absorbed by the beam. The RF-to-beam efficiency for CLIC is expected to be 98% [45].

The bunches within the Drive Beam pulse have a separation of 2 ns and come in trains of 122 bunches; the trains are phase-shifted by 180° of phase with respect to one another. This pattern is needed for the frequency multiplication process, as described in Sec. 2.2.2. In order for the phase shifted trains to experience an equal acceleration with the non-phase shifted trains, the frequency of the accelerating RF wave has been set to 1 GHz (see Sec. 2.2.2 and Fig. 2.8).

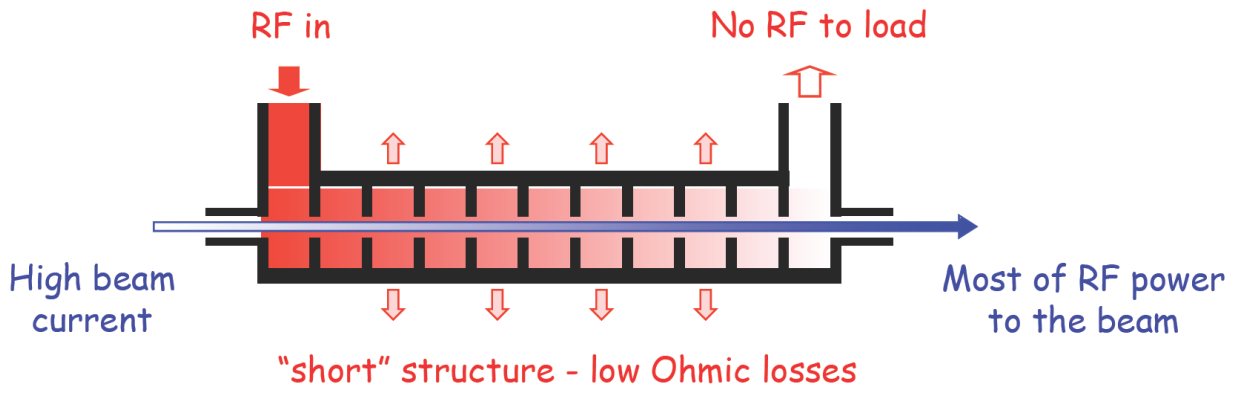

Figure 2.3: Principle of fully loaded acceleration [46].

The acceleration can be described by the RF filling function - the integrated accelerating voltage in the structure induced by a delta function RF wave as a function of time (see Fig. 2.4, left). The RF fill time, which is the time between the delta function entering the accelerating structure and the accelerating voltage falling back to zero, has been set for the Drive Beam structures to (73.2 m)/c. With this setting the RF filling time corresponds to the Drive Beam train length (244 ns). This allows cancellation of part of the RF errors at the frequency corresponding to 244 ns. It is expected that the errors will have a resonant peak at frequencies corresponding to the train length, since these resonant errors add up constructively during the recombination process (see Secs. 3.1.4 and 5.1.1). Hence, setting the length of the accelerating RF filling to the same value as the train length by a proper design of the accelerating structure will provide filtering for these critical resonant frequencies.

As will be shown later, for optimal filtering the RF wave filling function should also have a rectangular shape and be exactly 244 ns long (Fig. 2.4, left). The beam loading, which is the absorption of the RF wave energy by the bunches during their acceleration, is triangular along the structure, whose design is such as to reduce the loaded gradient to almost zero at the end of the structure itself, in order to operate in the full beam loading mode.

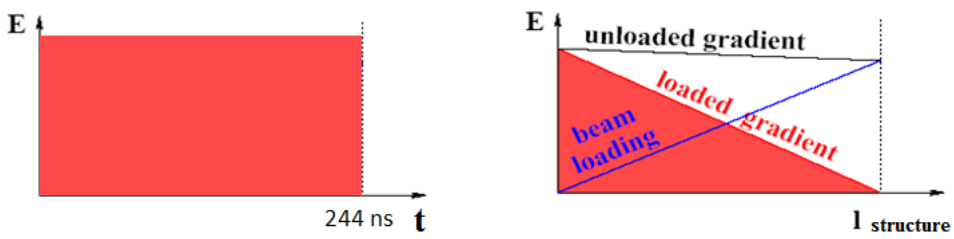

Figure 2.4: The optimal RF filling function vs. time after the RF wave enters the structure (left) and beam loading (right) along one Drive Beam accelerating structure.

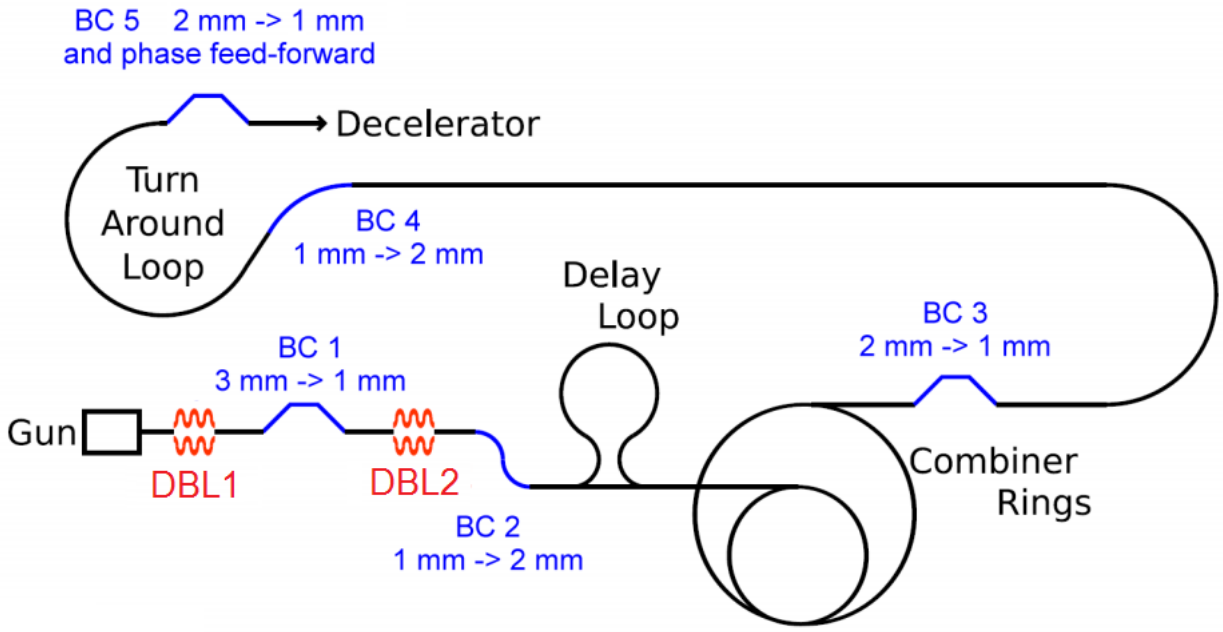

Figure 2.5: The layout of the Drive Beam complex showing the position of the Drive Beam linac sections (DBL) and of the bunch compression and decompression chicanes (BC) [32].

Compressor chicane

Fig. 2.5 shows the position of several compression and decompression chicanes (indicated as BC 1 to BC 5) along the Drive Beam. These chicanes are designed to compensate the effects of one another, so in first order they have no influence on the errors in beam parameters. Consequently, they are of minor importance for the simulation studies in the present thesis, which focuses on the first order effects in error propagation along the Drive Beam. The only chicane which is not compensated is the one located in the Drive Beam accelerator between DBL1 and DBL2, its position is shown in Fig. 2.6. This chicane is designed to reduce the length of the Drive Beam bunches from 3 mm to 1 mm at an energy of 300 MeV.

The bunch length reduction is performed in the following way: the series of dipole magnets modify the trajectory of the beam, so that the more energetic particles, which are positioned at the tail of the bunch, are deflected less strongly than the less energetic particles at the head of the bunch. Hence, the more energetic particles have a shorter path length in the chicane and are nearer to the bunch centre when leaving the chicane. The lower energy particles have a longer path length in the chicane and move from the head of the bunch towards the bunch centre as well. Consequently, the total length of the bunch is reduced. This process is referred to as longitudinal phase space rotation.

Different designs of the compressor chicane for the CLIC Drive Beam exist. The baseline design is schematically shown in Fig. 2.7. The blue boxes represent the dipole magnets, which bend the beam's trajectory. The red rhombus and triangles represent the quadrupole

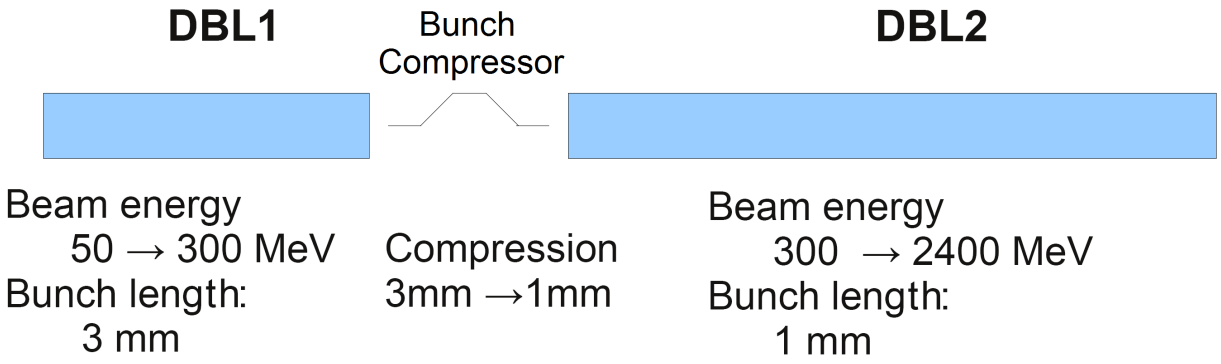

Figure 2.6: Compressor chicane position in the Drive Beam Linac [47].

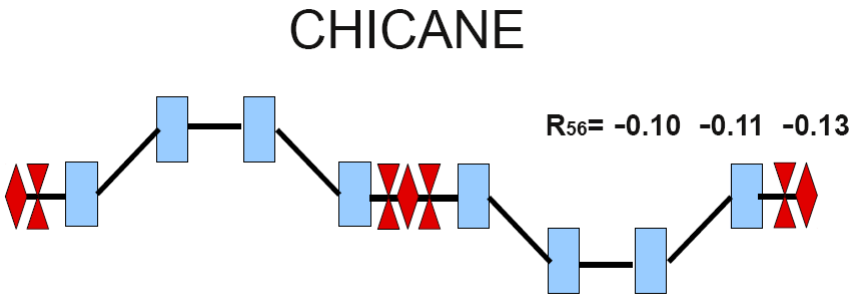

Figure 2.7: Scheme of the Drive Beam compressor chicane [47].

magnets which are designed to focus and defocus the beam. The optimal bunch compression factor R_{56} (see Sec. 1.3.1) has a value of -0.1 m, since this design has the largest tolerances [47].

2.2.2 Recombination scheme

The frequency of the Drive Beam bunches is multiplied by a factor two in the Delay Line and by factors three and four in the two following Combiner Rings (Fig. 2.2). Hence, when the Drive Beam reaches the 0.213 m long Power Extraction and Transfer Structures in the decelerator sector, the bunch frequency is 0.5 GHz $\times$ 2 $\times$ 3 $\times$ 4 = 12 GHz. The Drive Beam pulse length is c $\times$ 244 ns = 73.2 m and with a pulse current of 101 A it provides the accelerating RF power of 250 MW per metre to each Main Beam [43].

The frequency multiplication is designed in the following way: the bunches arriving at the Delay Line have a frequency of 0.5 GHz, and they are gathered in 244 ns long trains, which have a relative longitudinal phase shift of 180° forwards or backwards consecutively (Fig. 2.8). The trains are labelled as 'even' and 'odd' corresponding to the position of their bunches. The frequency of the accelerating modules is 1 GHz, so that all bunches are accelerated equally. The RF deflector at the injection point of the Delay Line has a frequency of 0.5 GHz, so that only bunches in even trains are steered into the Delay Line.

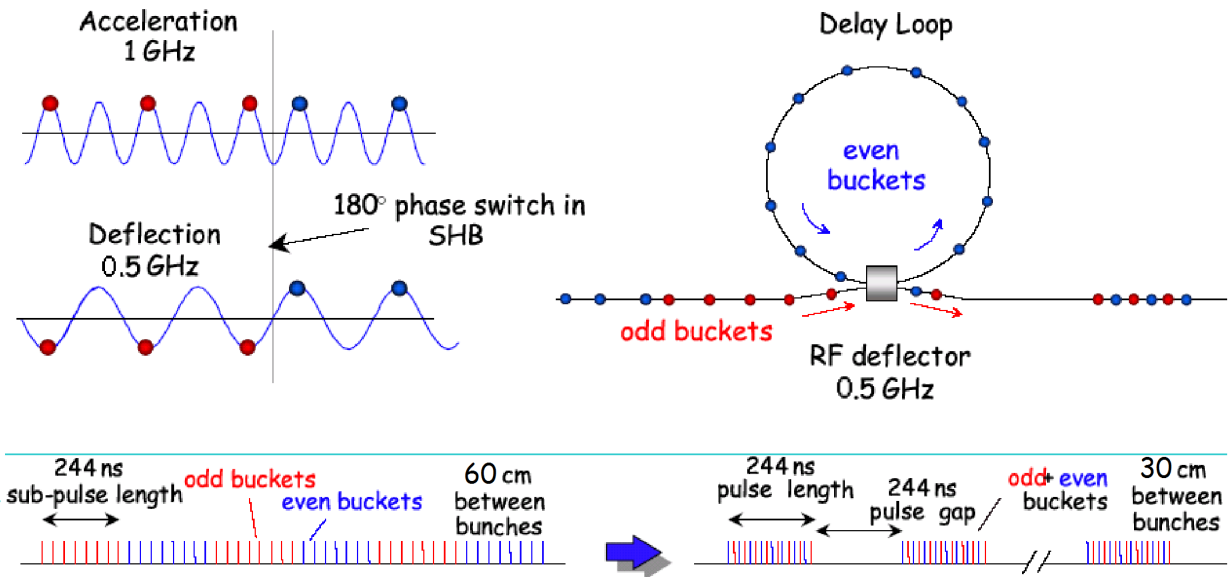

Figure 2.8: CLIC Drive Beam combination principle on the example of the Delay Line [32].

The path length for the trains in the Delay Line is 244 ns longer than the path length for the trains not steered into the Delay Line, so that each delayed train comes out of the Line simultaneously with the next (odd) train passing by the kicker. As a result, both trains leave the kicker together, their bunches being phase-shifted by 180°. Hence, trains of 244 ns length with 244 ns gaps between the subsequent trains are created, with a bunch frequency of 1 GHz within the trains. A similar principle is used in the first and second Combiner Rings with phase shift of 120° and 90° respectively.

2.3 PETS and Main Linac

After the Drive Beam has passed the recombination scheme and been recombined to the 12 GHz bunch frequency and 101 A current it is fed to the decelerator section. There, in the so-called Power Extraction and Transfer Structures (PETS), an electromagnetic RF wave is extracted from the Drive Beam and is fed to the Main Linac accelerator in order to accelerate the 1.2 A Main Beam to an energy of 1.5 TeV (Fig. 2.9). In this sense the whole CLIC machine is similar to a large power converter - energy of high current and low voltage beam is transformed into energy of low current and high voltage beam.

There are twenty-four decelerator sections per Drive Beam. The length of each decelerator section is 840 m to 1050 m, depending on its position along the Main Beam.

CLIC PETS

PETS are cylindrical structures composed of eight separate bars (see Fig. 2.10) with 23 mm aperture. There are 2.2 mm slots between the bars [32], which damp the transverse wakefield modes. The damping is performed by the introduction of lossy dielectric material close to

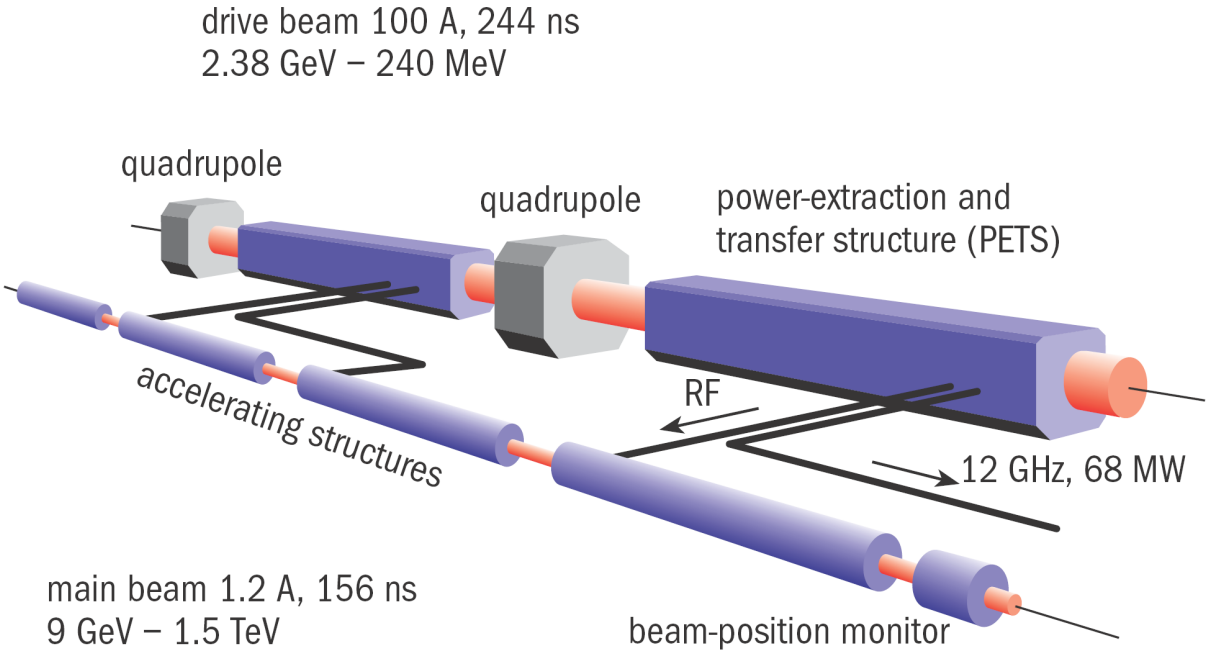

Figure 2.9: CLIC two-beam scheme: An RF wave is extracted from the Drive Beam and is fed through waveguides to the Main Beam [32].

the slot opening, which strongly strongly attenuates the transverse wakefields.

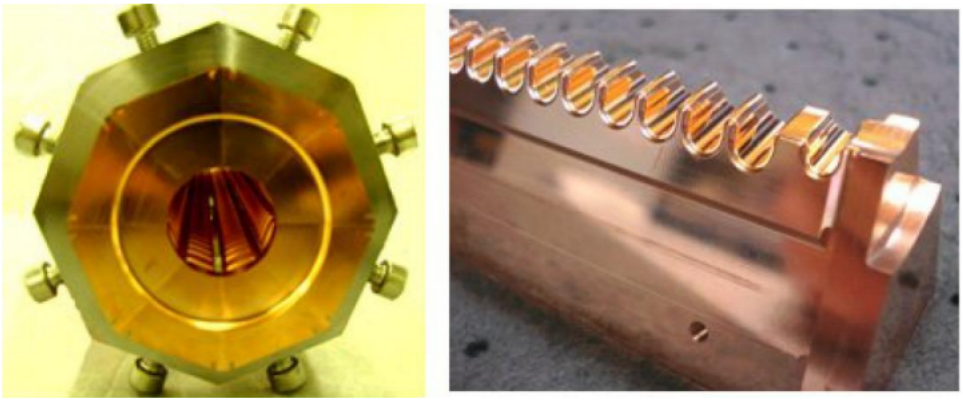

Figure 2.10: Power Extraction and Transfer Structures - view of the assembled structures (left) and structure profile of one bar (right). [32].

When the Drive Beam enters the structure, it induces wakefield oscillation in the low-impedance (R/Q = 2.2 kΩ/m) PETS. A simulation of such a wakefield is shown in Fig. 2.11. The wakefield propagates along the structure with a relatively high group velocity of 0.49 $\times$ c towards the waveguides.

The PETS structures are designed to extract 90% of the beam energy from the Drive Beam. This fraction is directly proportional to the collider's total efficiency and hence must

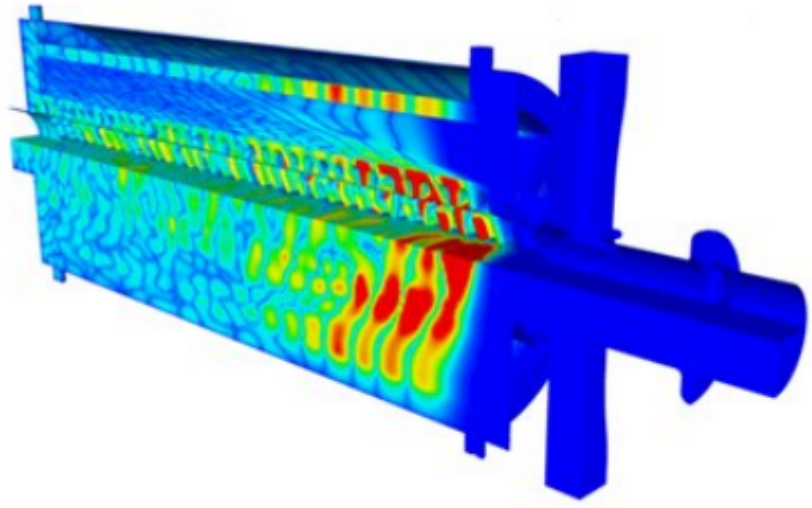

Figure 2.11: A snapshot of excited wakefelds at the time point of the bunch exiting the PETS [48]. The red colour represents a strong propagating electromagnetic field, the yellow and green colours represent the weaker dissipating fields.

be maximised; however a higher value is not achievable due to the emittance growth of the Drive Beam caused by the deceleration.

Main Linac

After extraction the RF wave is fed through specially designed waveguides to the Main Beam accelerating structures.

These 23 cm long Main Beam structures have a high impedance and operate at room temperature at a frequency of 12 GHz. Because of the normal conducting operating mode the heating due to the electrical resistance would overheat the structures if standing wave acceleration were used. Hence, a travelling wave propagating with a low group velocity of about $0.01 \times c$ is used for the acceleration.

The 156 ns long Main Beam trains have a 2 GHz bunch frequency, which is limited by long-range wakefields. The accelerating gradient of the structure is 100 MV/m including the beam loading effect (and 120 MV/m if operated unloaded) [43]. Achieving a low rate of electromagnetic breakdowns in the accelerating structures at this gradient is one of the main challenges of CLIC research and development studies.

The Drive Beam has been optimised to provide a highly stable RF wave for the Main Beam train acceleration. In order to compensate for the transient from the beam loading effect, an RF filling ramp of 88 ns length must be generated (Fig. 2.12, left). This is achieved by the modulation of the length of 180° phase shifted Drive Beam trains (see section 2.2.2) [49]. The resulting energy spread of the Main Beam is shown in Fig. 2.12, right.

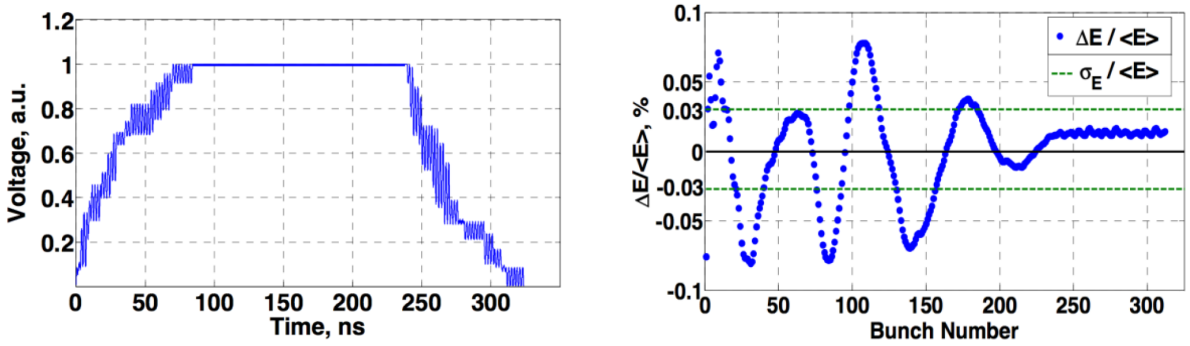

Figure 2.12: Left: the accelerating voltage for the optimized RF pulse in the Main Beam structures. Right: energy spread along the Main Beam train. The dotted blue line represents the relative energy error, the dashed green line represents the standard deviation of this energy error [50].

The peak RF power needed for the acceleration is about 250 MW per metre. This allows a nominal total beam power of 14 MW per Main Beam at the IP. CLIC's total power consumption at 3 TeV is estimated to be 582 MW [32].

2.4 Interaction point and detectors

2.4.1 Interaction point

The main challenge in the construction of a linear e^+e^- collider is achieving the luminosity sufficient for the intended precision measurements. In order to accomplish this the emittance and the beam size at the interaction point (IP) of the collider must be minimised to the lowest possible value.

The design values for the transverse horizontal (ϵ_x^*) and vertical (ϵ_y^*) emittance for the CLIC IP have been set to 660 nm rad and 20 nm rad, respectively [43]. The resulting beam spot size at the IP is designed to have a value of 45 nm in the horizontal plane and 1 nm in the vertical [43]. The value is not the same for both transverse dimensions so that the energy loss caused by the beam-beam interaction near the IP (called "beamstrahlung") [51] can be minimised. As Fig. 2.13 demonstrates, the horizontal emittance defined for CLIC has not been achieved at any existing collider or test facility. On the other hand, CLIC's vertical emittance is similar to the values achieved at the most advanced light sources in operation today. Consequently, the CLIC feasibility studies include extensive work on the stabilisation of the beam.

Several important beam parameters at the IP are summarised in Table 2.1. One can recognise that, despite quite a "flat" beam spot, due to the beamstrahlung the luminosity within 1% of the nominal energy is significantly lower then the total luminosity. This effect

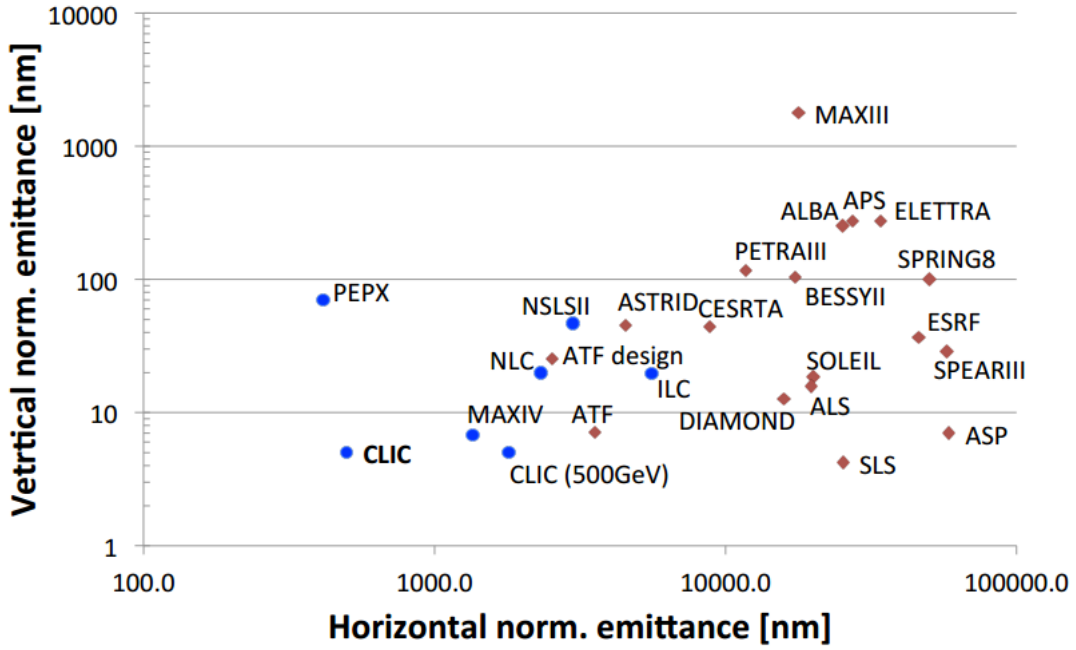

Figure 2.13: Horizontal and vertical normalised emittance values for the different existing (in red) and planned (in blue) accelerator facilities [32].

complicates the possibility of the precise energy scans mentioned in section 1.3.4.

Collision energy	3 TeV
Train frequency	50 Hz
Bunch frequency within the train	2 GHz
Train length	312 bunches
Total luminosity	5.9×10^{34} cm^{-2}s^{-1}
Luminosity within 1% of energy deviation	2.0×10^{34} cm^{-2}s^{-1}
Length of beam delivery section	2×2.75 km
Horizontal normalised emittance	660 nm rad
Vertical normalised emittance	20 nm rad
Vertical IP size (before the pinch effect)	1 nm
Horizontal IP size (before the pinch effect)	45 nm
Bunch length	44 μm

Table 2.1: Summary of CLIC parameters at the IP [43].

2.4.2 Detectors

There are several important requirements for the CLIC detectors, e.g. on jet energy and track momentum resolution, lepton identification efficiency and detector coverage [52]. Additionally, the detectors must be able to cope with short Main Beam bunch-to-bunch intervals of 0.5 ns.

In order to cover all requirements on the detectors and to be able to perform independent measurements to confirm the results, it has been decided to design two different detectors for CLIC. The detectors would share the interaction region and alternate several times a year, moved by a push-pull system (see Fig. 2.14).

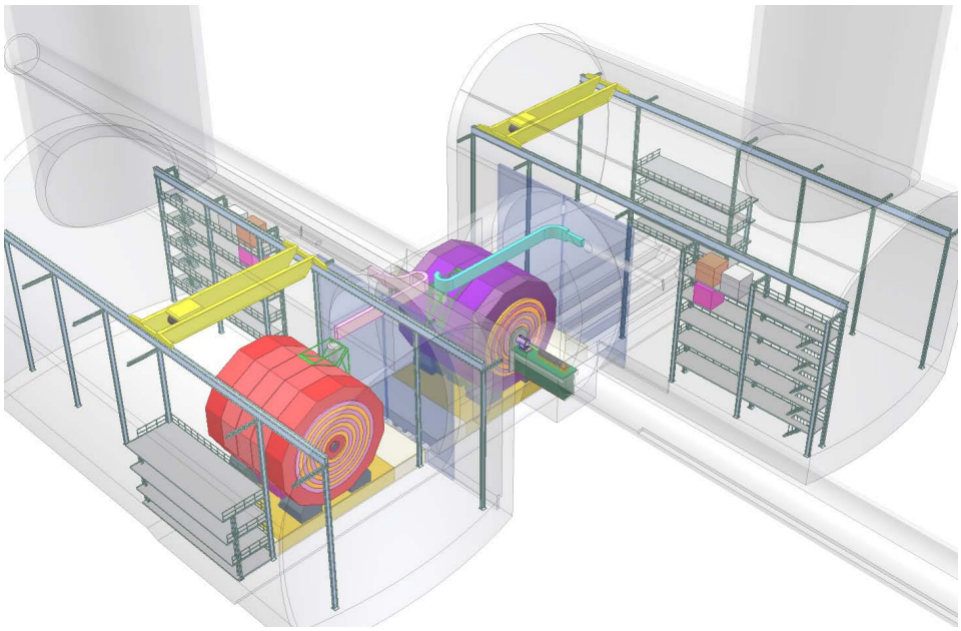

Figure 2.14: Scheme of CLIC interaction region with both detectors [52].

Since the detector requirements for CLIC and ILC are similar, it has been decided to modify the detectors proposed for ILC and to adapt them to CLIC. Both detectors, the International Large Detector (CLIC_ILD) and Silicon Detector (CLIC_SiD) have a vertex detector, tracker, electromagnetic and hadronic calorimeter, an outer iron yoke used for muon detection and a superconducting solenoid magnet in the centre of the detector (4 T field for CLIC_ILD and 5 T for CLIC_SiD) providing the magnetic field for the particles' momentum measurement. The main difference between the detectors is that the CLIC_SiD is based on a silicon tracking system, which is comparably small and is able to perform a fast charge collection. CLIC_ILD has a Time Projection Chamber, which provides a continuous tracking with relatively little material in the tracking volume itself. The diameter and length of both detectors are of the order of 13-14 m.

2.5 Stability requirements

The present section describes the stability requirements on the parameters of the Main and Drive Beams. This part of the introduction chapter is of particular importance for the studies presented in the current thesis. It depicts the most challenging aspects of the CLIC luminosity maintenance, constitutes the motivation behind the CLIC Drive Beam error propagation studies and describes the proposed phase feed-forward stabilisation system for the CLIC Drive Beam.

The beam delivery system of CLIC is optimised to focus the Main Beams, at their nominal energy of 3 TeV, at the IP with a beam spot size of 45 nm × 1 nm. However, the focal point of the quadrupoles in the beam delivery system depends on the beam energy, so that any errors in the Main Beam energy cause an increase of the beam spot size and consequently a luminosity loss. Fig. 2.15 presents the energy bandwidth spectrum at CLIC interaction region for the baseline linear lattice design near the IP (dotted blue curve) and the alternative non-linear lattice design (solid red curve), which involves using sextupole magnets as spoilers near the IP for the machine protection purposes [53]. The simulations presented in the current thesis are based on the baseline linear design.

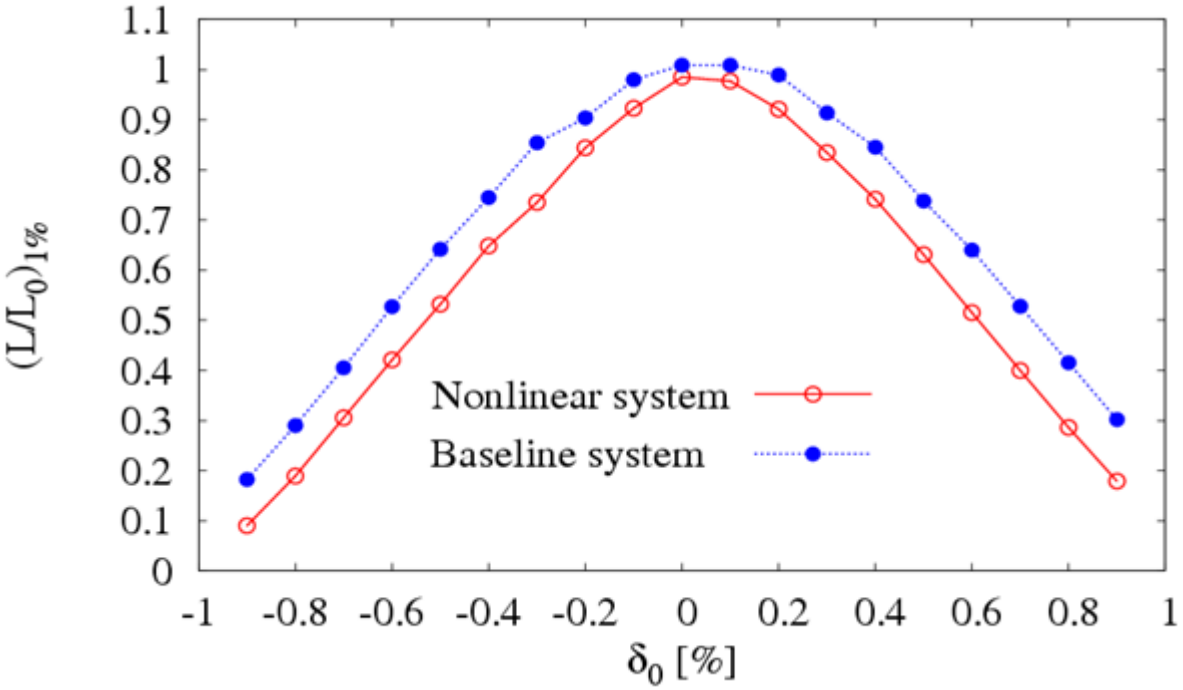

Figure 2.15: Relative peak luminosity within 1% of nominal beam energy E as a function of the energy offset $\delta_0 = \Delta E/E$ [53].

As a result of CLIC's limited energy bandwidth the Main Beam energy must be stabilised to a very high degree. Since the Main Beam acceleration is performed using RF waves extracted from the Drive Beam, the stability of the Drive Beam is of crucial importance for the luminosity maintenance.

Errors in the Drive Beam bunch charge σ_I and phase σ_ϕ contribute quadratically to the luminosity loss $\Delta\mathcal{L}$ (Eq. 2.1) [54]. Furthermore, the error in the bunch length σ_{σ_z} causes an error in the bunch form factor, and in order to maintain the same accelerating gradient the bunch charge must be increased. This consequently leads to further luminosity loss. Simulation studies show the following impact of errors in the Drive Beam parameters on the luminosity loss $\Delta\mathcal{L}$ [55]:

$$\frac{\Delta\mathcal{L}}{\mathcal{L}} \approx 0.01 \times \left[\left(\frac{\sigma_{\phi,coh}}{0.2^\circ}\right)^2 + \left(\frac{\sigma_{\phi,inc}}{0.8^\circ}\right)^2 + \left(\frac{\sigma_{I,coh}}{0.75\times10^{-3}I}\right)^2 + \left(\frac{\sigma_{I,inc}}{2.2\times10^{-3}I}\right)^2 + \left(\frac{\sigma_{\sigma_z,coh}}{1.1\times10^{-2}\sigma_z}\right)^2 + \left(\frac{\sigma_{\sigma_z,inc}}{3.3\times10^{-2}\sigma_z}\right)^2\right] \tag{2.1}$$

A relative phase error of 0.2° at 12 GHz between the Drive and the Main Beam will cause a luminosity loss of 1% if the error is constant along the twenty-four decelerator segments. This error is referred to as coherent phase error ($\sigma_{\phi,coh}$). The same luminosity loss can be caused by a random error of 0.8°, which is referred to as incoherent phase error ($\sigma_{\phi,inc}$).

In order to achieve the required phase stability, the tolerances for many parameters of the Drive Beam are very strict. E.g. for 1% luminosity loss due to beam phase errors the Drive Beam accelerator RF power has to be within 0.2% and the RF phase within 0.05° of the respective nominal value [56]. Fig. 2.16 demonstrates the tolerances along the CLIC Drive Beam. As one can recognise in the top left part of the figure, a feed-forward system is designed to stabilise the phase of the Drive Beam by about a factor of 12 (see section 2.5.1).

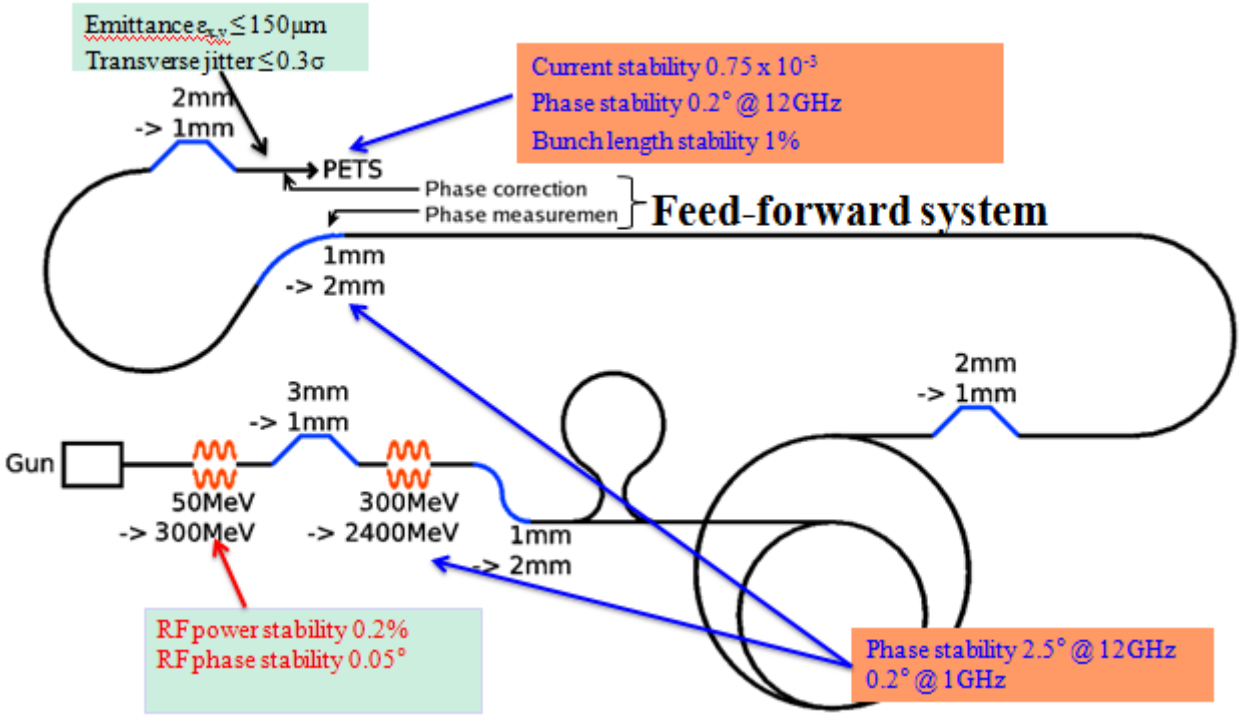

Figure 2.16: Tolerances of different parameters along the CLIC Drive Beam [57].

The stated Drive Beam tolerance requirements have to be met on the timescale of 88 ns, since this is the beam loading time of the Main Beam accelerating structures and errors on a shorter time scale will be, at least partially, filtered out by the structure's filling time.

2.5.1 Proposed Phase Feed-Forward System

The last compression chicane before the PETS which reduces the Drive Beam bunch length from 2 mm to 1 mm (see Fig. 2.16) can accept bunches with a phase error up to $\pm 10^\circ$ at 12 GHz. It has been decided that the chicane should be able to accept 4σ of the phase error, which leads to the RMS phase error tolerance of 2.5° at 12 GHz before the correction. After the correction the RMS phase error must be below 0.2° at 12 GHz (Eq. 2.1) in order to cause less then 1% luminosity loss. Consequently, it is necessary to reduce the bunch phase error by a factor $2.5^\circ/0.2^\circ \approx 12$ before the PETS using a feed-forward system.

The baseline design is to install the system at the final turnarounds before the decelerators (24 per beam), since it gives the possibility to use the phase measurement information to perform a feed-forward correction with an electromagnetic kicker at the same time as the corresponding bunches arrive at the respective kicker position. Putting the system as close as possible to the decelerator ensures that no significant phase changes will occur between the correction and the power extraction. An alternative design calls for installation of the system upstream, before the beam splits into 24 channels leading to the decelerators. This would reduce the number of required feed-forward systems from 24 to 1 per beam, potentially reducing the costs, but would make the design of the single feed-forward system more challenging.

The feed-forward system will be composed of a phase monitor, an amplifier and four electromagnetic kickers, which should provide transverse kicks to the beam sent through a chicane. Depending on the measured phase, the chicane trajectory can be set longer or shorter, thereby varying the time of flight of the bunches in the chicane and hence modifying their longitudinal position (see Fig. 2.17) [58]. The requirement is that the feed-forward system should be able to correct phase errors as large as 10° to the required average stability of 0.1° at 12 GHz [59].

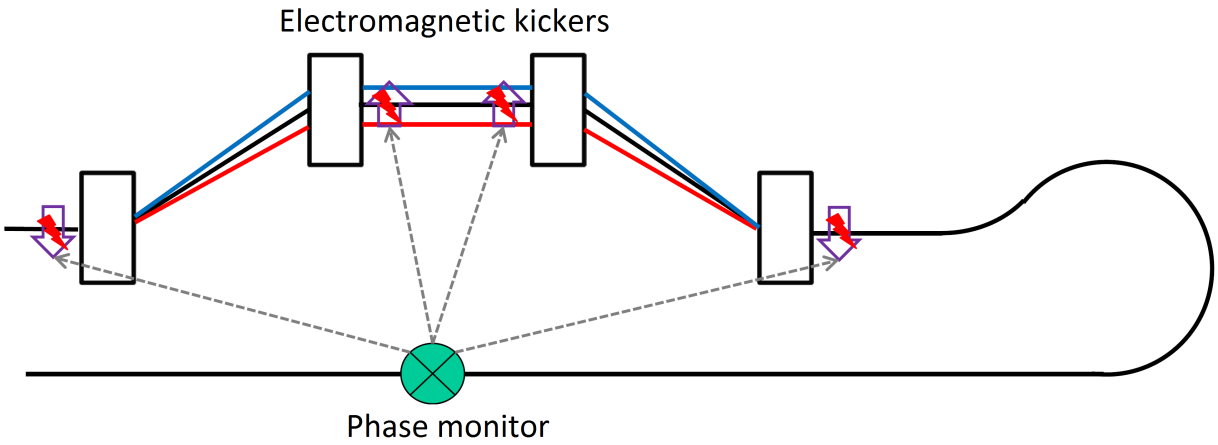

Figure 2.17: Scheme of the feed-forward chicane for CLIC Drive Beam phase correction [59].

Simulations show that it is possible to stabilise the longitudinal phase of the CLIC Drive

Beam to the required degree with such a feed-forward system (see Sec. 5.3) [60].

2.5.2 Synchronisation system

Similarly to the 1% luminosity loss resulting from the 0.2° at 12 GHz error in the relative Drive Beam - Main Beam phase, a luminosity loss of 1% can be also caused by a phase error of 0.6° at 12 GHz between the two Main Beams at the IP [61]. In order to align the Drive and Main Beam phases a global phase reference over 50 km is needed. The signal of the reference could be delivered to the decelerators by a distributed timing system. Such a system would allow measurement and correction of the Main and Drive Beam phase along the Main Linac. There are two approaches for the design of such a system [62].

The first approach (A) (Fig. 2.18, top) is to measure the phase of the outgoing Main Beams using the phase monitors and to transmit the phase information to a number of local oscillators [63]. The local oscillators can maintain the phase accurately enough until the Main Beam returns on the way to the IP. This system requires precise phasing between the outgoing Main Beams at the first booster linac near the interaction point (Fig. 2.19).

In the other approach (B) (Fig. 2.18, bottom) the master clock near the IP would define the nominal phase and distribute it as a signal cascade from one ∼900 m long decelerator segment to another. This system would establish the relative phase of the local timing clocks by an optical connection independently of the beams.

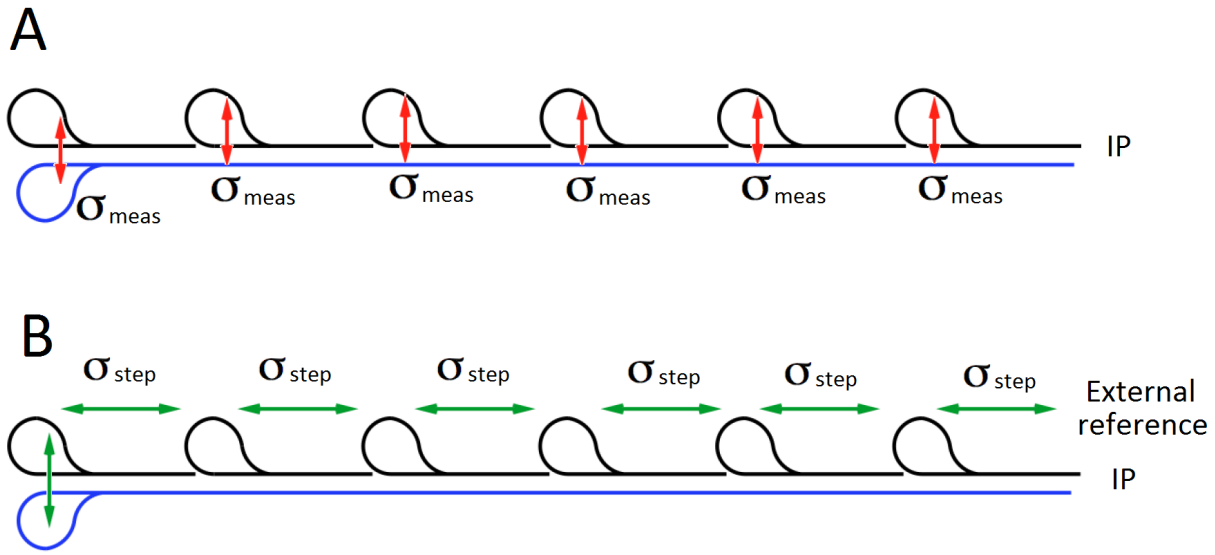

Figure 2.18: Propagation of the reference signal based on the Main Beam (A) and chained distribution of master clock signal (B).

Approach A has the advantage of having a relatively small error between the Main and Drive Beams, since the phase measurement at each Drive Beam decelerator is performed

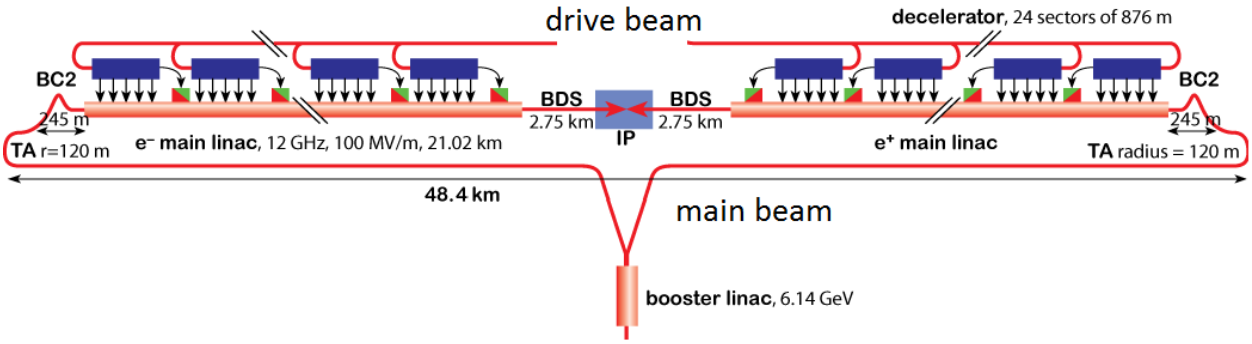

Figure 2.19: Layout of CLIC Main Linac at 3 TeV.

locally and hence no additional error is introduced during the distribution process. Only a phase measurement error σ_{meas} would be introduced at each phase monitor, which would be an incoherent error between the decelerator segments along the Main Beam linac (Eq. 2.1). The errors of the signal transmission from the Main Beam phase monitors to the Drive Beam, and the deviation of the local oscillators, are expected to be negligibly small.

Approach B allows correction of the Main Beam at its final turn-around, giving the possibility to reduce the jitter between the e^+ and e^- Main Beams. However, since the Drive Beam correction signal is transported from the master clock via an optical distribution system, the noise introduced by this system would reduce the effectiveness of the phase correction. The noise is expected to progress like a random walk starting at the master clock near the IP and progressing with an average phase error σ_{step} from one decelerator segment to the following one.

In the final CLIC design these approaches could potentially be combined.

The proposed timing distribution system is based on state of the art technology for signal distribution via optical fibres tested at XFEL (DESY, Hamburg) [64] [65]. This system is proven to provide <10 fs stability over distances of several kilometres [66].

The analysis determining the specifications of the second approach (B) and setting the requirements for the tolerances of this system is described in Sec. 5.3.3 and in [67].

2.6 CTF3

The CLIC Test Facility (CTF3) is a facility at CERN constructed for tests of the main CLIC feasibility concepts, such as power extraction, two beam acceleration and recombination, as well as of some beam stabilisation methods. The facility layout is presented in Fig. 2.20. The majority of the facility is a model of the CLIC Drive Beam except the Two Beam Test Stand (TBTS) where two-beam acceleration is tested.

The beam is injected into CTF3 by a high current thermionic gun [68] followed by three

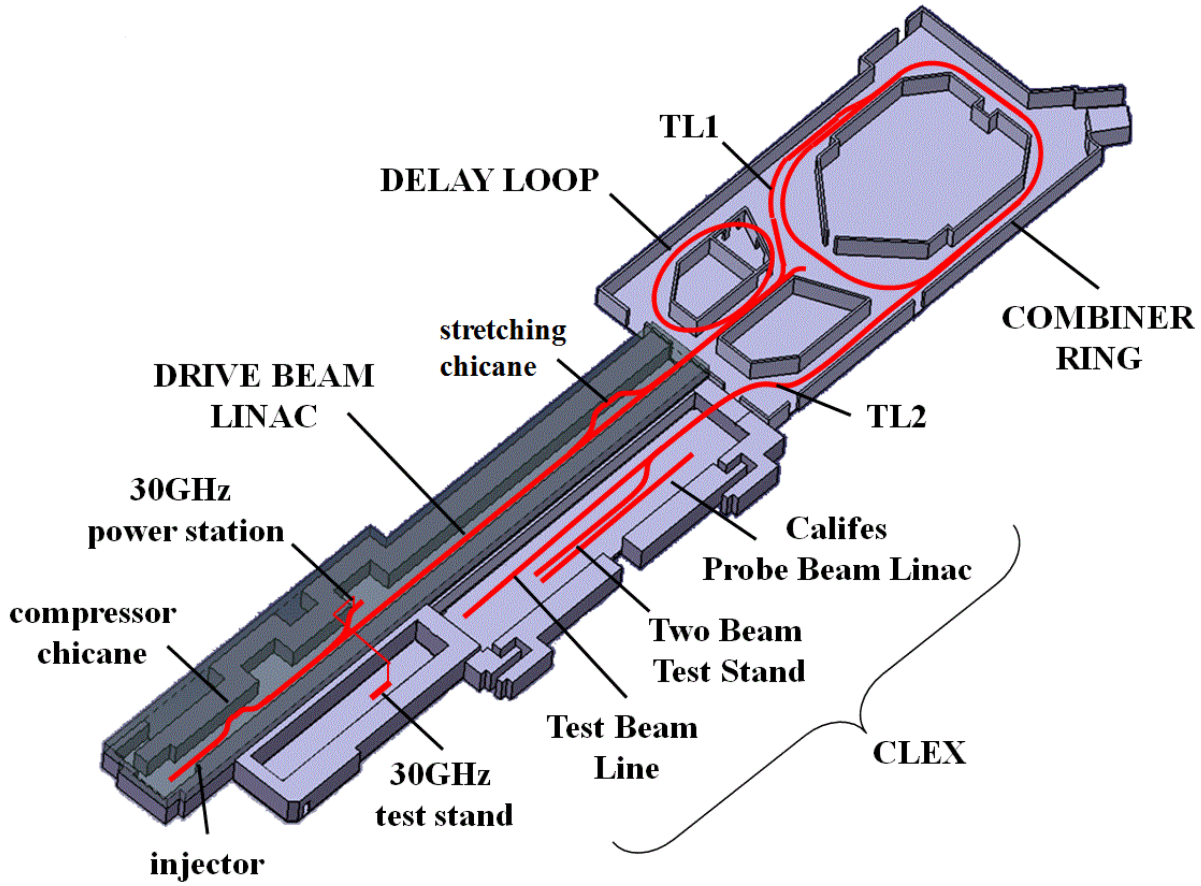

Figure 2.20: Layout of the CLIC Test Facility (CTF3) [59].

1.5 GHz sub-harmonic bunchers. Afterwards the beam is fed to the pre-buncher and buncher, both operating at 3 GHz. These can produce beam with a 3 GHz frequency for experiments with the uncombined beam and factor four combination, or a 1.5 GHz beam for factor eight combination experiments.

The Drive Beam linac is positioned directly after the buncher. It accelerates the beam to an energy of 150 MeV. The concept of normal conducting travelling wave acceleration is tested in this area. A compressor chicane is installed in the linac after the first two klystrons, where the beam energy is 20 MeV. The linac klystrons are operated in the full beam loading mode, so that the RF power is absorbed by the accelerating beam almost completely, as described in section 2.2.1. Fig. 2.21 shows the input and the output of the RF power measured at CTF3. The RF-to-beam efficiency in the experiments is 95.3%.

The linac is followed by a stretching chicane with a variable R_{56} value. There follow a 42 m long Delay Line and a 84 m long Combiner Ring. These systems operate as described in section 2.2.2, recombining the beam bunches by a factor of two and four respectively. Hence, a total recombination of a factor of eight can be achieved (see Fig. 2.22).

After the Combiner Ring the beam passes a dog-leg chicane TL2 and is fed either to the Test Beam Line (TBL) where beam deceleration can be studied, or to the Two-Beam

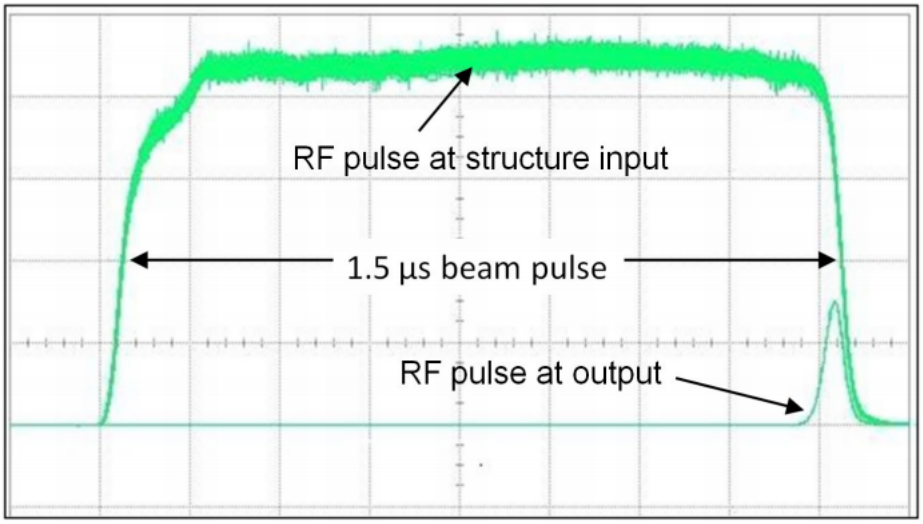

Figure 2.21: Measurement of RF power input and output at CTF3. The linac is operating with full beam-loading [32].

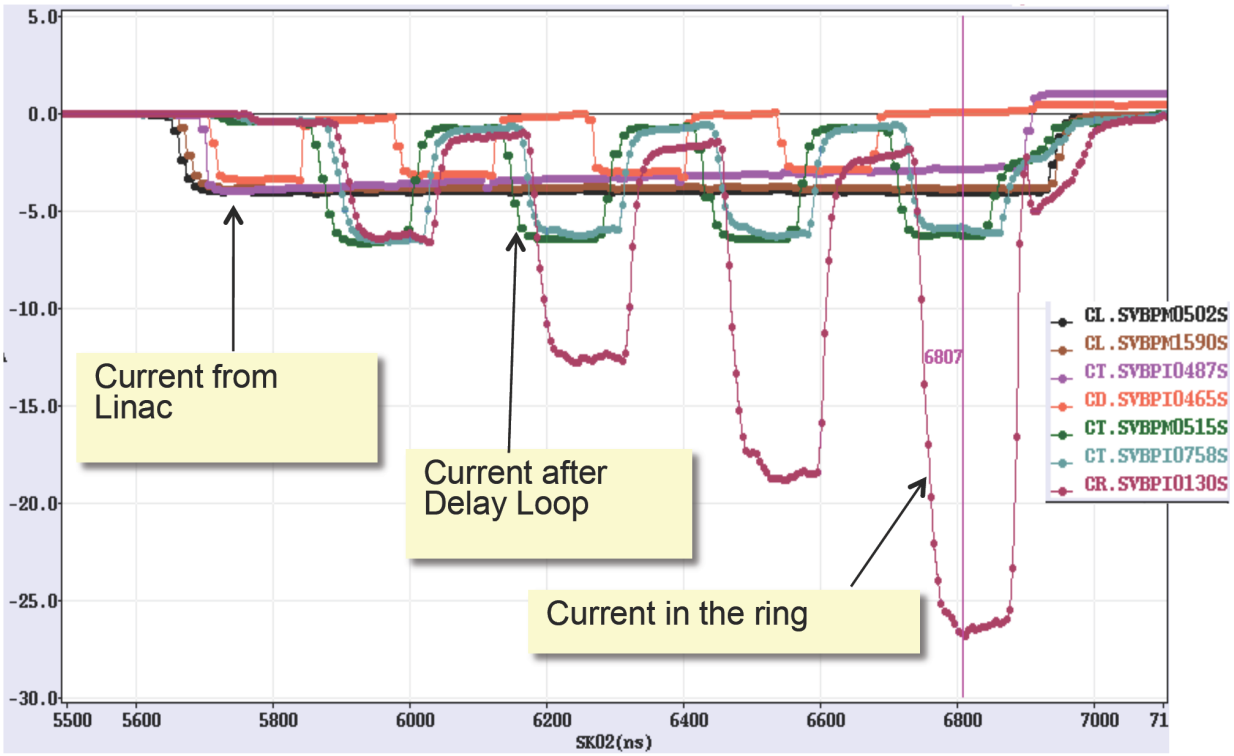

Figure 2.22: Recombination with factor eight demonstrated at CTF3 [69].

Test Stand (TBTS) where the RF wave extracted from the decelerating beam is used to accelerate the 200 MeV probe beam generated by the CALIFES injector. The 20 A Drive Beam is decelerated by 26% of its energy in 9 PETS structures and the produced total peak power is over 500 MW. In 2011 maximal gradient of 145 MV/m was measured in two-beam

tests at TBTS [32].

2.6.1 Beam stabilisation

Additionally to the proof-of-principle of the central concepts of CLIC, CTF3 is used for stability studies of several beam parameters.

The stability of the beam current has been significantly improved by the exchange of the electron gun heater and the introduction of a bunch charge feedback for correction of slow variations. The pulse-to-pulse charge variation has been reduced from $\Delta I/I = 2 \times 10^{-3}$ to 0.6×10^{-3}, which is below the CLIC specification of $\Delta I/I = 0.75 \times 10^{-3}$.

Additionally to the beam current stabilisation, the first prototype of a phase correction system for CTF3 is currently under development. It is planned to be installed in 2013. Three experiments are planned with the corrector:

- Pulse-to-pulse feedback system for the correction of the mean phase of the trains.
- Feedback system for the correction of the static errors within the trains.
- Feed-forward system for the correction of higher-frequency components.

These experiments are not set up in order to achieve at CTF3 the stability level required for CLIC, but for testing the phase correction system in order to predict and improve its performance when applied at CLIC.

A detailed analysis of the specifications for the prototype is presented in chapter 6.

Chapter 3

Software Tool for CLIC Drive Beam Error Analysis

Error tolerances for the Compact Linear Collider are very stringent and fulfilling these requirements is one of the main feasibility issues for the construction of the collider. The CLIC collaboration has performed extensive work on CLIC stabilisation in recent years. A part of this work is dedicated to the stabilisation of the Drive Beam.

In the framework of the study for the present thesis a software tool has been developed in the programming language C++ for the simulation of the error propagation along the CLIC Drive Beam. This software tool allows one to analyse the cumulative effect of errors in the first order approximation. Fig. 3.1 illustrates in a simplified diagram the operation of the tool. The tool simulates the errors in initial parameters such as beam charge and phase at the source, the phase and amplitude of the Drive Beam accelerating structures etc. It allows the tracking of the error propagation and transformation along the different sections of the Drive Beam complex. Finally, it performs the calculation of the impact of these errors on the Main Beam and the prediction of the total resulting luminosity loss of CLIC.

The tool is based on realistic and detailed modelling of Drive Beam and Main Beam accelerating structures. It includes the calculation of the interdependences of different parameters while considering multi-bunch effects. It is also possible to track the error propagation along the Drive Beam complex and calculate the effect of every component of the complex. Hence, with help of the program a precise analysis of the error profile along the CLIC Main Linac can be performed, which enables the calculation of the local tolerances, additionally to the calculation of the global tolerances, for the complete CLIC machine.

The present chapter is structured in the following way: Section 3.1.1 describes the beam parameters used in the simulation and the interdependences between them. Sections 3.1.2, 3.1.3, 3.1.4 and 3.1.5 present the models developed for the simulation of the Drive Beam sections and their impact on the Main Beam luminosity. Sections 3.2 and 3.3 describe the feedback and feed-forward system which could be employed for the Drive Beam stabilisation and how the components of these systems are modelled in the simulation tool.

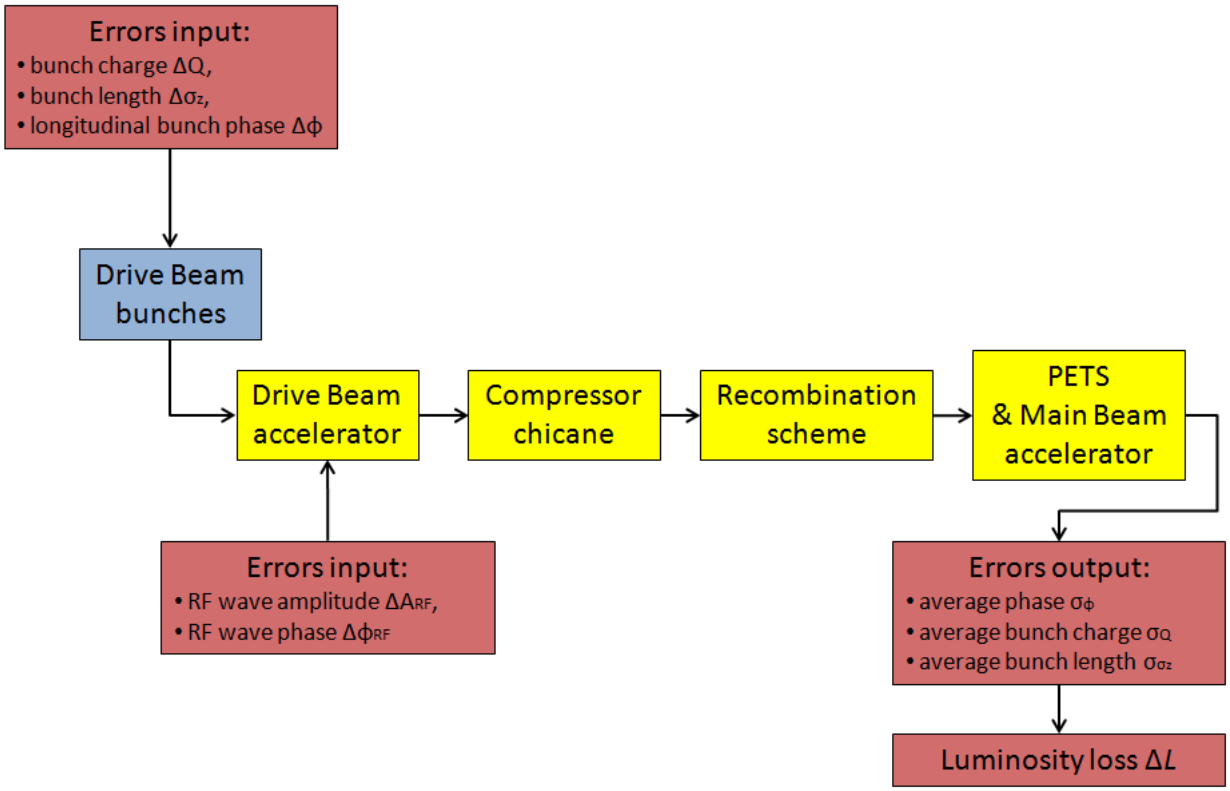

Figure 3.1: Simplified process diagram of operation of Drive Beam error tracking simulation tool.

3.1 Simulation models

3.1.1 Simulated parameters and their interdependences

The software tool can simulate an initial error in a number of Drive Beam parameters:

- longitudinal bunch phase $\Delta\phi$,
- bunch charge ΔQ,
- average energy of the bunch ΔE,
- bunch length $\Delta\sigma_z$,
- the RF wave amplitude in the klystrons ΔA_{RF} and
- the RF wave phase of the klystrons $\Delta\phi_{RF}$.

The value of the parameters along the Drive Beam pulse can be simulated in any particular way - e.g. one can assume a Gaussian distribution around the nominal value with a given standard deviation, measure the impulse response of the Drive Beam to an error

in one particular bunch etc. For most studies performed with the software tool the error was assumed to be a sinusoidal wave in the time domain. Modifying the frequency of the sinusoidal error allows one to calculate the effect of this error on the other parameters and on the Main Beam luminosity as a function of error frequency. For most studies an interval between 50 Hz, which corresponds to the train frequency of CLIC, and 20 MHz, which corresponds to the RF fill time of the Main Beam accelerating structures (about 50 ns), has been chosen.

Drive Beam bunch number

The number of the bunch is the only value which does not change during the beam propagation along the Drive Beam complex. It starts with zero for the bunch in the front of the pulse and increases by one for each following bunch.

The number of bunches in each Drive Beam train for CLIC at the nominal energy of 3 TeV is 122, corresponding to a 244 ns train length [43]. The tracking software uses the older value of 120 bunches per Drive Beam train [32]. The results of the simulation, however, are not expected to differ significantly.

In the case of operating at low energies the number of bunches in each train can vary depending on the mode of operation (see Sec. 5.5). The sum of the number of bunches for an odd and an even train remains however 240 for every mode, so the total number of bunches in one Drive Beam pulse stays constant for all modes.

The number of trains per Drive Beam pulse is $2 \cdot (3 \cdot 4 \cdot 24 + 2) = 580$. Simplistically one would assume the number to be $2 \cdot 3 \cdot 4 \cdot 24 = 576$, since each train is recombined with a factor two in the Delay Line and factors three and four in the two Combiner Rings and is led to one of 24 Drive Beam decelerator sectors. However, due to the non-trivial recombination pattern in the first Combiner Ring (see Section 3.1.4) four additional trains per pulse are required. The resulting total number of bunches per Drive Beam pulse is $580 \cdot 120 = 69\,600$.

Longitudinal position of Drive Beam bunches z

The longitudinal position z defines the nominal bunch position along the Drive Beam pulse. It is set by the outgoing Main Beam or by the master clock near the IP (see Sections 2.5.2 and 5.3.3). z is defined as zero for the first bunch before the recombination scheme, with positive z direction being opposite to the movement of the beam, so that the following bunches have higher z values than the preceding. At the source the bunches have a spacing of 2 ns, corresponding to the 0.5 GHz frequency of the uncombined Drive Beam. Trains of 122 bunches are shifted by 1 ns to higher and lower z values consecutively for recombination purposes (see Section 2.2.2). The z value of the bunches changes in the recombination scheme (Section 3.1.4). The z parameter is used in the simulation of accelerator and decelerator modules to define the longitudinal bunch position in the convolution function (see Sections

3.1.2 and 3.1.5).

Longitudinal phase error of Drive Beam bunches $\Delta\phi$

The longitudinal phase error of Drive Beam bunches $\Delta\phi$ is the deviation of the longitudinal position of Drive Beam bunches from their nominal phase. $\Delta\phi$ is used as a separate parameter from the longitudinal Drive Beam bunch position z in order to ease the calculations. The scale of $\Delta\phi$ (μm) is well below the scale of z (cm) and hence the impact of phase errors can be neglected for the calculations involving z.

There is an initial non-zero $\Delta\phi$ from the Drive Beam electron source; additionally $\Delta\phi$ can be generated by errors in the charge and energy of the bunches as well as by phase errors of the Drive Beam linac. $\Delta\phi$ is used to determine the Main Beam luminosity loss.

Drive Beam bunch charge error ΔQ

The nominal charge of each Drive Beam bunch is $Q_{nom} = 8.4\ nC$. The deviation from the nominal charge is the bunch charge error ΔQ. ΔQ influences the beam loading in the Drive Beam accelerator. Since the Drive Beam accelerator operates in the full beam loading mode the charge errors impact significantly the energy to which the bunch is accelerated - e.g. a bunch with charge larger than nominal absorbs more RF power than nominal and hence the accelerating structure does not operate fully loaded. Additionally ΔQ has an impact on the phase in the compressor chicane.

The expected initial error of the bunch charge has been estimated in the studies on the Drive Beam source development (see Section 5.2) [70].

Drive Beam bunch energy error ΔE

The nominal energy of the Drive Beam after the acceleration is $E_{nom} = 2.4$ GeV. However the errors in the RF filling of the Drive Beam accelerator structures due to the RF amplitude and phase jitter in the klystrons can cause a deviation of the beam energy ΔE. It can also be caused by the errors in beam loading due to the bunch charge errors of the Drive Beam ΔQ.

Drive Beam bunch length error $\Delta\sigma_z$ and bunch form factor F

The nominal bunch length $\sigma_{z,nom}$ changes along the Drive Beam complex as illustrated in Fig. 3.2, having a value of 1 mm in the decelerator.

However a deviation of the bunch length $\Delta\sigma_z$ can be caused at the electron source, if in the pre-buncher or the buncher some errors occur, or in the compressor chicane if ΔQ is non-zero [71]. Also errors of the Drive Beam RF phase or amplitude can lead to bunch length errors in the chicane.

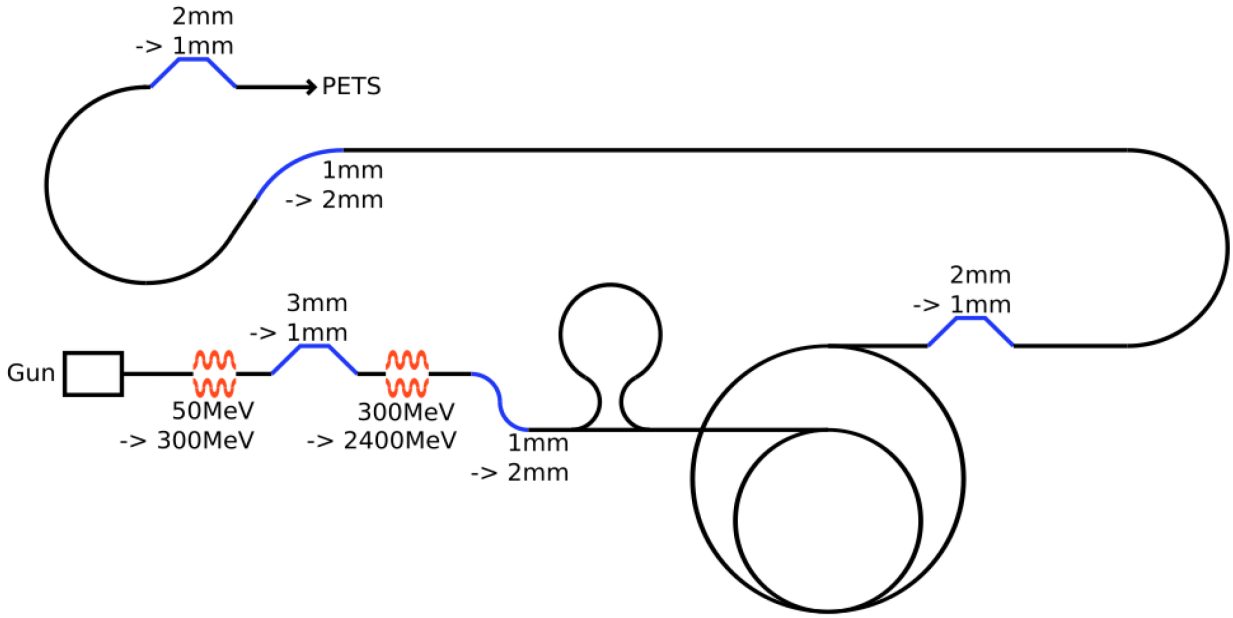

Figure 3.2: The scheme of the Drive Beam complex showing the changes in the nominal bunch length [61].

The bunch length errors change the form factor F, which determines the RF power extracted at the PETS. F is defined as the squared absolute value of the Fourier transform of the electron distribution density [72] :

$$F(\lambda) = |\int_{-\infty}^{\infty} \rho(z) \cdot e^{2i\pi z/\lambda}\, dz| \tag{3.1}$$

with $\rho(z)$ being the electron density distribution in the bunch and λ being the wavelength of the RF wave.

We assume a simplified model for the electron density distribution of the bunch with the length σ_z with centre at the position z to be

$$\rho(z) = \frac{1}{2}(\delta(z - \frac{1}{2}\sigma_z) + \delta(z + \frac{1}{2}\sigma_z)) \cdot \frac{2\pi}{\lambda} \tag{3.2}$$

with δ being the Dirac delta function. Using that assumption one can calculate the bunch form factor as

$$\begin{aligned} F &= \left|\int_{-\infty}^{\infty} \rho(z) \cdot e^{2i\pi z/\lambda}\, dz\right| \\ &= \left|\frac{\lambda}{2i\pi}\left(\frac{2\pi}{\lambda}\right)\frac{1}{2} \cdot \left(e^{i\pi\sigma_z/\lambda} + e^{-i\pi\sigma_z/\lambda}\right)\right| \\ &= \left|\frac{1}{2i}\left[\cos\left(\frac{\pi\sigma_z}{\lambda}\right) + \sin\left(\frac{\pi\sigma_z}{\lambda}\right) + \cos\left(-\frac{\pi\sigma_z}{\lambda}\right) + \sin\left(-\frac{\pi\sigma_z}{\lambda}\right)\right]\right| \end{aligned} \tag{3.3}$$

Considering that the cosine function is symmetric and the sine function is antisymmetric yields

$$F = \left|\cos\left(\frac{\pi\sigma_z}{\lambda}\right)\right| \tag{3.4}$$

This definition is valid only for $\sigma_z \leq \lambda/2$. One can recognise that an increase of the bunch length leads to a decrease of the form factor, so that $F \approx 1$ for $\sigma_z \to 0$ and $F \approx 0$ for $\sigma_z \to \lambda/2$. This result is consistent with what one would expect from the definition in Eq. 3.2, since in case of $\sigma_z \to \lambda/2$ the charge would not be located at the nominal longitudinal position of the bunches, but rather be equally distributed in the space between them. In the case of CLIC, for the value of $\lambda = \frac{c}{f} = \frac{3{\cdot}10^8\ m/s}{12\ GHz} = 25$ mm and for the nominal bunch length at the PETS of $\sigma_z = 1$ mm, the nominal form factor is $F_{CLIC} = 0.992$.

The RF power P extracted at the PETS is proportional to I^2F^2 with I being the Drive Beam current and F the form factor [73]. Since P must be held constant for the stable Main Beam acceleration, the Drive Beam current must be readjusted in proportion to $1/F$ for any change of F. As a consequence of this necessary readjustment, any deviations of the bunch length and the form factor lead to the deviations of the Drive Beam bunch charge.

Drive Beam accelerator - phase, amplitude and beam loading errors

The deviation of the phase $\Delta\phi_{RF}$ and the amplitude ΔA_{RF} of the RF wave in the Drive Beam accelerating structures impacts the energy of the Drive Beam. Also, errors in bunch charge and bunch phase of the beam passing the accelerating structures cause errors in the beam loading, which in turn lead to beam energy errors.

Main Beam luminosity loss

The errors in phase, charge and length of the Drive Beam bunches in the PETS are convolved with the Main Beam RF filling and beam loading functions (see Section 3.1.5 for more details). The result specifies the Drive Beam error impact on the Main Beam. The Main Beam luminosity loss is calculated with Eq. 2.1 from the root mean square value of $\Delta\phi$, ΔI and $\Delta\sigma_z$ signified as σ_ϕ, σ_I and σ_{σ_z} respectively in the equation. Since the error values of the Drive Beam bunches can be set independently in the simulation, they represent incoherent errors in the equation, $\sigma_{\phi,inc}$, $\sigma_{I,inc}$ and $\sigma_{\sigma_z,inc}$, respectively.

3.1.2 Drive beam accelerator

In the Drive Beam accelerator the RF phase error and RF amplitude error lead to beam energy error ΔE. Additionally, bunch charge and phase errors cause a beam loading error in the accelerator, hence leading to additional ΔE. ΔE consequently causes a phase error in the chicane (see section 3.1.3).

In order to determine ΔE caused by these factors, the RF potential and the wake potential have to be calculated. By integrating the RF and wake potentials over the RF filling time or the beam loading time, respectively, one obtains the RF filling and beam loading functions described in Sec. 2.2.1. Since the RF filling time and the beam loading time are constant for a given structure, the RF and wake potentials would be ideally expected to have rectangular and triangular form, respectively. However, the simulations of the wave and bunch propagation within the Drive Beam accelerating structures show that the forms of these functions are not exactly rectangular and triangular. Figs. 3.3 and 3.4 show the result of the simulations for the RF potential and wake potential, performed in the frequency domain with help of the GdfidL simulation tool [74],and then transformed into the time domain via the Fourier transform [75]. The beam loading function in Fig. 3.3 shows the absorption of the accelerating energy by a single Drive Beam bunch with the nominal charge of 8.4 nC. The beam loading function must be convolved with the Drive Beam error functions for each bunch individually. The beam loading along the Drive Beam accelerating structure presented in Fig. 2.4, right, results from the cumulative beam loading of the Drive Beam bunches with 0.5 GHz frequency in the steady state mode.

Higher order resonances are also included in the calculation. The resolution of the simulation in the frequency domain is limited; as a consequence the results display a strong oscillation of the potential functions, in particular of the RF potential function (Fig. 3.4), which is unphysical.

The software tool for the Drive Beam error propagation uses the beam loading amplitude function (Fig. 3.3) and RF potential function (Fig. 3.4) from the simulation [76] instead of the theoretical rectangular and triangular functions, which allows the tracking results to be significantly more realistic. Because of the unphysical oscillations, however, a linear approximation of these functions is necessary. The linear approximation also makes the calculation process significantly more efficient.

The approximation is expressed by a linear function starting at its maximal value and crossing zero after 228 ns (see Eq. 3.5), which is indicated in Fig. 3.3 with a solid red line.

$$A_{BL}(t) = A_{BL,max} \cdot \left(1 - \frac{t}{228\ \text{ns}}\right) \tag{3.5}$$

with fill time t defined as fill length s displayed in Fig. 3.3 divided by the speed of light c, $t = \frac{s}{c}$.

For the approximation of the RF filling three functions are used: the first one reducing the maximal potential by 33% within the first 234 ns, the second one reducing the value by 47% from the maximal value within the next 34 ns and finally the last one crossing zero after an additional 180 ns. The total length of the function is therefore 448 ns. The approximation is expressed in Eq. 3.6 and is indicated by the solid red lines in Fig. 3.4.

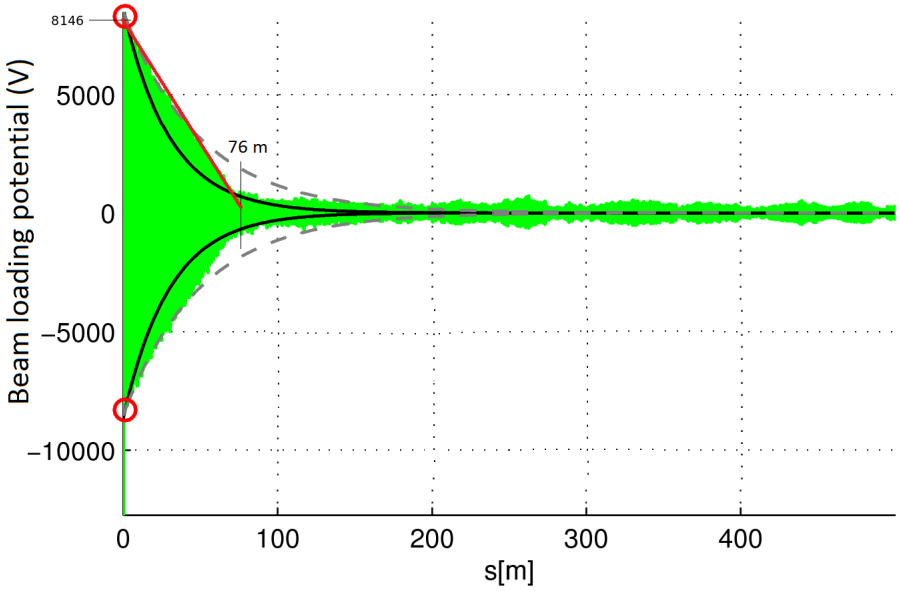

Figure 3.3: Simulation result for beam loading amplitude (V) of CLIC Drive Beam cavities (in green) as a function of distance from the bunch (m). Two exponential approximations are indicated by the black solid and the dashed lines. The linear approximation is indicated by a red line [76].

$$
\begin{aligned}
A_{RF}(t) &= A_{RF,max} \cdot \left(1 - 0.33 \cdot \frac{t}{234\ \text{ns}}\right) \text{ for } 0\ \text{ns} \leq t < 234\ \text{ns} \\
&= A_{RF,max} \cdot \left(0.67 - 0.47 \cdot \frac{t - 234\ \text{ns}}{268\ \text{ns} - 234\ \text{ns}}\right) \text{ for } 234\ \text{ns} \leq t < 268\ \text{ns} \\
&= A_{RF,max} \cdot \left(0.2 - 0.2\frac{t - 268\ \text{ns}}{448\ \text{ns} - 268\ \text{ns}}\right) \text{ for } 268\ \text{ns} \leq t < 448\ \text{ns}.
\end{aligned} \tag{3.6}
$$

The shape of the function is not exactly rectangular due to the dispersion and reflections of the RF wave within the accelerating cavities, as well as due to the structure tapering and RF losses. For instance, Fig. 3.5 shows the result of a simulation of the RF wave propagating through the structure as a function of time. The RF wave amplitude entering the structure (top) has a form of a sharp Gaussian peak, however due to the dispersion the amplitude of its reflection (middle) and of the transmission (bottom) is not Gaussian and is spread over time. Hence, the electromagnetic field experienced by the bunch passing the structure decreases with time, as one can see in Fig. 3.4.

The amplitudes of the RF filling A_{RF} and beam loading A_{BL} are calibrated so that the integrated RF filling is twice as large as the integrated beam loading (Eq. 3.7), since the klystrons operate in the fully loaded mode (see Section 2.2.1).

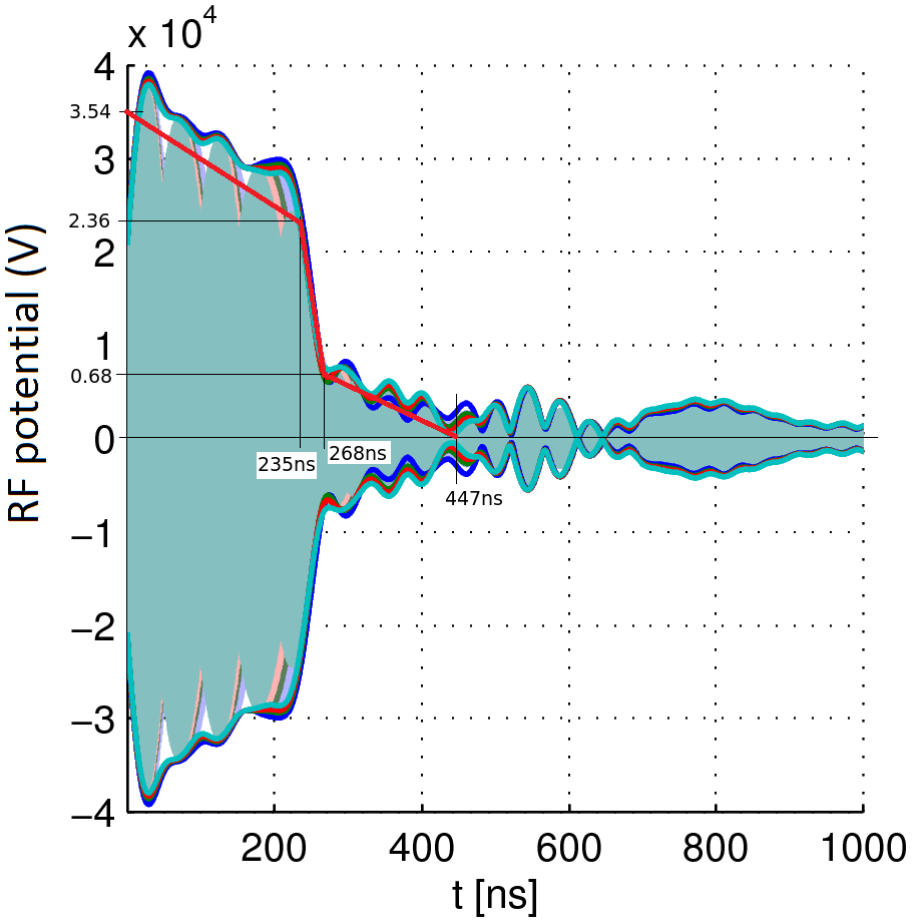

Figure 3.4: Simulation result for RF filling potential (V) as a function of time (ns) for CLIC Drive Beam cavities. The linear approximation is indicated by the red lines [76].

$$\int_{0\ \mathrm{ns}}^{448\ \mathrm{ns}} A_{RF}(t_1)dt_1 = 2 \cdot \int_{0\ \mathrm{ns}}^{228\ \mathrm{ns}} A_{BL}(t_2)dt_2 \tag{3.7}$$

The errors in both functions must be convolved with the Drive Beam pulse in order to determine their impact on the Drive Beam parameters. Since for the Drive Beam error tracking software the relevant values of the functions are at the position of the bunches, it is useful to use the discrete version of the convolution operation, which is defined as:

$$conv(f,g)(i) = \sum_{j=1}^{J} f(i-j) \cdot g(j) \tag{3.8}$$

In the case of the Drive Beam error tracking software $f(i-j)$ corresponds to the energy error of the Drive Beam bunches before entering the accelerating structures, $g(j)$ is the RF filling potential or the beam loading amplitude function, J is the number of Drive Beam

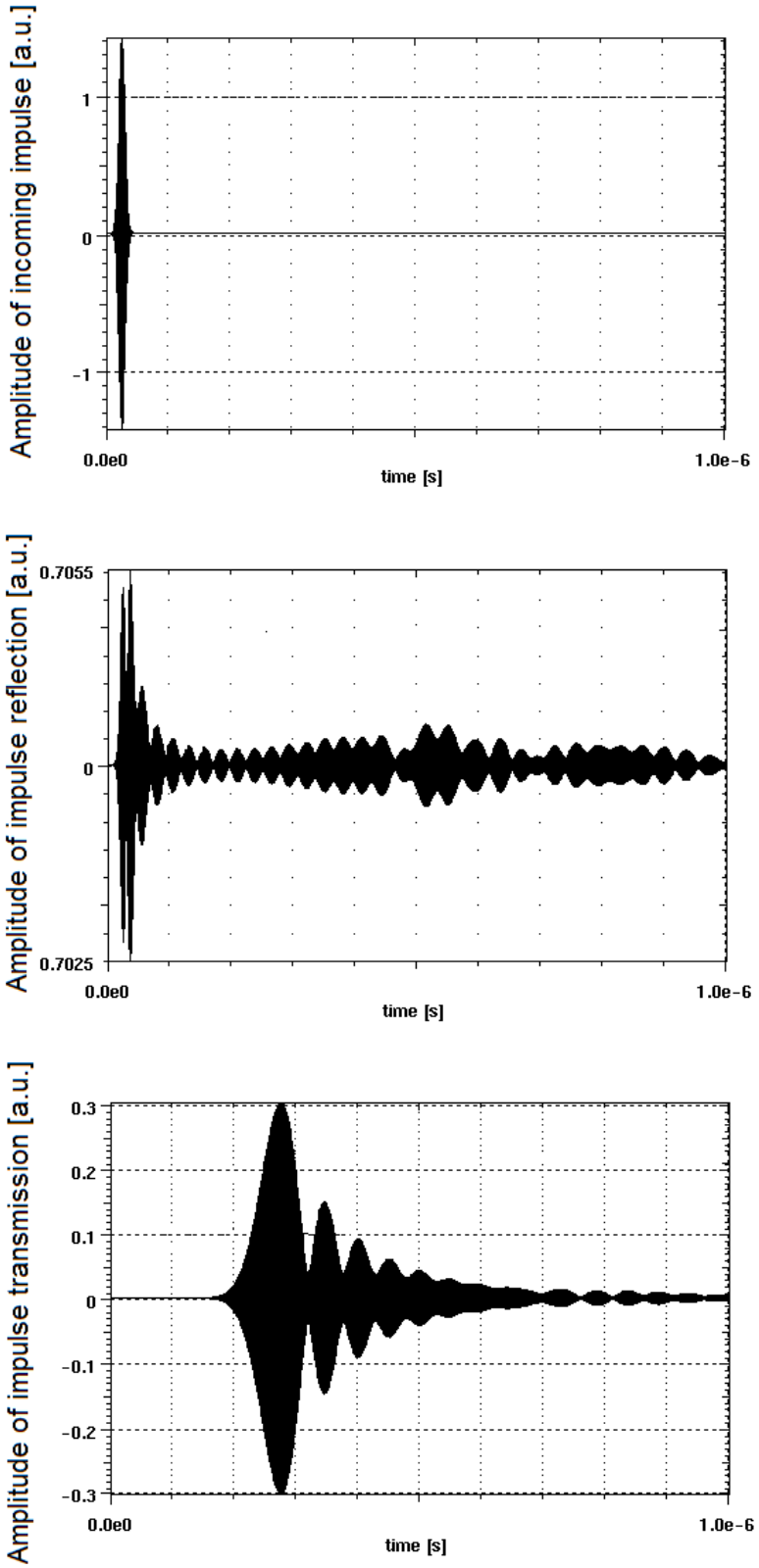

Figure 3.5: The amplitude (in arbitrary units) of the RF wave entering the Drive Beam accelerating structure (top), amplitude of its reflection (middle) and the RF amplitude at the exit of the structure (bottom) as a function of time (s) [76].

bunches within the RF filling time or the beam loading time respectively, and $conv(f, g)$ is the resulting error in the Drive Beam energy of the bunch with bunch number i. The maximal value of i is the total number of bunches per Drive Beam pulse, which is 69 600. The maximal value of j corresponds to the number of the Drive Beam bunches impacted by one RF wave or by the wake field of one bunch, $J = (448\text{ ns})/(2\text{ ns}) = 224$ for the RF filling potential and $J = (228\text{ ns})/(2\text{ ns}) = 114$ for the beam loading amplitude. Hence, the Drive Beam energy error induced in the accelerating structures can be calculated as

$$\Delta E_i = \sum_{j=1}^{224} \Delta A_{RF,i-j} \cdot A_{RF,j} - \sum_{k=1}^{114} \Delta Q_{i-k} \cdot A_{BL,k}. \tag{3.9}$$

The negative sign between the two terms is explained by the fact that A_{RF} represents an accelerating, and A_{BL} a decelerating, electromagnetic field.

3.1.3 Compressor chicane

In the compressor chicane instabilities in several parameters cause errors in the other parameters. The chicane lattice simulations [47], [71], [56] performed with the PLACET tool [77] have identified the parameter interdependences and their influence on one other for the different chicane designs (see examples in Figures 3.6 and 3.7).

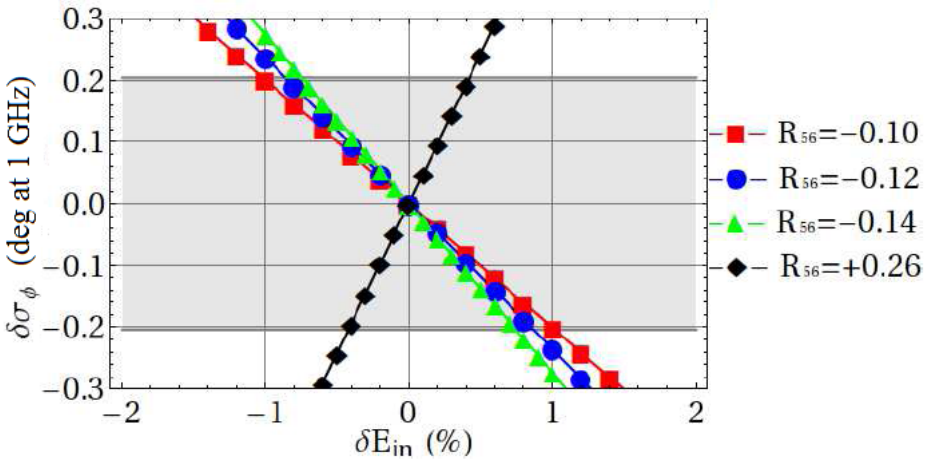

Figure 3.6: Drive Beam phase error at the compressor chicane (deg. at 1 GHz) vs. relative beam energy error (%) at linac entrance with different R_{56} values [56].

Since the compressor chicane has a non-zero bunch compression factor (R_{56}), the energy error contributes to the phase error when the bunches propagate through the chicane. Also the phase $\Delta\phi_{RF}$ or amplitude ΔA_{RF} errors of the Drive Beam accelerating structures before the chicane lead to the beam receiving an erratic energy increase. This leads to further phase error when the beam propagates through the chicane, as above.

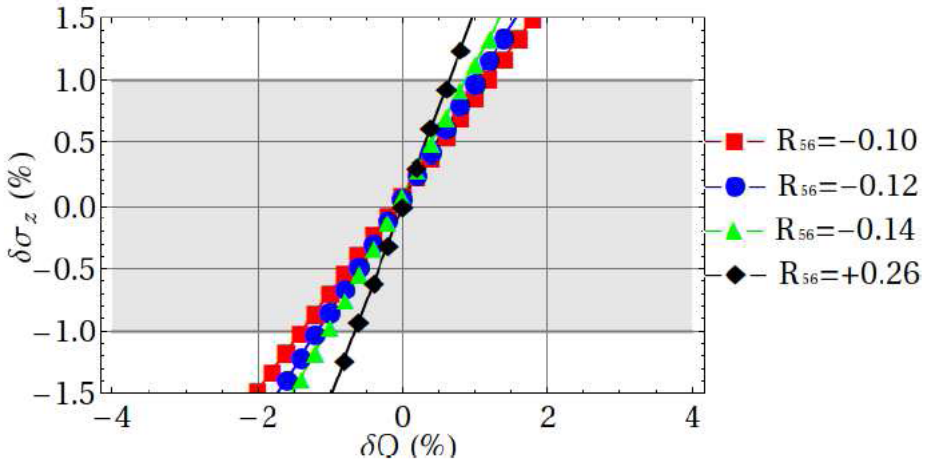

Figure 3.7: Relative bunch length error at the compressor chicane (%) vs. relative bunch charge error (%) with different R_{56} values [56].

The errors in the bunch charge ΔQ contribute to the energy error as well - since the Drive Beam accelerating structures operate in the fully loaded mode (see Sec. 2.2.1) the erratic beam loading impacts strongly the total energy absorbed by the beam. This leads to phase error in the chicane. Also, if the beam already has a phase error $\Delta\phi$ when it enters the chicane, this phase error is increased.

These interdependences for the baseline chicane design with $R_{56} = -0.1$ m have been implemented into the software tool for Drive Beam error tracking. They have been modelled in the first order approximation as linear parameter transformations summarised in Tab. 3.1. The table demonstrates how the bunches entering the Drive Beam linac and the compressor chicane with an error in a particular parameter (from one of the table's columns) leave the chicane with additional errors in other parameters (arrayed in the table's rows). E.g. a bunch entering the linac with an energy error of 1% would have at the chicane entry a relative energy error of 0.17%, since the energy of the beam is increased by a factor of six from 50 to 300 MeV in the first section of the Drive Beam linac (see Sec. 2.2.1 and Fig. 2.6). Considering the bunch compression factor of -0.1 m the additional phase error of the beam at the exit of the chicane would be

$$\Delta\phi_{chicane\ exit} = (\Delta E_{linac\ entry}/6) \times R_{56} = 0.17\% \times (-0.1\ \text{m}) = -170\ \mu\text{m}. \tag{3.10}$$

The results of the impact of Drive Beam accelerator errors (RF phase error and RF amplitude error) in the chicane [71] are also considered in the calculation.

3.1.4 Recombination scheme

In the recombination scheme the errors of the Drive Beam bunch parameters remain unchanged, since the R_{56} value of the Delay Line and the Combiner Rings is assumed to be

	ΔE [%] (*linac entry*)	$\Delta\sigma_z$ [mm]	ΔQ [%]	$\Delta\phi$ [deg@1GHz] (*chicane entry*)	$\Delta\phi_{RF}$ [deg@1GHz]	ΔA_{RF} [%]
ΔE [%]	1	0	0.005	0	0.06	-0.018
$\Delta\sigma_z$ [mm]	0	1	0.01	0.09	-0.09	-0.024
ΔQ [%]	0	0	1	0	0	0
$\Delta\phi[\mu$m] (*chicane exit*)	-170	0	20	80	750	-850
$\Delta\phi_{RF}$ [deg@1GHz]	0	0	0	0	1	0
ΔA_{RF} [%]	0	0	0	0	0	1

Table 3.1: Matrix of CLIC Drive Beam parameter interdependences in linear approximation [47]. The errors in the parameters of incoming bunches (columns) contribute in the compressor chicane to the errors in the parameters of the outgoing bunches (rows).

zero and the compressing and decompressing chicane pairs compensate the effects of one another. The only change induced by the recombination scheme affects the z position of the bunches. The Delay Line simulation distinguishes between bunches belonging to the even and the odd trains (see Section 2.2.2) depending on their z positions. The z position of the even bunches is then increased by 240 ns, simulating the delay induced by the Delay Line. The Combiner Rings operate in a similar way, delaying the incoming trains by $n \times 2 \times 240$ ns with $n = 2$, 1 and 0 consecutively in CR1 and $m \times 6 \times 240$ ns with $m = 3$, 2, 1 and 0 consecutively in CR2. The factor 2 for CR1 results from the fact that the incoming trains are already recombined to 1 GHz frequency by the Delay Line and come with 240 ns intervals; the factor 6 for CR2 is needed for the same reason, since the recombined 3 GHz trains after the Delay Line and CR1 have 5×240 ns intervals.

The sequence of beam extractions from the first Combiner Ring is non-trivial. As stated above, in CR1 the beam must be combined by a factor three and extracted in regular intervals of 6×244 ns for the proper operation of the second Combiner Ring. In order to satisfy both of these conditions, the second 1 GHz train arriving at CR1 must be extracted without recombination, as shown in Fig. 3.8. In this figure, the 1 GHz trains are represented by coloured points, they are injected from the left, circulate clockwise in the ring and are extracted to the right. There are 2×240 ns passing between the steps; the circumference of the ring is 4×240 ns, so each step signifies one half of a turn in the ring. The trains on the left are injected once per step and are located 240 ns from the injection, so that they are recombined during the injection process with the trains circulating in the ring. Doublets and triplets of points represent the trains with a combination factor of two and three, and hence with bunch frequency of 2 GHz and 3 GHz, respectively.

Figure 3.9 demonstrates the z-position of Drive Beam bunches after passing the complete recombination scheme as a function of their z-position before the recombination. The train with the lowest z-position after the recombination scheme is the 1 GHz bunch frequency train extracted from the first Combiner Ring without recombination. It is not used for the Main Beam acceleration. The following 12 GHz bunch frequency trains are used for Main Beam acceleration.

Despite the fact that the recombination scheme does not impact the errors of the Drive

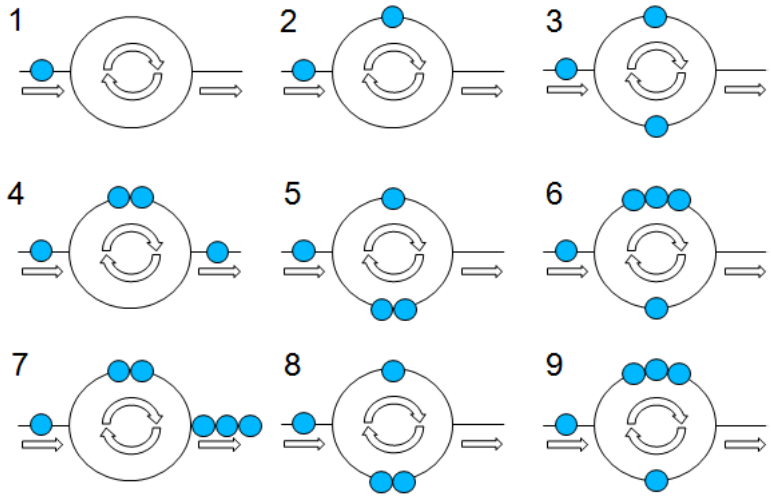

Figure 3.8: Scheme of first several circulations in the first Combiner Ring. In step 4 the 1 GHz bunch frequency train is extracted without recombination.

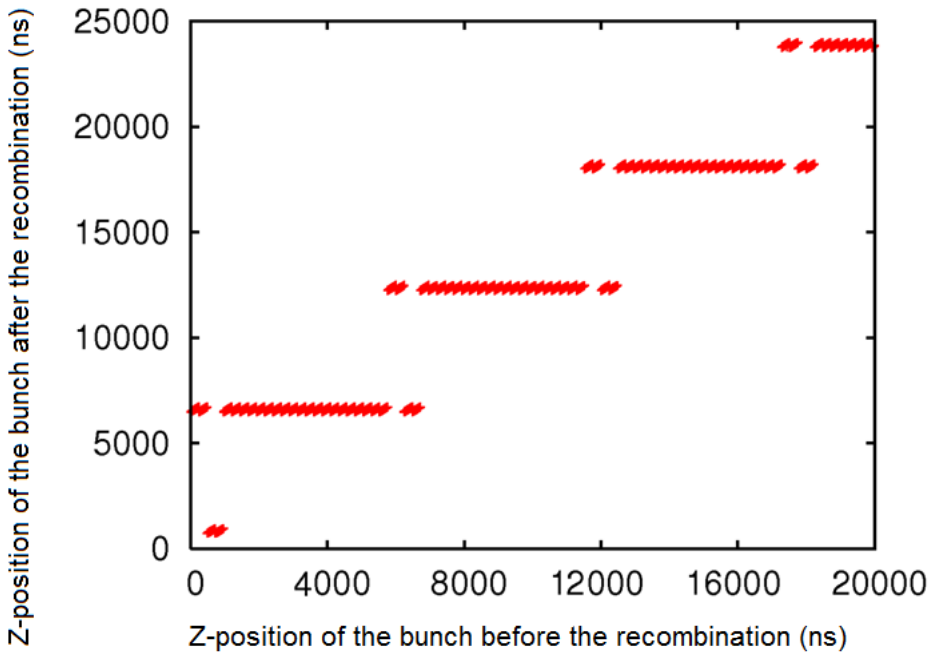

Figure 3.9: Bunch z-position before and after passing Drive Beam recombination scheme.

Beam bunches, the recombination introduces a significant filtering effect. This occurs in the following way: when the trains are recombined in the Delay Line and in the Combiner Rings, the errors from different trains come together in one train (Fig. 3.10) and the error functions overlap. In case when the wavelength of the error jitter is the same as the train length, the errors add up constructively. However, if the wavelength of the error jitter is not in resonance with the train length, errors of the bunches positioned next to each other

cancel out on the time scale of several tens of nanoseconds, which is the time scale of RF filling in Main Beam accelerating structures (see Sections 2.3 and 3.1.5). Consequently, these errors have a significantly lower impact on the Main Beam and effectively are filtered by the recombination scheme.

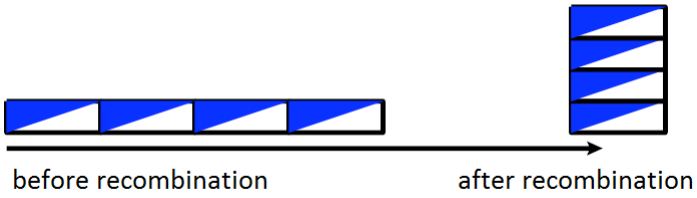

Figure 3.10: Depiction of train errors' overlap. The blocks on the left and right represent the trains before and after the recombination, respectively. After the recombination the error functions of the trains overlap.

3.1.5 PETS and Main Linac

After the calculation of the Drive Beam errors propagating through the linac, passing the chicane and being recombined in the Drive Beam recombination scheme, one needs to calculate the impact of these errors on the Main Beam. One can consider the ideal (error free) extraction of the RF wave from the Drive Beam, since the extraction errors are expected to be negligibly small. After the extraction the RF wave function, which includes the errors from the Drive Beam, is convolved with the beam loading (Fig. 3.11) and RF potentials (Fig. 3.12) functions of the Main Beam accelerating structures. The beam loading and RF potentials are the results of simulations with the HFSS code [78], performed in the frequency domain around the resonant peak in the interval from 11.7 GHz to 12.3 GHz [49].

Similarly to the calculation for the Drive Beam described in Section 3.1.2, the Main Beam RF filling potential and the beam loading amplitude are linearly approximated. The beam loading is approximated by one linear function (see solid red line on Fig. 3.11), going from the maximum amplitude value to zero in 51 ns (Eq. 3.11).

$$A_{BL,MB}(t) = A_{BL,MB,max} \cdot \left(1 - \frac{t}{51\ \text{ns}}\right) \tag{3.11}$$

The RF filling potential is approximated by three functions indicated by the solid red lines on Fig. 3.12. The function reduces the potential from its maximum by 35% within the first 45 ns, then by a further 54% within the next 17 ns and then to zero within the next 43 ns, making the total RF filling time 105 ns.

$$A_{RF,MB}(t) \;=\; A_{RF,MB,max} \cdot \left(1 - 0.35 \cdot \frac{t}{45\ \text{ns}}\right) \text{ for } 0\ \text{ns} \leq t < 45\ \text{ns} \tag{3.12}$$

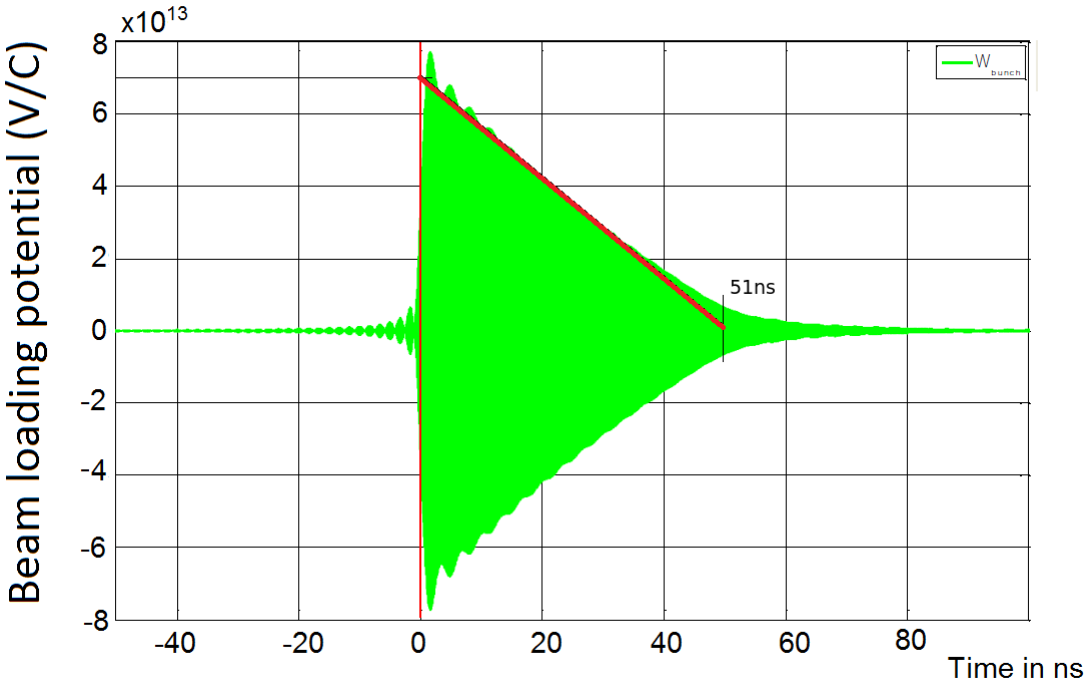

Figure 3.11: Simulation result for beam loading amplitude (V/C) as a function of time for CLIC Main Beam cavities [49]. The linear approximation is indicated by a red line.

$$= A_{RF,MB,max} \cdot \left(0.65 - 0.54 \cdot \frac{t - 45\text{ ns}}{62\text{ ns} - 45\text{ ns}}\right) \text{ for } 45\text{ ns} \leq t < 62\text{ ns}$$

$$= A_{RF,MB,max} \cdot \left(0.11 - 0.11 \cdot \frac{t - 62\text{ ns}}{105\text{ ns} - 62\text{ ns}}\right) \text{ for } 62\text{ ns} \leq t \leq 105\text{ ns}$$

The beam loading amplitude integrated over time is thereby about 18% of the integrated RF potential.

The functions of the RF potential and the beam loading amplitude are convolved with the phase and charge errors of the Drive Beam bunches. The values of the convolution function are calculated with an interval of 0.5 ns, which corresponds to the Main Beam bunch frequency of 2 GHz. Since one 156 ns long Main Beam train is accelerated in each of the 24 decelerator sections by a separate 240 ns long Drive Beam train, the contributions of the Drive Beam trains from the different decelerator sections must be added up in order to calculate the total impact of the Drive Beam errors on the Main Beam. Thereby it is necessary to consider that the nominal RF phase of the Main Beam accelerating structures is $\phi_{MB,nom} = 8°$ for the first twenty decelerator sections and $\phi_{MB,nom} = 30°$ for the last four sections before the Beam Delivery System. So the convolution result must be multiplied with $\sin 8°$ for first twenty Drive Beam trains and with $\sin 30°$ for last four trains. Hence, for the Main Beam bunch number k the impact of the phase error $\sigma_{\phi,MB}$ and the charge error $\sigma_{Q,MB}$ can be calculated as the sum of the phase errors of all preceding Drive Beam bunches in the interval of 105 ns along all 24 decelerators, convolved with the Main Beam RF filling and beam loading functions, normalised by the nominal RF phase (Eqs. 3.13, 3.14

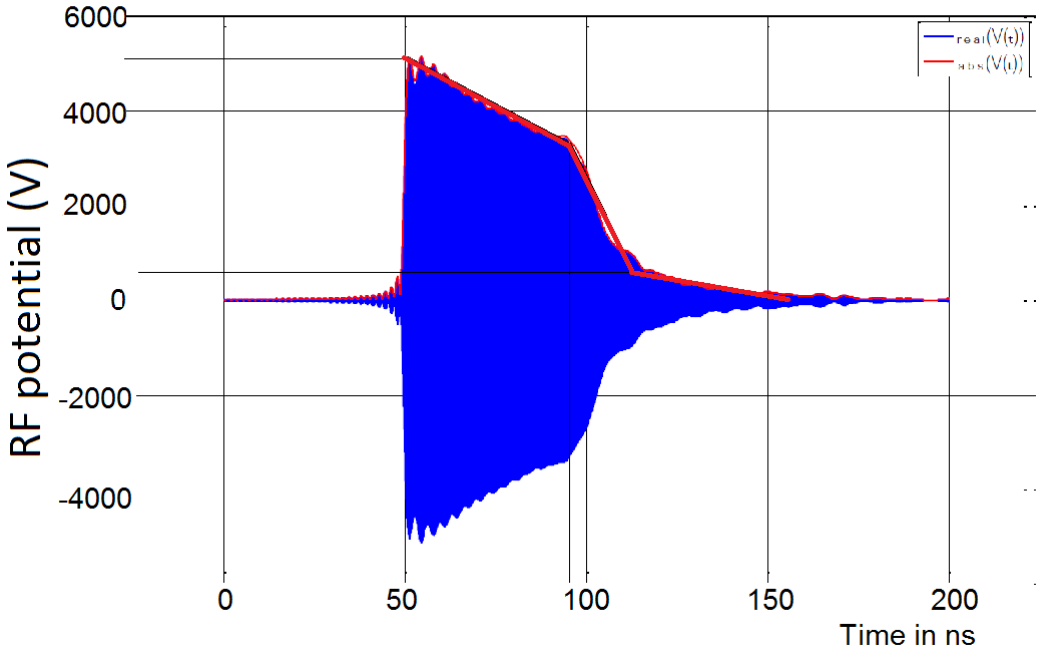

Figure 3.12: Simulation result for RF filling potential (V) as a function of time (ns) for CLIC Main Beam cavities [49]. The linear approximation is indicated by the red lines.

and 3.15):

$$\sigma_{\phi,MB}(t(k)) = \frac{\int_{t'=0}^{105\ \mathrm{ns}} \sum_{i=1}^{24} \Delta\phi(t(k)-t') \cdot A_{MB,loaded}(t') \cdot \phi_{MB,nom,i} \cdot dt'}{\int_{t'=0}^{105\ \mathrm{ns}} \sum_{i=1}^{24} A_{MB,loaded}(t') \cdot \phi_{MB,nom,i} \cdot dt'} \tag{3.13}$$

$$\sigma_{Q,MB}(t(k)) = \frac{\int_{t'=0}^{105\ \mathrm{ns}} \sum_{i=1}^{24} \Delta Q(t(k)-t') \cdot A_{MB,loaded}(t') \cdot \phi_{MB,nom,i} \cdot dt'}{\int_{t'=0}^{105\ \mathrm{ns}} \sum_{i=1}^{24} A_{MB,loaded}(t') \cdot \phi_{MB,nom,i} \cdot dt'} \tag{3.14}$$

$$\sigma_{\sigma_z,MB}(t(k)) = \frac{\int_{t'=0}^{105\ \mathrm{ns}} \sum_{i=1}^{24} \Delta\sigma_z(t(k)-t') \cdot A_{MB,loaded}(t') \cdot \phi_{MB,nom,i} \cdot dt'}{\int_{t'=0}^{105\ \mathrm{ns}} \sum_{i=1}^{24} A_{MB,loaded}(t') \cdot \phi_{MB,nom,i} \cdot dt'} \tag{3.15}$$

with

$$A_{MB,loaded}(t') = A_{RF,MB}(t') - A_{BL,MB}(t') \tag{3.16}$$

and

$$\begin{aligned} \phi_{MB,nom,i} &= \sin 8^\circ \text{ for } 1 \leq i \leq 20 \\ &= \sin 30^\circ \text{ for } 21 \leq i \leq 24,\ i \in \mathbb{N}. \end{aligned} \tag{3.17}$$

Using $\sigma_{\phi,MB}$, $\sigma_{Q,MB}$ and $\sigma_{\sigma_z,MB}$ in the Eq. 2.1 [55] as $\sigma_{\phi,inc}$ and $\sigma_{I,inc}$ and $\sigma_{\sigma_z,inc}$ respectively, the luminosity loss of CLIC can be calculated as

$$\frac{\Delta\mathcal{L}}{\mathcal{L}} = 0.01 \times \left[\left(\frac{\sigma_{\phi,MB}}{0.8^\circ} \right)^2 + \left(\frac{\sigma_{Q,MB}}{2.2 \times 10^{-3} Q_{nom}} \right)^2 + \left(\frac{\sigma_{\sigma_z,MB}}{3.3 \times 10^{-2} \sigma_z} \right)^2 \right] \tag{3.18}$$

3.2 Charge feedback model

The errors in bunch charge of the Drive Beam Q can lead to a significant luminosity loss, as it can be seen in Eq. 2.1. In order to stabilise the Drive Beam current, a feedback system must be introduced. This system would measure the bunch charge error and send a signal to the Drive Beam source, which would correct the charge of the following bunches. The current section describes the functionality of a potential feedback. It discusses the implication of the proportional-integral-derivative controller into the simulation and describes how the feedback latency and gain times can be optimised.

3.2.1 PID Controller

One of the standard feedback algorithms is a so called proportional-integral-derivative controller (PID controller). The proportional and integral parts of PID controller can be used for so called proportional feedback (Eq. 3.19), which calculates the correction C_i as the sum of the measured value of the previous bunch charge error ΔQ_{i-1} and the correction applied to the previous bunch C_{i-1}, multiplied with the respective gain factors a_{prop} and a_{int}.

$$C_i = a_{prop} \cdot \Delta Q_{i-1} + a_{int} \cdot C_{i-1} \tag{3.19}$$

The so called differential feedback (Eq. 3.20) uses all three elements of the PID controller and hence additionally calculates the change of the measured charge value ΔQ and correction value C between last two bunches with indices $(i-1)$ and $(i-2)$, multiplied with the appropriate gain factor a_{diff}.

$$C_i = a_{prop}\Delta Q_{i-1} + a_{int} C_{i-1} + a_{diff,1}(\Delta Q_{i-1} - \Delta Q_{i-2}) + a_{diff,2}(C_{i-1} - C_{i-2}) \tag{3.20}$$

3.2.2 Optimisation of feedback latency time t_l

There is necessarily a delay between the bunch charge measurement and the correction in the source, called the 'latency time' of the feedback system, t_l. The latency time is a sum of the times required by the monitors and electronics for the data acquisition (t_{da}), the signal transfer time from the measurement point to the beam source (t_{sig}) and the signal processing time of the correction system (t_{cor}):

$$t_l = t_{da} + t_{sig} + t_{cor} \tag{3.21}$$

Assume the bunch charge jitter has one dominant frequency, $f_{\sigma_Q,dom}$ with a corresponding period $t_{\sigma_Q,dom} = 1/f_{\sigma_Q,dom}$. The necessary condition for the feedback to have a stabilising impact on the beam is that the charge errors of the bunches affected by the correction have similar values to the bunches at which the error was measured. This condition is satisfied if the feedback latency time is much smaller than the dominant period of the bunch charge error, $t_l \ll t_{\sigma_Q,dom}$. As a consequence, the feedback is more effective for low frequencies of the bunch charge errors. Also feedback can be effective if its latency is of the same length as the dominant jitter frequency, $t_l \approx t_{\sigma_Q,dom}$. In this case the feedback is said to be resonant with the jitter (see Fig.3.13, top). However, if the latency is only half of the dominant jitter wavelength, $t_l \approx \frac{1}{2}t_{\sigma_Q,dom}$, the feedback system doubles the error, since the correction is applied displaced 180° of error phase, and so the correction has the same sign as the error itself (see Fig. 3.13, bottom). Such a feedback would reduce the beam stability and must be avoided.

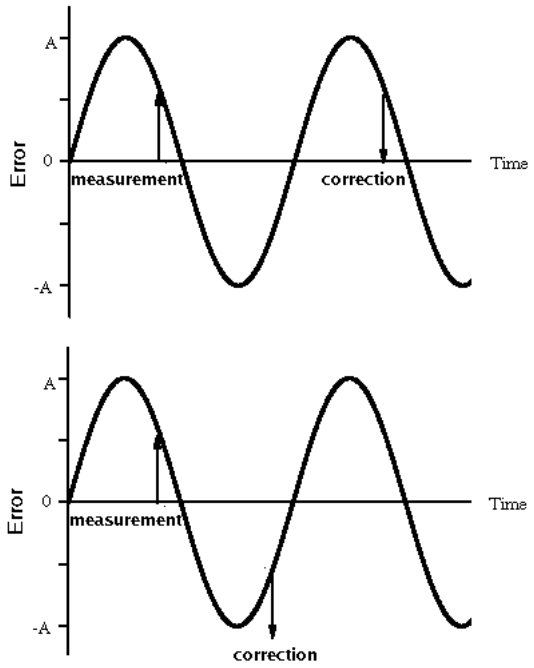

Figure 3.13: Illustration of the action of a feedback system resonant (top) and anti-resonant (bottom) to the dominant jitter frequency. The error in arbitrary parameter is plotted as a function of time.

An illustration of that result can be provided by a calculation of the response of the proportional and differential feedback systems on a single incoming Dirac delta function impulse. Calculating the discrete Fourier transform of the impulse response leads to distributions shown in Fig. 3.14, where the value of the impulse response is plotted as a function of the jitter frequency f_{σ_Q} over the frequency corresponding to feedback latency time $f_l = 1/t_l$. For the jitter frequencies for which the impulse response has a value below one, the feedback

system will on average improve the stability of the parameter, for the other frequencies the error will be amplified.

As one can see, at low frequencies or frequencies near the resonance with the jitter the Fourier transform values of the differential feedback are lower, and hence at these frequencies the differential feedback would be more efficient.

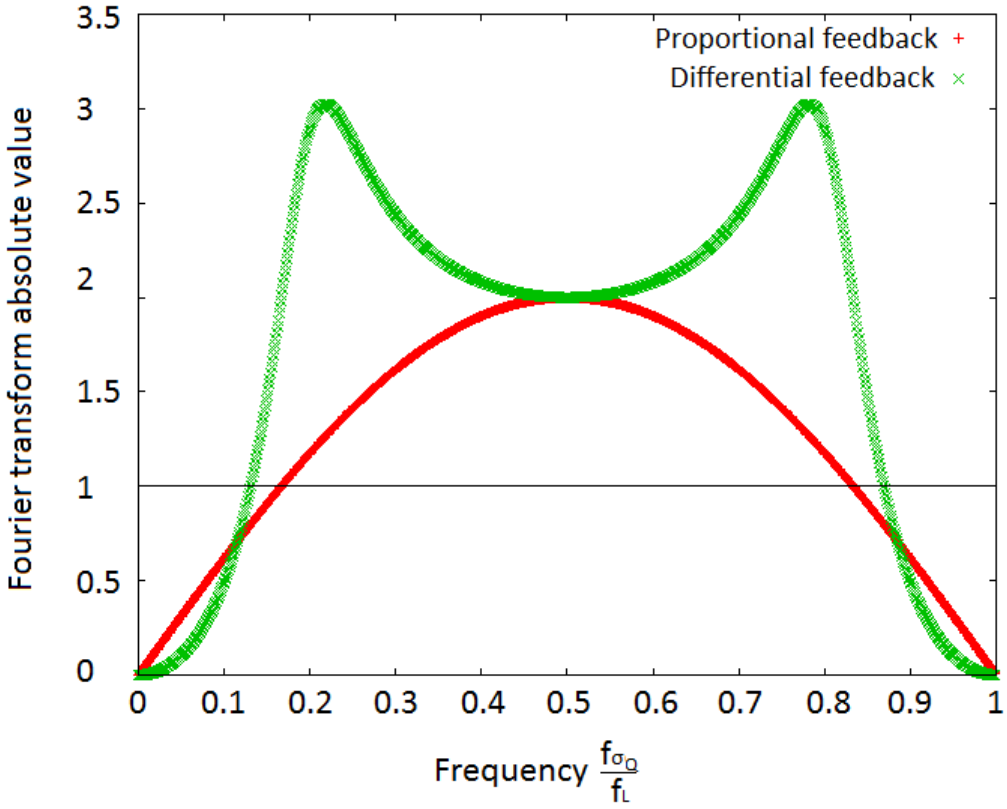

Figure 3.14: Error amplitude as a function of jitter frequency for the impulse response of proportional (red) and differential (green) feedbacks.

3.2.3 Feedback gain time t_g

In addition to the feedback latency time t_l described in Sec. 3.2.2, the feedback system amplifier cannot provide a correction signal with an infinite time resolution; the feedback system needs some time for the full correction to be applied. The operation of the FONT system shows that the rise of the amplifier signal is approximately linear [79], hence for the purpose of the present simulation studies the signal is averaged over the time t_g corresponding to the bandwidth of the amplifier as $t_g = 0.35/f_{bw}$ [80]. This time is called the feedback gain time.

t_l and t_g are always non-zero for real feedback systems, so that the bunch-to-bunch correction presented in Eqs. 3.19 and 3.20 is not possible if the sum of t_l and t_g is larger

than the bunch spacing (t_{bsp}). Since t_{bsp} at CLIC is very short (2 ns before the recombination of the Drive Beam and 83 ps after) the latency time and gain time have to be taken into account in the simulations. In order to implement t_l and t_g into the simulation one can express them in terms of the number of bunch spacing intervals. E.g. for the uncombined Drive Beam, with bunch spacing of 2 ns and $t_l = 160$ ns, one could use $t_l = 80$. Using this approach Eqs. 3.19 and 3.20 can be transformed to the following equations for proportional (Eq. 3.22) and differential feedback (Eq. 3.23) respectively:

$$C_i = \frac{1}{t_g}\sum_{j=1}^{t_g}[y_{i-t_l-j} + C_{i-t_l-j}] \tag{3.22}$$

$$C_i = \frac{1}{t_g}\sum_{j=1}^{t_g}[y_{i-t_l-j} + C_{i-t_l-j} + (y_{i-t_l-j} - y_{i-2\times t_l-j}) + (c_{i-t_l-j} - c_{i-2\times t_l-j})] \tag{3.23}$$

A demonstration of the application of the proportional feedback (Eq. 3.22) is presented in Fig. 3.15. The phase error is plotted as a function of the bunch number. In bunch number two an error of a value normalised to one is introduced. After the latency $t_l = 5$ bunches the feedback system responds and provides a correction. The gain time is $t_g = 5$ bunches, so that the effect of the correction in applied to five following bunches with a fifth of the original nominal error being corrected at each of them.

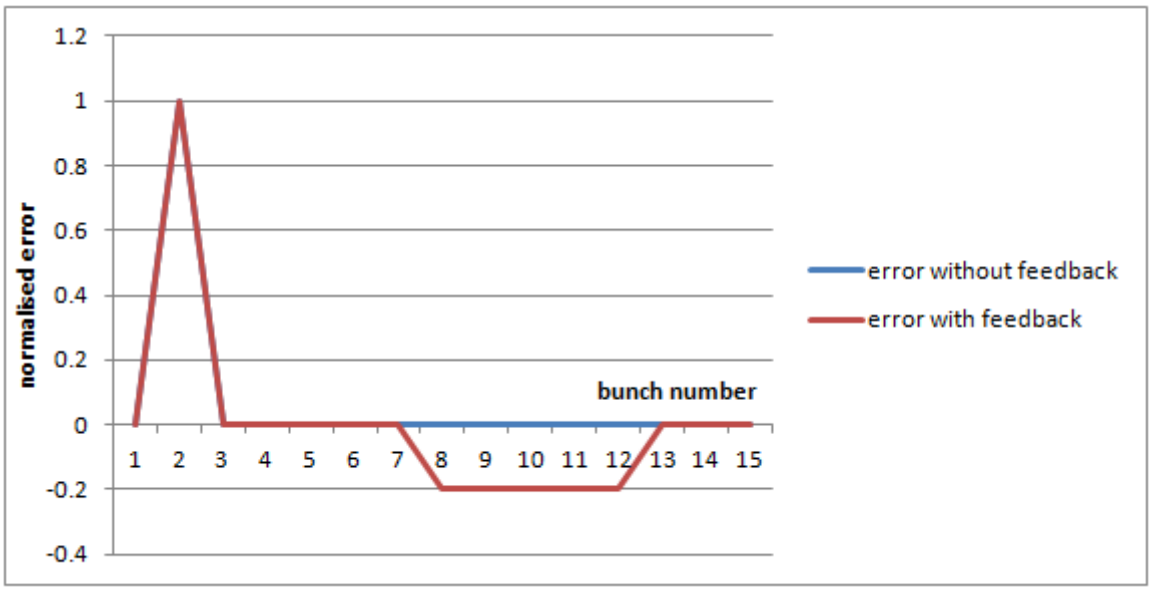

Figure 3.15: Illustration of the feedback system simulation. A normalised error at bunch number two is introduced, the error of a system without feedback (in blue) and with feedback (in red) is plotted as a function of bunch number.

3.3 Phase feed-forward

A feed-forward system is a stabilisation system similar to a feedback: feed-forward also measures the parameter errors, amplifies the measurement signal and provides a correction. The main difference between feed-forward and feedback is the fact that measurement data in the case of a feed-forward are available at the position of correction before the arrival of the bunches. Since the bunches in a high-energy accelerator move with a speed approaching the speed of light, the feed-forward is only possible if there is a turnaround of the beam. The turnaround of the Drive Beam before the decelerator section can be used for a longitudinal phase feed-forward system, as described in Section 2.5.1.

The simulation of the feed-forward can be also performed with the help of Eqs. 3.22 and 3.23. The latency time, t_l, in the case of feed-forward can be reduced to zero (Fig. 3.16) or even be negative (Fig. 3.17). It is given by Eq. 3.24 (compare with Eq. 3.21 for the feedback latency time):

$$t_l = t_{da} + t_{amp} + t_{sig} + t_{fit} - t_{beam} \tag{3.24}$$

with t_{da} being the time needed for the data acquisition, t_{amp} the processing time of the amplifier, t_{sig} the signal propagation time through the cables, t_{beam} the time the beam needs to propagate from the phase monitors through the turnaround to the correction modules and t_{fit} being a free parameter, which can be optimised in order to minimise the error impact on the Main Beam (see Sec. 5.3).

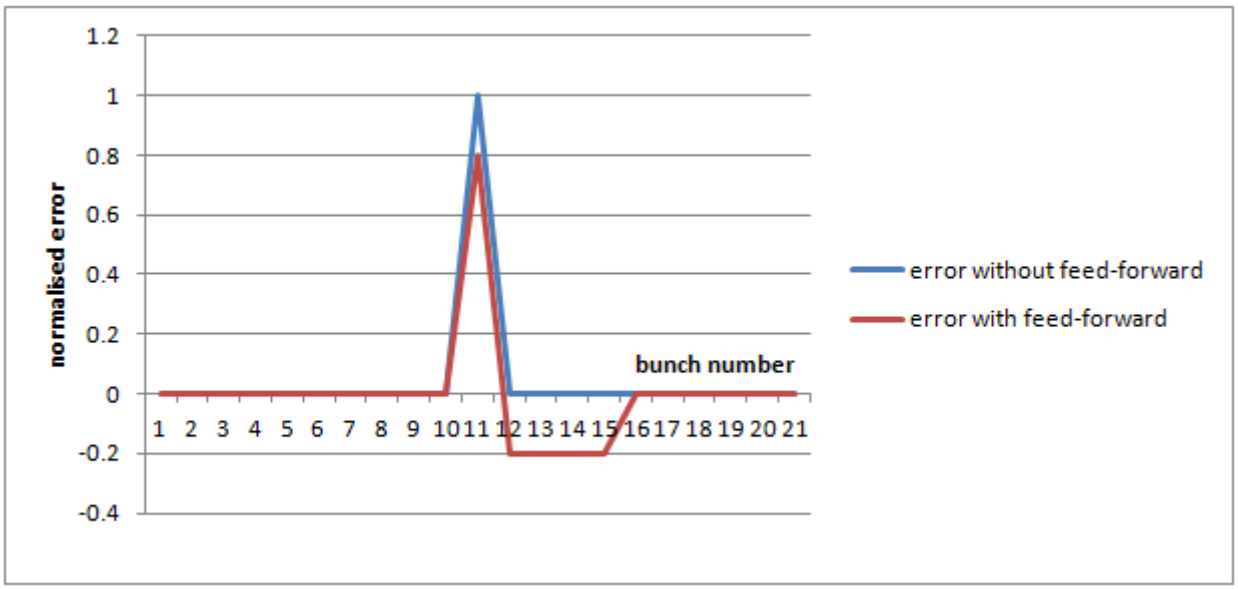

Figure 3.16: Illustration of the feed-forward simulation with $t_l = 0$ and $t_g = 5$. A normalised error at the bunch number eleven is introduced, the error without (blue) and with (red) feed-forward application is plotted as a function of bunch number.

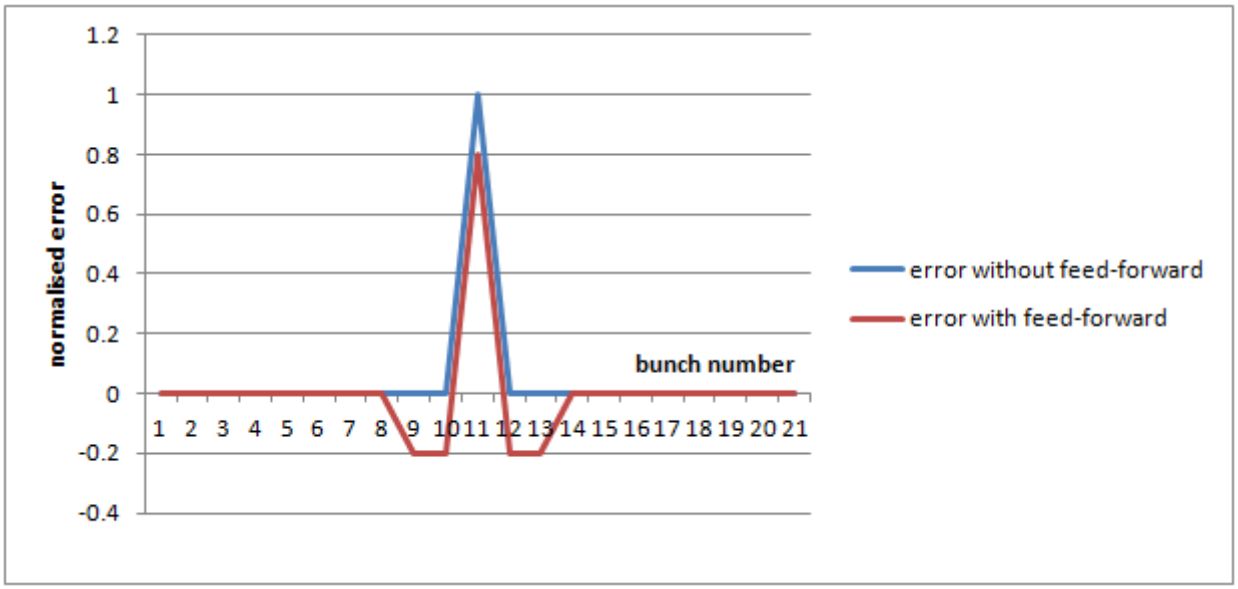

Figure 3.17: Illustration of the feed-forward simulation with $t_l = -\frac{1}{2}t_g$ and $t_g = 5$. A normalised error at the bunch number eleven is introduced, the error without (blue) and with (red) feed-forward application is plotted as a function of bunch number.

Since the gain time t_g is defined by the bandwidth of the amplifier, it cannot be reduced to zero. The influence of different amplifier bandwidths on the feed-forward operation can be seen in Fig. 3.18. The normalised error is introduced at bunch number eleven and averaging of the feed-forward system is performed with $t_g = 5$ (red curve) and $t_g = 11$ (green curve). As one can recognise, the lower bandwidth (longer averaging time) feed-forward "smears" the correction effect over the larger number of bunches and hence is less efficient for the high-frequency errors. A detailed analysis of the amplifier bandwidth impact on the feed-forward correction efficiency is presented in Sec. 5.3.2.

Phase monitors

Phase monitors are devices for measuring the longitudinal position of the beam bunches. These are modules comparing the electromagnetic signal in the beamline resonant with the bunch frequency with a nominal phase signal. However, the resolution of the monitors is limited. Hence, the signal that the feed-forward system receives as input for the correction has additional noise. To simulate it in the Drive Beam software tool the phase error is convolved with the noise function of the monitor.

The software tool also offers the possibility to simulate the filtering of the monitor signal with a filter, e.g. a Chebyshev filter, in order to remove noise frequencies not resonant with the bunch frequency.

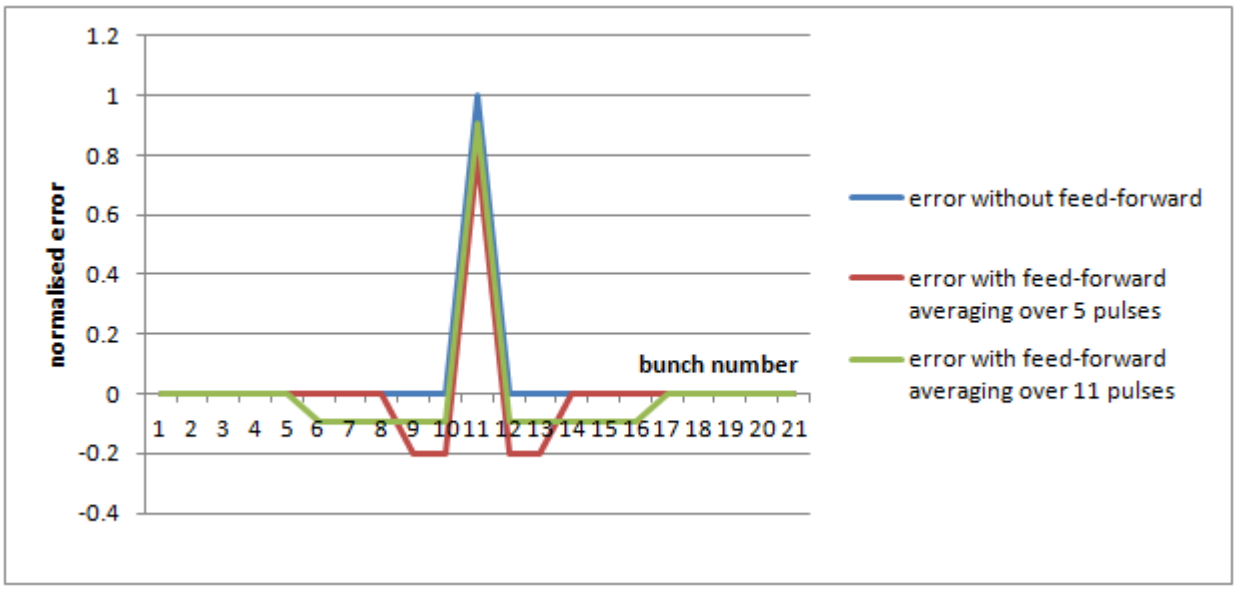

Figure 3.18: The error without (blue) and with feed-forward application with $t_g = 5$ bunches (red) and $t_g = 11$ bunches (green) is plotted as a function of bunch number. A normalised error at the bunch number eleven is introduced.

Synchronisation system

Additional input noise for the feed-forward correction is provided by the phase synchronisation system described in Sec. 2.5.2. In approach A the Main Beam is used to align the Drive Beam. Consequently, the errors of the Main Beam phase measurement are included into the correction signal for the Drive Beam and Eq. 3.22 has to be used with an additional term $\Delta\phi_{i-t_l-j}(meas)$:

$$C_i = \frac{1}{t_g}\sum_{j=1}^{t_g}\left[\Delta\phi_{i-t_l-j} + C_{i-t_l-j} + \Delta\phi_{i-t_l-j}(meas)\right]. \tag{3.25}$$

For approach B the master clock in the centre of the detector is used as a reference phase input for the Main and Drive Beams. The simulation tool allows to implement the errors of the signal distribution along the accelerator. A random walk of the phase error can be simulated from one decelerator sector to another in both directions from the interaction point of CLIC. Assuming that the additional phase error introduced at each decelerator sector has a value $\sigma_{\phi,step}$, the total phase error caused by the distribution system at segment number i counted from the CLIC IP can be calculated as $\sum_{j=1}^{i}\sigma_{\phi,step}$.

3.4 Summary

The current section summarises the methodology of the simulation studies for the CLIC Drive Beam stabilisation and gives a brief overview of the software tool developed for this

purpose.

The software tool is written in the C++ programming language and uses the results of separate simulation studies ([76], [47], [71], [56], [49] and [55]). The initial errors in the following CLIC Drive Beam parameters can be simulated:

- bunch charge ΔQ,
- bunch length $\Delta\sigma_z$ and bunch form factor F,
- longitudinal bunch phase $\Delta\phi$,
- average energy of the bunch ΔE,
- the RF wave amplitude in the klystrons ΔA_{RF} and
- the RF wave phase of the klystrons $\Delta\phi_{RF}$.

The software tool uses realistic Drive Beam RF filling and beam loading functions, which are the results of an independent simulation [76]. With the help of these functions (in a linear approximation) it calculates the impact of the errors on the amplitude and phase of the Drive beam klystrons as well as on the beam loading errors due to the Drive Beam current variation.

The impact of the compressor chicane installed in the Drive Beam linac at an energy of 300 MeV is calculated using the results of the simulation studies [47], [71] and [56]. The contribution of the errors in some CLIC Drive Beam parameters to the errors in other parameters is summarised in Tab. 3.1.

A full model of the recombination scheme has been implemented, repositioning the Drive Beam bunches longitudinally for further calculations in the PETS.

The extraction of the RF wave at the PETS is assumed to be error-free. The model for the RF filling and beam loading functions of the Main Beam accelerating structures [49] has been approximated linearly and implemented into the software tool. From the Drive Beam errors in longitudinal phase (σ_ϕ), bunch length (σ_{σ_z}) and bunch charge (σ_Q) transmitted to the Main Beam, the software tool calculates CLIC's luminosity loss according to the energy bandwidth of the CLIC beam delivery system presented in Eq. 3.18 [55].

The models for the proposed charge feedback and phase feed-forward systems have been implemented into the tool. The charge feedback system would be installed near the source of the Drive Beam and correct the measured errors of the bunch charge and beam current. The possibility to set (and optimise) the latency time and gain duration for the feedback system have been included into the software tool.

The feed-forward system would be installed at the final turnaround of the Drive Beam before it enters the PETS. The signal processing and transfer time of the feed-forward should

be faster then the time of the beam needed to pass the turn-around loop, so no latency time is needed for the simulation of the feed-forward system. However, the feed-forward system amplifier has a limited bandwidth, so a possibility to set the gain duration parameter has been included into the simulation software.

Chapter 4

Verification of software tool functionality

It is necessary to verify the correct functionality of the software tool before using it for the simulation studies. In order to perform such verification one can compare the software tool simulation output of each Drive Beam section with the results of independent calculation for some simple cases. In the current chapter the comparison is presented in four different sections, each corresponding to one segment of the Drive Beam:

- Sec. 4.1 demonstrates the impact of the Drive Beam accelerator RF amplitude errors on the beam energy.
- Sec. 4.2 presents the calculation of the bunch length error caused by the bunch charge error in the compressor chicane.
- Sec. 4.3 shows the recombination performed step-by-step at the Delay Line, the first and the second Combiner Rings.
- Sec. 4.4 analyses the impact of Drive Beam phase errors on the Main Beam in the PETS and Main Beam accelerating structures. The calculation is performed for a single Drive Beam bunch phase error and constant Drive Beam phase offset.

For each study only one example is presented in this chapter; however, a full functionality test of all parameters in all sections included in the simulation tool has been performed.

4.1 Drive Beam accelerator

In order to test the functionality of the Drive Beam accelerator simulation module, an impulse response test has been executed. A 2 ns long error in the Drive Beam accelerating RF amplitude with the relative value of $\Delta A_{RF}/A_{RF,nom} = 0.38\%$ has been simulated. The value has been selected so that a constant offset of $A_{RF}/A_{RF,nom} = 0.38\%$ would lead to a phase

error corresponding to the CLIC tolerance of 14 μm.

The beam energy error resulting from the 2 ns long RF amplitude impulse is presented in Fig. 4.1 as a function of bunch number. One can clearly recognise the shape of the energy error to be similar to the RF filling potential for CLIC Drive Beam cavities presented in Fig. 3.4. The maximal energy error value is at bunch number 1001 and has a value $\Delta E = 0.16$ MeV. This value is reduced at bunch number 1117 (which is 234 ns away) to $\Delta E = 0.11$ MeV, corresponding to a reduction of 33.1%. Bunch number 1134 (additional 34 ns away) has an energy error of $\Delta E = 0.03$ MeV, corresponding to an additional reduction of 47.6%. Bunch number 1224, being 448 ns away from bunch 1001 has no energy error. Comparing this function progression with the one presented in Sec. 3.1.2 shows that the shape of the convolution function used in the simulation tool corresponds to the shape of the function approximating the Drive Beam RF filling potential. Adding up the energy errors of bunches 1001 to 1224 yields

$$\sum_{i=1001}^{1224} \Delta E_i = 18.37 \text{ MeV} \tag{4.1}$$

which corresponds to 0.77% of E_{nom}. This integrated value is twice the relative value of $\Delta A_{RF}/A_{RF,nom} = 0.38\%$ for the following reason: the energy of the Drive Beam corresponds to the integrated beam loading of the Drive Beam accelerating structures. The normalisation of the integrated A_{RF} presented in Sec. 3.1.2 has been set to be twice the integrated beam loading function (Eq. 3.7). Consequently, the errors in the Drive Beam RF potential have twice the effect on the Drive Beam energy.

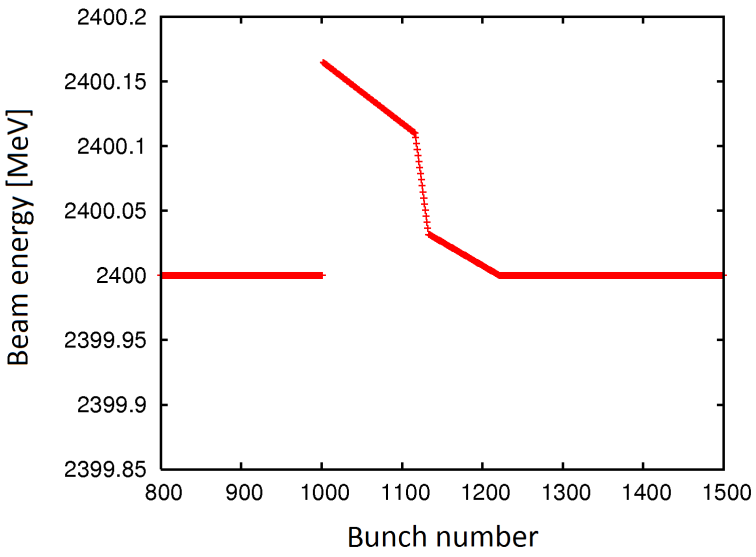

Figure 4.1: Drive Beam energy as a function of bunch number in the case that the Drive Beam accelerating RF amplitude has a 2 ns long relative error of 0.38%.

4.2 Compressor chicane

In the current section the examination of the compressor chicane simulation is presented. The Drive Beam bunches are set to have a bunch charge deviating from the nominal charge $Q_{nom} = 8.4$ nC by $\pm 0.01\% \cdot n$, $n = \{-10, -9, ..., 9, 10\}$. The compression factor in the compressor chicane is charge dependent [56], so that the bunch length varies according to the bunch charge error value.

Bunch length errors must be compensated by the change of the beam charge, as has been described in Sec. 3.1.1. This compensation can be performed by a feedback system, which has been included into the software tool simulation. However, this effect is not considered in the result presented in the current subsection in order to isolate and separately test the effect of the compressor chicane on the beam in the simulation tool.

Fig. 4.2 shows the bunch length as a function of the bunch charge. One can recognise that the dependence has the same form as the one displayed in Fig. 3.7. A bunch charge error of 0.1% causes a bunch length error of 0.001 mm in the simulation output. This is in perfect agreement with the results of of the underlying studies [47] [71] [56], results of which have been presented in Sec. 3.1.3 and included via a linear approximation in Tab. 3.1.

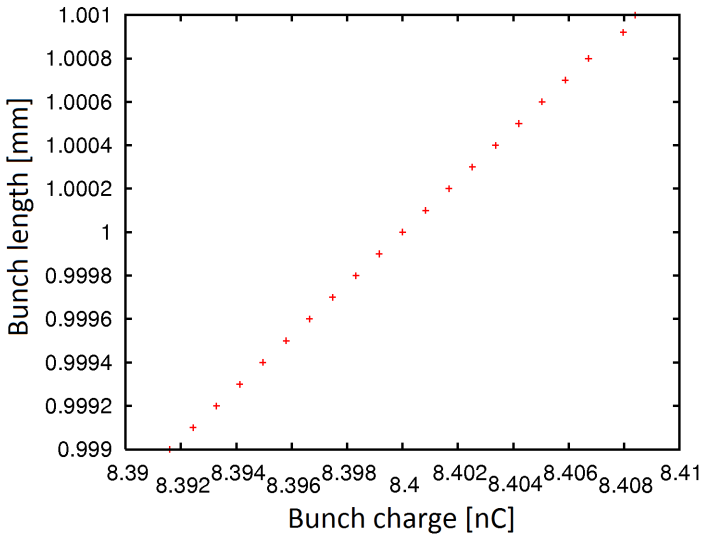

Figure 4.2: Drive Beam bunch length as a function of bunch charge after the beam passes the compressor chicane.

4.3 Recombination scheme and bunch z-position

In the recombination scheme the z-position of the Drive Beam bunches is modified. Each of the sectors, the Delay Line and the two Combiner Rings, shift the bunches grouped in trains to higher z-values in a predefined pattern. For the test of this simulation module the bunch z-position was tracked as a function of the unchanging bunch number and displayed after

each recombination scheme sector.

Fig. 4.3 shows the bunch z-position before the Drive Beam enters the Delay Line. One can recognise that the bunch z-position follows the bunch number, and the average bunch-to-bunch interval is 2 ns. The 180° phase shifts of the buckets (see Sec. 2.2.1) are responsible for 1 ns bunch position alterations and are not recognisable due to the resolution and the zoom factor of the plot.

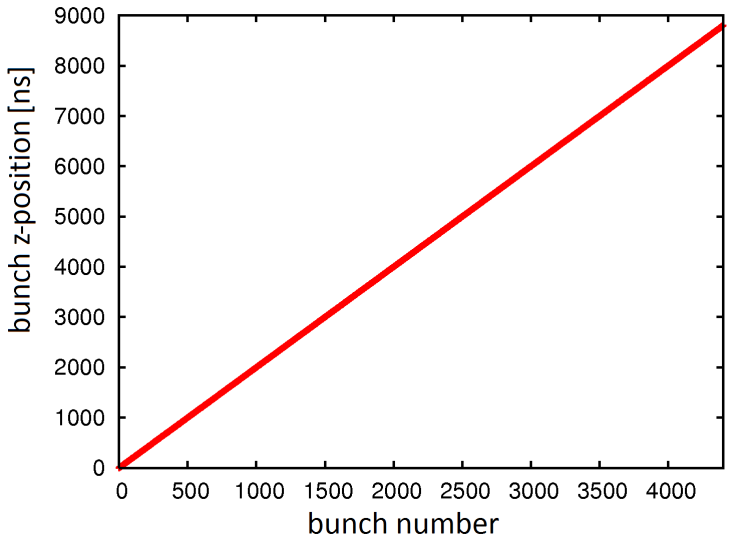

Figure 4.3: Drive Beam bunch z-position as a function of bunch number before the beam enters the Delay Line.

In Fig. 4.4 the bunch z-position is displayed after the bunches pass the Delay Line. The 'even' 120 bunches long trains described in Sec. 2.2.2 (starting with the train number zero) have been delayed by 240 ns in the Delay Line. As can be seen in the diagram they are overlapped with the 'odd' trains and occupy the same 240 ns long intervals in z-position, with bunch-to-bunch distance within this intervals being 1 ns. The z-position space previously occupied by the 'even' trains is left without bunches, forming 240 ns long gaps.

After passing the first Combiner Ring, the simulation output of the bunch z-position forms a pattern presented in Fig. 4.5. The 1 GHz trains have been delayed by $n \times 2 \times 240$ ns with $n = 2$, 1 and 0 consecutively, as described in Sec. 3.1.4. At this stage six 0.5 GHz trains occupy the same z-position intervals and the frequency within the intervals is 3 GHz. An exception is given by the two trains with bunch numbers 240-359 and 360-479, which are extracted without recombination in the first Combiner Ring, as described in Sec. 3.1.4.

When the Drive Beam trains pass the second Combiner Ring, they are delayed by $m \times 6 \times 240$ ns with $m = 3$, 2, 1 and 0 consecutively. The result is that the same z-position interval is occupied by twenty-four overlapped 0.5 GHz trains, forming a 12 GHz beam. The two trains not recombined in the first Combiner Ring leave the second Combiner Ring also without recombination. The simulation output of the bunch z-position after passing the

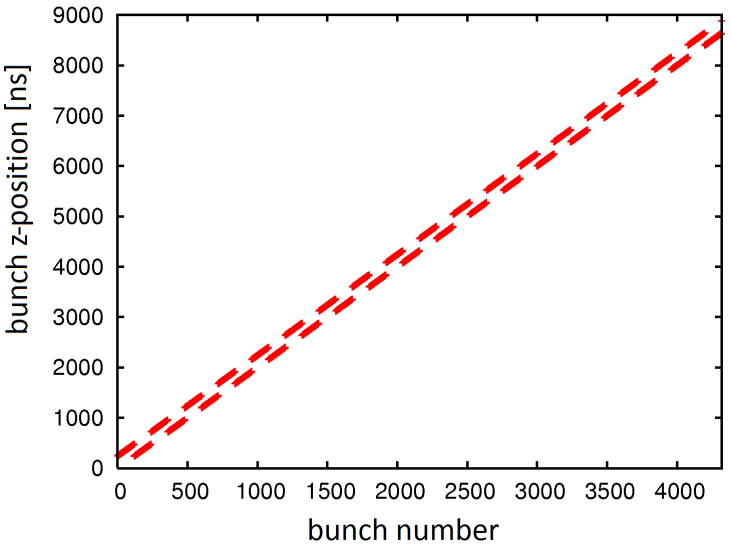

Figure 4.4: Drive Beam bunch z-position as a function of bunch number after the beam has passed the Delay Line.

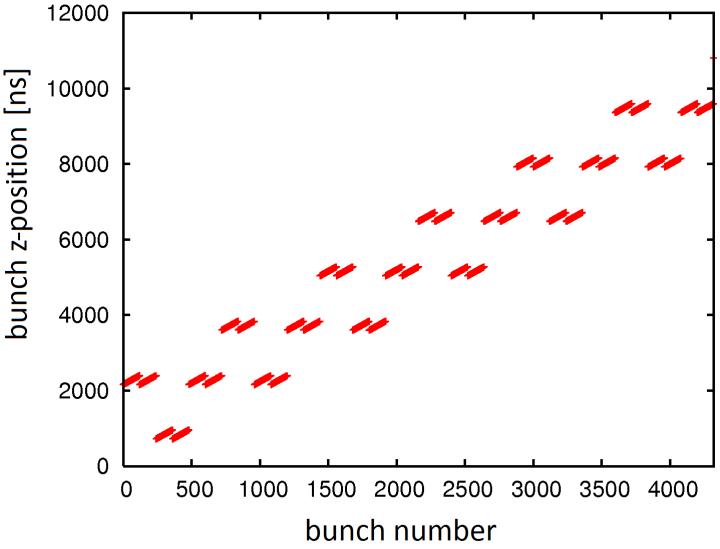

Figure 4.5: Drive Beam bunch z-position as a function of bunch number after the beam has passed the first Combiner Ring.

second Combiner Ring is presented in Fig. 4.6.

The sequence of the Drive Beam bunch z-position patterns displayed in figures 4.3, 4.4, 4.5 and 4.6 demonstrates that the software tool simulates the propagation of the Drive Beam through the recombination scheme correctly, according to the operation principle described in sections 2.2.2 and 3.1.4.

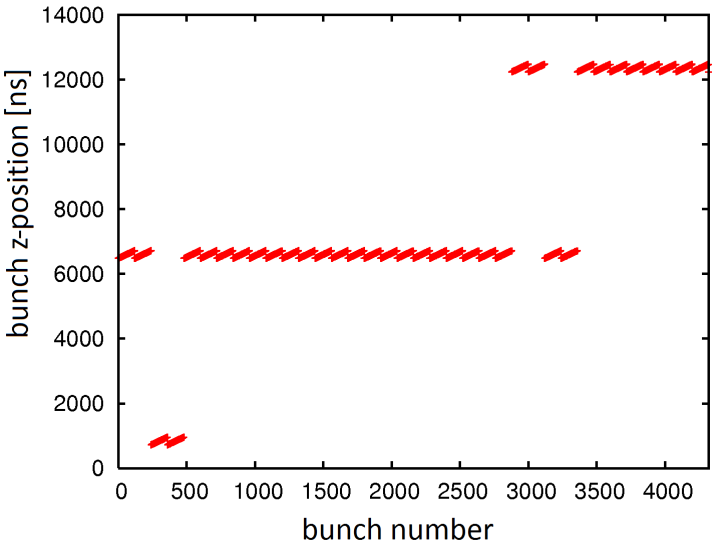

Figure 4.6: Drive Beam bunch z-position as a function of bunch number after the beam has passed the second Combiner Ring.

4.4 Impact of Drive Beam errors on the Main Beam

The significance of the Drive Beam errors is measured by its effect on the Main Beam. In the present section the simulation output for the Drive Beam error in a single bunch and a constant parameter offset in all Drive Beam bunches will be compared with the results of an independent calculation, similarly to Sec. 4.1.

4.4.1 Single bunch error propagation

It is feasible to perform a comparative calculation of a single Drive Beam bunch error propagation for the errors in bunch length and in longitudinal phase. The Drive Beam energy errors caused by the errors in the RF amplitude or phase of the Drive Beam accelerating structures or due to the bunch charge errors qualify less for independent calculation, since the convolution of the Drive Beam error function would have to be performed with the Drive Beam and the Main Beam RF structure functions (see Sections 3.1.2 and 3.1.5).

These calculations are too extensive to be performed without a rigorous automatised program, since the number of summands in them for each bunch is given by the length of the RF filling of the structure divided by the bunch spacing of the respective beam. So for the Drive Beam RF structure function convolution the number of summands is 448 ns/2 ns= 224 and for the Main Beam RF structure function convolution it is 105 ns/0.5 ns= 210. In the case of the errors in bunch length and in longitudinal phase only one convolution calculation with the Main Beam structure is needed, since the bunch length and longitudinal phase are not impacted by the errors in the Drive Beam accelerating structures. This fact makes it possible to calculate this convolution independently for some particular Main Beam bunches. On

the other hand, in order to calculate the convolution with the Main Beam structure for one particular bunch for the energy errors the full result of the Drive Beam structure convolution would be needed.

Calculating the impact of a single Drive Beam bunch longitudinal phase error on the Main Beam, a bunch from the first twenty recombined trains has been selected. This bunch arrives at one of the first twenty decelerators, meaning that the nominal RF phase of the Main Beam accelerator is $\phi_{MB,nom} = 8^\circ$ (see Sec. 3.1.5). Also the bunch must not be positioned in the trains that are not used for the Main Beam acceleration (bunch numbers 240 to 479, see Sec. 3.1.4). E.g. bunch number 1000 satisfies these conditions and is used for the comparison calculation example. For the value of the bunch length error at bunch number 1000 the value corresponding to the Drive Beam tolerance for the incoherent phase error is used:

$$\Delta\phi(t_0) = 0.8^\circ \times \delta(t_0 - 1000) \stackrel{\wedge}{=} 55.6\ \mu\text{m} \times \delta(t_0 - 1000) \tag{4.2}$$

with δ being the Dirac delta function.

Since the error is non-zero for only one bunch, the effect of the Drive Beam recombination scheme is that it merely shifts the bunch to a higher z-position value, without the train overlap having any significant effect on the result of the Main Beam convolution calculation. Using Eq. 3.13 to calculate the Drive Beam phase error impact on the Main Beam bunch with index t_0 yields

$$\Delta\phi_{MB}(t_0) = \frac{\int_{t'=0}^{105\ \text{ns}} \Delta\phi(t_0 - t') \cdot (A_{RF,MB}(t') - A_{BL,MB}(t')) \cdot \sin 8^\circ \cdot dt'}{\int_{t'=0}^{105\ \text{ns}} (A_{RF,MB}(t') - A_{BL,MB}(t')) \cdot \sin 8^\circ \cdot dt'} \tag{4.3}$$

Defining the z-position for the Main Beam bunches analogue to the Drive Beam, with the z-value being zero for the very first bunch and increasing for the following bunches, the Main Beam phase error $\Delta\phi_{MB}(z)$ has a distribution presented in Fig. 4.7.

The first bunch of the Main Beam experiencing the phase error has a longitudinal offset of 0.084 μm with respect to the accelerating RF wave. The value is reduced to 0.075 μm after 45 ns, to 0.014 μm after an additional 34 ns and finally to zero within the last 43 ns, making the length of the total error impact to be 105 ns. The function is flatter than the RF filling potential presented in Sec. 3.1.5 by about 18%, since the Main Beam loading has been included in the calculation.

The integrated value of the Main Beam phase error is

$$\int_{t=t_0}^{t_0+105\ \text{ns}} \Delta\phi_{MB} \cdot dt = 9.28\ \mu\text{m} \tag{4.4}$$

which corresponds to 1/6 of the incoming Drive Beam phase error of 55.6 μm. The reason for this is the fact that the Drive Beam has a bunch frequency of 12 GHz at the PETS and the Main Beam, in contrast, has only 2 GHz bunch frequency in the Main Beam accelerating

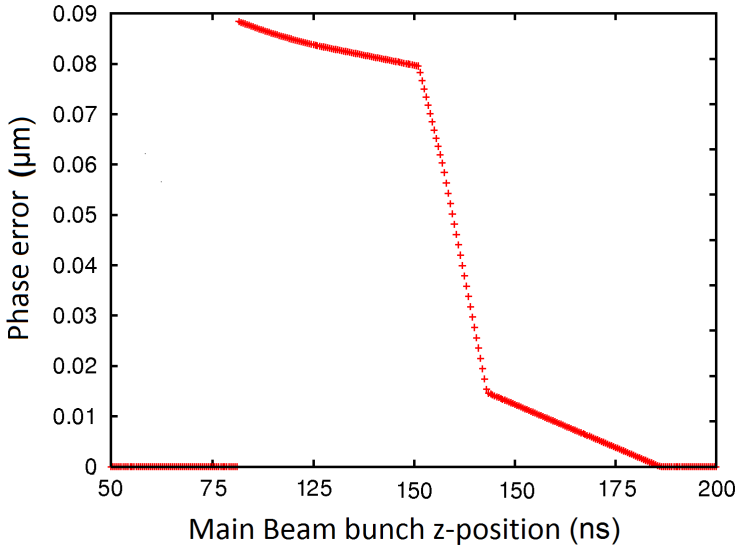

Figure 4.7: Phase error of the Main Beam bunches relatively to the accelerating RF as a function of Main Beam z-position for a single Drive Beam bunch phase error.

structures. Hence, on average the error of each Drive Beam bunch is responsible for 1/6 of the Main Beam accelerating RF error at the position of the Main Beam bunches.

4.4.2 Impact of constant parameter offset

A similar calculation of $\Delta\phi_{MB}$ from Eq. 4.3 can be performed for a constant offset of the Drive Beam phase, this time using the Drive Beam tolerance for the coherent phase error:

$$\Delta\phi_{const} = 0.2^\circ \triangleq 14\ \mu\text{m}. \tag{4.5}$$

Eq. 3.13 can be simplified in the following way:

$$\sigma_{\phi,MB}(t(k)) = \frac{\int_{t'=0}^{105\ \text{ns}} \sum_{i=1}^{24} \Delta\phi_{const} \cdot A_{MB,loaded}(t') \cdot \phi_{MB,nom,i} \cdot dt'}{\int_{t'=0}^{105\ \text{ns}} \sum_{i=1}^{24} A_{MB,loaded}(t') \cdot \phi_{MB,nom,i} \cdot dt'} \tag{4.6}$$

$$\Leftrightarrow \sigma_{\phi,MB}(t(k)) = \Delta\phi_{const} \cdot \frac{\int_{t'=0}^{105\ \text{ns}} \sum_{i=1}^{24} A_{MB,loaded}(t') \cdot \phi_{MB,nom,i} \cdot dt'}{\int_{t'=0}^{105\ \text{ns}} \sum_{i=1}^{24} A_{MB,loaded}(t') \cdot \phi_{MB,nom,i} \cdot dt'} \tag{4.7}$$

$$\Leftrightarrow \sigma_{\phi,MB}(t(k)) = \Delta\phi_{const} \tag{4.8}$$

The simple result of Eq. 4.8 is consistent with the simulation tool output presented in Fig. 4.8.

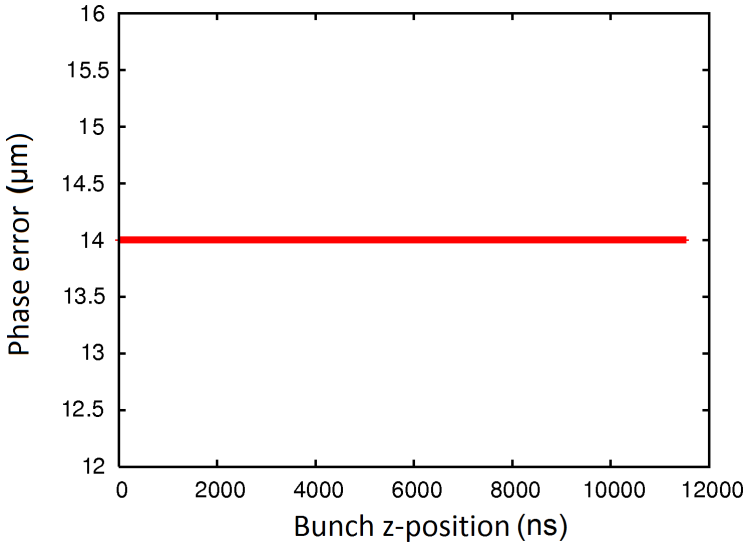

Figure 4.8: Phase error of the Main Beam bunches relatively to the accelerating RF as a function of Main Beam z-position for a constant Drive Beam phase offset.

4.5 Conclusion of verification studies

It has been demonstrated that the software tool for the Drive Beam error propagation simulation delivers output consistent with the results of independent calculations. The simple case of convolution of the Drive Beam accelerating structure RF potential error with the Drive Beam has been found to deliver quantitatively the same results for the Drive Beam energy error as described in Sec. 3.1.2. The parameter interdependences induced by the compressor chicane have been studied for the example of bunch length error generated by charge error and has been found to correspond to the simulation results of the underlying study. The propagation of the Drive Beam through the recombination scheme has been tracked step-by-step and it has been shown that the simulation tool correctly reassembles the operation mode of the recombination scheme sections. Finally, the convolution of the Drive Beam error function with the Main Beam has been studied for the examples of a single Drive Beam bunch phase error and constant Drive Beam phase offset and has been confirmed to be consistent with the results of an independent calculation.

Chapter 5

Simulation results for CLIC

The current chapter presents the results of the simulations of error propagation along the Drive Beam and of the correction of these errors. The simulations are performed with the software tool described in detail in chapter 3. The goal of the simulations is to track the propagation of the beam through different CLIC modules (such as Drive and Main Beam accelerating structures, the recombination scheme, the compressor chicane etc.) and to estimate the effect of the bunch charge and phase errors on CLIC's luminosity.

The simulations are necessary to define the tolerances for the Drive Beam errors and the specifications for the Drive Beam stabilisation systems, such as bunch charge feedback system and phase feed-forward system. Also alternative design options for CLIC such as a distributed timing system, longer Drive Beam accelerating structures and low energy operation modes have been simulated and analysed with the results being presented in the current chapter.

Section 5.1.1 describes the filtering provided by the recombination scheme and the convolution of the beam error function with the Main Beam accelerating structures. In section 5.1.2 the calculation of the impact of Drive Beam accelerating structure errors is presented. The effect of the Drive Beam bunch charge feedback and of the phase feed-forward stabilisation systems is estimated in sections 5.2 and 5.3 respectively, where the bandwidth requirements for these two systems are described. The latter includes the analysis of the distributed timing system specifications, which have been calculated analytically and verified by a software tool simulation. Section 5.4 presents the investigation of the impact of different RF filling times on the error filtering in the Drive Beam accelerator. Section 5.5 shows how the error filtering and correction change if CLIC is operated in low energy operation modes described in [81] and [82].

5.1 Error filtering along the Drive Beam

With the tracking software tool the Drive Beam errors can be simulated to have any user-defined distribution. It is most useful, however, to represent the tracking simulation result

as the total root mean square (RMS) error of a parameter as a function of the incoming parameter jitter frequency. This way the error filtering by the different Drive Beam sections can be demonstrated step-by-step and critical jitter frequencies can be identified. The corresponding luminosity loss can be calculated from this distribution with Eq. 3.18.

5.1.1 Error filtering in the recombination scheme and Main Beam acceleration structures

As described in Sec. 3.1.4, the recombination scheme combines the Drive Beam trains of 240 ns length and the error functions of these trains overlap. Since the sinusoidal error function is used for the simulation, one can analyse the impact of each wavelength setting separately. The result of the Drive Beam recombination and convolution with the RF filling function of the Main Beam accelerating structures is displayed in Fig. 5.1. For the simulation illustrated in the figure a sinusoidal incoming phase error of equal amplitude normalised to unity at all frequencies (white noise) has been used.

The error with zero frequency, corresponding to the constant offset of the phase, is unfiltered and the value of the error remains the same after the recombination and convolution with the Main Beam RF filling and beam loading functions. The errors at all other frequencies are reduced and suppressed by the recombination scheme.

The errors with a wavelength of 240 ns are resonant with the train length, and so after the recombination and the convolution the error at corresponding frequencies remains unsuppressed. The errors at non-resonant frequencies are combined randomly and hence cancel out significantly when convolved with Main Beam RF filling and beam loading functions. Consequently, one can observe peaks at the resonant frequencies of $n/240$ ns $=$ 4.17 MHz $\times$ n, $n \in \mathbb{N}$ and strong error reduction for the non-resonant frequencies. The peaks have a maximum at the error value of about 0.707, since this value corresponds to the RMS of a sinusoidal function with an amplitude of unity.

In the following the reduction of the error due to the bunch recombination and subsequent convolution with the Main Beam RF filling and beam loading functions will be referred to as recombination scheme error filtering.

5.1.2 Error filtering in the Drive Beam accelerating structures

The current section describes the impact of the errors in the Drive Beam accelerating structures on the beam error. The errors in the amplitude and phase of the Drive Beam accelerator RF filling function are convolved with the beam energy error function. Also the errors in the bunch charge of the beam impact the beam loading, which introduces additional beam energy error (for more detailed description of error interdependence see Secs. 3.1.1 and 3.1.2).

In the first two subsections the simulation is performed for an ideal RF filling function and an ideal beam loading function. In the following subsection the results of the simulation

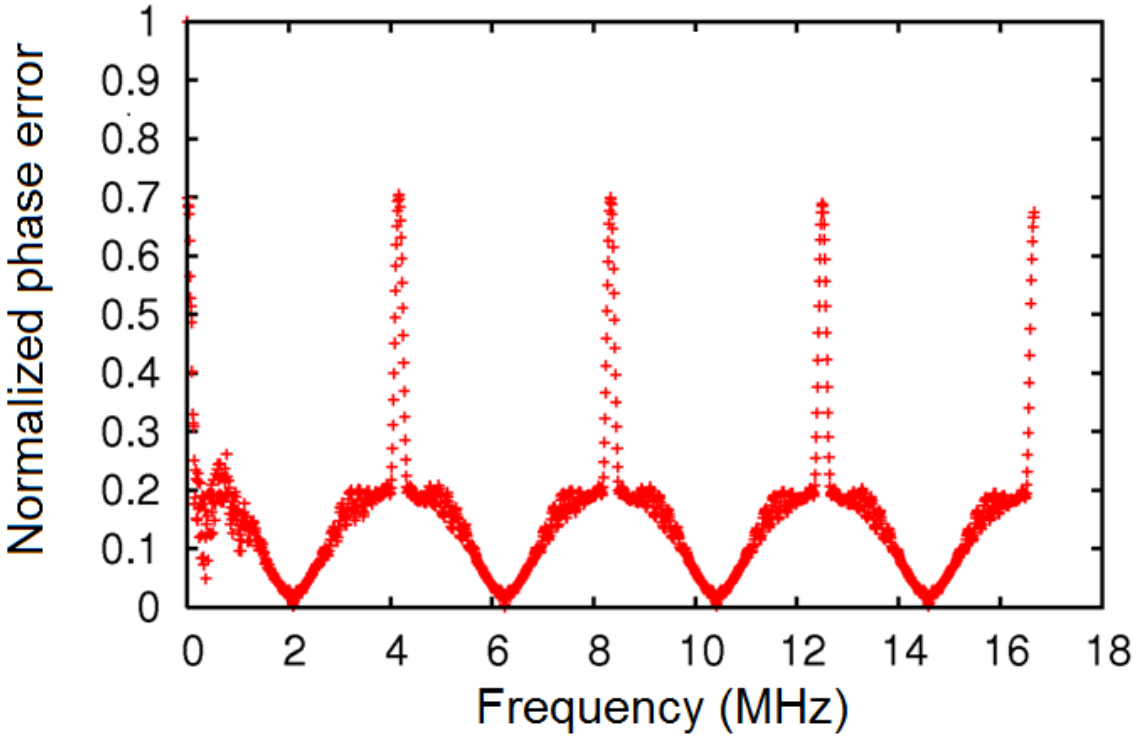

Figure 5.1: Phase error amplitude as a function of frequency after filtering by the recombination scheme and Main Beam acceleration structures. The incoming phase error has a white noise distribution with amplitude normalised to unity.

with the realistic RF filling and beam loading functions [75] are presented.

Filtering by the ideal RF filling function

An ideal RF filling function has a constant RF filling amplitude over the RF filling time, as demonstrated in Fig. 2.4, left. The result of the convolution of an error in the amplitude or phase of the accelerating RF wave with the beam error function is presented in Fig. 5.2. The distribution represents the amount of Drive Beam accelerating structure error transmitted to the beam as a function of error frequency. The error amplitude has been normalised to one, so the distribution represents the filtering factor of the ideal Drive Beam accelerating structures. The filtering factor is defined here as the error amplitude after the filtering divided by the error amplitude before the filtering.

One can clearly recognise that this filtering factor is frequency dependent, similarly to the recombination scheme error filtering. Errors with higher frequencies are filtered out much more effectively than lower frequency errors. The reason for this is the fact that for higher frequencies the convolution with the RF filling time involves averaging over a larger intervals of a sinusoidal error function. Consequently the RMS of the result of such averaging is lower.

If the wavelength of the error function is equal to the length of the RF wave, the signal is filtered out completely, leading to the dips visible in Fig. 5.2 at frequencies of $n \times 4.17$ MHz.

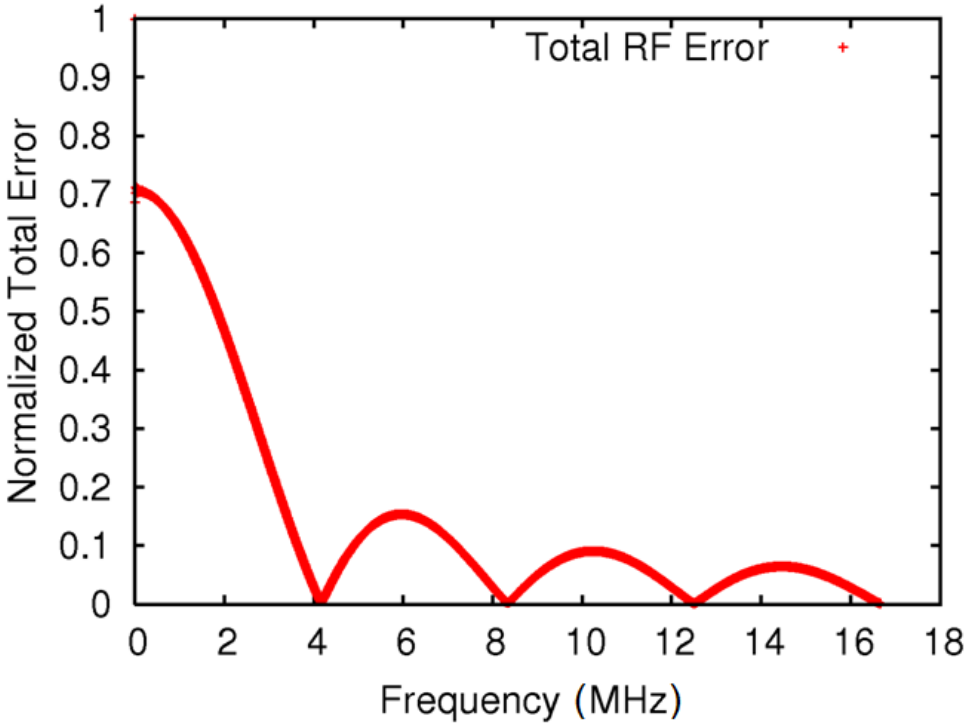

Figure 5.2: Filtering factor of the ideal RF filling function for different RF amplitude or RF phase jitter frequencies.

Multiplying the filtering factor distribution from Fig. 5.2 with the phase error after the recombination scheme filtering calculated above (Fig. 5.1) yields the total error at the PETS induced by the Drive Beam accelerating structures. Such total phase error for the incoming white noise error (amplitude normalised to one) in the Drive Beam accelerator phase is displayed in Fig. 5.3. One can recognise that the peaks present in Fig. 5.1 are filtered out, since for the ideal CLIC Drive Beam accelerating structure the RF filling time has the same value of 240 ns as the Drive Beam train length, so the peaks visible in Fig. 5.1 are multiplied with the dips displayed in Fig. 5.2. In this sense Fig. 5.3 visualises the purpose of the choice for the ideal Drive Beam accelerator to have an RF fill time equal to the Drive Beam train length: the filtering effect of the convolution with the RF filling function is applied exactly at the resonant frequency peaks of the error function, 4.17 MHz $\times$ n.

Filtering by the ideal beam loading function

The ideal beam loading function has a linear decrease over the beam loading time. Convolution of the beam loading function with the normalised bunch charge error function leads to the distribution shown in Fig. 5.4.

The distribution represents the filtering factor of the beam loading function for the Drive Beam accelerating structures. The filtering by the beam loading function is more significant for the higher frequencies, similarly to the filtering by the RF filling function. However, since

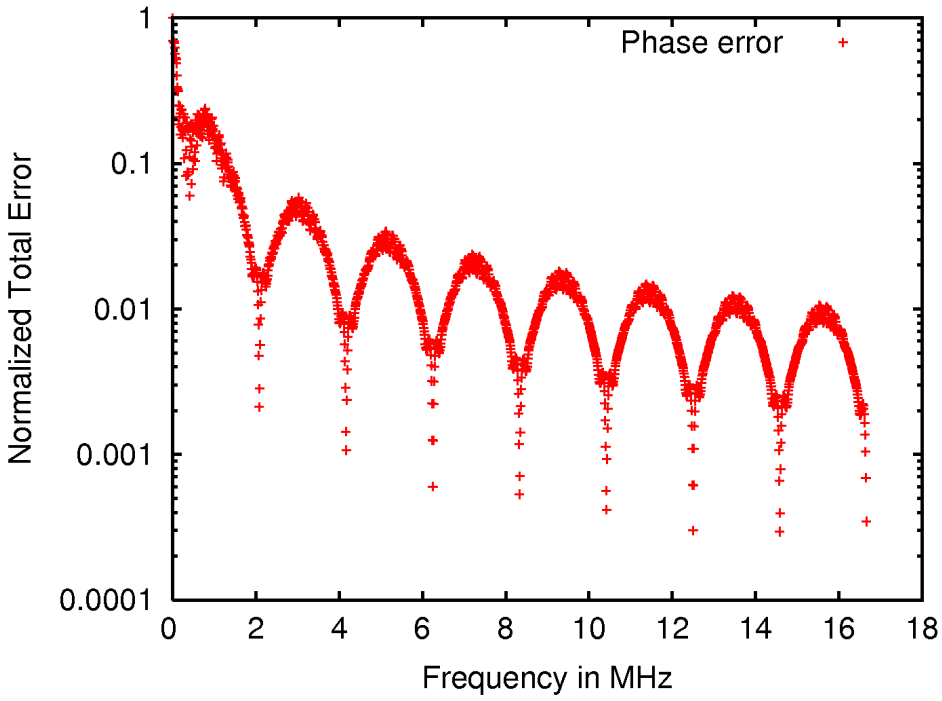

Figure 5.3: Phase error, caused by different frequencies of RF amplitude or RF phase jitter, after the filtering by the recombination scheme and the ideal Drive Beam RF filling function.

the beam loading function does not have a constant value, as the RF filling function does, but linearly decreases, the convolution of the beam loading function with the beam error function is not a simple averaging. The dips produced by the filtering with the RF filling function are not present in the beam loading function filtering. Consequently, the critical frequencies cannot be filtered out as effectively as with a constant RF filling function. This can be demonstrated by the multiplication of the recombination scheme error filtering distribution (Fig. 5.1) with the beam loading filtering distribution (Fig. 5.4). The result is presented in Fig. 5.5. The resonant peaks of the phase error remain after filtering with the linearly decreasing beam loading function.

With realistic RF filling and beam loading functions

Realistic Drive Beam RF filling and beam loading functions have been calculated in a simulation study [75] and have been presented in Chapter 3.1.2 (Figs. 3.3 and 3.4). In order to calculate the realistic impact of the Drive Beam accelerator on the beam errors the functions have been approximated linearly and convolved with the Drive Beam error function. The result of the convolution is illustrated in Figs. 5.6 and 5.7.

Fig. 5.6 demonstrates the phase error caused by a 0.05% Drive Beam accelerating structure RF amplitude error. For the distribution shown in Fig. 5.7 the phase error is caused by a 0.1% error in bunch charge: bunch charge error leads to an error in beam loading and ultimately to phase error (see Secs. 3.1.1 and 3.1.4 for more details). These error values

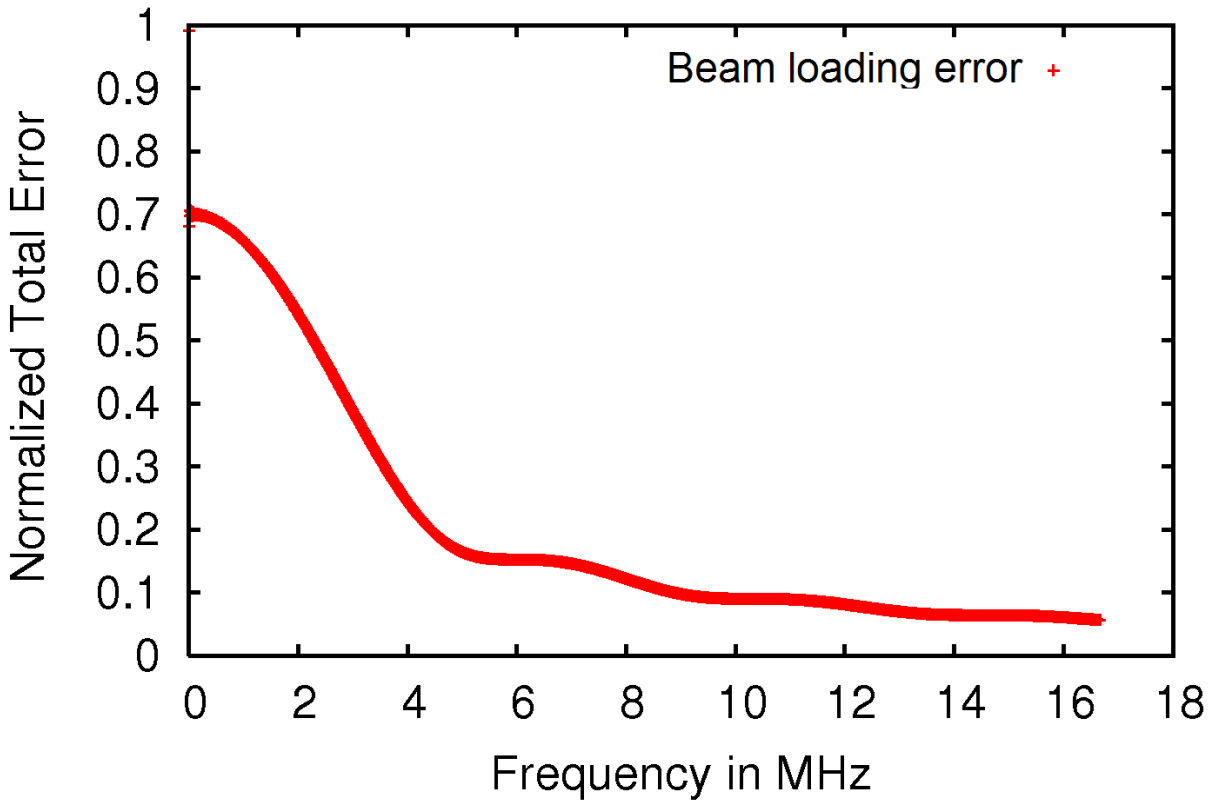

Figure 5.4: Filtering factor of the ideal beam loading function for different bunch charge jitter frequencies.

represent tolerances on the charge and RF amplitude stability. In the case that these error values are coherent along the Drive Beam decelerator sections they cause 175 μm Main Beam RF phase error (see zero-frequency point in Figs. 5.6 and 5.7) and a resulting 1% luminosity loss. However, one can see a significant filtering effect of the errors with the non-zero frequencies.

The realistic RF filling function (Fig. 3.4) differs strongly from the ideal RF filling function (Fig. 2.4, left). Hence, the filtering of the critical resonant frequencies is not as optimal in the distribution in Fig. 5.6 as in Fig. 5.3. The peaks are, however, significantly suppressed.

The realistic beam loading function (Fig. 3.3) has approximately the form of the ideal beam loading function. Consequently, the error filtering is also very similar in Figs. 5.5 and 5.7. However the beam loading function is not optimal for filtering of the resonant peak frequencies, and so it is recognisable that the phase error is more effectively suppressed if it is caused by the Drive Beam RF amplitude error and not by the bunch charge error (compare Figs. 5.6 and 5.7).

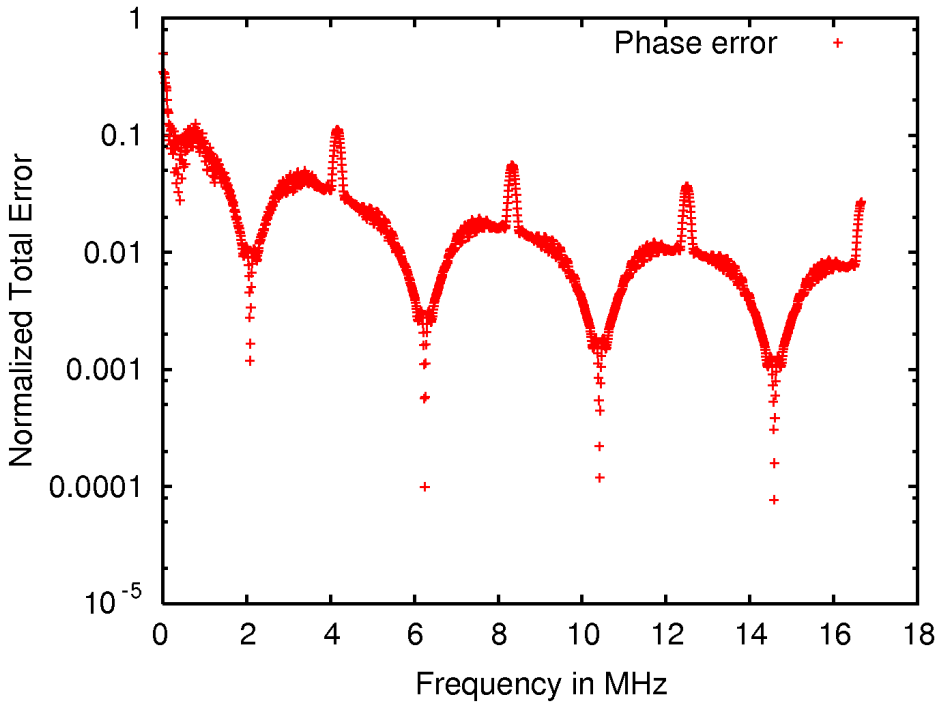

Figure 5.5: Phase error, caused by the white noise jitter of the bunch charge, after the filtering by the recombination scheme and the ideal Drive Beam beam loading function for different jitter frequencies.

The realistic RF filling and beam loading functions are used in all calculations presented in the following sections of the current chapter in order to increase the precision of the analysis.

5.2 Drive Beam bunch charge feedback system

Before the direct stabilisation of the Drive Beam phase (see Sec. 5.3), it is helpful to minimise the errors in the parameters which lead to the phase error. The software tool allows one to simulate the action of feedback and feed-forward stabilisation systems on any parameter of the Drive Beam. An example of such a feedback stabilisation system for the Drive Beam bunch charge is discussed in the present subsection.

For the maximal allowed luminosity loss of 1% the bunch charge stability tolerance is 0.1%. At CTF3 a combination of a thermionic gun and a sub-harmonic bunching system is used as an electron source for the Drive Beam [68]. A similar electron source is considered as a baseline design for CLIC Drive Beams [32]. The stability level achieved at CTF3 injector is 6 $\times 10^{-4}$, which is below the stated CLIC requirement [83].

An alternative design option for CLIC Drive Beam source,the PHIN photo-injector, is

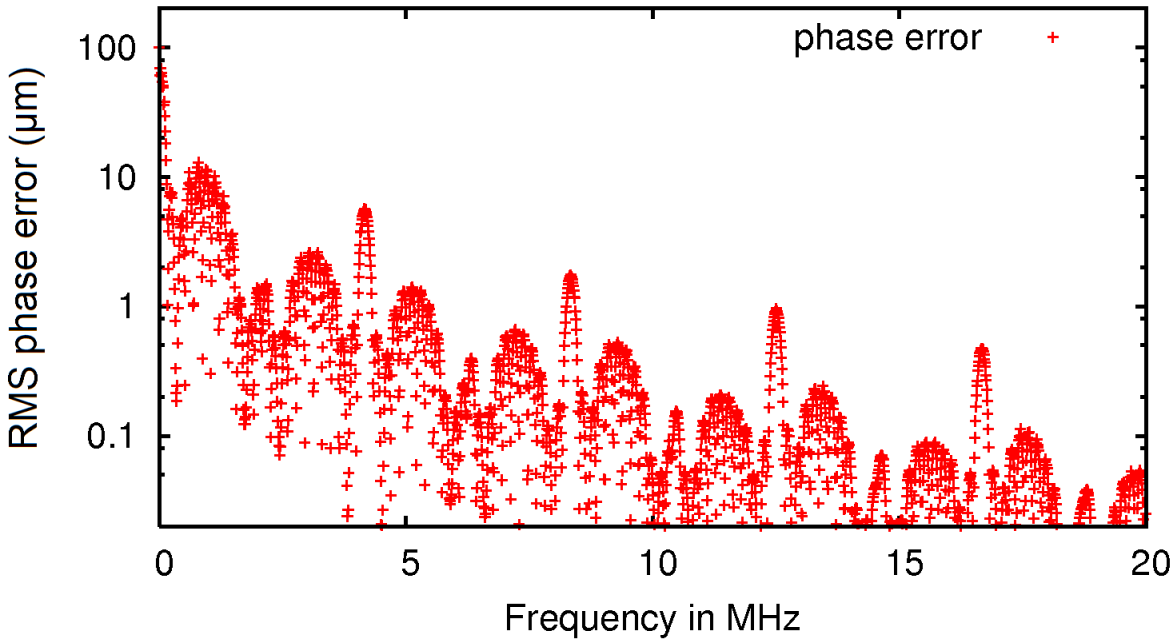

Figure 5.6: Phase error caused by 0.05% Drive Beam RF amplitude jitter at different frequencies, calculated with realistic RF filling function.

under consideration. It should reduce the amount of beam charge outside of the bunches, which is accumulated in the so-called satellites, and momentary constitutes about 8.5% of the total current of CTF3 Drive Beam [84]. The prototype of PHIN photo-injector, however, only reaches the stability of 0.25% [85]. Consequently, an additional stabilisation is required, which can be performed by a fast feedback system. This system would measure the beam current and correct it at the electron gun within one Drive Beam pulse.

An example of one such potential feedback system is presented in Fig. 5.8. The red points represent the phase error without feedback correction. The phase error in this case is caused by the 0.1% Drive Beam bunch charge jitter, analogous to the error presented in Fig. 5.7. The green points represent the phase error after application of a feedback system.

The feedback latency time t_l, which is the time between the measurement of the bunch charge and the correction, has been set to 110 ns. The gain duration t_g, which is the time needed for the application of the full correction, has been set to 10 ns. The gain duration is non-zero due to limited bandwidth of the system's amplifier. A linear rise of the signal during the gain time has been measured at the FONT amplifiers [79] and hence is assumed for the simulations.

As has been explained in Secs. 3.2.2 and 3.2.3 the impact of a feedback system is not always stabilising. The figure shows that while the error at some frequencies is reduced (e.g. frequencies below 1 MHz, second resonant peak etc.), at some frequencies the error

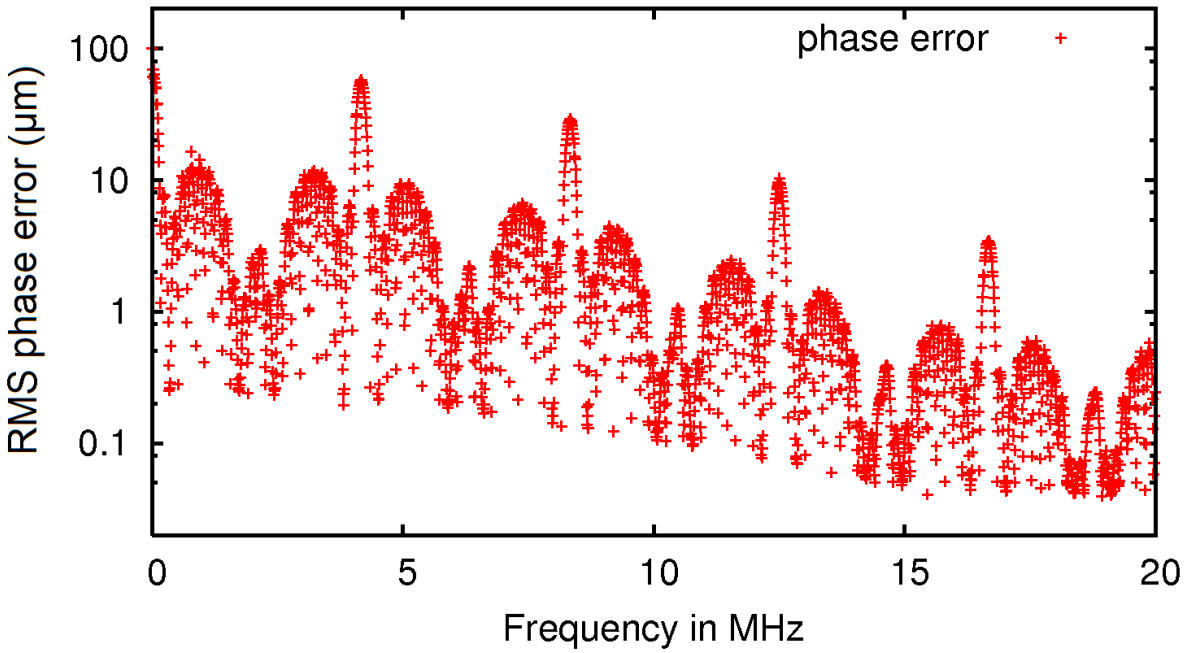

Figure 5.7: Phase error caused by 0.1% Drive Beam bunch charge jitter at different frequencies, calculated with realistic beam loading function.

is amplified (e.g. the first and the third resonant peaks). Generally, the feedback has a correcting effect on the jitter if jitter frequency is resonant with the feedback latency, which is in this case at the frequencies of $n/(110\text{ ns}+10\text{ ns}) = n \times 8.33\text{ MHz}, n \in \mathbb{N}$. The feedback destabilises the beam at the anti-resonant jitter frequencies, which are in this case $(1/2+n)/(110\text{ ns}+10\text{ n}s) = (1+2n) \times 4.17\text{ MHz}, n \in \mathbb{N}$.

Feedback systems with different settings of the latency time t_l and the gain duration t_g reduce the error more effectively at different error frequencies. For example, the impact of a realistic feedback system with latency of 200 ns and gain duration of 40 ns is shown in Fig. 5.9. It reduces the error for the most critical frequency bands - the frequency below 0.5 MHz and the first resonant peak at 4.17 MHz.

The important issue to note is that any feedback system with a bandwidth of at least several MHz reduces the low frequency noise significantly. Fig. 5.10 demonstrates the phase error without feedback (red), with $t_l = 110$ ns, $t_g = 10$ ns feedback (green) and with $t_l = 200$ ns, $t_g = 40$ ns feedback (blue) for the frequency range from 0 to 0.5 MHz. The error for the first several hundreds of kHz is significantly filtered by both feedback systems. The frequency resolution of the simulation has been chosen to be 50 Hz per step for the first 50 kHz and 1 kHz per step for the higher frequencies.

The latency t_l and the gain duration t_g of the feedback system can be optimised. The

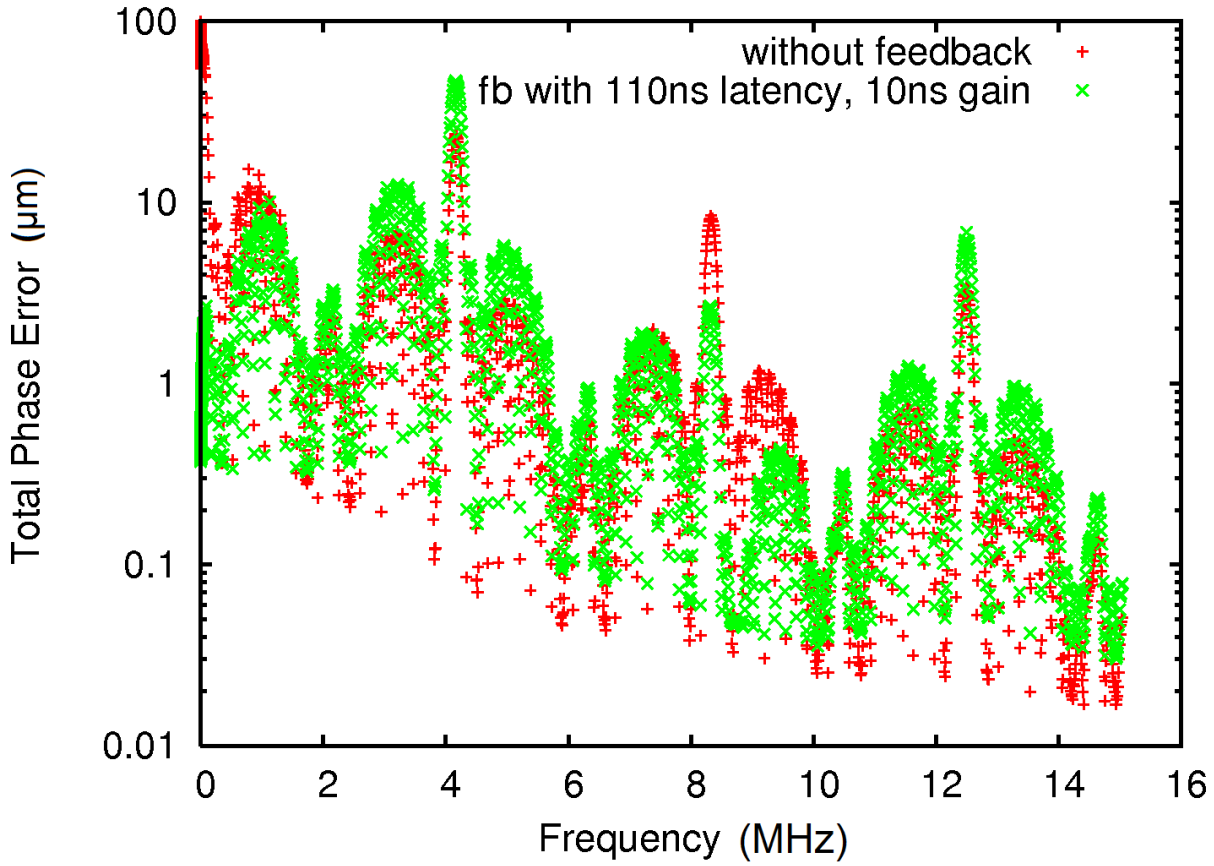

Figure 5.8: Phase error caused by 0.1% bunch charge jitter without feedback (red) and after feedback with 110 ns latency and 10 ns gain duration (green).

variation spectrum of these two parameters is presented in Fig. 5.11. For this study, a white noise between zero frequency and 20 MHz was assumed.

The best values for the correction efficiency are achieved when the sum of latency time and gain duration is of the order of 240 ns, corresponding to the length of the recombined trains. If the bunch charge correction happens after approximately this time, the bunches with the corrected values are positioned next to the bunches at which the errors were measured. Hence the errors will cancel out on a time scale of the Main Beam RF filling. This effect allows one to reduce the error at the $n \times 4.17$ MHz peaks that remain largely unfiltered by the recombination scheme error filtering.

The distribution shows that the error at a high gain duration time is relatively low, independent of the feedback latency. The reason for it is that the correction with a high gain duration is still very effective for the filtering of the low frequency errors, and the effect of the anti-resonant correction (Sec. 3.2.2) is decreased by the prolonged application time of the correction signal.

The weak absolute minimum of the distribution is at a latency time of 240 ns and a gain duration time of 0 ns. However, such a bandwidth is not possible to achieve. Estimation of the overall improvement of the phase error by a bunch charge feedback can be made by the

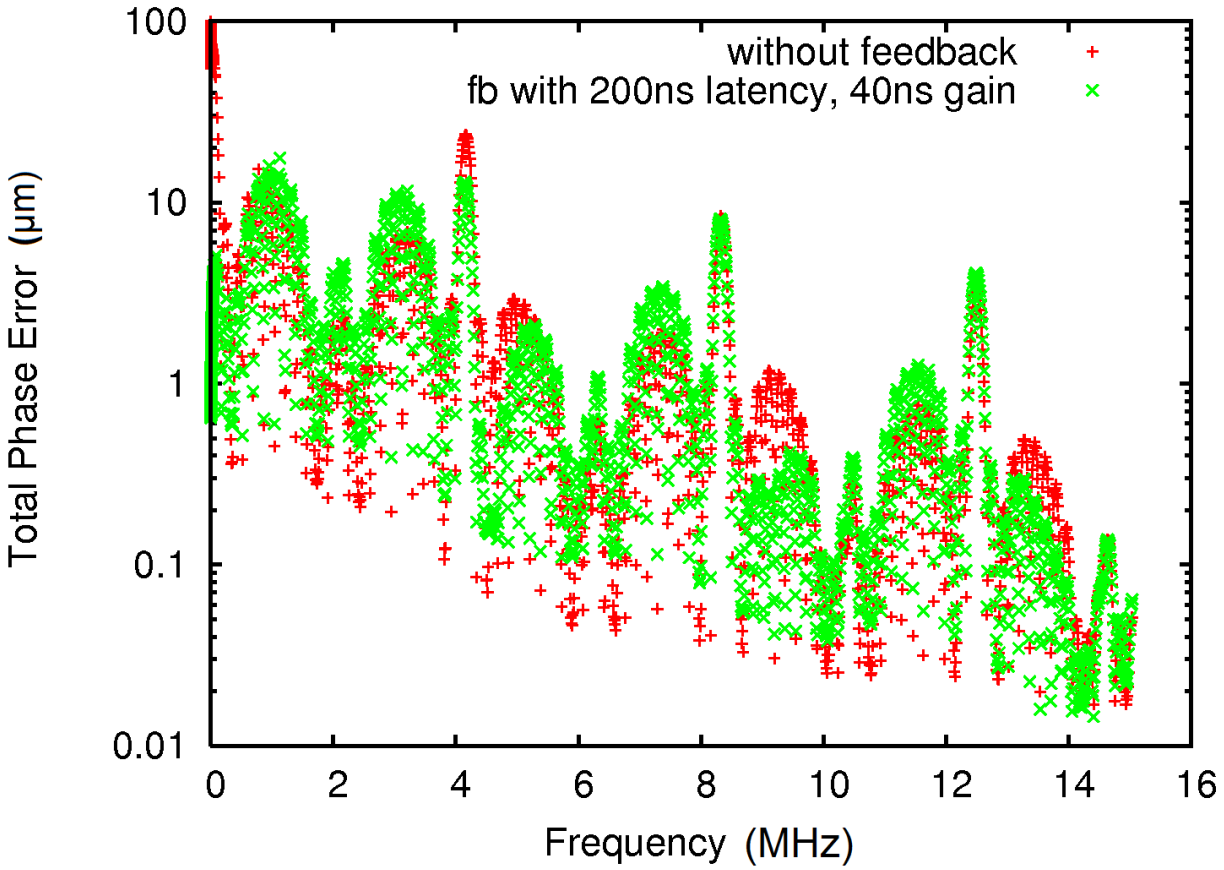

Figure 5.9: Phase error caused by 0.1% bunch charge jitter without feedback (red) and after feedback with 200 ns latency and 40 ns gain duration (green).

integrated average error $\sigma_{\phi,total}$:

$$\sigma_{\phi,total} = \sqrt{\frac{1}{20\ \text{MHz}} \int_{0\ \text{Hz}}^{20\ \text{MHz}} \sigma_\phi^2(f) df}. \tag{5.1}$$

The integration must be performed with the Euclidean norm, since the phase errors at different frequencies are linearly independent. Calculation of $\sigma_{\phi,total}$ for a realistic feedback bandwidth of 8.75 MHz (corresponding to the gain duration of $t_g = 0.35/(8.75\ \text{MHz}) = 40$ ns) with a latency time of 200 ns, the application of which is illustrated in Fig. 5.9, yields RMS errors of

- $\sigma_{\phi,total} = 6.14\ \mu$m without feedback and
- $\sigma_{\phi,total} = 3.35\ \mu$m with feedback.

This result implies that the phase stability can be improved by 45% with the help of a realistic feedback system. However, the improvement is insufficient for the stabilisation

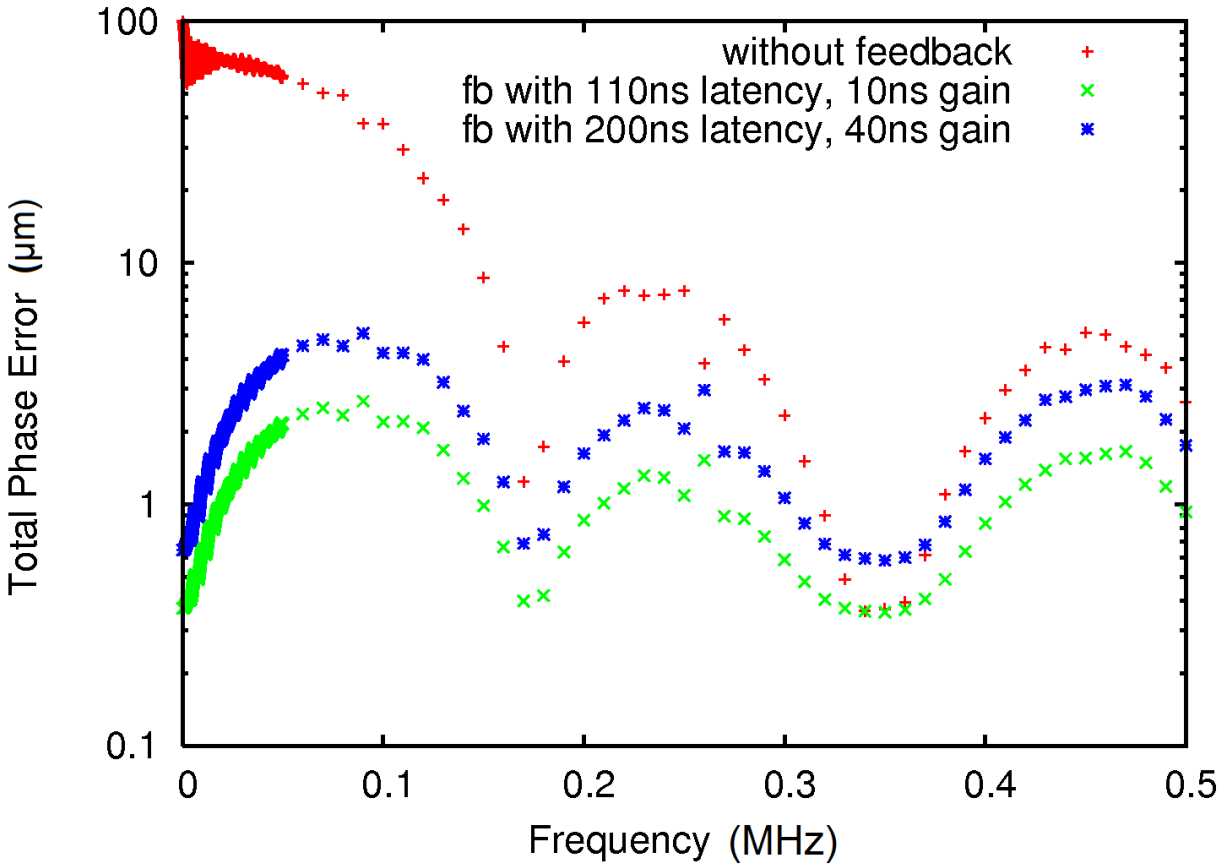

Figure 5.10: Phase error at lower frequencies without feedback (red) and after feedback with 110 ns latency and 10 ns gain duration (green) and 200 ns latency and 40 ns gain duration (blue).

requirement defined above: the bunch charge stability of 0.25% achieved at the PHIN experiment [85] would need a reduction by a factor of 2.5 in order to satisfy the CLIC stability requirement of 0.1%. Hence, an additional stabilisation system is needed to reduce the beam phase error caused by the bunch charge errors in CLIC injector. Such a stabilisation can be provided by a phase feed-forward system (see Sec. 5.3).

5.3 Drive Beam phase feed-forward system

The feed-forward system described in Sec. 3.3 is designed to reduce the phase error on average by a factor of twelve, with the tolerance before the feed-forward correction being 175 μm and after the correction being 14 μm.

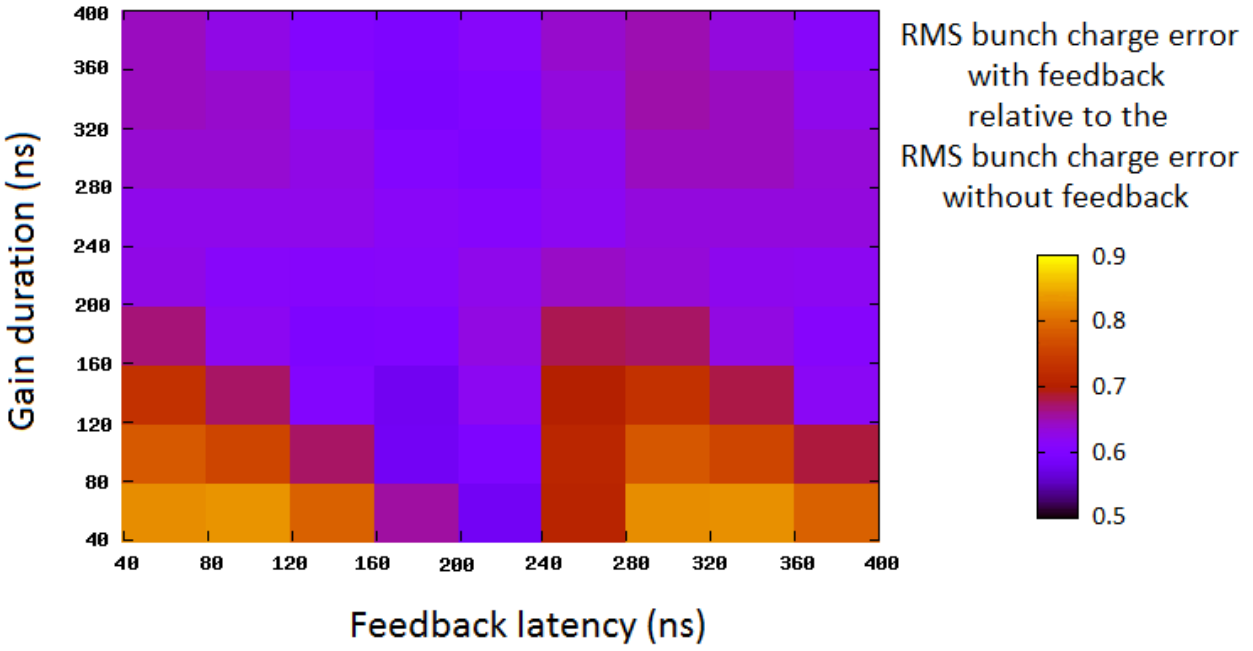

Figure 5.11: Total bunch charge error as a function of gain duration and latency time of the charge feedback system. A normalized white noise before the recombination scheme filtering and the feedback application is assumed.

5.3.1 Timing of feed-forward correction application

The correction can be applied before the beam arrival at the correction module, as described in Sec. 3.3. So the feed-forward system is simulated with the software tool in the same way as a feedback system, but with a negative latency time t_l. Modifying t_l leads to different performances of the feed-forward correction for the same gain duration time t_g. An example of such modification is presented in Fig. 5.12 - the feed-forward correction with the gain duration time of 20 ns (corresponding to 17.5 MHz bandwidth of the feed-forward amplifier signal) is applied at the bunch at which the error has been measured (illustrated in Fig. 3.16) or half of the gain duration time before it (Fig. 3.17).

In order to calculate the optimal latency time t_l the result of convolution of the Drive Beam phase error function with the Main Beam RF filling and beam loading amplitude functions (Eq. 3.13) must be minimised. The best correction efficiency can be achieved if the latency time t_l is set to minus half of the gain duration t_g, $t_l = -\frac{1}{2}t_g$. With that setting the bunch with the measured signal is positioned in the centre of the correction. This optimal setting for t_l will be used for all following studies presented in the thesis.

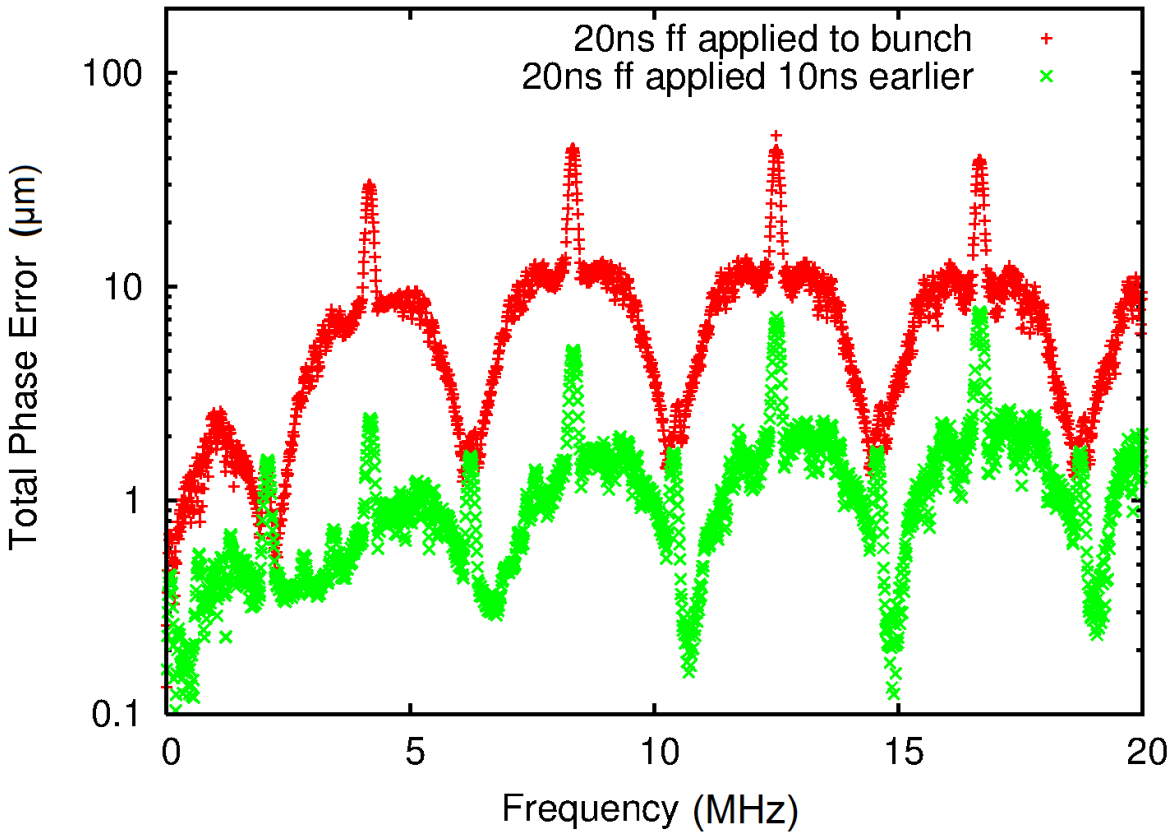

Figure 5.12: Phase error as a function of jitter frequency with 20 ns gain duration feed-forward. The feed-forward correction application starts at the bunch with the measured error (red curve) and 10 ns earlier (green curve).

5.3.2 Impact of the feed-forward bandwidth on the correction effectiveness

The feed-forward system has, similarly to the feedback system, a limited bandwidth and a linear rise of the amplifier signal during the gain time. Fig. 5.13 demonstrates the effect of feed-forward systems with different amplifier bandwidths on the phase error. The red distribution represents the phase error of incoming white noise with amplitude of 175 μm after the recombination scheme error filtering. The green and blue distributions show this phase error after the application of a feed-forward correction with 50 ns and 10 ns gain time respectively.

The feed-forward significantly improves the phase stability, in particular in the low-frequency spectrum. For instance, a feed-forward system with a realistic bandwidth of 11.7 MHz (corresponding to 30 ns gain time) improves the white noise phase error between 0 and 1 MHz by a factor of 80. Since the filtering by the recombination scheme and error convolution with the Drive and Main Beam RF structure functions is more effective for high frequency noise, the feed-forward is an effective complementary stabilisation system.

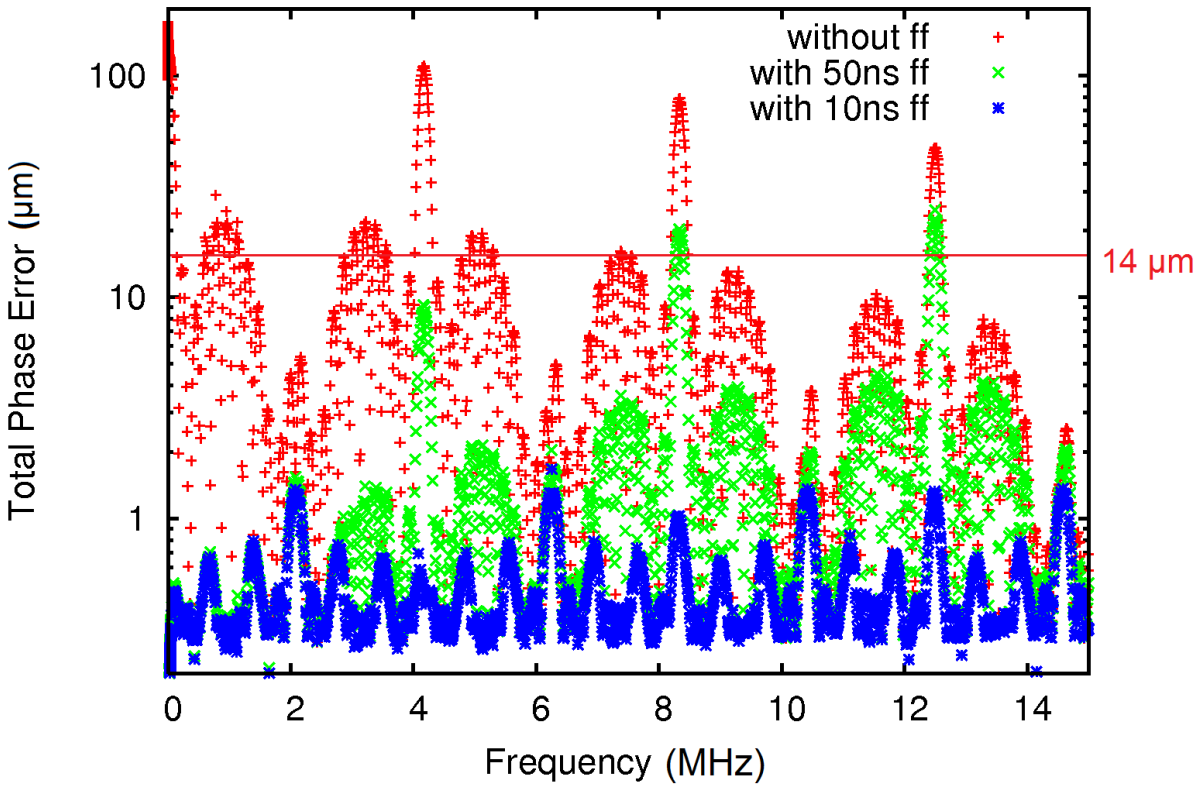

Figure 5.13: Phase error as a function of jitter frequency without feed-forward (red) and with 50 ns (green) and 10 ns (blue) gain duration feed-forward. The tolerance of 14 μm phase error resulting from the BDS energy bandwidth is indicated with a horizontal red line.

The overall efficiency of the feed-forward system strongly depends on the gain duration time t_g, with shorter gain duration being more effective at higher frequencies. The figure of merit for a feed-forward correction can be defined by the integration of the phase error amplitude $\sigma_\phi(f)$ over the jitter frequency plotted in Fig. 5.13 (see Eq. 5.2). The integration must be performed with the Euclidean norm as in Eq. 5.1, since the phase errors at different frequencies are linearly independent. The phase error amplitude can be multiplied by the noise power spectrum $P(f)$ in order to obtain results not only for the white noise ($P(f) = const.$), but also for arbitrary noise spectra, e.g. for pink ($P(f) \propto 1/f$) and red noise ($P(f) \propto 1/f^2$).

$$\mathcal{A} = \sqrt{\int_{50\ \mathrm{Hz}}^{20\ \mathrm{MHz}} \sigma_\phi^2(f) P(f) df} \tag{5.2}$$

It is necessary to set a positive lower frequency limit for integration, since the pink and white noise spectra are divergent at zero frequency. The limit is set to 50 Hz, since this

frequency corresponds to the CLIC Main Beam pulse repetition rate. The wavelength of the jitter at 50 Hz is $c \times 20$ ms, hence the error change along the $c \times 140$ ns long Main Beam is insignificant (about $\sin(140 \text{ ns}/ 20 \text{ ms}) = 7 \times 10^{-6}$ of error amplitude) and so the 50 Hz error can be considered as almost coherent along the Main Beam. Also, the feed-forward system is designed to perform the intra-pulse phase corrections, hence the jitter frequencies below the train repetition rate are of minor importance for the stabilisation simulation.

The 20 MHz upper limit has been selected because it corresponds to an RF fill time of the Main Beam accelerating structures (about 50 ns) and hence the errors above this frequency are filtered out sufficiently by the convolution with the Main Beam RF filling function. Also, as it has been demonstrated in Sec. 5.1, the recombination scheme error filtering is very effective for the high frequency jitter and hence this jitter has a small contribution to the overall phase error of the Main Beam and to CLIC's luminosity loss.

Fig. 5.14 displays the integrated amplitude $\mathcal{A}$ calculated in Eq. 5.2 of the phase error caused by the Drive Beam bunch charge (top) and RF phase (bottom) errors, which have been presented for the case of recombination scheme error filtering in Figs. 5.6 and 5.7. The first entry on the x-axis in Fig. 5.14 represents the integrated phase error amplitude before the filtering by the recombination scheme. This value is normalised to unity for each curve and the following values are calculated relative to it. The second entry on the x-axis is the value of $\mathcal{A}$ after the recombination scheme error filtering. The following entries represent the values of $\mathcal{A}$ after feed-forward correction with different bandwidths, indicated by the corresponding gain times in nanoseconds.

The diagram shows that for the white noise the reduction of the overall error due to the filtering by the recombination scheme is more significant than for the pink and red noise. The reason for this is the fact that the white noise has a larger high-frequency component than the pink and the red noise and the recombination scheme filters out the high frequency errors more effectively. The error with a constant value is not impacted by the recombination scheme at all. On the other hand, the feed-forward system with lower bandwidth performs much better on the constant error as well as on red and pink noise, since it filters mostly the low frequency noise component. A higher bandwidth of the feed-forward system (corresponding to the lower gain duration) is required in order to achieve a significant level of correction for the white noise. The bandwidth requirements for the pink and red noise are more relaxed.

The inverted function $1/\mathcal{A}$ defines the tolerance improvement factor for a particular noise type. Fig. 5.15 displays the improvement of the phase tolerance due to the recombination scheme filtering and the phase feed-forward system, analogous to Fig. 5.14. The values are normalised to the tolerance after the recombination scheme filtering, but before the impact of the feed-forward system. One can recognise that in order to achieve the required improvement factor of twelve for the constant offset, as well as for the red and pink noise, the feed-forward system with a bandwidth of 0.35/240 ns = 1.46 MHz is fully sufficient. However, for a correction of white noise by a factor of twelve a higher bandwidth is required. For example, the feed-forward system with a bandwidth of 0.35/20 ns = 17.5 MHz would improve the phase tolerance by a factor of 16.60 for the phase errors induced by the white

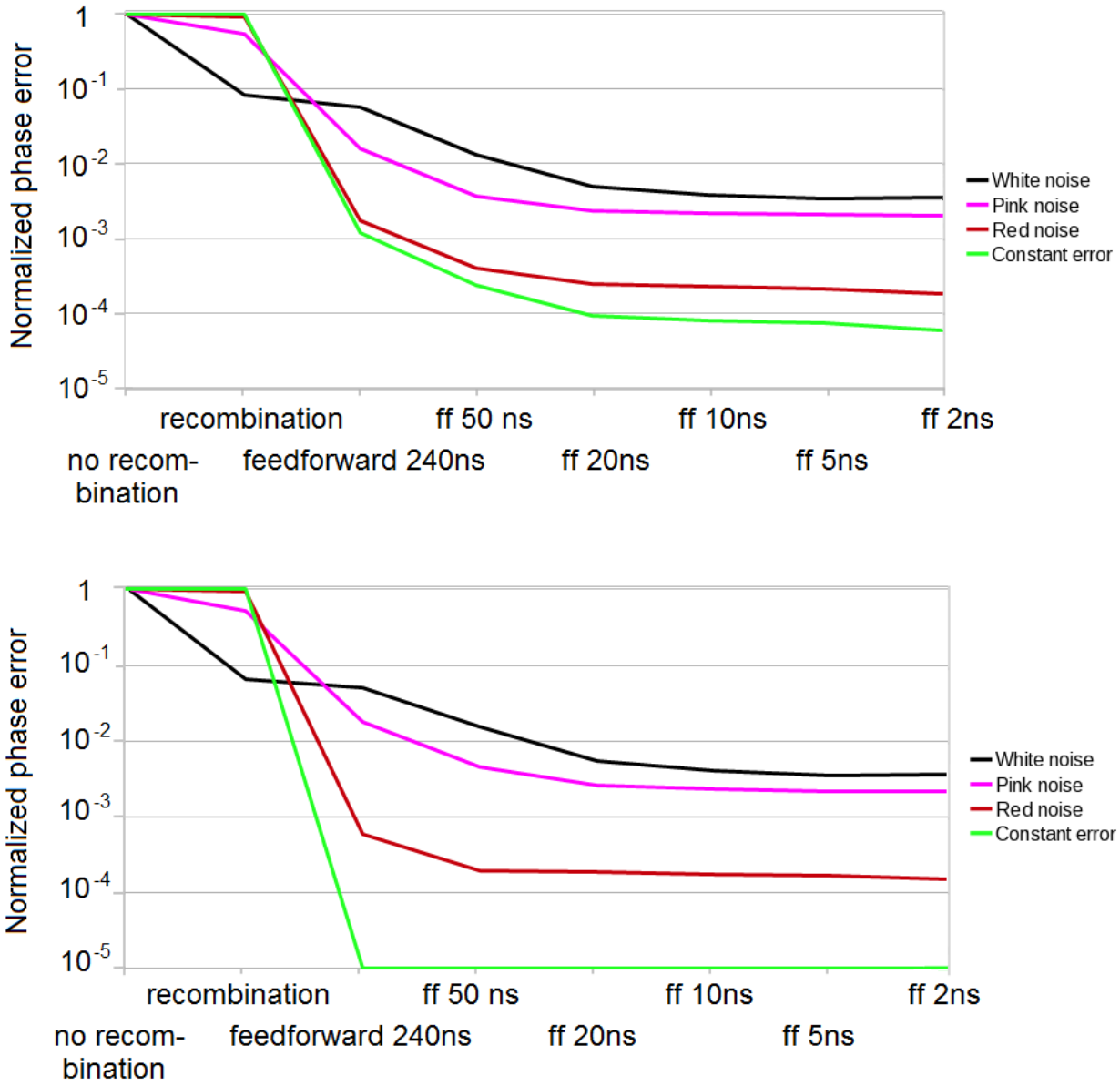

Figure 5.14: Normalized phase error generated by bunch charge errors (top) and Drive Beam RF phase errors (bottom) for different noise spectra. The error value is plotted before recombination (first entry on x-axis), after filtering by the recombination scheme (second entry on x-axis) and after feed-forward correction with different gain times (following entries on x-axis) [60].

noise bunch charge jitter and by a factor of 11.98 for the phase errors induced by the white noise jitter of the RF phase.

Consequences for CLIC design

The simulation of the feed-forward system application at CLIC has shown that the correction efficiency is strongly dependent on the amplifier's rise time, with shorter rise time provid-

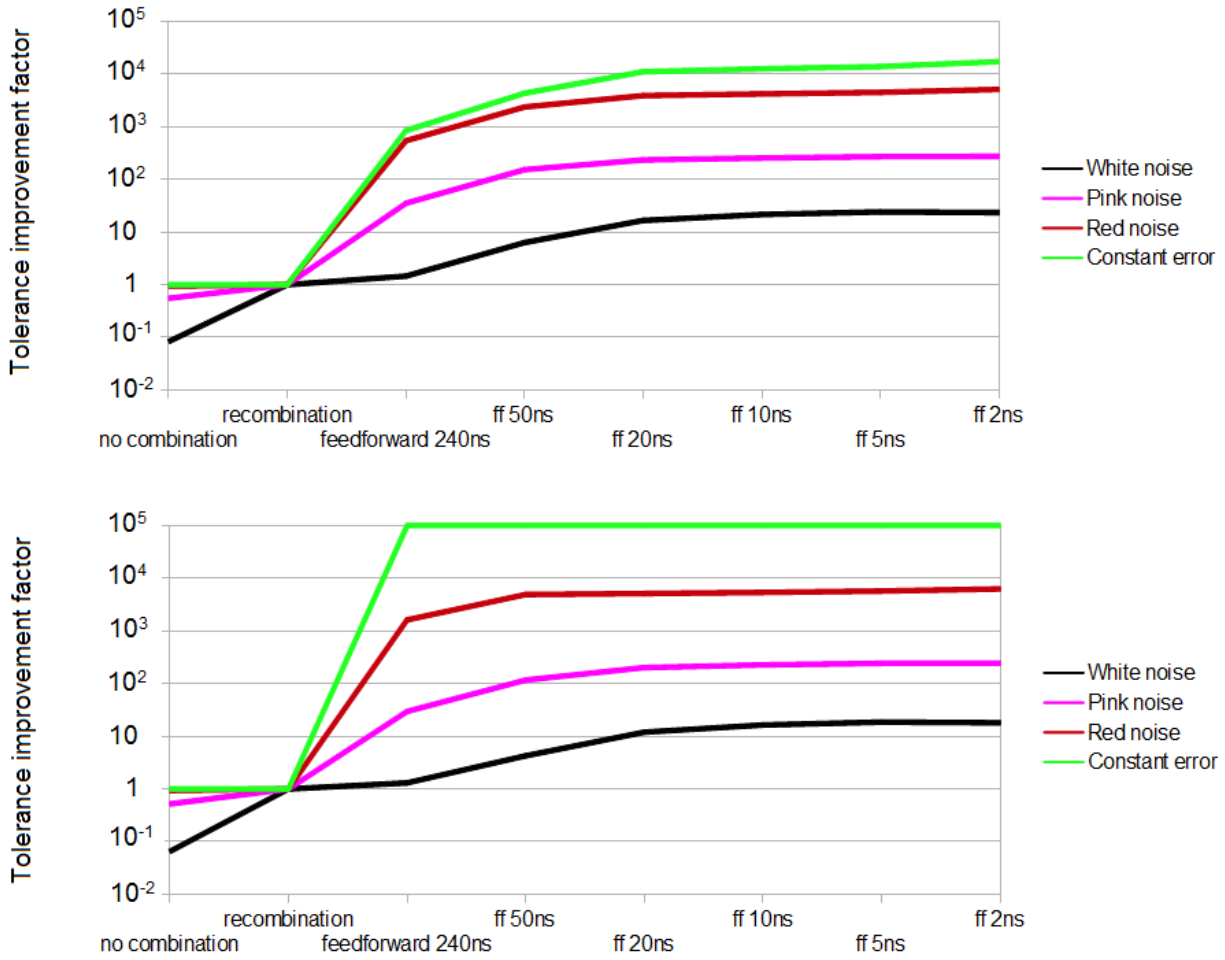

Figure 5.15: Tolerance improvement for the phase error generated by bunch charge errors (top) and Drive Beam RF phase errors (bottom) for different noise spectra, normalised to the tolerance value after the recombinations scheme. The tolerance improvement is plotted before recombination (first entry on x-axis), after filtering by the recombination scheme (second entry on x-axis) and after feed-forward correction with different gain times (following entries on x-axis).

ing higher correction effectiveness. However, even slower amplifiers can produce a sufficient correction of the phase error, if the phase jitter frequency is low enough. Consequently, the bandwidth of the system must be selected according to the frequency spectrum anticipated for the phase error at the final turnaround loop.

In the ideal case, when the phase measurement, signal distribution and signal transfer are error free and the amplifier's kick is linear, the 1.46 MHz amplifier bandwidth is sufficient for the correction of the pink and red phase noise as well as of a constant phase offset. To reduce the phase error by the specified factor of twelve for the white noise an amplifier bandwidth of 17.5 MHz or larger is required.

The monitor noise is present in any real phase measurement and it has a strong effect on the final phase error: the feed-forward system will use the monitor signal for the correction of the phase error, hence the phase measurement noise must be quadratically added to the phase error after (and not before) the feed-forward correction. The high-frequency component of the phase monitor noise will be automatically filtered due to the limited bandwidth of the feed-forward amplifier, but the monitor noise tolerance for frequencies below the amplifier's bandwidth must be held very tight ($\ll 0.2^\circ$ at 12 GHz, which is the cumulative CLIC tolerance for all phase error effects) in order for the feed-forward system to function effectively.

The noise in the signal distribution system cannot be simply quadratically added to the total phase error after the correction, since the distribution noise amplitude differs along the CLIC accelerator. A detailed analysis of the distribution noise propagation is presented in Sec. 5.3.3.

5.3.3 Specifications of the distributed timing system

For the successful operation of the phase feed-forward correction the signal of the nominal phase must be distributed along the almost 50 km long CLIC collider. Two different approaches for the synchronisation of phase signal have been described in Sec 2.5.2 and the principle of the signal distribution at the turnaround sectors of the Drive and Main Beams is shown in Fig. 5.16. The analysis of the specification for approach B, the distributed timing system, is presented in the current section. The section describes the principle of the timing distribution and the results of the calculation of the required timing system stability.

Principle of time distribution and phase correction

Figure 5.16 B shows how the signal from the master clock is used as the synchronisation signal for the local oscillators. The nominal phase signal (indicated in green) is forwarded by the distributed timing system (indicated by the brown line) to the final turnaround of the Main Beam. There the signal is compared with the phase measurement of the Main Beam (indicated by the blue line) from the phase monitors (indicated in red). The signal difference is sent as a correction signal to the kicker chicane and the Main Beam bunches are corrected to the nominal phase value after the Main Beam passes the final turnaround. Simultaneously, the distributed timing system signal is compared with the phase measurement signal of the Drive Beam (indicated by the black line). The feed-forward system processor (indicated by larger light-blue boxes) amplifies and sends the correction signal to the Drive Beam kicker chicane, correcting the phase of the Drive Beam bunches to the nominal value as well.

This procedure is performed for each Main Beam only once, since there is only one Main Beam turnaround at the outermost section of CLIC. The Drive Beam is corrected at each of the 24 decelerator sections. The signal is stored for the time between its arrival from the

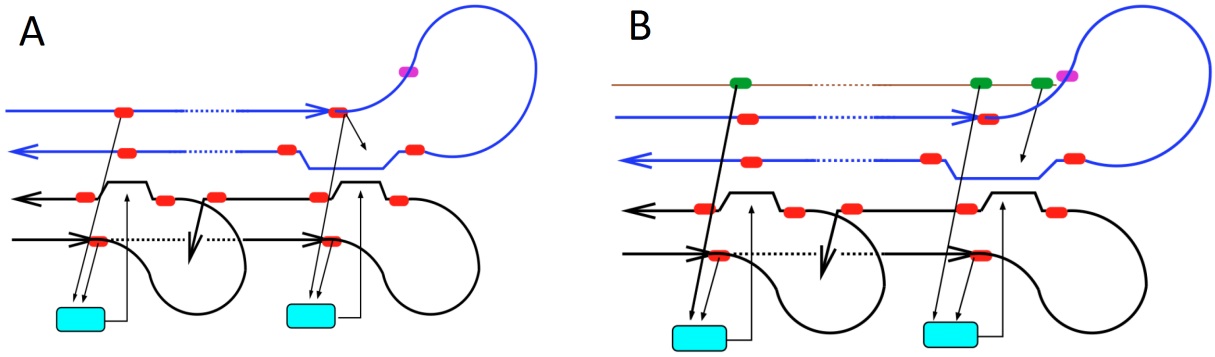

Figure 5.16: Phase correction system based on the Main Beam phase measurement (A) and on the external master clock (B) [61]. The Main Beam is depicted in blue, the Drive Beam in black, the independent optical system in brown. The small arrows indicate the signal transmission. The red blocks represent the phase monitors and the larger light-blue boxes the feed-forward processor. The green blocks represent the signal of the distributed timing system.

distributed timing system and the time of the phase correction with the help of highly stable local oscillators, which have been ordered to be tested at CTF3 [32]. The master clock itself has a particular noise spectrum. The impact of the noise on the local oscillators can be reduced by integrating the signal over time intervals longer than the beam propagation time through the machine (≈ 0.2 ms).

The phase measurements of the Main and Drive Beam after the chicanes ensure that the provided correction has an accurate value. If this is not the case, it could mean that the path length of the beams in the chicane is not as predicted, the chicane has the wrong R_{56} value or that the waveguide length has changed (e.g. due to temperature variation). To correct for these changes a pulse-to-pulse feedback system can be introduced. Provided the changes are slow enough, the measured value of the correction error can be used to adjust the relative definitions of the monitors' nominal phase. The new definitions will ensure that the correction for the next pulse will set the Drive Beam bunches closer to their nominal position. Hence, high stability of the local oscillator clocks must be ensured on a timescale of at least 20 ms, which is the pulse-to-pulse interval of CLIC.

In order to determine the phase error tolerance for signal transfer between the two subsequent decelerators labelled as σ_{step} (see Fig. 2.18, B), one must calculate the impact of this error on the total phase error. We will assume a random walk of the phase error, which starts from the master clock near the IP and propagates along the machine step by step from one Drive Beam decelerator segment to another.

e^+ and e^- Main Beams phase tolerance

For the incoming Main Beams the relative phase tolerance at the IP is 0.6° @ 12 GHz $\hat{=}$ 42 μm $\hat{=}$ 140 fs [61] which corresponds to a 1% luminosity loss. Hence, one must ensure that the total phase error introduced by the distributed timing system σ_{dts} is below (140 fs)/$\sqrt{2}$ for each of the Main Beams.

In addition to the 24 decelerator modules, each about 900 m long, one must consider that the beam delivery system of each Main Beam is about 2.75 km long [43]. To simplify the calculation it will be assumed that the distributed timing system for the Main Beam is 27, instead of 24, sectors long, hence about 2.7 km longer. One can consider the errors at each of the segments as linearly independent. Hence, the tolerance for the phase error introduced in each segment is given by

$$\sigma_{step,mm,1\%} = \frac{140 \text{ fs}}{\sqrt{27} \times \sqrt{2}} = 19.05 \text{ fs} \hat{=} 5.72 \ \mu\text{m}. \tag{5.3}$$

where the subscript mm indicates the requirement resulting from the Main Beam to Main Beam phase error tolerance. The stated correction system error would cause a luminosity loss of 1%. However, in reality the largest part of the tolerance budget will be reserved for the beam itself and not for the reference jitter. Hence, the calculation only determines the upper limit for the distribution error but not the effective system requirement, which will depend on the expected beam phase jitter. Defining the distribution system requirement to cause maximally a 0.1% luminosity loss, one obtains

$$\sigma_{step,mm,0.1\%} = \frac{5.72 \ \mu\text{m}}{\sqrt{1\% \ / \ 0.1\%}} = 1.81 \ \mu\text{m}. \tag{5.4}$$

An advantage of the distributed timing system is that it allows one to loosen the phase tolerances on the outgoing Main Beam by a factor of 7, since the phase correction at the final turnaround of the Main Beam can reduce the phase error [54], [86].

Also, the phase correction can compensate for the change in the Main Beam path length, provided the path length change is slow enough. In particular, the timescale of the change must be significantly larger than the 20 ms interval between the Main Beam pulses.

Main beam - Drive Beam phase tolerance

The error σ_{step} that causes a 1% luminosity loss can also be calculated from the Main Beam - Drive Beam relative phase error tolerance. The total error σ_{tot} introduced by the phase correction system at each decelerator must be below 0.8° @ 12 GHz for uncorrelated errors (see Sec. 2.5).

We assume a random walk of the distribution error segment by segment. The error at the segment with index i counted from the IP is given by $\sum_{j=1}^{i} \sigma_{step} = i \cdot \sigma_{step}$. The total error introduced by the distributed timing system σ_{dts} is given by the sum of the errors in all segments. One should also consider that the Main Beam bunches are positioned at 30°

of the RF wave in the four segments nearest to the IP and at 8° in other twenty segments. Hence σ_{dts} can be calculated with

$$\sigma_{dts}^2 = \sum_{i=1}^{24}\left[\sum_{j=1}^{i}[\sigma_{step}\times(\sin 8^\circ + H[4-j]\times(\sin 30^\circ - \sin 8^\circ))]^2\right] \tag{5.5}$$

with H being the Heaviside function. One can transform the equation to:

$$\sigma_{dts}^2 = \sum_{i=1}^{4}\left(\sum_{j=1}^{i}(\sigma_{step}\times\sin 30^\circ)\right)^2 + \sum_{i=5}^{24}\left(\sum_{j=1}^{4}(\sigma_{step}\times\sin 30^\circ) + \sum_{j=5}^{i}(\sigma_{step}\times\sin 8^\circ)\right)^2 \tag{5.6}$$

$$\Leftrightarrow \sigma_{dts}^2 = (\sigma_{step}\times\sin 30^\circ)^2\times\sum_{i=1}^{4}(i)^2 + (\sigma_{step}\times\sin 8^\circ)^2\times\sum_{i=1}^{20}\left(4\frac{\sin 30^\circ}{\sin 8^\circ}+i\right)^2 \tag{5.7}$$

Normalising σ_{dts}^2 by the RMS value of the stated sine functions by

$$\phi_{RF,incoh} = \sum_{i=1}^{4}(\sigma_{step}\times\sin 30^\circ)^2 + \sum_{i=5}^{24}(\sigma_{step}\times\sin 8^\circ)^2 \tag{5.8}$$

and calculating the sums, one obtains

$$\sigma_{step,md,1\%} = 0.059^\circ \stackrel{\wedge}{=} 4.12\ \mu\text{m} \tag{5.9}$$

where the subscript md indicates the requirement from the Main Beam to Drive Beam phase error tolerance. This value is of the same order of magnitude as the tolerance given by the Main Beam - Main Beam phase error consideration ($\sigma_{step,\text{mm},1\%} = 5.72\ \mu$m) calculated in the previous subsection. Defining a specification of the distribution system as above by the maximal luminosity loss of 0.1% yields the requirement for the reference stability

$$\sigma_{step,md,0.1\%} = \frac{4.12\ \mu\text{m}}{\sqrt{1\%\ /\ 0.1\%}} = 1.30\ \mu\text{m}. \tag{5.10}$$

Combined phase tolerance

The luminosity loss from the reference jitter has been calculated independently for Main Beam - Main Beam and Main Beam - Drive Beam phase error tolerances. In reality the same reference jitter σ_{step} would cause a luminosity loss via both channels,

$$\begin{aligned}\Delta\mathcal{L}_{total} &= \Delta\mathcal{L}_{md} + \Delta\mathcal{L}_{mm}\\ &= 1\%\times\left(\left(\frac{\sigma_{step}}{\sigma_{step,md,1\%}}\right)^2 + \left(\frac{\sigma_{step}}{\sigma_{step,mm,1\%}}\right)^2\right)^2\end{aligned} \tag{5.11}$$

Solving this equation for the tolerance of $\Delta\mathcal{L}_{total} = 1\%$ yields $\sigma_{step} = 3.34\ \mu$m. However, $\Delta\mathcal{L}_{total} = 0.1\%$ defines the specification of $\sigma_{step} = 1.06\ \mu$m average error introduced by the distributed timing system at each decelerator segment.

5.4 Modification of Drive Beam accelerating structure RF filling time

Introduction and cost considerations

After the publication of the CLIC Conceptual Design Report [32] the cost optimisation of CLIC has become one of the most important design issues. In the framework of the re-baselining campaign different scenarios of cost optimisation are under consideration [87].

The Drive Beam linac accounts for 77% of the total cost of the CLIC Drive Beam [87]. One of the cost reduction methods would be to increase the gradient of the Drive Beam accelerating structures while reducing the total length of the linac. This option would operate with a smaller number of longer accelerating structures with a higher RF filling time.

Up to the point in the thesis the RF filling and beam loading functions of the Drive Beam accelerator have been used according to the baseline design and the simulation results from [75] and [76] presented in Sec. 3.1.2. In the current section the consequences of modification of the RF filling time pertaining to the error filtering by the Drive Beam RF filling are examined.

Error filtering with modified RF filling times

For the nominal RF filling time the error filtering in the Drive Beam accelerator has been described in Sec. 5.1.2 and the impact of the phase feed-forward stabilisation system has been calculated in Sec. 5.3. The results for the phase error caused by the 0.05% jitter in the Drive Beam accelerator RF amplitude are displayed in Fig. 5.17; the realistic RF filling and beam loading functions have been used. The solid red curve depicts the resulting Drive Beam phase error at the PETS without a feed-forward correction and the dashed blue curve represents the phase error after the correction by a feed-forward system with 30 nm gain length, which corresponds to a realistic 11.7 MHz feed-forward amplifier bandwidth, which is assumed for the study in the current section.

The length of the Drive Beam RF filling function can be changed in the simulation tool. Fig. 5.18 presents the phase error caused by the same source as for Fig. 5.17. The phase error after the 11.7 MHz feed-forward correction for the nominal RF filling time of the Drive Beam accelerator is represented by the dashed blue curve. The solid yellow curve represents the error for the RF filling time being triple the nominal.

The longer RF filling time means that the convolution of the Drive Beam error function with the accelerator RF filling function is performed over a longer time interval. Because of that, the errors within a longer RF filling time can compensate each other, so that filtering by the structure with a longer RF filtering time is more effective. This is particularly the case for the frequencies between $1/(3 \times 240\ \text{ns}) = 1.39$ MHz and $1/240$ ns$= 4.16$ MHz, since

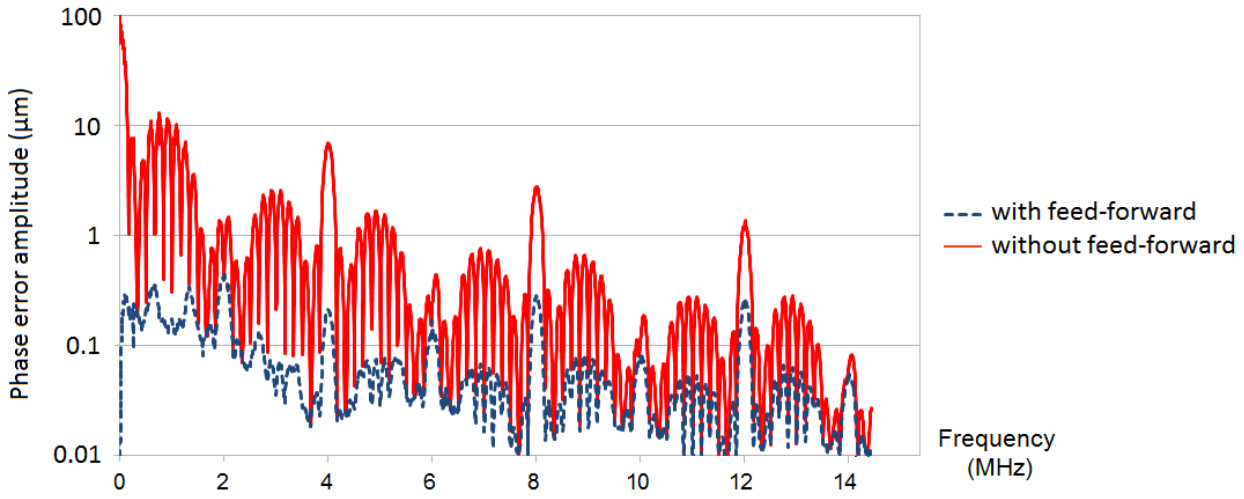

Figure 5.17: Phase error caused by 0.05% jitter in the accelerator RF amplitude without feed-forward correction (solid red) and with 11.7 MHz bandwidth feed-forward correction (dashed blue).

the largest portion of the integrated RF filling for the nominal function lies within 240 ns (see Fig. 3.4), and for the function with the triple of the nominal RF filling time within 3×240 ns.

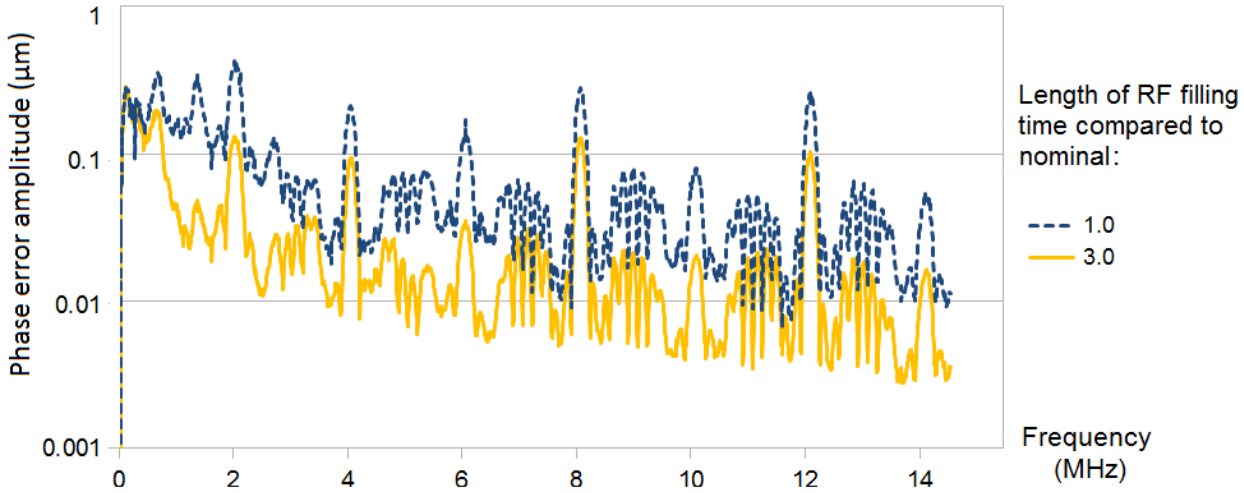

Figure 5.18: Phase error caused by jitter in the accelerator RF amplitude for the nominal (dashed blue) and triple (solid yellow) RF filling time with a 11.7 MHz feed-forward correction (linear frequency scale).

The phase error for different orders of magnitude in frequency can be seen more clearly in Fig. 5.19. For phase errors below 0.1 MHz the difference in filtering for the two Drive Beam RF filling settings is minimal, since the dominant contribution to the filtering for these frequencies is given by the feed-forward system. For errors around 1 MHz and above the longer structure performs significantly more effective filtering.

It is interesting to note that the error with a frequency of about 0.1 MHz has the highest amplitude, in particular for the longer RF filling time structure. Each of the filtering effects, by the recombination scheme, by the Drive Beam accelerator and by the feed-forward system filter this error band, however they perform best at other frequencies so that the region around 0.1 MHz remains the least filtered part of the spectrum.

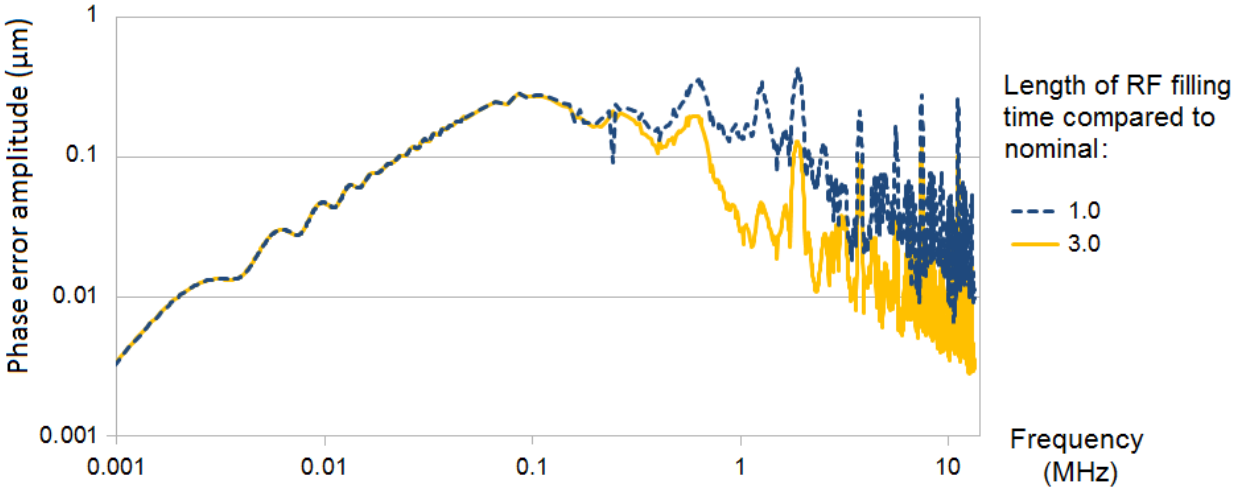

Figure 5.19: Phase error caused by jitter in the accelerator RF amplitude for the nominal (dashed blue) and triple (solid yellow) RF filling time with a 11.7 MHz feed-forward correction (logarithmic frequency scale).

The effectiveness of the filtering by the Drive Beam accelerating structures with the different RF filling time settings can be presented as a phase error ratio of the new RF filling time to the nominal one. Examples of such ratios as a function of frequency are displayed in Fig. 5.20. The top figure represents the phase error of the RF filling time scaled by a factor of 0.8 from nominal. For almost all frequencies the phase error is higher in this case than with the nominal RF filling time. It is especially high for the peaks at $n \times 4.17$ MHz, since the nominal Drive Beam accelerator filling time is set explicitly to filter out these peaks.

The $n \times 4.17$ MHz peaks are also filtered less effectively by the RF filling time scaled by the factor of 1.4 of the nominal (Fig. 5.20, middle). However, since the errors are filtered over longer time intervals than for the nominal structure, the total error of this RF filling time setting is lower than for the nominal one.

The accelerating structure with the double RF filling time (Fig. 5.20, bottom) filters the error more effectively than the baseline structure on for almost all frequencies. It is also the case for the peak frequencies of $n \times 4.17$ MHz, since the effective filtering of this structure is applied at $\frac{n}{2} \times 4.17$ MHz and hence includes the peak frequencies at $n \times 4.17$ MHz.

Integrating the error over the frequency according to Eq. 5.2 shows the overall effectiveness of the filtering by each of the RF filling time settings (see Fig. 5.21). The general trend shows that the error is reduced for any increase of the RF filling time. The nominal

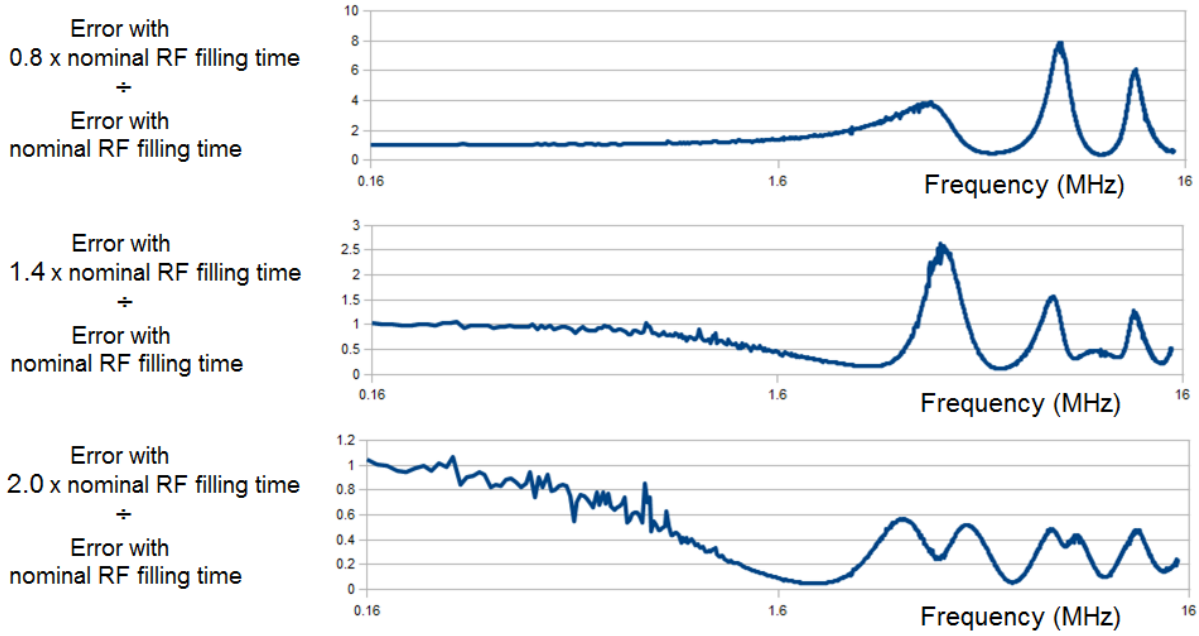

Figure 5.20: The ratio of the phase error (caused by jitter in the accelerator RF amplitude) filtered by the modified RF filling time structures to the one filtered by the nominal structure. The modified structures have an RF filling time of 0.8 (top), 1.4 (middle) and 2.0 (bottom) relative to the nominal structure.

structure performs particularly well, since it is able to partially filter out the error peaks at $n \times 4.17$ MHz. Because of this, the change of the error between the nominal RF filling time and RF filling time scaled by factor of 1.2 is rather small - the error is decreased only by 3.2%. However the error decreases by 17.2% from nominal if the RF filling time is scaled by a factor of 1.4, by 25.2% if RF filling time is scaled by 1.6 and by 39.4% if the RF filling time is scaled by 2.0.

Consequently, for white noise, prolonging the RF filling time of the structure is beneficial from the point of view of the Drive Beam tolerances.

Analysis for different noise spectra

For the different sorts of noise, however, the fraction of the error filtered out by the RF filling is not the same. Fig. 5.22 shows the phase error after the filtering by the nominal Drive Beam RF filling time (dashed blue) and the Drive Beam structures with the triple RF filling time (solid yellow). The incoming white noise is displayed in the top diagram, the pink noise in the middle and the red noise at the bottom. The filtering factor of different RF filling times for all three noise types is the same, however the low frequency component is dominant for the pink noise and even more dominant for the red noise. Since the Drive Beam RF does not have a significant impact on the low frequency noise, the difference in the overall error for the various RF filling times is small.

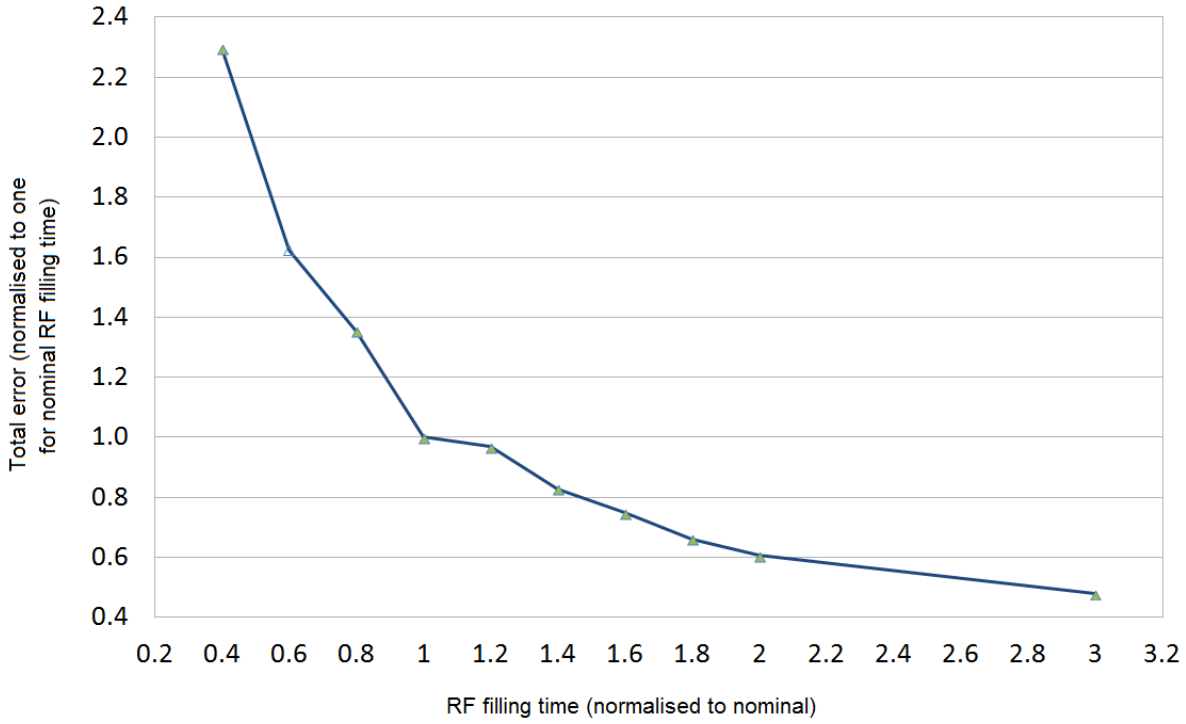

Figure 5.21: Total phase error caused by jitter in the accelerator RF amplitude as a function of the RF filling time of Drive Beam accelerating structures. The phase error is induced by white noise in the accelerator RF amplitude.

Fig. 5.23 shows the total noise integrated over frequency according to Eq. 5.2. The dashed blue curve represents the total error for white noise already displayed in Fig. 5.21. The dotted yellow and solid green curves represent the phase error for the pink and red noise respectively. These curves stay very close to the value of unity for all RF filling times, varying by $\pm 3\%$ for the pink noise and $\pm 0.3\%$ for the red noise.

This fact implies that the less expensive Drive Beam accelerating structures with a longer RF filling time can be also implemented from the point of view of error filtering for the pink and red noise - although the longer RF filling time has almost no impact on the phase error, a significant cost reduction of the Drive Beam linac can be achieved.

Consequences for CLIC design

The RF fill time of the Drive Beam accelerating structures has been set on purpose to 240 ns in order to filter out the RF amplitude and phase errors, which would be resonant with the Drive Beam train length. However, since the RF filling function is not perfectly rectangular, the RF structures do not filter out the resonant frequencies fully.

Increasing the length of the RF fill time of the structures allows the errors to be averaged out on longer time scales. As a consequence, the total beam phase error resulting from the

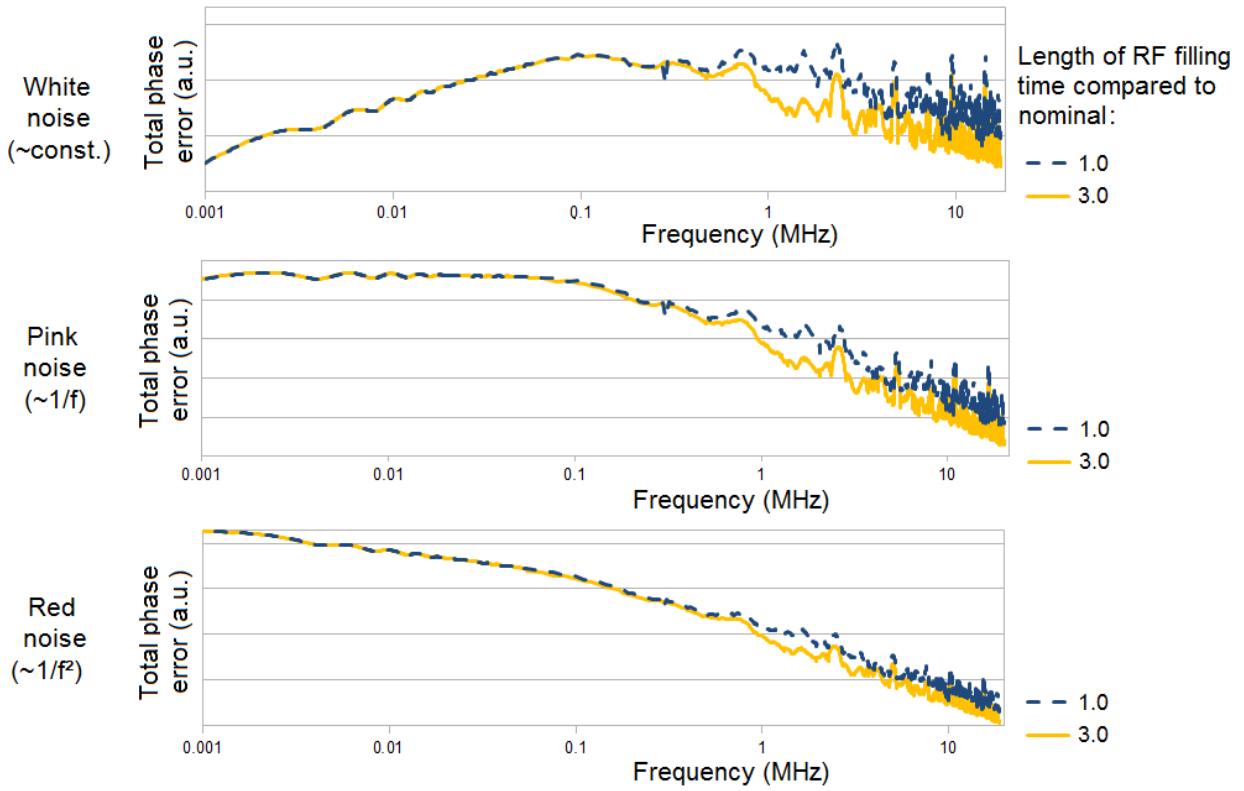

Figure 5.22: Total phase error caused by jitter in the accelerator RF amplitude as a function of jitter frequency for nominal (dashed blue) and triple (solid yellow) RF filling time of Drive Beam accelerating structures. The phase error is induced by white noise (top diagram), pink noise (middle) and red noise (bottom) in the accelerator RF amplitude.

errors in the RF amplitude and phase decreases. E.g. for the proposed increase of the RF fill time by a factor of 1.4 the total phase error decreases by 17.2% in the case of white noise RF amplitude and phase errors. The total error for the pink and red noise is decreased insignificantly, by less than 1%.

In summary, the analysis shows that the prolongation of the RF fill time of the Drive Beam accelerating structures is beneficial to irrelevant from the point of view of CLIC tolerances, depending on the noise spectrum. Given that such prolongation can lead to a significant cost reduction, it should be taken account of as a valid option in CLIC cost feasibility considerations.

5.5 Low Energy recombination modes

In addition to the nominal operation mode with a centre-of-mass energy of 3 TeV described in Sec. 2.2.2, other modes for the operation of the machine at lower energy are needed. The low energy operation is necessary to study the properties of the particles that are expected, or hoped to be discovered, at CLIC. CLIC must allow the possibility of energy scans, which

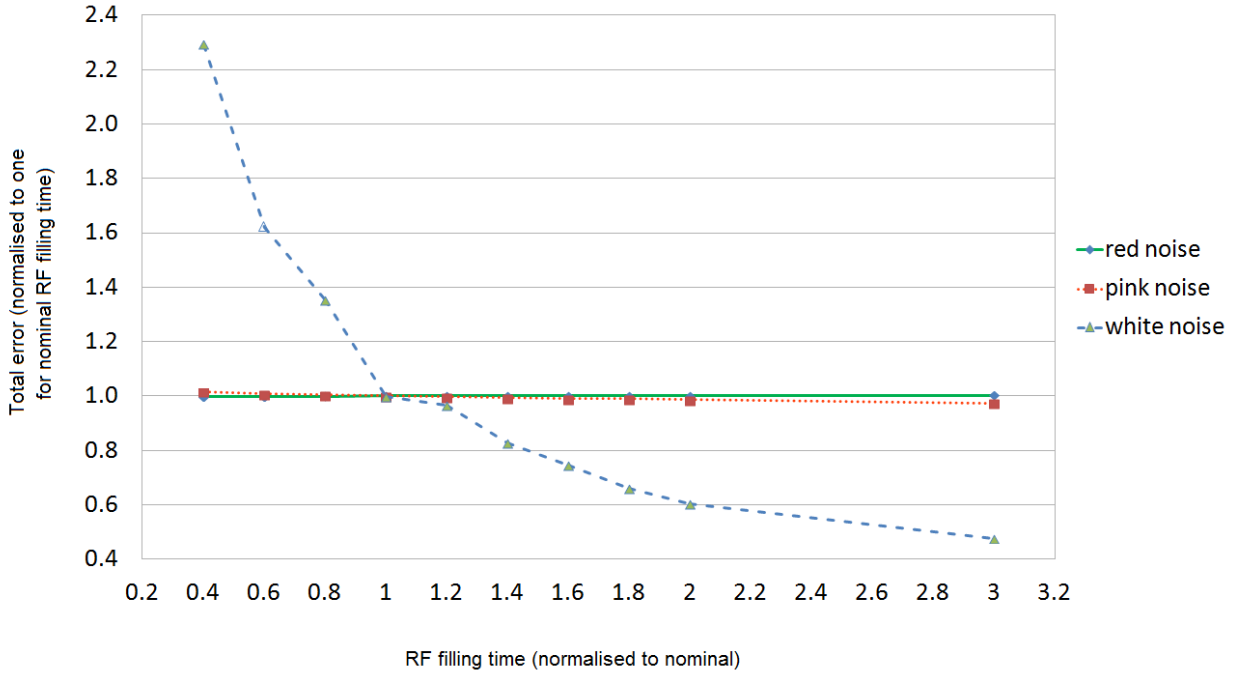

Figure 5.23: Total phase error caused by jitter in the accelerator RF amplitude as a function of the RF filling time of Drive Beam accelerating structures. The phase error is induced by white noise (dashed blue curve), pink noise (dotted yellow curve) and red noise (solid green curve) in the accelerator RF amplitude.

can be performed by reduction of the accelerating gradient in the Main Linac.

CLIC error tolerances require the bunch charge N_1 or N_2 to be reduced proportionally to the collision energy E [88]. This leads to a significant luminosity drop, since the luminosity as stated in section 1.3 is given by

$$\mathcal{L} = f_{rep} N_b \frac{N_1 N_2}{4\pi\sigma_x\sigma_y} \tag{5.12}$$

In order to compensate for the luminosity loss at least partially, it is planned to increase the pulse length and consequently the number of bunches per pulse N_b. This pulse length increase can be performed for several stages of energy reduction, which defines the different energy operation modes [88].

The baseline design implies the construction of four different Delay Lines for different energy modes. The Combiner Rings, in contrast, will be designed in order to be able to accommodate all possible pulse lengths in the same structure. The length of the Combiner Rings is 292.8 m for CR1 and 439.2 m for CR2.

The current section presents a brief description of the recombination patterns for the lower energy modes (a full description can be found in [81]) and focuses on the error estimation for these modes (see also [82]). The effect of the phase feed-forward system for lower energy operation modes is also calculated.

5.5.1 Nominal 3 TeV operation mode

At the nominal operation mode CLIC Drive Beam trains with both even and odd buckets are 240 ns long. After the recombination of the buckets in the Delay Line, the beam consists of 240 ns long 1 GHz trains and 240 ns long gaps. The first Combiner Ring will be filled with two trains simultaneously, separated by two gaps (see Fig. 5.24). When next two trains arrive, they will be combined with the ones circulating in the ring, up to the combination factor of three. Afterwards, the trains will be extracted from the Combiner Ring. The second train injected into the first Combiner Ring must be extracted before it is combined (see Sec. 3.1.4 for more details). In the second Combiner Ring trains of 3 GHz frequency and 240 ns length, separated by 5×240 ns long gaps, circulate four times, being recombined with the following trains at the end of each cycle.

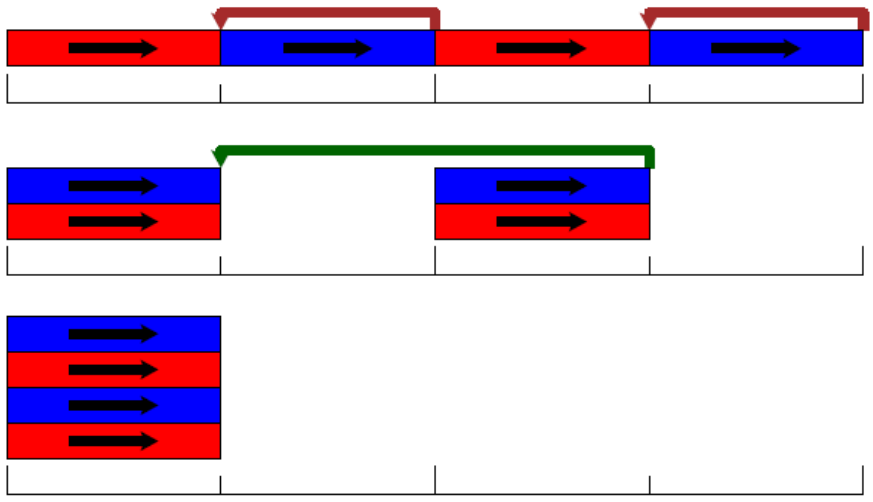

Figure 5.24: The recombination scheme switching pattern of the nominal 3 TeV mode - 120 even and 120 odd buckets [89].

5.5.2 Lower energy operation modes

2.25 TeV mode

The 2.25 TeV mode requires the train length of $4/3 \times 240$ ns and a corresponding Delay Line length. Hence, it is planned to produce 160 even buckets followed by 80 odd buckets, then 80 even buckets followed 160 odd buckets and so on (see Fig. 5.25).

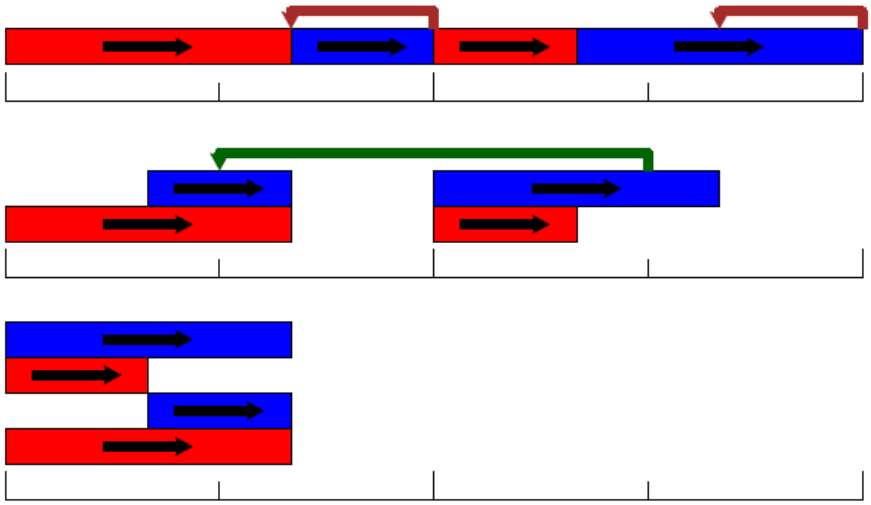

Figure 5.25: The recombination scheme switching pattern of the 2.25 TeV mode - even and odd trains come alternating in groups [89].

Fig. 5.26 shows the output of the simulation tool for the z position of the bunches recombined according to the pattern for 3 TeV (top) and for 2.25 TeV (bottom). The distribution shows that for the 2.25 TeV case in contrast to the 3 TeV case the recombination for each interval of the train is performed by a factor of 18 instead of 24. The trains are longer by a factor of 4/3.

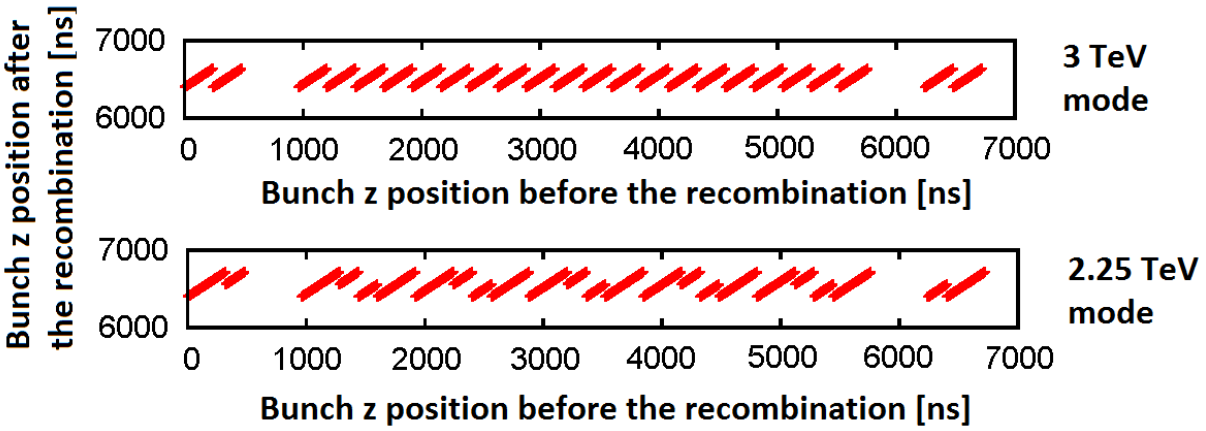

Figure 5.26: Bunch position after the recombination with the nominal 3 TeV mode switching pattern (top) and with the 2.25 TeV mode switching pattern (bottom).

Other lower energy modes

For the 2 TeV mode the train length must be $3/2 \times 240$ ns. The switching pattern is similar to the 2.25 TeV mode and implies the alternation between 120 even and 120 odd buckets, then 180 even and 60 odd and afterwards 60 even and 180 odd.

The 1.5 TeV mode has a train length of 2 × 240 ns, so the first Combiner Ring accommodates only one of the trains instead of two and the second Combiner Ring two instead of four [89]. The recombination factors provided by Combiner Rings stay the same.

The switching pattern for the 1.125 TeV mode is analogous to the 2.25 TeV mode.

5.5.3 Consequences for the error propagation and correction

Main Beam gradient error

The Delay Line and the Combiner Rings have the same deflector frequency at nominal and low energy modes. Hence, they create the Drive Beam with 12 GHz bucket frequency with some of the buckets not being filled with bunches instead of creating a train with equidistantly distributed bunches. E.g. the bucket frequency for 2.25 TeV mode is not 9 GHz, but 12 GHz with 1/4 of the buckets being empty.

Because of that, the resulting Main Beam RF wave amplitude will not be stable. Preliminary calculations estimate the resulting Main Beam energy jitter being of the order of several parts per mille, which is above the Drive Beam tolerance limit. However, since different switching patterns are used from one Drive Beam train to another (see e.g. Fig. 5.25), the overall energy spread of the Main Beam will be to some extent compensated.

Main Beam accelerator RF phase error

In order to suppress the resonant peaks for the nominal energy case, the RF filling time of the Drive Beam accelerating structures has been set to 240 ns. As a result the phase error caused by the Drive Beam accelerator RF errors, i.e. the resonant peaks at $n \times 4.17$ MHz, are suppressed (compare Figs. 5.6 and 5.7). This filtering can be set up only for one frequency and its multiples. For the various lower energy modes the train lengths differ, and hence not all resonant peaks can be filtered out by fitting the Drive Beam RF filling time to them. Fig. 5.27 demonstrates this for the example of the 2.25 TeV mode - in this mode the 480 ns long trains are divided into approximately 320 ns and 160 ns long parts, which are recombined. Hence the resonant modes are at $n \times 2.1$ MHz, $n \times 3.1$ MHz and $n \times 6.3$ MHz. A white noise Drive Beam RF amplitude error of 0.05% has been used as input.

The peaks at n × 4.1 MHz are significantly suppressed, but the rest of the peaks remain unfiltered. The total RMS phase error is 5.58° at 12 GHz compared with 4.96° at 12 GHz for the 3 TeV case. This difference is not large, however the feed-forward system functions much less effectively, in particular because the large peaks at 2.1 and 6.3 MHz are not suppressed. E.g. for 20 MHz feed-forward bandwidth the total RMS error drops only to 1.05° at 12 GHz compared with 0.11° for the 3 TeV case.

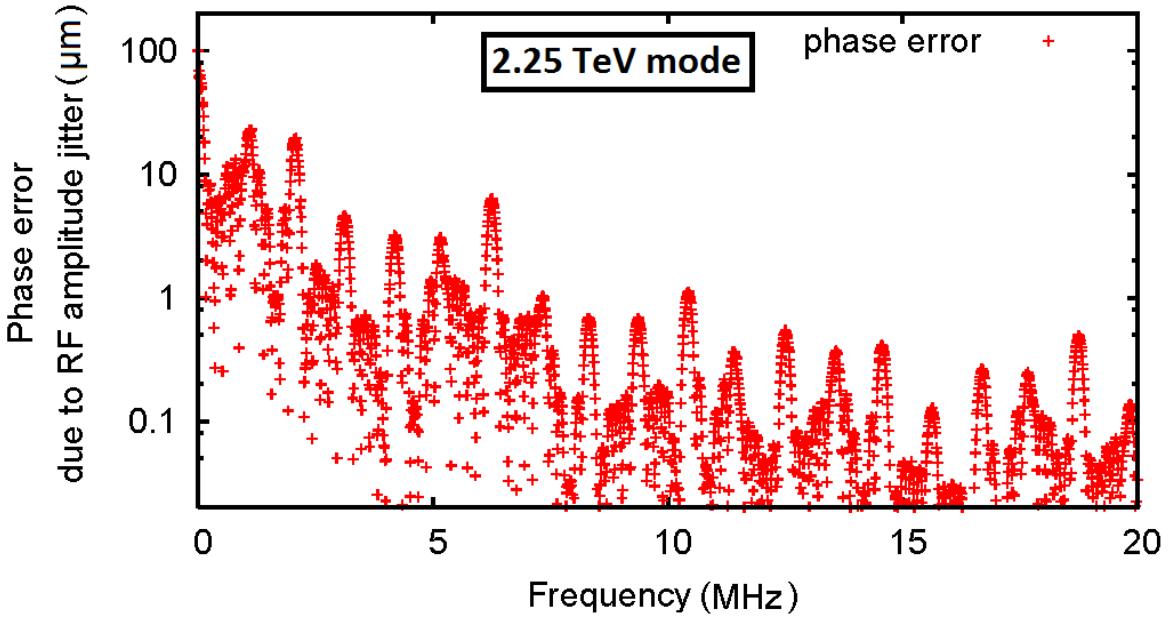

Figure 5.27: Main Beam RF phase error caused by 0.05% Drive Beam RF amplitude error for 2.25 TeV mode.

This means that the feed-forward stabilisation is less effective for the lower energy modes. Additional systems for the Drive Beam RF phase and amplitude stabilisation have to be implemented in order to maintain the high level of luminosity, if the CLIC machine with a nominal energy design is to be operated in low energy modes extensively.

5.6 Chapter summary

Error filtering by the Drive and Main Beam RF structures and the recombination scheme

A filtering of the Drive Beam bunch charge and phase errors is provided by the recombination scheme and a consecutive convolution of the beam errors with the Main Beam RF filling and beam loading functions. The Drive Beam errors are filtered in the frequency spectrum of several MHz very effectively. The low frequency errors (below 100 kHz) are, however, not well filtered. Also the error peaks at frequencies $n \times 4.17$ MHz resonant with the Drive Beam train length of 244 ns are not effectively filtered.

The errors in the parameters of the Drive Beam accelerating structures, such as RF phase and amplitude, as well as errors of the Drive Beam bunch charge leading to erratic beam loading of the Drive Beam accelerating structures, have been simulated. Drive Beam RF filling and beam loading functions have been designed have a fill time of 244 ns in order to filter out errors resonant with the length of the Drive Beam trains. The structures hence provide a reasonable filtering at frequencies of $n \times 4.17$ MHz, which remain unfiltered by

the recombination scheme. However, the simulations have shown that the realistic RF filling and beam loading functions are not identical with the defined ideal function, and hence the filtering is not optimal.

The simulations have also revealed that after the filtering described above an additional Drive Beam error reduction is necessary. The effect of two active Drive Beam stabilisation systems has been analysed: the bunch charge feedback system and the phase feed-forward system.

Bunch charge stabilisation via a feedback system

The charge feedback system, which would measure the bunch charge near the source of the Drive Beam and correct the errors at the source, has been shown to have the best performance with a latency time of 240 ns and a gain duration time of zero nanoseconds. Since such a gain duration time is not feasible, the effect of a system with a latency time of 200 ns and gain duration time of 40 ns has been studied. It has been found to reduce the bunch charge error by about 45%, which is not sufficient for the stabilisation of the PHIN-based electron source, since the bunch charge stability must be improved by a factor of 2.5, from the stability of 0.25% achieved at the PHIN source experiment to the CLIC specification of 0.1%.

Phase stabilisation via a feed-forward system

The feed-forward correction system has been found to be an effective method for the Drive Beam phase stabilisation, especially for the low frequency phase jitter. It would be installed at the final turnaround of the Drive Beam before each decelerator segment. A bandwidth of at least 17.5 MHz would be required to correct the white noise in the Drive Beam phase by the required factor of twelve, the bandwidth requirements for the different types of noise have been found to be more relaxed.

The distributed timing system has been found to be a viable alternative to the phase measurement of the outgoing Main Beams for the distribution of the nominal phase signal along the Drive and Main Beams. However, to satisfy the specification of 0.1% luminosity loss due to the distribution errors, the system must introduce less than 1.06 μm average error at each decelerator segment. This value is not achieved in the associated experiment at DESY yet, though an approach of optical signal transition (without a transformation into electric signal at each decelerator) could possibly improve the stability of the distribution by the required value.

An increase of the RF fill time and the RF structure length is considered as a possible cost reduction strategy. The simulation of the different RF fill times has revealed that the overall filtering effect for the RF amplitude and phase jitters is stronger for the longer RF fill times, especially if these jitters have a large high-frequency component. Consequently,

from the point of view of the Drive Beam stability there are no objections to such a strategy.

Phase stability in low energy operation modes

The nominal CLIC design operating in the lower energy modes is more sensitive to the Drive Beam errors compared with the operation at CLIC's nominal energy of 3 TeV. This is caused by the different recombination patterns of the lower energy modes, which cause the Drive Beam to have a non-nominal train length at the PETS. The filtering by the Drive Beam accelerator for the RF phase and amplitude errors as well as beam loading errors, which has been designed to reduce the error resonant with the nominal train length of 244 ns, is not functioning optimally. E.g. the white noise in Drive Beam phase causes at the PETS (after the feed-forward application) about ten times higher RMS error for the 2.25 TeV mode than for the 3 TeV mode. Hence, additional beam stabilisation strategies must be considered if CLIC is to be operated frequently in the lower energy modes.

Chapter 6

CTF3 phase measurement, analysis and simulations

The CLIC Test Facility CTF3 has been designed to test the feasibility of the technologies that are planned to be used in CLIC construction and operation, as described in Sec. 2.6. The level of beam stability required at CLIC cannot be tested at CTF3 to a full degree, however some of the stabilisation systems can be implemented and examined for their functionality.

The current chapter presents the measurements at CTF3 and data analysis performed in order to design a phase stabilisation system prototype. This prototype is in development by the FONT group of the University of Oxford and is planned to be installed at CTF3 in the second half of 2013.

Section 6.1 presents the measurement of the CTF3 beam phase with the monitors installed along the Drive Beam and the analysis of the error propagation dynamics. The sources of the measured phase error are identified in Sec. 6.2. Section 6.3 describes the suggested design of a phase stabilisation system prototype for CTF3 and presents the simulations predicting the prototype's performance.

Data measurements of the CTF3 beam phase have been performed by the author in collaboration with CTF3 colleagues, in particular with Emmanouil Ikarios. Statements that are not a result of the author's own work, are marked as such and the citation source is stated.

6.1 Phase measurement results along CTF3

There are seven phase monitors installed along the beam path of the CTF3 facility. Their position is indicated with blue arrows in Fig. 6.1.

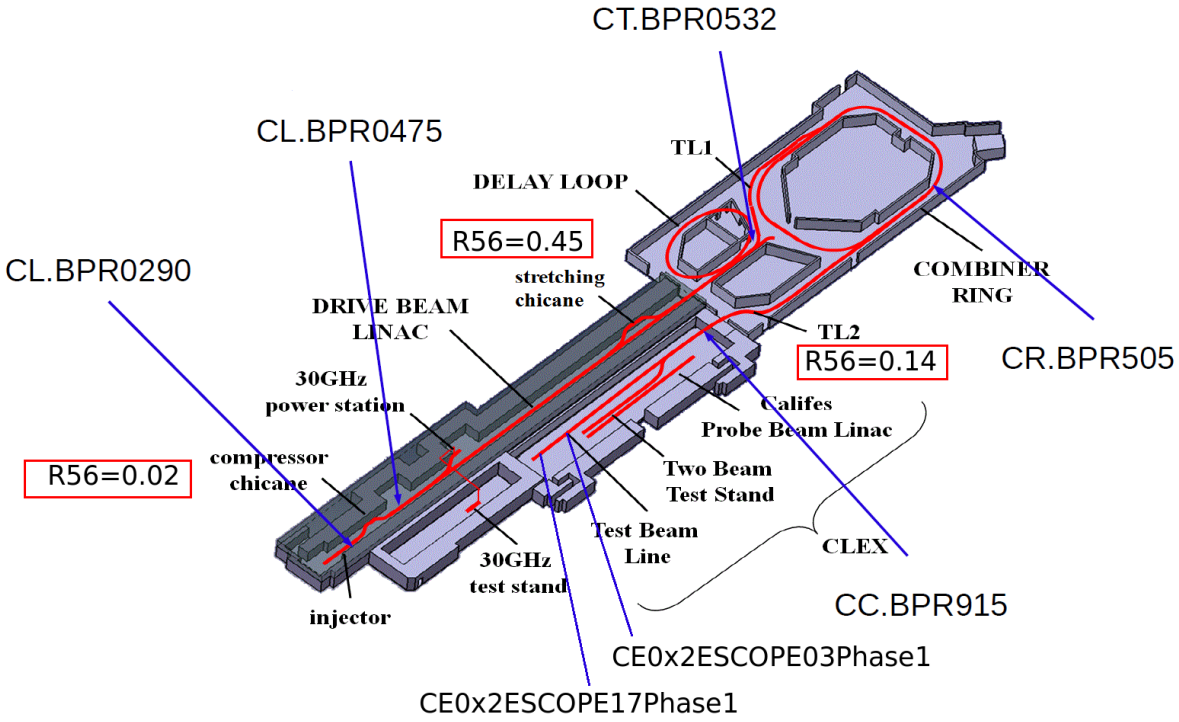

Figure 6.1: Layout of the CLIC Test Facility. The positions of the phase monitors are indicated by the blue arrows and the R_{56}-values (in meters) of the chicanes are highlighted by the red boxes.

Two monitors (CL.BPR0290 and CL.BPR0475) are installed in the CTF3 Drive Beam linac. They will be referred to as CL290 and CL475 in the following. The CT.BPR0532 monitor is installed after the Delay Loop extraction point but before the TL1 dogleg chicane, it will be referred to as CT. The CR.BPR505 is installed in the Combiner Ring and will be referred to as CR. After the beam is ejected from the Combiner Ring and passes the TL2 dogleg chicane its phase is measured by the CC.BPR915 monitor, called CC in the following. CL290, CL275, CT, CR and CC monitors are button pick-ups [90] [91]. Finally, in the Test Beam Line (TBL) two monitors measure the phase of the RF wave extracted at the PETS; these monitors will be sequentially referred to as CE03 and CE17.

By the end of 2012 two new monitors designed and produced by the Frascati National Laboratory (INFN) were installed after the stretching chicane but before the Delay Loop [92]. The signal from these monitors is not included in the presented datasets. After commissioning the Frascati monitors will provide the input signal for the feed-forward amplifier powering the phase correction kicker, which is planned to be implemented into the TL2 chicane.

The CT and CC monitors are positioned at the locations nearest to, respectively, the

measurement and the correction points of the future phase feed-forward system. For this reason the signal from these monitors is of particular importance for the feed-forward system prototype simulations presented in Sec. 6.3.

The phase measurements presented in the current section were performed on 30th November 2011 with 383 CTF3 trains. The train repetition rate of CTF3 is 0.8 Hz meaning that the measurement has been performed over about eight minutes. Other measurements performed in 2012, including the ones running over a longer period of time (about 6 hours), are consistent with the presented data set [93]. The beam was not combined in the Delay Loop and the Combiner Ring, it had a bunch frequency of 3 GHz along the whole CTF3 complex. The train length of the CTF3 Drive Beam is about 1.2 μs. The CL290, CL475 and CT phase monitors deliver 125 data points along the train, meaning that their time resolution is about 10 ns. The CR and CC monitors deliver 226 points, having a time resolution of about 5.3 ns and CE03 and CE17 monitors deliver 285 data points corresponding to 4.2 ns time resolution.

The absolute measured value of the phase is of minor importance, since it depends on the calibration zero-setting, which can be selected freely (within some range limits). Also the sign of the measurement can be selected freely and hence carries no information about the beam. The relevant information is the relative change of the phase with time, the pulse-to-pulse jitter as well as the slow changes in the average beam phase and the average train profile. These phase characteristics will be examined in the following.

Average phase of the train

Averaging the phase along each Drive Beam train leads to the distributions presented in Fig. 6.2. The measured average phase of the train is plotted as a function of the train number. The phase monitors are sorted from the top to the bottom first on the left and later on the right side of the figure corresponding to their position along the beam.

One can recognise that the phase error pattern changes significantly along the machine. The CL290 monitor has much lower resolution than the following CL475 monitor, since the pulse-to-pulse noise of CL290 is significantly higher. The phase error in both monitors lies however mainly within $\pm$ 2° at 12 GHz. The phase error increases for all following monitors, having a pulse-to-pulse jitter of $\pm$ 7° and a slower drift (on a timescale of minutes) of about 10°.

The average phase error of the trains is well correlated after the stretching chicane installed between the CL475 and CT monitors (see Fig. 6.1). Tab. 6.1 shows the correlation of the average train phase between all the monitors for the complete dataset. The absolute value of the correlation constant for the monitors after the chicane (CT and following) is consistently larger than 0.7.

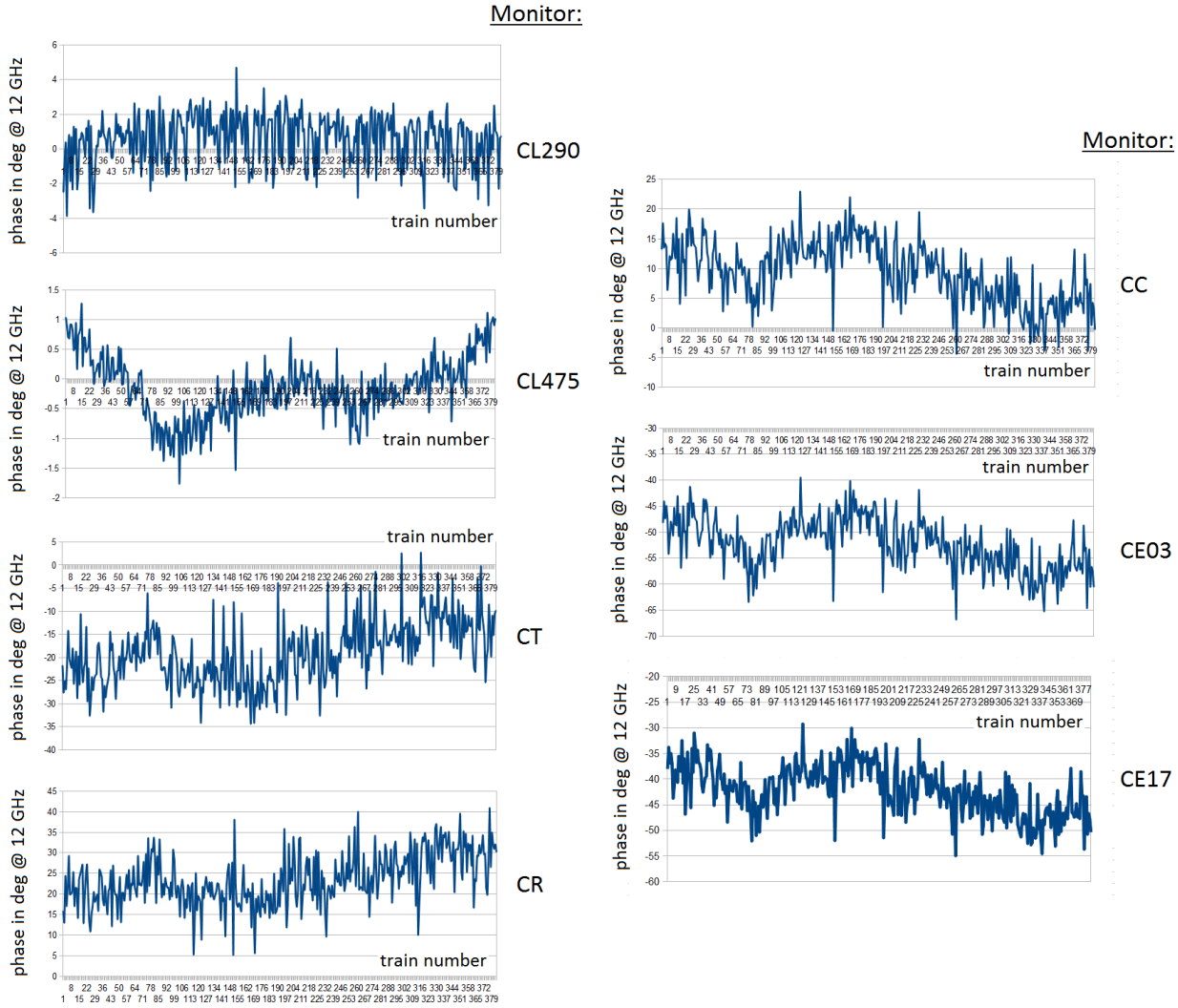

Figure 6.2: Average phase of 383 subsequent trains at CTF3 plotted against the train number for all seven phase monitors.

Average train profile

Fig. 6.3 demonstrates the measured phase profile of one train, averaged over the 383 trains from the dataset. The points on the x-axis correspond to the time resolution steps of the monitors described above. The head of the train corresponds to the higher x-values on the plots, the tail corresponds to the lower values.

The first two monitors have quite similar phase error distributions within the train (vertically mirrored). After the initial rise of the phase error from zero to a maximum the error curve is parabolically shaped with a total amplitude of over 50° at 12 GHz. The parabolic shape of the curve is caused by the operation of the pulse compressors installed at the CTF3 klystrons. This large phase error leads to an additional effort in designing the feed-forward system, since it requires the correction kicker range to be higher and the beam phase

	CL290	CL475	CT	CR	CC	CE03	CE17
CL290	1						
CL475	-0.233	1					
CT	-0.028	0.213	1				
CR	0.034	0.205	0.728	1			
CC	0.054	-0.213	-0.841	-0.802	1		
CE03	0.033	-0.127	-0.817	-0.776	0.952	1	
CE17	0.035	-0.152	-0.823	-0.779	0.955	0.996	1

Table 6.1: Correlation constants of the measured average phase error of the trains between the different monitors.

monitors being calibrated for a higher measurement range, hence reducing their resolution. However, this parabolic phase error shape within the train is of low relevance for the CLIC phase stabilisation studies, since CLIC Drive Beam klystrons are not designed to have pulse compressors and hence are not expected to have such a phase error shape.

The shape of the curve changes for the following monitors and stays consistent between them - for about the first two thirds of the train (800 ns) the phase error is comparably small (within $\pm$ 20° at 12 GHz); afterwards there is a strong phase error increase of over 100° at 12 GHz. This demonstrates that the phase error within the trains is significantly higher than the average phase variation from pulse to pulse (compare scales on the y-axis in Figs. 6.1 and 6.3), so not only an inter-train, but also an intra-train stabilisation is necessary for the system.

In order to understand the dynamics of these distributions better, one can not only calculate the average train profile, but also track the change of the sections of this profile between the different trains. For this, the train is divided into five intervals of similar length of 1200 ns / 5 = 240 ns, as shown in Fig. 6.4.

Then the standard deviation of the average phase of interval with label k ($k = \{1, 2, 3, 4, 5\}$) is calculated as:

$$\sigma_k = \sqrt{\frac{1}{383}\sum_{i=0}^{383}\left(\frac{1}{N}\sum_{j=0}^{N}\phi_{i,j} - <\phi>_k\right)^2} \tag{6.1}$$

with $\phi_{i,j}$ being the measured phase at the position j in train number i, $<\phi_k>$ being the average phase measured within the interval k, and N being the number of the time resolution steps within the interval length of 240 ns (N=25 for CL290 and CL475 monitors, N=45 for CT, CR and CC monitors and N=57 for CE03 and CE17 monitors).

Calculating $\sigma_{interval}$ for each of the five intervals leads to the value presented in Tab. 6.2. The table shows that the centre of the train (intervals 2, 3 and 4) deviates more from its average position than the head (interval 5) and the tail (interval 1) of the train. The

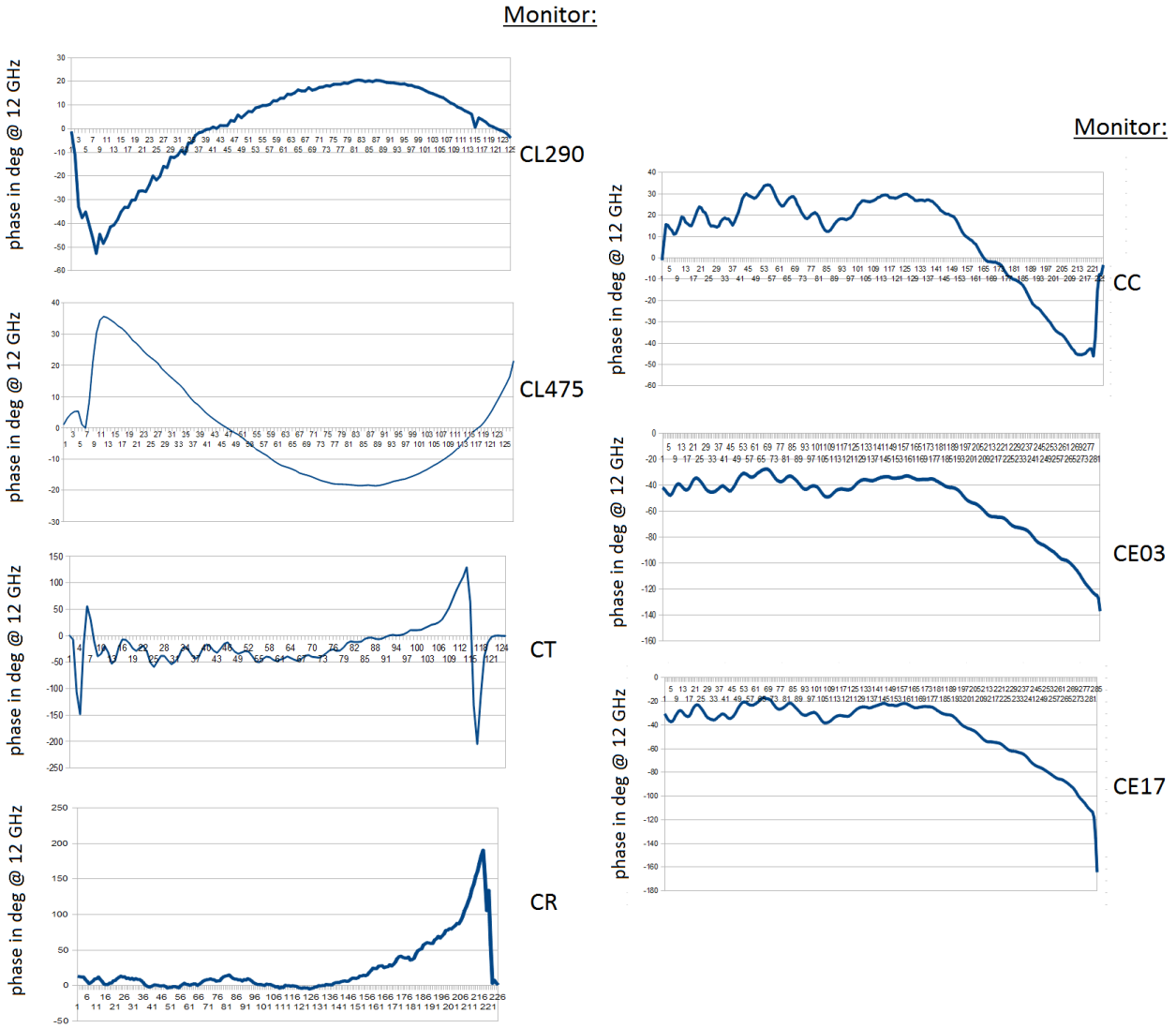

Figure 6.3: Phase profile of CTF3 train, averaged over 383 subsequent trains. Each point on the x-axis represents a resolution point, full train length on the x-axis is about 1.2 μm.

deviation of the whole train average is typically slightly smaller than the deviation of the intervals, which means that the change of the phase error in the intervals is to some extent in opposite directions and hence it is partially compensating for the average phase.

6.2 Determination of phase error sources

As Fig. 6.2 and Tab. 6.2 demonstrate, the phase error significantly increases between the CL475 and CT monitors. Since the beam is not combined and hence does not pass the Delay Loop, there is only one lattice element between CL475 and CT monitors that can significantly impact the phase error - the Frascati stretching chicane. This chicane has an R_{56} value of 0.45 m and hence transforms beam energy error into the phase error.

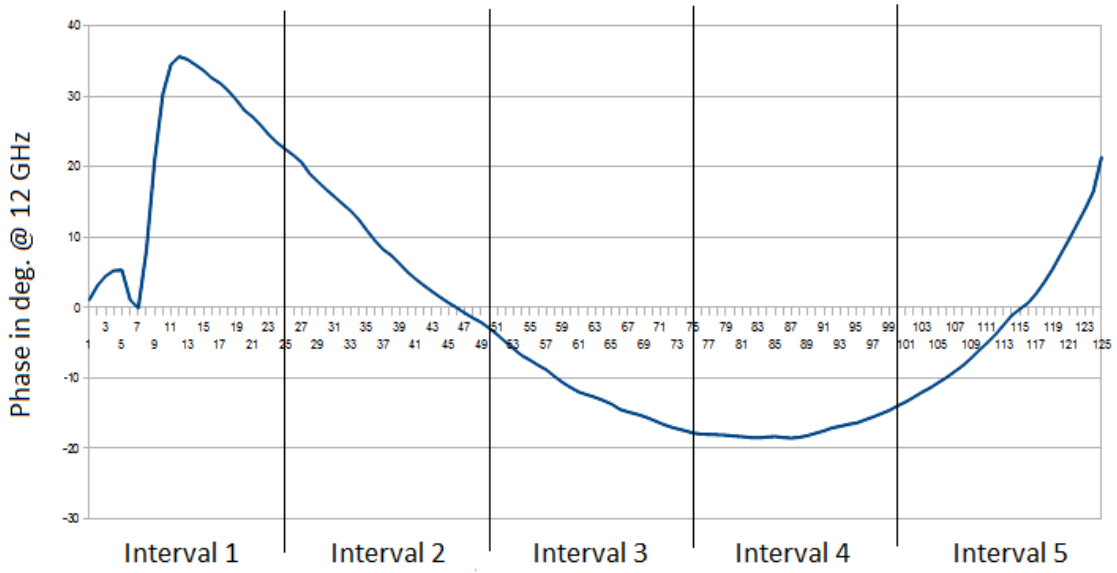

Figure 6.4: Phase profile along the average train measured at CL475 monitor, divided in five equal intervals.

Monitor	Interval 1	Interval 2	Interval 3	Interval 4	Interval 5	Whole train
CL290	1.24	1.39	2.21	2.4	1.74	**1.45**
CL475	0.52	0.62	0.62	0.64	0.65	**0.52**
CT	9.77	10.06	10.09	5.47	4.46	**6.77**
CR	6.75	7.31	6.93	8.06	8.96	**6.31**
CC	4.62	7.08	7.49	6.77	4.19	**5.25**
CE03	4.59	6.06	6.83	6.46	5.31	**5.00**
CE17	4.88	6.22	7.12	6.79	4.53	**4.90**
All monitors	**4.85**	**5.46**	**6.35**	**6.64**	**5.79**	**4.93**

Table 6.2: Phase standard deviation in degrees at 12 GHz. The train is divided into five equal intervals, each about 0.24 μs long, with interval 1 being at the tail and interval 5 at the head of the train.

The phase error measured after the stretching chicane at the CT monitor has several possible components with different origin. These components are:

- Phase monitor noise.
- The phase error present before the stretching chicane and directly transmitted downstream of the chicane.
- The beam phase error in the linac leads to errors in the acceleration and, consecutively, to the beam energy errors. The energy error is transformed into the phase error at the chicane.
- Linac klystrons operate with phase or amplitude errors. These errors generate beam

energy error, which is transformed into the phase error at the chicane.

6.2.1 Possible source of additional phase error introduced in the stretching chicane

The estimation of the contribution of each component to the phase error at the CT monitor is presented in the following section. In order to conduct such estimation a second measurement was performed in November 2012. In addition to the phase measurement along the beam presented in the previous subsection the dispersive beam energy measurement was performed and the amplitude and phase data of the CTF3 linac klystrons were collected. Also, the design of the stretching chicane was modified, so that additionally to the nominal R_{56} value of 0.45 m also the values of 0.2 m and 0.0 m could be implemented [94]. The measurement was performed twice for each setting of R_{56} for approx. 10 minutes, with the sequence of the R_{56} settings being (in meters) $0.0 \rightarrow 0.2 \rightarrow 0.45 \rightarrow 0.2 \rightarrow 0.0 \rightarrow 0.45$. The first three of these measurements will be referred to as first dataset in the following, the last three will be labeled as the second dataset. The total time span for all six measurements amounted to several hours.

The RMS of the phase error measured at the first four monitors for the dataset from November 2012 is plotted in Fig. 6.5. Similarly to the previous measurements, one can see the strong increase of the phase error (by about a factor of 10) between the CL475 and CT monitors for the datasets with $R_{56} = 0.45$ m. The increase is lower when the R_{56} value is set to 0.2 m and there is no significant phase error increase for $R_{56} = 0.0$ m. This means that the directly transmitted beam phase error from the linac and the monitor noise contribute to less than 2° at 12 GHz phase error measurement at the CT monitor.

The measured phase error significantly increases at the next monitor, CR, for all datasets. The examination of the noise structure leads to the conclusion that this error increase can be explained by an additional random noise with standard deviation of 7.67° at 12 GHz, which is independent of the R_{56} setting in the stretching chicane [90]. The cause of this noise is probably poor monitor resolution, however other possible sources such as jitter of the Combiner Ring magnets, errors in the deflectors and non-zero R_{56} value of the Combiner Ring are under examination [93].

The phase error train profiles before and after the chicane are presented in Fig. 6.6 (data from the second dataset). The displayed diagrams show the average measured value of the train phase at the given position within the train, with the RMS of the variation plotted as an error bar at this position. The plots of the data from the CL475 monitor, positioned before the chicane, are displayed at the top of the figure; the plots of the CT monitor measurement, positioned immediately after the chicane, are displayed at the bottom of the figure. For a setting of $R_{56} = 0.45$ m one can observe a larger beam phase variation at any point along the train after the chicane. For the $R_{56} = 0.0$ m setting the standard deviation of the beam within the train remains the same after the beam passes the chicane. Also, as it has already

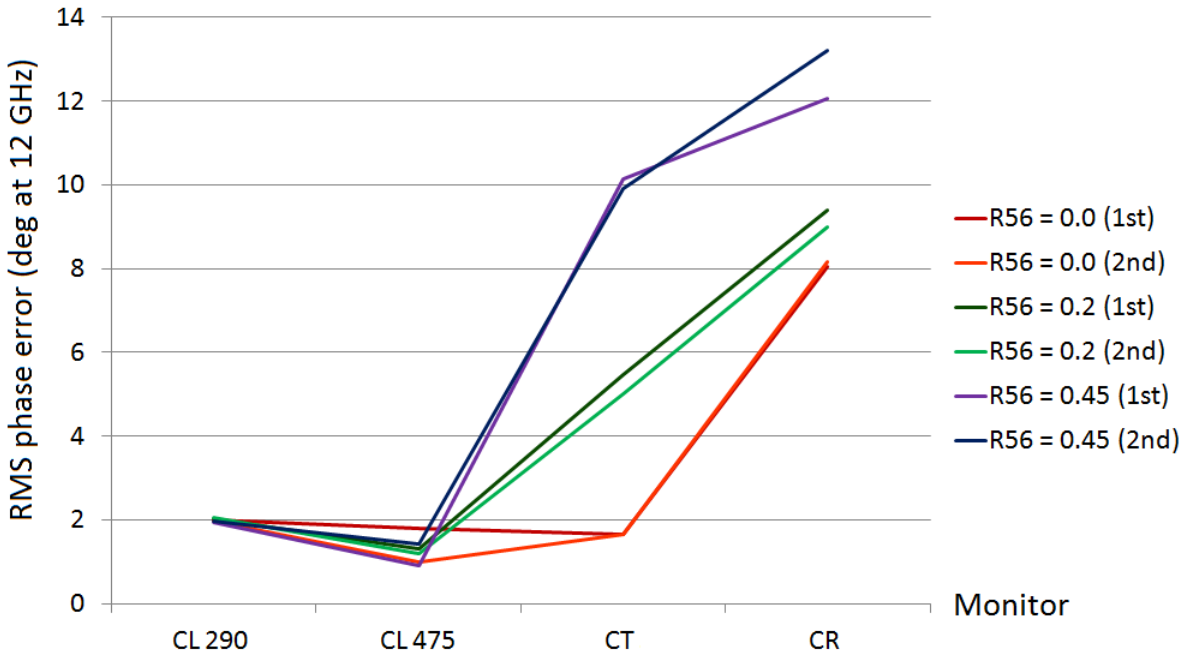

Figure 6.5: Average phase error measured at first four monitors at CTF3 with different R_{56} settings of the stretching chicane for the first and the second datasets.

been shown in Fig. 6.3, a significant change of the phase profile shape can be observed in the case of $R_{56} = 0.45$ m.

The measurement data show that a large proportion of the phase error is generated in the stretching chicane. Subtracting the phase error measured before the chicane σ_ϕ(CL475) from the error after the chicane σ_ϕ(CT) yields the additional error introduced in the chicane. This error can be divided by the R_{56} value in order to investigate the impact of the chicane on the beam phase. The result of such calculation is presented in Tab. 6.3.

R_{56}	σ_ϕ(CL475)	σ_ϕ(CT)	σ_ϕ(CT) - σ_ϕ(CL475)	(σ_ϕ(CT) - σ_ϕ(CL475)) / R_{56}
0 (dataset 1)	1.80	1.65	-0.15	
0.2 (dataset 1)	1.31	5.47	4.16	20.80
0.45 (dataset 1)	0.90	10.13	9.23	20.51
0 (dataset 2)	0.98	1.65	0.67	
0.2 (dataset 2)	1.18	5.02	3.84	19.20
0.45 (dataset 2)	1.41	9.91	8.50	18.89

Table 6.3: The phase error at the monitors CL475 and CT (in deg at 12 GHz) depending on the R_{56} setting of the stretching chicane (in m).

The table demonstrates that in both datasets for the non-zero R_{56} settings the additional error in the chicane is proportional to the chicane's R_{56} setting. This leads to the hypothesis that the dominant portion of the phase error increase between the monitors CL475 and CT is caused by beam energy error that is transformed into phase error at the chicane. A detailed

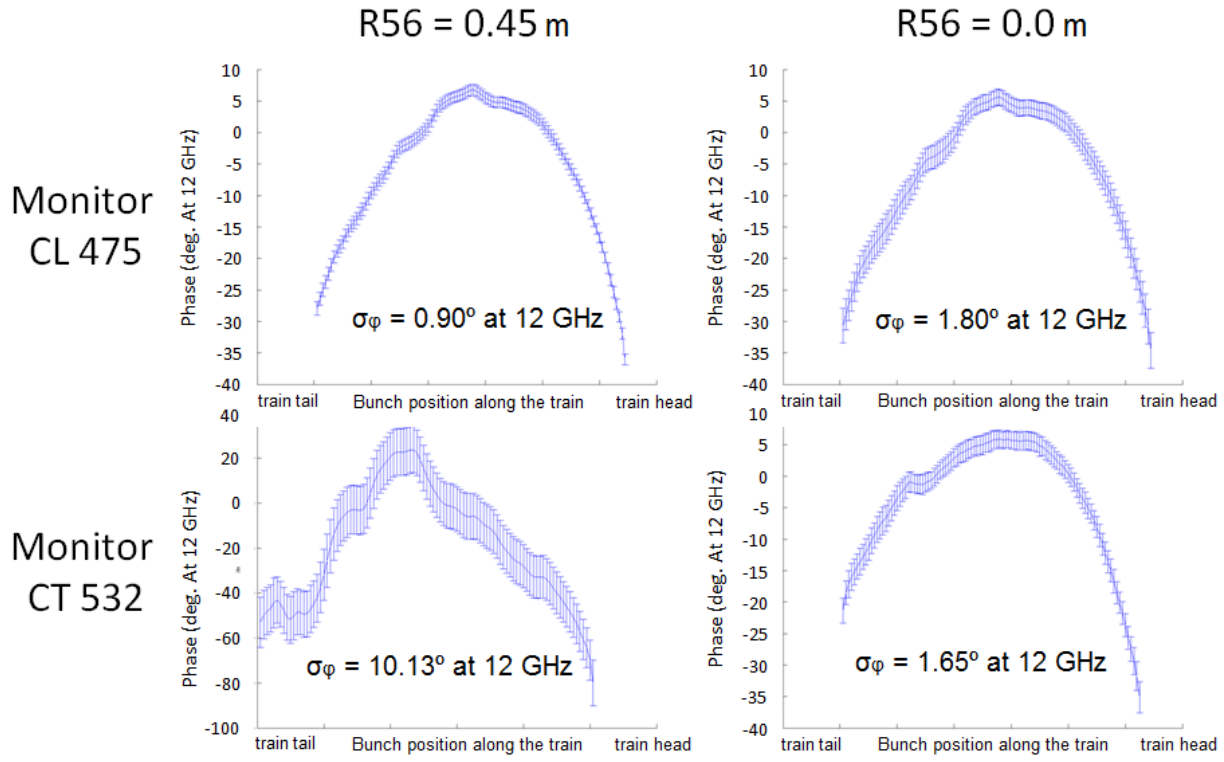

Figure 6.6: Plot of the CTF3 trains' RMS phase profile before (top) and after (bottom) the chicane for the second dataset with $R_{56} = 0.45$ m (left) and $R_{56} = 0.0$ m (right) [93].

test of this hypothesis is presented in the next section.

6.2.2 Beam energy after the CTF3 linac

The energy of the beam can be measured directly via a dispersion measurement at one of the magnets along the Drive Beam. The nearest measurement point to the stretching chicane and to the CT phase monitor is the TL1 dog-leg chicane with the BPI0608 monitor. The horizontal signal of this monitor is proportional to the energy error of the beam.

The phase error change in the chicane is plotted against the energy error measured by the BPI0608 monitor in Fig. 6.7 for the first and second datasets on the top and the bottom of the figure, respectively. A clear correlation in the distribution is visible; the correlation constant is approx. -0.8 for both datasets. This high correlation supports the hypothesis that the additional phase error is caused by the energy error present at the end of the CTF3 Drive Beam linac.

The additional phase error introduced in the chicane is on average 9.23° at 12 GHz (=640 μm) for the first dataset and 8.50° at 12 GHz (=590 μm) for the second dataset, respectively. Considering the R_{56} value of the stretching chicane to be 0.45 m, these phase

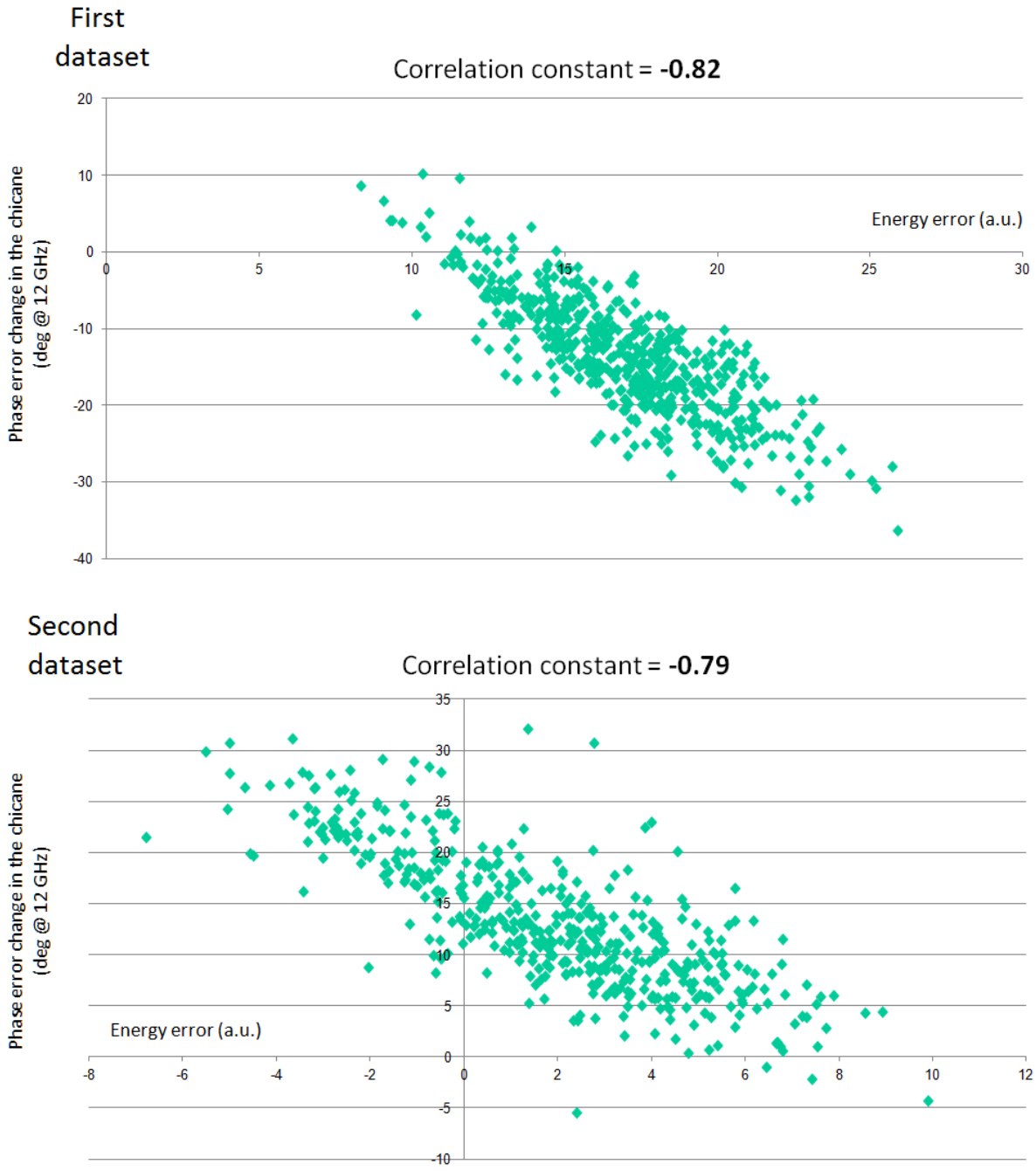

Figure 6.7: Scatter plot of the phase error change in the chicane vs. the dispersive energy measurement in the transfer line (BPI0608 monitor) for the first (top) and second (bottom) datasets with $R_{56} = 0.45\ m$.

errors could be caused by RMS energy errors of 0.14% for the first dataset and 0.13% for the second dataset, respectively. Unfortunately, a calibration of the dispersive phase measurement was not possible with the setting of the monitor for the current datasets. If the possibility of calibrated energy measurements at the TL1 dog-leg chicane would arise, it could be useful to verify the consistency between the energy variation measurement and

the calculated energy variation from the additional phase error introduced in the stretching chicane.

6.2.3 Phase error in the linac

One of the possible sources of the measured energy error at the TL1 chicane is the beam phase error in the Drive Beam linac. Bunches entering the accelerating cavities with erratic longitudinal position are not at the location of the nominal gradient in the accelerating RF wave. Hence, these bunches receive an energy error during the acceleration process.

In order to investigate the impact of this effect, the energy error measured at the BPI0608 monitor has been correlated with the phase measurement data from the CL475 phase monitor, which is positioned in the linac (Fig. 6.8). The CL475 monitor has been selected for this purpose, since compared with the CL290 monitor it shows a smaller pulse-to-pulse error and overall error (see Fig. 6.2), leading to the assumption that its background monitor noise is lower. The correlation plot for the second dataset (bottom) in Fig. 6.8 displays a significant correlation. For the first dataset (top) the correlation constant value is, however, rather low.

Additionally, the phase error in the linac can be set in correlation with the additional phase error at the chicane. The correlation plots for the first and second datasets are displayed in Fig. 6.9 top and bottom, respectively. The correlation values are similar to the ones presented in Fig. 6.8, being slightly higher, possibly because of the better relative resolution of the phase measurement compared with the dispersive energy measurement. One can also clearly recognise that the slope of the correlation is larger than one, implying that there is a significant amplification of the phase noise at the stretching chicane occurring.

The displayed correlations between the phase error in the linac and the beam energy error, as well as with the phase error change in the chicane, are not sufficient to explain the origin of the latter two errors to the full amount. Consequently, additional energy error sources are investigated in the following subsection.

6.2.4 Klystron amplitude and phase errors

Impact of klystron amplitude errors on the beam energy

Another possible source of the beam energy error is the erratic amplitude and phase of the accelerating klystrons in the CTF3 Drive Beam linac. The data for the klystrons have been collected and the correlations with the measured beam phase and the additional phase error in the chicane are presented in the current subsection.

Fig. 6.10 presents the correlation of the klystron amplitude with the beam phase error change in the chicane and the beam energy for the first (top) and the second (bottom)

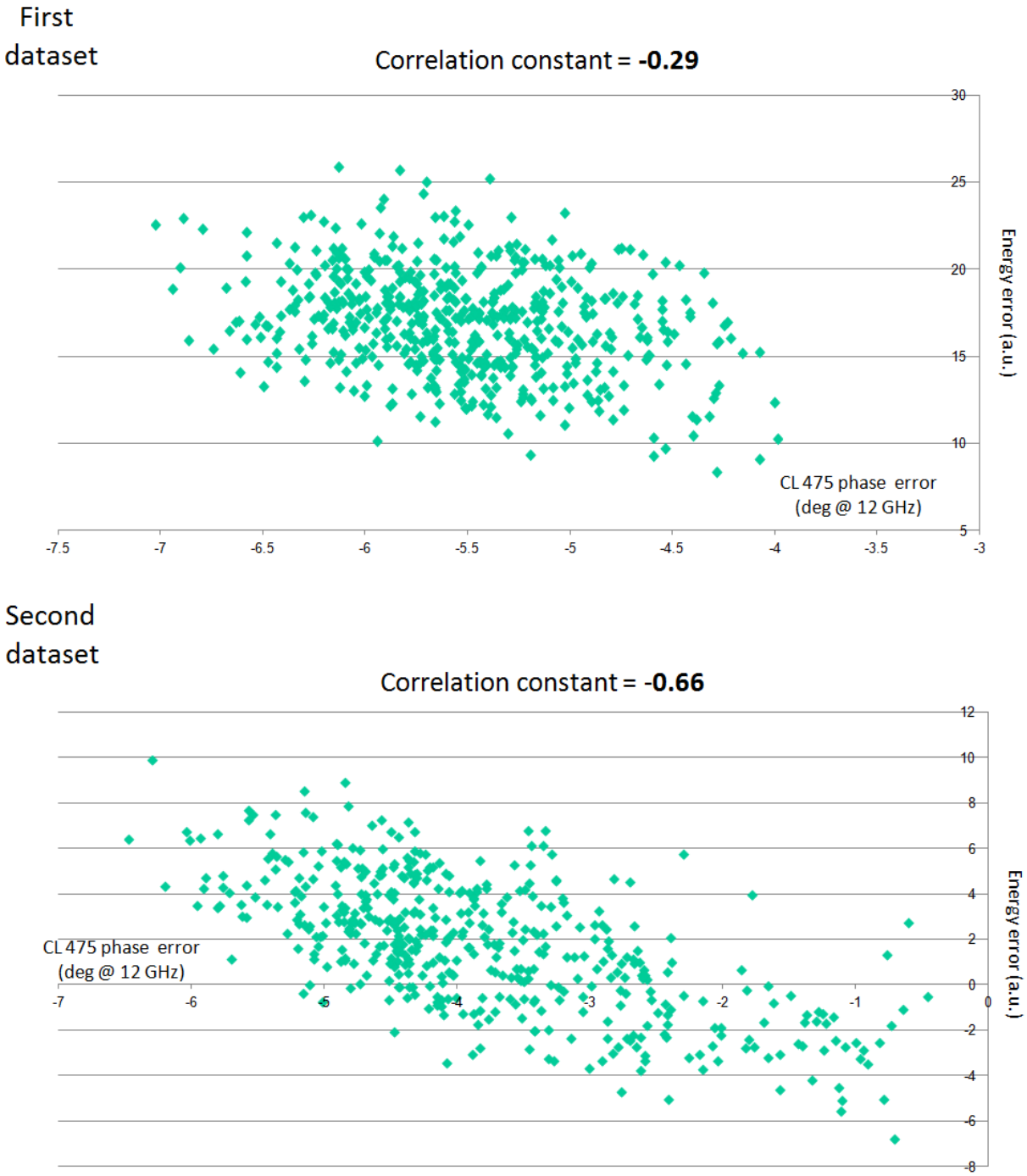

Figure 6.8: Scatter plot of the beam energy vs. the incoming phase error measured at CL475 monitor for the first (top) and second (bottom) datasets with $R_{56} = 0.45$ m.

datasets. The klystron names are plotted on the x-axis, going downstream from left to right along the CTF3 Drive Beam linac. The correlation constant is plotted on the y-axis for each klystron individually.

The correlation constant absolute value is comparably small, below 0.3 for all of the

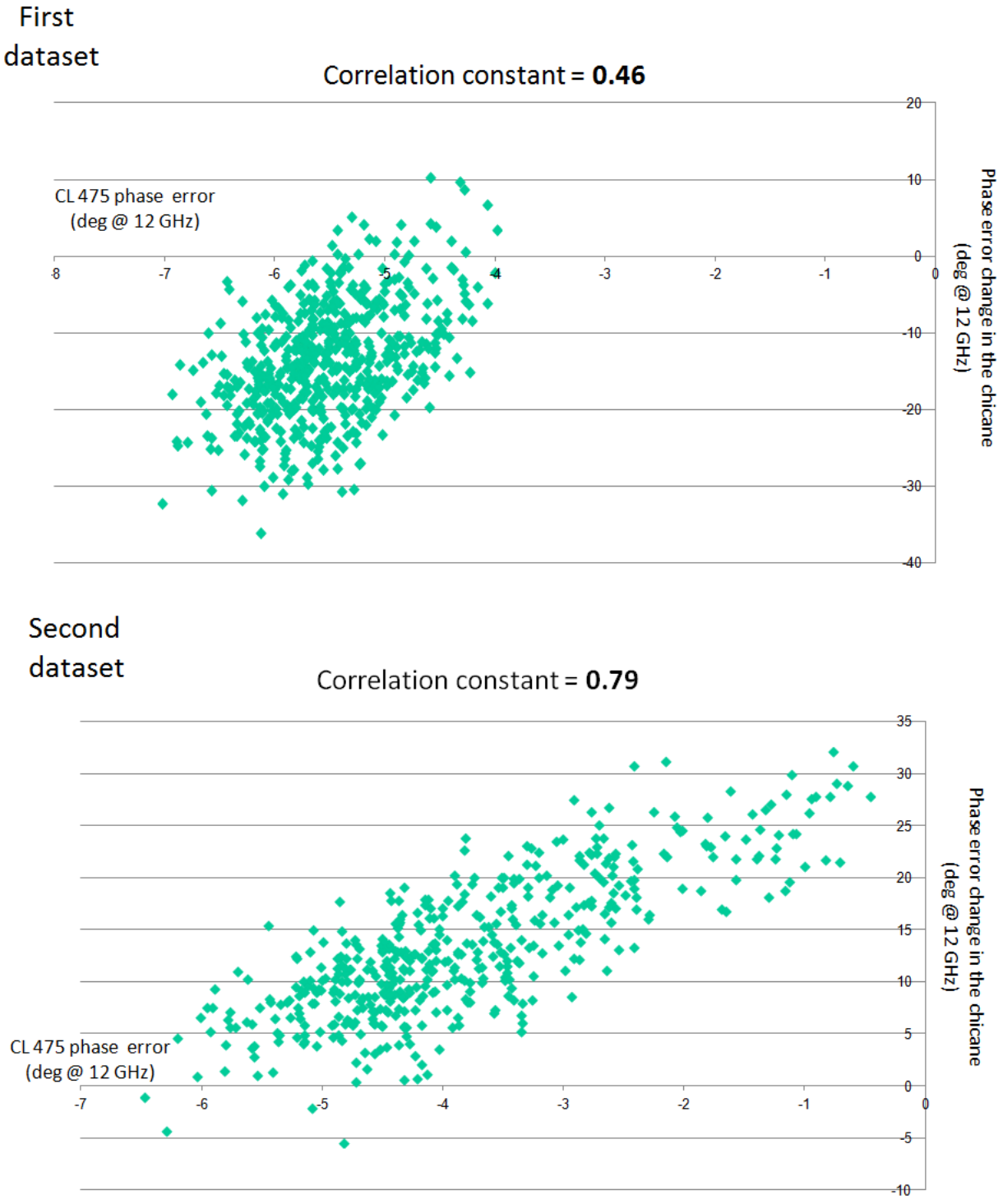

Figure 6.9: Scatter plot of the phase error change in the chicane vs. the incoming phase error measured at CL475 monitor for the first (top) and second (bottom) datasets with $R_{56} = 0.45$ m.

klystrons. This leads to the conclusion that the klystron amplitude jitter does not affect the beam energy and the additional beam phase error in the chicane significantly.

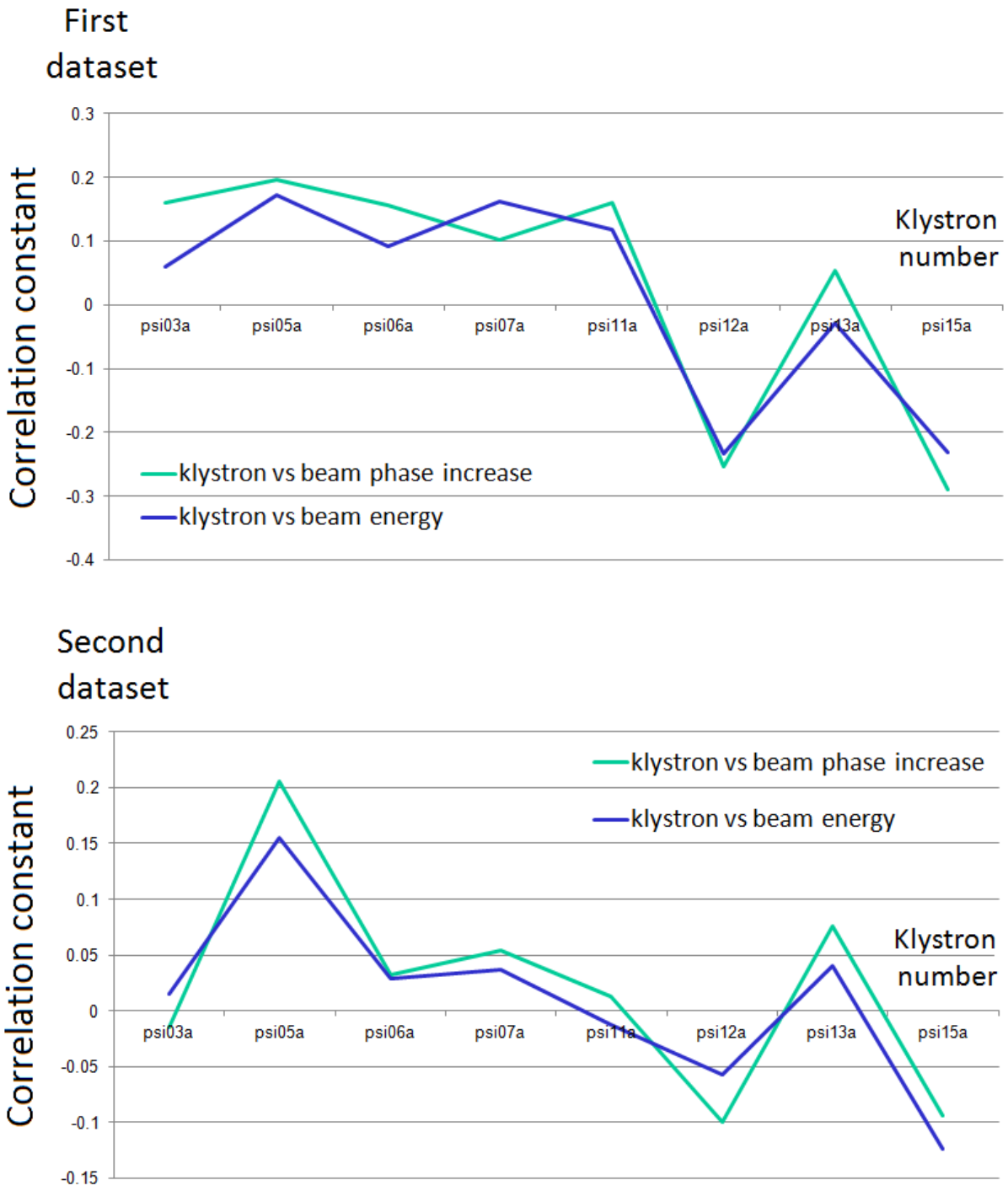

Figure 6.10: Correlation between phase error change in the chicane and klystron amplitude error for the first (top) and second (bottom) dataset with $R_{56} = 0.45$ m.

The shape of the curves for the correlation with the beam phase error increase in the chicane (light blue) and with the beam energy error (dark blue) is similar, which is consistent with the hypothesis of the additional phase error being caused by the beam energy error.

The calculation of the quadratic sum of the correlation constants of all klystron amplitude measurements of the first dataset with the beam phase error increase yields the value of 0.53 and with the beam energy error the value of 0.44. For the second dataset the values are 0.27 and 0.22 respectively (summarised in Tab. 6.4). These values can be considered as the cumulative correlation of all klystron amplitude errors with the beam phase error increase and beam energy error. They signify how strongly the amplitude jitter of all klystrons impacts the beam in total. This value does not consider, however, the correlations between the klystron amplitude datasets and hence is only of relevance if these correlations are sufficiently small.

Impact of klystron phase errors on the beam energy

A correlation of the measured klystron phase with the beam phase error increase and the beam energy error is presented in Fig. 6.11. In this case, however, there is a significant correlation of the phase of the first two klystrons with the stated beam parameters for both datasets. This correlation shows that the phase jitter of the first two klystrons is responsible for a significant portion of the energy error.

The shape of the curves for the phase correlation with the beam phase error increase in the chicane and with the beam energy error is similar.

The RMS error of the klystron phase jitter is comparable for all of the klystrons, being within a relative factor of two. Consequently, the fact that the beam energy is very sensitive to the klystron phase variation of only the first two klystrons is not induced by these two klystrons having a particularly large phase error.

Klystron data	beam phase error increase	beam energy
Amplitude (dataset 1)	0.53	0.44
Amplitude (dataset 2)	0.27	0.22
Phase (dataset 1)	0.93	0.77
Phase (dataset 2)	0.86	0.78

Table 6.4: Quadratic sums of correlation constants of the klystron phase and amplitude data with the phase error increase in the stretching chicane and the measured beam energy.

Calculating the quadratic sum of the correlation constants of klystron phase, as in the klystron amplitude case, yields 0.93 for the phase error increase and 0.77 for the beam energy error for the first dataset (see Tab. 6.4) and 0.86 and 0.78 respectively for the second dataset. These values are considerably higher than the values of the klystron amplitude correlation and they imply that the beam energy error, as well as the phase error, increase at the chicane is strongly impacted by the klystron phase jitter. The correlation of the measured phase between the klystrons is rather small, being maximally 0.3 and having an average value of 0.16.

It is interesting to note that the cumulative correlation of klystron phase with the stated

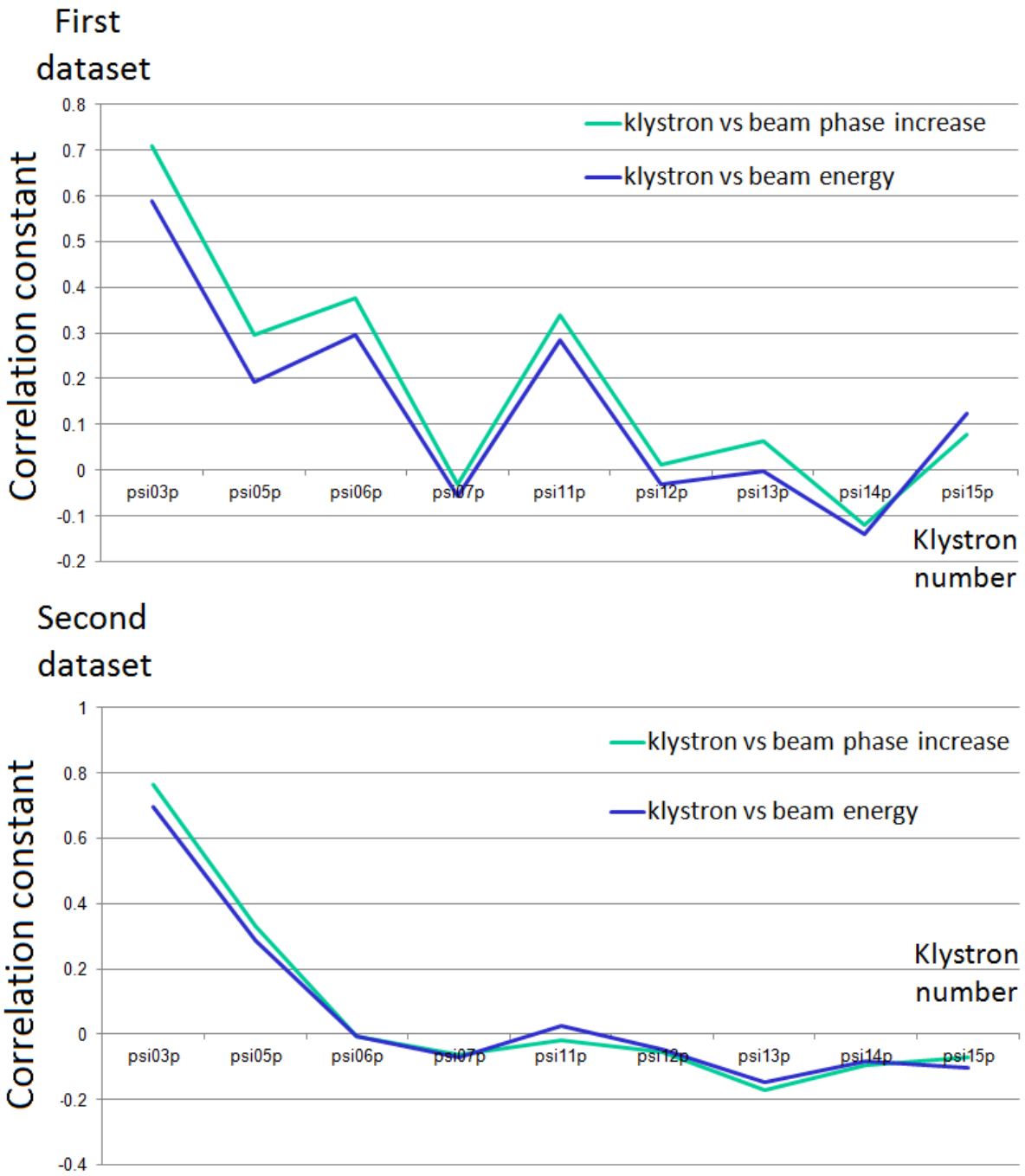

Figure 6.11: Correlation between phase error change in the chicane and klystron phase error for the first (top) and the second (bottom) datasets with $R_{56} = 0.45$ m.

beam parameters is higher for the first dataset, for which the correlation of initial beam phase error with the energy is lower (see Figs. 6.8 and 6.9). This can mean that the beam energy error is caused in the linac by both the beam phase error and the klystron phase error and, depending on the measurement time and the machine settings, each of the parameters can be more or less dominant in influencing the energy of the outgoing beam. Additional measurements should be performed in order to verify this possible conclusion.

Impact of the klystron phase error on the beam phase

A possible explanation for a particular sensitivity of the beam energy to the errors of the first two klystrons is the fact that the first two klystrons are responsible for the bunching of the beam. The phase errors in these klystrons hence could lead directly to phase error of the beam, which has, as a consequence, an energy error when it leaves the linac.

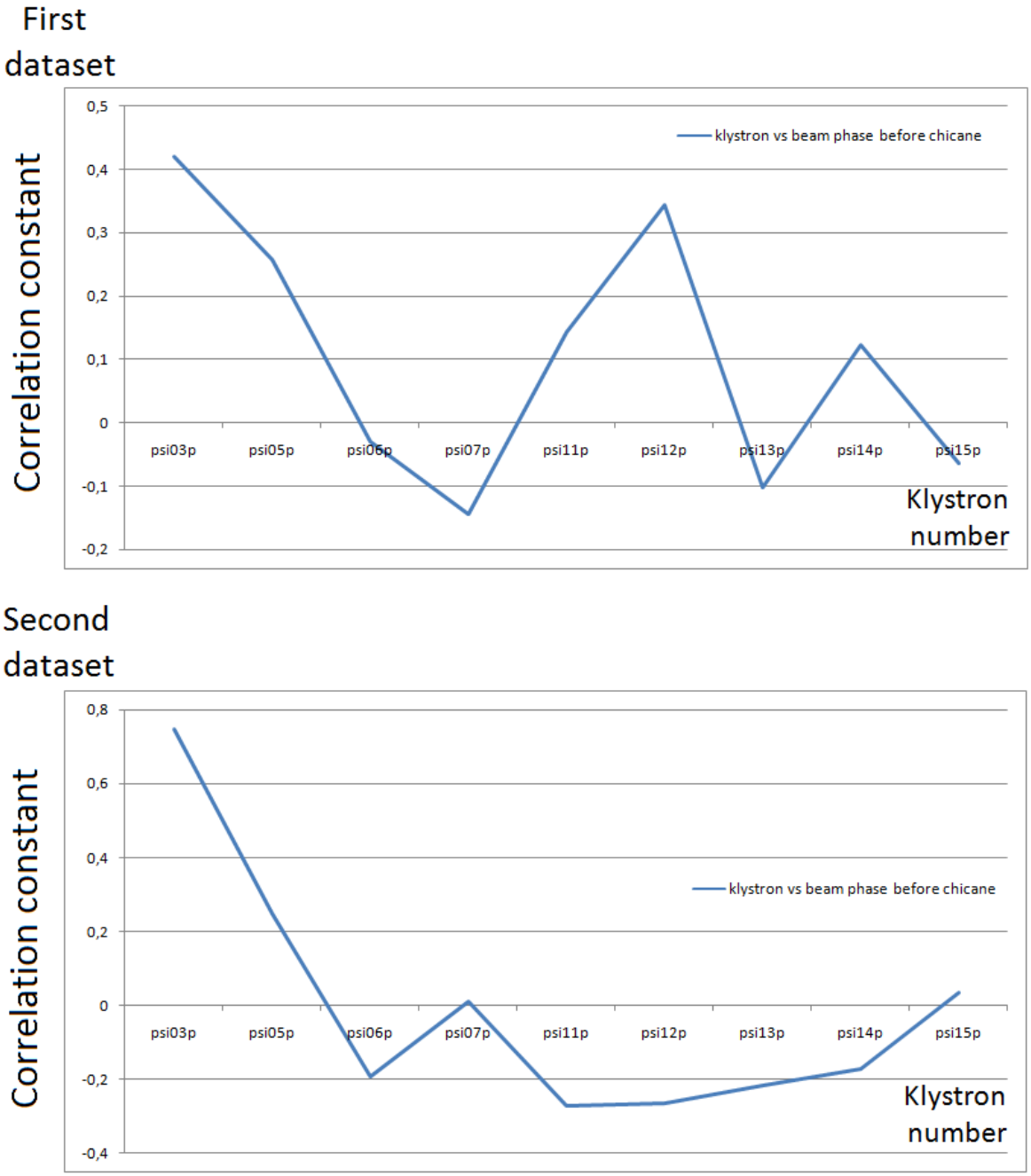

Figure 6.12: Correlation between phase error before the stretching chicane (monitor CL475) and klystron phase error for the first (top) and the second (bottom) datasets with $R_{56} = 0.45$ m.

This hypothesis is confirmed by the plots displayed in Fig. 6.12, which shows show the correlation of each klystron phase with the beam phase measured at the CL475 monitor, which is positioned at the end of the linac but before the stretching chicane, for the first (top) and the second (bottom) datasets. The displayed correlation is significant for the first two klystrons; the shape of the correlation curve is generally similar to the curve representing the correlations of the klystron phase with the beam energy in Fig. 6.11. The curves are, however, not identical even within the monitors' resolution, meaning that though the identified error sources are responsible for a significant portion of the beam energy error and the phase error increase in the chicane, the mechanism of action of these error sources is not direct. The measurements rather indicate that the phase jitter of the first two klystrons is influencing the phase and energy simultaneously, with beam phase error leading to further beam energy error in the linac. This energy error is then transformed into additional beam phase error in the stretching chicane.

6.3 Phase stabilisation system prototype for CTF3

A prototype of the phase correction system is currently in development and is planned to be installed at CTF3 in the second half of 2013. Two systems have been considered for the correction of the beam phase - a feedback system correcting the average phase error of the train and a feed-forward system for the intra-train phase correction. The dataset used for the simulation is the result of the measurement of 383 CTF3 trains on 30 November 2011 already analysed in Sec. 6.1.

A theoretical description of the functionality of feedback and feed-forward systems has been presented in Sec. 3.2 and 3.3. The current section summarises the performed studies that estimate the effect of these two stabilisation systems on the CTF3 beam phase error and to predict the resulting correction factor.

6.3.1 Performance simulation of phase feedback correction

The feedback correction simulation uses the average phase of the train measured at the TL2 dog-leg chicane and corrects the deviation of this average phase from the nominal value on the next train at the same position (TL2 chicane). As a first order approximation it is assumed that the amplifier and the electromagnetic kicker do not induce any additional noise.

The standard deviation of the average phase of the train over a period of measurement is considered as a figure of merit. It is defined as

$$\sigma_\phi = \sqrt{\frac{1}{M}\sum_{m=1}^{M}(\phi_{train,m} - <\phi_{train}>)^2} \tag{6.2}$$

with $M = 383$ being the number of trains and

$$\phi_{train,m} = \frac{1}{N}\sum_{n=1}^{N}\phi_n \tag{6.3}$$

being the average phase within the train m, where N is the number of the bunches per train and ϕ_n the measured phase of the bunch. $< \phi_{train} >$ is the average phase of all trains. It is not possible to measure the phase of each bunch individually, so the time resolution steps are of a length of approx. 10 ns. The feedback is calculated by

$$(\phi_{train,fb})_m = (\phi_{train})_m - a \cdot (\phi_{train})_{m-1} \tag{6.4}$$

with a being the feedback gain parameter. The optimal gain parameter is proportional to the quotient of the RMS errors at the point of measurement (σ_{meas}) and correction (σ_{corr}) as well as to the correlation constant between the measurement and correction data ($\rho_{meas,corr}$) (see section 5.1.4 in [79]):

$$a = \frac{\sigma_{corr}}{\sigma_{meas}} \cdot \rho_{meas,corr} \tag{6.5}$$

Since in the case of a feedback system the measurement and correction are performed very close to each other, the RMS error of the beam phase can be considered as equal at the locations of the measurement and the correction. The correction is performed on the train following the one at which the error has been measured, hence the correlation constant $\rho_{meas,corr}$ is calculated between the RMS phase errors of two subsequent trains. In the case of the presented measurements the $\rho_{meas,corr}$ constant is 0.61, so in addition to calculating the simple one-to-one feedback with a=1, the calculation with a=0.61 has been performed (see Fig. 6.13).

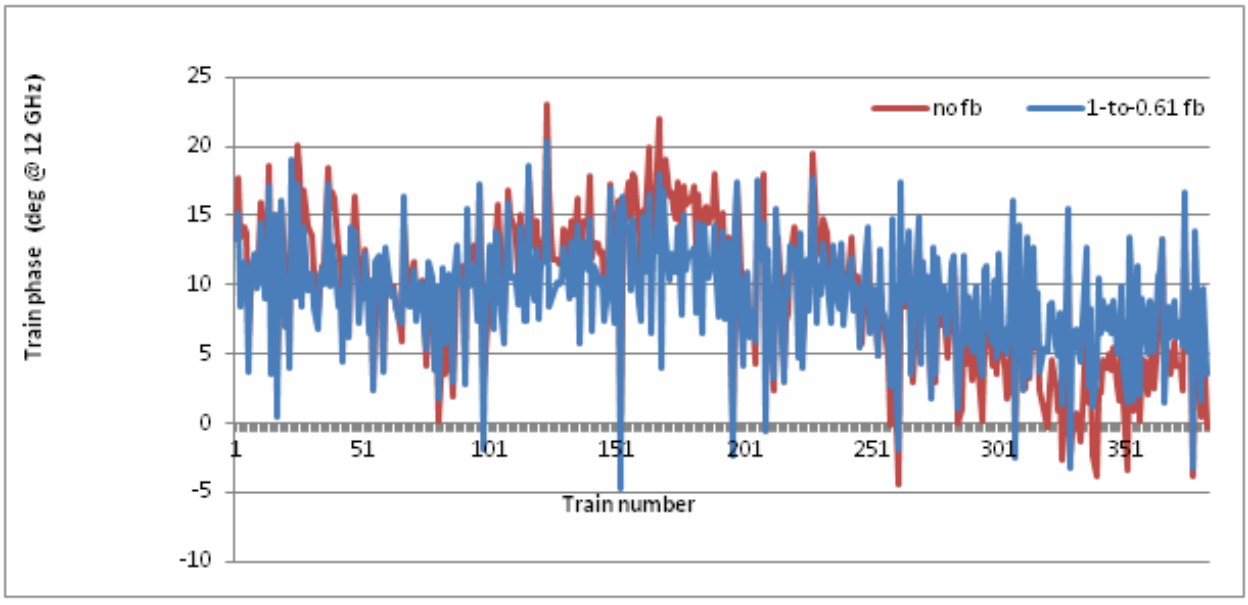

Figure 6.13: Train mean phase with and without feedback.

Tab. 6.5 demonstrates the result for the standard deviation of the average train phase σ_ϕ. The feedback has in total a stabilising impact on the beam and the best correction value is delivered by the gain factor $a = 0.61$. The correction factor between the system with and without feedback is, however, not particularly high - the average error is reduced by 1.11° at 12 GHz or 21% of the original error. Since the pulse-to-pulse jitter and hence the assumed resolution of the phase monitors lies in the order of 1-2° at 12 GHz (see Sec. 6.1), the measurement of the improvement provided by a potential phase feedback system at CTF3 correcting the average train phase would be rather difficult. It could become a feasible option though with the new phase monitors [92], if they satisfy their design specification of phase measurement resolution of 0.1° at 12 GHz.

Feedback type	σ_ϕ in degrees at 12 GHz
No feedback	5.25
1-to-1 feedback	4.59
1-to-0.61 feedback	4.14

Table 6.5: Standard deviation of the average train phase with and without feedback.

6.3.2 Performance simulation of CTF3 feed-forward phase correction system

Feed-forward system design

The phase stabilisation feed-forward system at CTF3 is designed in the following way - it should perform the phase measurement before the Combiner Ring at the Transfer Line 1 (TL1) chicane and send the signal to the amplifier, which will activate the kickers and correct the beam in the Transfer Line 2 (TL2) chicane (see Fig. 6.1 and the scheme in Fig. 6.14).

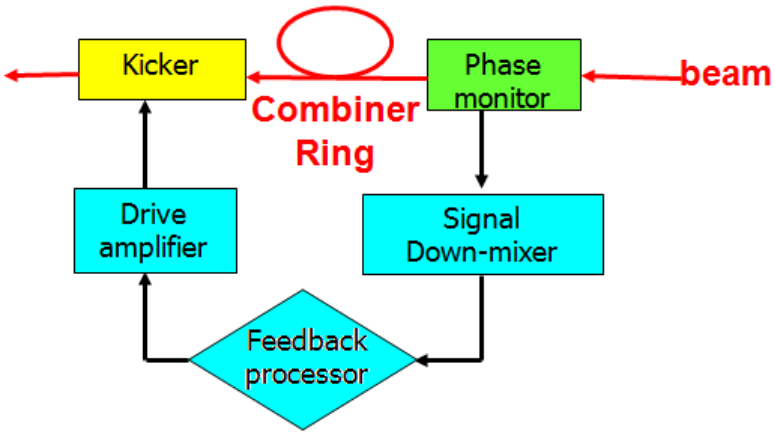

Figure 6.14: Scheme of phase feed-forward system modules [59].

The design of the chicane is different for CTF3 and CLIC: since at CTF3 there is not enough space for a full chicane with four electromagnetic kickers, the correction system is planned to be integrated into the TL2 chicane (see Fig. 6.15) [59].

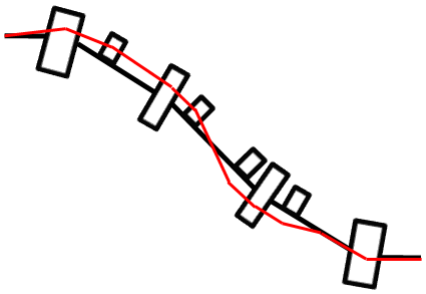

Figure 6.15: Depiction of the beam trajectory in TL2 chicane bent by the feed-forward kickers [59].

The bunches need about 380 ns to propagate from TL1 to TL2, hence this defines the latency of all the components of a feed-forward system. It is possible, if necessary, to increase this time by circulating the bunches in the Combiner Ring. The demonstration of the phase correction will initially be performed on the non-combined beam with 3 GHz bunch frequency and a train length of 280 ns. The eventual goal is to be able to correct the combined beam of 12 GHz bunch frequency. The system should be usable up to a train length of 420 ns.

The bandwidth of the amplifier is planned to be about 50 MHz with an eventual target of 70 MHz for future designs. The 960 mm electrodes of the electromagnetic kicker with an aperture of 40 mm should provide a kick range of ± 1.2 kV and a beam trajectory angle kick of up to ± 1 mrad and hence a maximal phase correction of ± 17° at 12 GHz [59] with the current amplifier design.

Simulation methods and results

Since the feed-forward is an intra-train correction, it is useful to define the following standard deviation as a figure of merit:

$$\sigma_\phi = \sqrt{\frac{1}{M \cdot N} \sum_{m=1}^{M} \sum_{n=1}^{N} (\phi_{mn} - < \phi >)^2} \tag{6.6}$$

with M being the number of the trains and N being the number of the 10 ns time resolution steps within the train, as previously defined. ϕ_{mn} represents the measured phase of the train m at the position n within the train and $< \phi >$ is the average measured phase of all trains defined as

$$< \phi >= \frac{1}{M \cdot N} \sum_{m=1}^{M} \sum_{n=1}^{N} \phi_{mn}. \tag{6.7}$$

The feed-forward is calculated with

$$\phi_{mn,ff} = \phi_{mn} - \frac{1}{t_{rise}} \sum_{i=n-t_{rise}/2}^{n+t_{rise}/2} a \cdot \phi_{mi} \tag{6.8}$$

with t_{rise} being the rise time of the feed-forward system. The bandwidth of the amplifier prototype has been set to 50 MHz, which means that the rise time of the signal for the kicker is $t_{rise} = \frac{0.35}{f_{BW}} = \frac{0.35}{50\ \text{MHz}} = 7$ ns. However, since the time resolution of the present phase monitors is only 10 ns, constituting the bottleneck of the feed-forward system bandwidth, this value was used as a rise time in the simulation.

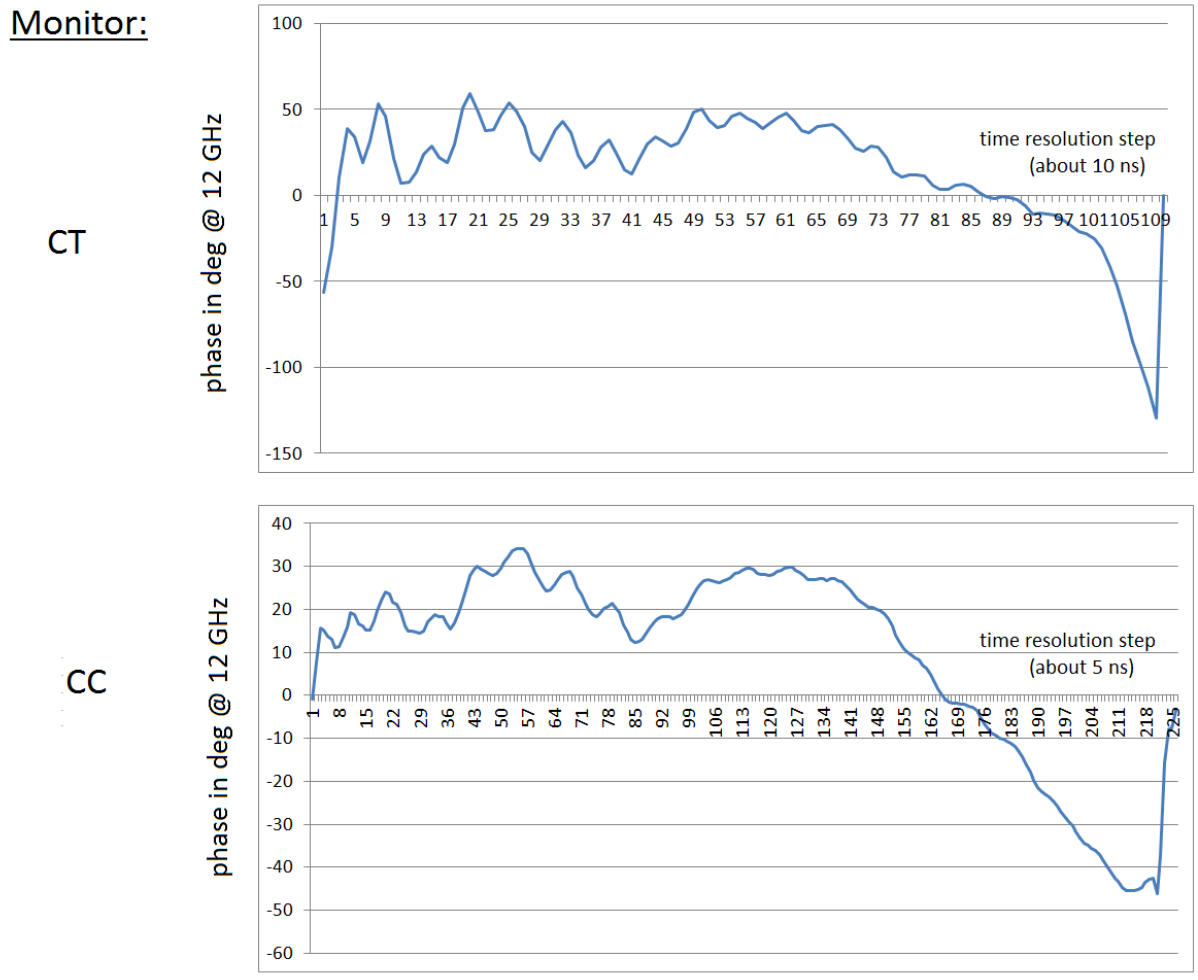

Figure 6.16: Measured phase error at CT and CC monitors along the average train. Monitors are positioned next to TL1 and TL2 chicanes respectively.

In the same manner as for the feedback, a one-to-one correction with $a = 1$ has been performed. Also, since the correlation between the measurements at TL1 and TL2 is 0.85 (compare the diagrams in Fig. 6.16), and the standard deviation of the measurements is different (see Tab. 6.6), a feed-forward has been calculated by multiplying the signal amplitude at TL1 according to Eq. 6.5 with $a = 0.84 \cdot (\sigma_{TL2}/\sigma_{TL1}) = 0.50$. Also the limitation of

the maximal correction that can be provided by a feed-forward system (± 17° at 12 GHz) has been considered.

Monitor position and feed-forward type	σ_ϕ in degrees at 12 GHz
TL1	39.48
TL2 without feed-forward	23.30
TL2 with 1-to-1 feed-forward	26.06
TL2 with 1-to-0.5 feed-forward	14.88
TL2 with 1-to-0.5 feed-forward and with 17° limit	15.35

Table 6.6: Standard deviation of bunch phase with and without feed-forward.

Consequences for the feed-forward system prototype design

The realistic intra-train feed-forward system with 50 MHz amplifier bandwidth could provide a correction of the phase RMS error from 23.3° to 15.35° at 12 GHz at the TL2 chicane. This is a sufficient improvement of the phase stability by 34%, also the phase standard deviation difference of 7.95° at 12 GHz can be measured by the monitors currently installed at CTF3. Hence, the inspection of the feed-forward system functionality can be performed via a measurement at the same monitor with the feed-forward system being subsequently turned on and off.

However, the correlation between the measurements along the beamline at CTF3 is not high enough to allow the test of feed-forward functionality by a direct measurement before and after the kicker. Nevertheless, in case that measurements with the new phase monitors produced by INFN reveal a higher correlation between the phase error at TL1 and TL2 chicanes, such a direct test will become possible.

In such case, additionally to the performance test of the feed-forward system, it could be potentially possible to achieve at CTF3 the phase stability level required for CLIC. For this to happen the R_{56} value of the stretching chicane must be set to zero and the new phase monitors must perform the measurements within the specification precision level of 0.1° at 12 GHz. The feed-forward would be applied over the time of 280-420 ns in the central interval of the pulse, in which the phase deviation is in the order of 2-3° at 12 GHz, and possibly correct the phase error by about a factor of twelve. For such test, additional phase errors must not be introduced downstream from the chicane.

6.4 Chapter summary

The Drive Beam phase measurements have been performed at CTF3 in 2011 and 2012. These measurements have revealed a strong parabolic shape of the beam phase profile within each Drive Beam train, with a total amplitude of over 50° at 12 GHz. This shape is caused by the pulse compressors of the CTF3 phase and is not expected to be present in the CLIC machine.

A study of the average train phase propagation has shown a strong increase (by about a factor of ten) of the RMS in the stretching chicane. The cause of this increase has been shown to be the erratic beam energy in the chicane. Several possible causes for the energy errors have been identified: the beam phase varies at the CTF3 source and hence causes the beam to obtain an erratic energy in the linac. Also, the phase jitter of the first two klystrons of the Drive Beam linac, which are responsible for the bunching of the beam, have been found to cause a significant impact on the beam phase and, consequently, on the beam energy. The klystron phase jitter also directly contributes to the erratic energy absorption by the Drive Beam. The klystron amplitude jitter, on the other hand, has not been found to cause any significant effect on the beam energy and phase.

The simulations of the phase correction system prototype for the CTF3 have shown that a slow inter-pulse feedback system will produce a hardly measurable effect on the CTF3 phase stability, reducing the RMS phase error by only 1.11° at 12 GHz. However, the simulations of the intra-pulse fast feed-forward system with a bandwidth of 50 MHz predict that the prototype will significantly reduce the RMS phase error by 7.95° at 12 GHz. This effect would be measurable even with the monitors installed at CTF3 at the moment; the new monitors produced by Frascati Institute are in commissioning (status: spring 2013) and are expected to provide an even better phase measurement resolution. An extensive testing of the feed-forward system's functionality and effectiveness will be possible after its planned installation in the second half of 2013.

Chapter 7

Conclusions and suggested further work

The current and final chapter summarises the methodology and the results of the studies on the CLIC Drive Beam phase stabilisation presented in the thesis.

Luminosity recovery is one of the major challenges of the CLIC design. Proof of the possibility to stabilise CLIC to a sufficient degree is an indispensable step in CLIC feasibility studies. Consequently, the work on CLIC stabilisation, in particular on CLIC Drive Beam longitudinal phase stabilisation, is one of the main areas of CLIC research and development efforts.

Section 7.1 summarises the crucial elements of the CLIC design and describes the methodology used for the CLIC Drive Beam propagation studies. It also summarises the results of the simulation studies of the Drive Beam propagation and presents the conclusions about the beam error tolerances without stabilisation system as well as with charge feedback and phase feed-forward systems. The specifications for feed-forward system parameters, such as amplifier bandwidth, and for the distributed timing system stability, are stated. The change of error tolerances for the low energy operation mode, as well as for the various RF filling times of the Drive Beam accelerating structures, is described.

Section 7.2 summarises the phase measurements performed at the CTF3 facility, together with the data analysis and results, with conclusions about the sources of CTF3 phase error and predictions of the effect of the proposed phase stabilisation system.

7.1 Phase stabilisation for CLIC

7.1.1 CLIC design

The Compact Linear Collider (CLIC) is a proposed e^+e^- collider being developed at CERN. It is designed to accelerate the electron and positron beams with an acceleration gradient of 100 MV/m and collide them at a nominal energy of 3 TeV.

The RF wave needed for such acceleration cannot be provided by any conventional RF source, hence the two beam solution has been chosen. The so-called Drive Beam with low energy and high current is used to deliver RF power for the acceleration of the high energy, low current Main Beams, which are brought into collision.

The beam spot size at the interaction point (IP) of the CLIC Main Beams is 45 nm horizontally and 1 nm vertically [43], which is a very challenging value to achieve. This dictates strict tolerances on the relative phase difference between the Drive and Main Beams: a random phase error with RMS of 0.8° @ 12 GHz will cause a luminosity loss of 1% [54]. Also the tolerance for the relative phase between the two Main Beams at the interaction point (IP) is 0.6° @ 12 GHz [61].

7.1.2 Methodology of Drive Beam error propagation simulation

The aim of the simulation studies for CLIC presented in the thesis is to track the Drive Beam propagation and to estimate the impact of the beam errors, in particular the phase errors, on the Main Beam and consequently on CLIC's luminosity. The simulation has included four major sections of the Drive Beam complex - the Drive Beam linac, the compressor chicane, the recombination scheme and the Power Extraction and Transfer Structures (PETS) with the Main Beam linac modules. The Drive Beam linac accelerates the beam and can impact the beam stability because of the amplitude and phase errors of the linac klystrons. Also, the phase errors of the beam result in energy errors when the beam passes through the linac. The compressor chicane reduces the Drive Beam bunch length and, because of the non-zero R_{56} value, errors in beam energy are transformed into beam phase errors. Additionally, the chicane causes bunch charge errors to impact the phase stability. The recombination scheme repositions the bunches longitudinally, which influences the timing of the errors when the RF wave is extracted from the Drive Beam in the PETS. After extraction the RF wave is used for the Main Beam acceleration and because of the limited energy bandwidth of the Main Beam interaction point the Drive Beam errors result in luminosity loss.

The simulation program tool calculations are based on the results of independent studies of the RF wave propagation in the Drive Beam accelerating structure [75], the compressor chicane [56] and the RF propagation in the Main Beam accelerating structures [49]. The RF filling and beam loading functions for the Drive and the Main Beams have been approx-

imated linearly.

Errors in the bunch charge ($\sigma_{Q,MB}$), length ($\sigma_{\sigma_z,MB}$) and phase ($\sigma_{\phi,MB}$) of the Drive Beam contribute quadratically to CLICs luminosity loss according to Eq. 7.1 [55]. Errors in the other parameters transform into the bunch length and phase errors at the compressor chicane of the Drive Beam and hence also ultimately lead to luminosity loss.

$$\frac{\Delta\mathcal{L}}{\mathcal{L}} = 0.01 \times \left[\left(\frac{\sigma_\phi}{0.8^\circ}\right)^2 + \left(\frac{\sigma_Q}{2.2\times10^{-3}Q_{nom}}\right)^2 + \left(\frac{\sigma_{\sigma_z}}{3.3\times10^{-2}\sigma_z}\right)^2\right] \tag{7.1}$$

All modules of the program have been tested for their correct functionality. A comparison of the simulation results with the independent analytical calculation has been performed for the errors in each parameter in a single bunch as well as for a constant parameter offset.

7.1.3 Results of simulation studies for the CLIC Drive Beam tolerances

The interdependence of the different errors in the chicane leads to a variety of additional tolerance limits on the beam parameters. The beam energy error contributes to additional phase error, which sets the upper limit on the energy error to 1% considering the phase error tolerance of 2.5° at 12 GHz before the feed-forward correction. Also the bunch length variation tolerance of 1% dictates a single bunch charge tolerance of 1%. However this is valid only for incoherent errors along the beam. The coherent bunch charge error must be below 0.1%, as dictated by the Main Beam accelerator RF amplitude tolerance.

The simulations have demonstrated that the recombination scheme of the Drive Beam reduces the impact of the Drive Beam errors on the Main Beam. Since the bunches are recombined to a higher frequency some of the low frequency errors overlap within the RF filling time of the Main Beam accelerating structures and hence can cancel each other out. The filtering by the Drive Beam recombination scheme is particularly effective for error frequencies of several MHz, except for frequencies with wavelength resonant to the Drive Beam train length of 240 ns. Hence, after the recombination scheme filtering the resonant peaks at $n \times 4.17$ GHz remain mostly unfiltered. Also the low frequency noise (< 100 kHz) is fairly well filtered by the recombination scheme.

The errors in the amplitude and phase of CLIC Drive Beam accelerating structures, as well as in the bunch charge of the Drive Beam, are convolved with the RF filling and beam loading functions in order to calculate their impact on the Drive Beam energy. The resulting beam energy error amplitude differs depending on the incoming error frequency - the RF and bunch charge errors at high frequencies are transformed into beam energy errors to a significantly smaller amount than lower frequency errors. Also there are frequencies

corresponding to the RF filling time of the Drive Beam accelerating structures, at which the errors are significantly suppressed. For the nominal design of CLIC these frequencies have been selected to be at $n \times 4.17$ GHz, which allows suppression of the error peaks that are not filtered by the recombination scheme. The form of the RF filling function is however not rectangular, and so the efficiency of the suppression factor is rather limited.

7.1.4 Impact of charge feedback system on Drive Beam tolerances

The bunch charge feedback system is designed to measure the current (and consequently the bunch charge) of the Drive Beam and to send a correction signal to the Drive Beam source to stabilise the bunch charge to its nominal value. However, as with any feedback system, the bunch charge feedback system reduces the error amplitude for some frequencies and increases it for the others. The feedback system can be set to reduce the noise at the frequencies of the peaks which remain unfiltered by the recombination scheme by setting the sum of latency time and gain time of the feedback system to 240 ns. This way the noise reducing effect of peak suppression is stronger than the noise increasing effect at the frequencies between the peaks, and hence the overall impact of the system is stabilising. Assuming a latency time of 200 ns and an amplifier gain time of 40 ns as well as ideal beam current monitors and error free signal amplification, transmission and bunch charge correction, the overall white noise error of the system can be reduced by 45%, and hence the bunch charge tolerance can be loosened by this amount. The electron source used in CTF3 experiments has a relative current stability of 6×10^{-4}, which is below the CLIC current stability requirement of 0.1%. However an alternative design using the PHIN electron source [85] has only achieved a bunch charge stability of 0.25% and requires a relative improvement of 60% in order to satisfy CLIC requirements. The improvement provided by the charge feedback system is hence insufficient to stabilise the beam current at CLIC provided by a PHIN-based source.

7.1.5 Impact of phase feed-forward system on Drive Beam tolerances

Feed-forward system performance and requirements

A feed-forward chicane is designed to correct the phase of the bunches at the final turnaround of the Drive Beam before the decelerators from RMS phase error value of 175 μm to 14 μm. The feed-forward system analysis has demonstrated a strong potential reduction of the phase error, in particular for the low frequency noise ($\approx$ factor 80 for the white noise up to 1 MHz with a realistic 30 ns feed-forward bandwidth).

A strong dependence of the correction factor on the feed-forward bandwidth has been demonstrated. It has also been shown that for the noise with more dominant low frequency components the bandwidth requirements on the feed-forward system are less tight. The required phase stabilisation by a factor of 12 could be achieved for the red and pink noise spectra with a 1.46 MHz feed-forward amplifier bandwidth (for errors with frequencies from 50 Hz to 20 MHz). The same improvement factor could be possible for white noise only

with 17.5 MHz amplifier bandwidth. Hence, the bandwidth requirements of the system depend on the frequency spectrum anticipated for the phase error at the final turnaround loop. The results are, however, in any case encouraging, since even the bandwidth requirement of 17.5 MHz is realistic to fulfill [95].

Impact of distributed timing system

The nominal phase signal can be defined by the phase measurement at the outgoing Main Beam. However, this approach does not allow to correct the phase errors between the e^+ and e^- Main Beams at their final turnaround. Hence, another approach of a distributed timing system, which will forward the master clock signal to the Main Beam turnaround region and to the Drive Beam decelerators, has been studied. The allowed phase jitter of the distributed timing system at each decelerator segment has been calculated to be 3.34 μm for 1% luminosity loss from both the Main-to-Main and Main-to-Drive Beam tolerances. This value is met by demonstrated performances [64], [65], which proves the feasibility of the distributed timing system. However, ideally the specification would be tighter - 0.1% luminosity loss, which requires a distribution system stability of 1.06 μm per segment. Hence, it has to be investigated whether the noise can be significantly reduced.

The demonstrated performance of the signal distribution includes the transformation of the optical signal into electrical and vice versa. One possible solution is chaining the distribution by splitting the optical signal at each decelerator, using one part of the signal as a reference and amplifying the other part and sending it to the next decelerator. This would help to avoid transformation noise and might allow one to reach the specified target. A dedicated approach would be needed to prove this concept experimentally. It will be also necessary to demonstrate the reliability of the signal distribution technology to operate unattended in the tunnel.

Drive Beam accelerating structures RF filling time

A cost reduction proposal resulting in the lengthening of the Drive Beam accelerating structure and prolonging its RF filling time has been investigated. It has been found that a severe prolongation (by more than 20%) of the RF filling time would cause a more effective filtering of the beam error by the Drive Beam accelerating structures. The filtering is particularly strong for the errors with frequencies over 100 kHz. As a consequence, the filtering difference is noticeable for white noise (e.g. the total error is decreased by 17.2% for the structure RF filling time scaled by factor 1.4), however the difference for red or pink noise is rather insignificant (less than 3%).

Hence, there are no concerns from the point of view of error tolerances for the implementation of the Drive Beam accelerating structures with longer RF filling time. In the case of a strong high-frequency noise component in the accelerating structures error the longer RF filling time structures would be even beneficial.

CLIC operation at lower energy modes

Operation of the nominal design of the CLIC machine is possible not only at the maximal energy of 3 TeV, but also at lower energy. In the low-energy modes operation, in order to compensate for the resulting luminosity loss, the length of the Drive and Main Beam trains can be increased, which requires the use of different Drive Beam recombination patterns [89]. The recombination patterns lead to gradient errors in the Main Beam linac and the amplitude of these errors must be investigated.

The Drive Beam accelerating structure has been optimised to cancel out resonant errors for the nominal energy mode; however, it cannot be adapted to filter out the resonant errors for all train lengths at all lower energy modes. Consequently, the phase error is higher for these modes and the feed-forward system cannot reduce it sufficiently - e.g. for the same incoming error, the Drive Beam accelerating structure filtering and the 7 MHz bandwidth feed-forward correction reduce the total error by a factor of ten more effectively for the nominal mode than for the 2.25 TeV mode. Hence, additional filtering or correction methods must be considered.

7.2 Phase stabilisation at CTF3

The phase stabilisation concept for CLIC can be tested first at CTF3 for its feasibility and effectiveness. A number of feedback systems have been implemented for the different beam parameters [96]. A prototype of a phase correction system is currently under development and is planned to be installed at CTF3 in the second half of 2013.

The measurements of CTF3 Drive Beam phase error have been performed and allow one to simulate the error propagation along CTF3 in order to predict the impact of the correction system prototype on the phase errors [95]. These predictions show that the effect of an inter-train feedback, correcting the average phase of each train, would be rather limited and difficult to measure. The intra-train feed-forward system prototype, however, will have a measurable effect on CTF3 phase errors, allowing experimental test of its functionality. The feed-forward amplifier bandwidth limitation of 50 MHz and the correction range limitation of 17° at 12 GHz reduces the effectiveness of the correction only slightly. There exists a possibility of achieving the required CLIC phase stability level at CTF3, if the new phase monitors produced by INFN will satisfy the measurement precision level of 0.1° at 12 GHz and will show a significantly higher correlation of the phase data between the TL1 and TL2 chicanes.

Source of the phase error at CTF3

It has been found that the phase error in the CTF3 facility increases by about a factor of ten after the beam passes the stretching chicane, which has a nominal R_{56} value of 0.45 m. The R_{56} value of the chicane has been modified and it was found that the additional phase error

introduced in the chicane is proportional to the chicane's R_{56} value. It has been shown that the additional phase error in the chicane is strongly correlated with the directly measured beam energy error. The beam energy error has been found to be caused for the most part by the Drive Beam klystron phase jitter as well as by the phase error of the beam entering the chicane. Consequently, an implementation of a klystron phase feedback stabilisation system has been planned.

Bibliography

[1] Sylvia Berryman. "Stanford Encyclopedia of Philosophy, entry on Democritus". Library of Congress Catalog Data: ISSN 1095-5054. http://plato.stanford.edu/entries/democritus/#2.

[2] Amedeo Avogadro. "Essay on a Manner of Determining the Relative Masses of the Elementary Molecules of Bodies, and the Proportions in Which They Enter into These Compounds". Journal de Physique 73 (1811), 58-76. http://web.lemoyne.edu/~giunta/avogadro.html.

[3] J. J. Thomson. "Cathode Rays". Philosophical Magazine, 44 (1897), p. 293. http://web.lemoyne.edu/~GIUNTA/thomson1897.html.

[4] H. Geiger. "The Scattering of the α-Particles by Matter". Proceedings of the Royal Society vol. A83, p. 492-504. http://www.chemteam.info/Chem-History/Geiger-1910.html.

[5] M. Breidenbach et al. "Observed Behavior of Highly Inelastic Electron-Proton Scattering". Physical Review Letters 23, p. 935-939.

[6] N. Bohr. "On the Constitution of Atoms and Molecules". Philosophical Magazine 26 (153), p. 476-502. http://web.ihep.su/dbserv/compas/src/bohr13b/eng.pdf.

[7] A. Einstein. "Ueber einen die Erzeugung und Verwandlung des Lichtes betreffenden heuristischen Gesichtspunkt". Annalen der Physik 17, p. 132-148. DOI: 10.1002/andp.19053220607.

[8] A. Einstein. "Zur Elektrodynamik bewegter Koerper". Annalen der Physik 17: 891. http://www.fourmilab.ch/etexts/einstein/specrel/www/.

[9] Hadron collider experiments group Stony Brook University (New York). http://sbhep-nt.physics.sunysb.edu/HEP/AcceleratorGroup/index.html.

[10] S.L. Glashow. "Partial-symmetries of weak interactions". Nuclear Physics 22: p. 579-588.

[11] A. Salam et. al. "Elementary Particle Physics: Relativistic Groups and Analyticity". Eighth Nobel Symposium. Stockholm: Almquvist and Wiksell, 367.

[12] S. Weinberg. "A Model of Leptons". Physical Review Letters 19: p. 1264-1266.

[13] T. Muta. "Foundations of quantum chromodynamics: an introduction to perturbative methods in gauge theories". World Scientific. ISBN 978-981-279-353-9.

[14] M.E. Peskin & D.V. Schroeder. "An introduction to quantum field theory". Harper-Collins, 1995, ISBN 0-201-50397-2.

[15] ATLAS collaboration. "Observation of a New Particle in the Search for the Standard Model Higgs Boson with the ATLAS Detector at the LHC". Physics Letters B 716: p. 1-29. http://arxiv.org/pdf/1207.7214v2.pdf.

[16] CMS Collaboration. "Observation of a new boson at a mass of 125 GeV with the CMS experiment at the LHC". Physics Letters B 716: p. 30-61. http://arxiv.org/abs/1207.7235.

[17] J. Ellis et.al. "A Historical Profile of the Higgs Boson". CERN-PH-TH/2012-009. http://arxiv.org/pdf/1201.6045v1.pdf.

[18] H. Miyazawa. "Baryon Number Changing Currents". Prog. Theor. Phys. 36: p. 1266-1276.

[19] H. Miyazawa. "Spinor Currents and Symmetries of Baryons and Mesons". Phys. Rev. 170: p. 1586-1590.

[20] The ALEPH Collaboration et.al. "Precision Electroweak Measurements on the Z Resonance". Phys. Rept. 427: p. 257-454 (2006). http://arxiv.org/abs/hep-ex/0509008.

[21] X. Cid Vidal & R. Cid. "lhc-closer.es". http://www.lhc-closer.es/php/index.php?i=1&s=4&p=7&e=2.

[22] BE/ABP accelerator physics group CERN. "MAD-X Home Page". http://madx.web.cern.ch/madx/.

[23] The Indiana University. "High Energy Physics web page". http://hep.physics.indiana.edu.

[24] LHCb Muon Group Home Page. http://lhcb-muon.web.cern.ch/lhcb-muon/figures/LHC_layout.jpg.

[25] H1 & ZEUS Collaborations. "QCD analysis and determination of alphas using the combined H1 and ZEUS inclusive cross sections together with the jet production cross section measured by the H1 and the ZEUS experiments." H1prelim-11-034, ZEUS-prel-11-001. https://www.desy.de/h1zeus/combined_results/jets/PDFjets.pdf.

[26] D. Brandt et.al. "Accelerator Physics at LEP". Rep. Prog. Phys. 63 (2000) 9391000 (2000). http://jwenning.web.cern.ch/jwenning/documents/lepmain_sl.pdf.

[27] ILC Global Design Effort & World Wide Study. "ILC Reference Design Report". http://www.linearcollider.org/about/Publications/Reference-Design-Report. August, 2007.

[28] ILC Global Design Effort & World Wide Study. "ILC Reference Design Report, Executive Summary". http://ilcdoc.linearcollider.org/record/6321/files/ILC_RDR_Volume_1-Executive_Summary.pdf?version=4. P. I-13.

[29] ILC Global Design Effort & World Wide Study. "ILC Reference Design Report, Executive Summary". http://ilcdoc.linearcollider.org/record/6321/files/ILC_RDR_Volume_1-Executive_Summary.pdf?version=4. P. I-11.

[30] ILC Global Design Effort & World Wide Study. "ILC Reference Design Report, Executive Summary". http://ilcdoc.linearcollider.org/record/6321/files/ILC_RDR_Volume_1-Executive_Summary.pdf?version=4. P. I-12.

[31] CLIC-CTF3 Collaboration. "CLIC Collaboration Members and Observers". http://clic-meeting.web.cern.ch/clic-meeting/CTF3_Coordination_Mtg/Table_MoU.htm. Status 17/07/2012.

[32] CLIC-CTF3 Collaboration. "A Multi-TeV Linear Collider based on CLIC Technology, CLIC Conceptual Design Report". CERN-2012-007. http://project-clic-cdr.web.cern.ch/project-CLIC-CDR/CDR_Volume1.pdf.

[33] A. Blondel et. al. "LEP3: A High Luminosity e^+e^- Collider to study the Higgs Boson". CERN-ATS-NOTE-2012-062 TECH. http://arxiv.org/abs/1208.0504.

[34] R. Raja et al. "Recent Progress in Neutrino Factory and Muon Collider Research within the Muon Collaboration". PACS numbers: 13.10.+q, 14.60.Ef, 29.27.-a, 29.20.Dh. http://www.fnal.gov/projects/muon_collider/prstab/prstab.pdf.

[35] L. Hendrickson et al. "Simulations of IP Feedback and Stabilization in the NLC" (2004). SLAC-PUB-10492, EPAC-2004-THPLT156.

[36] A. Seryi. "Shaky Road to Subnanometer Beams. NLC Ground Motion, Vibration and Stabilization Studies". SLAC-PUB, 8825 (May 2001). http://www.slac.stanford.edu/cgi-wrap/getdoc/slac-pub-8825.pdf.

[37] R. Apsimon. "The Development and Implementation of a Beam Position Monitoring System for use in the FONT Feedback System at ATF2." p. 14-17, D.Phil. thesis, University of Oxford (2011).

[38] S. Molloy. "A fast feedback system designed to maintain luminosity at a linear collider". PhD thesis, Queen Mary College, University of London (2006).

[39] J. Resta Lopez. "CLIC IP beam-based feedback". CLIC Workshop 2009, CERN, 12-16 October 2009. http://indico.cern.ch/contributionDisplay.py?contribId=61&confId=45580.

[40] CERN Website. http://public.web.cern.ch/public/en/About/About-en.html.

[41] CERN Member States Website. http://international-relations.web.cern.ch/International-Relations/ms/.

[42] CLIC-CTF3 Collaboration. "A 3 TeV e^+e^- Linear Collider Based on CLIC Technology". CERN-2000-008, p. 6.

[43] CLIC parameter table. http://clic-meeting.web.cern.ch/clic-meeting/clictable2010.html.

[44] CLIC-CTF3 Collaboration. "A Multi-TeV Linear Collider based on CLIC Technology, CLIC Conceptual Design Report". CERN-2012-007, p. 29. http://project-clic-cdr.web.cern.ch/project-CLIC-CDR/CDR_Volume1.pdf.

[45] P. Urschuetz et. al. "Efficient long-pulse fully-loaded CTF3 linac operation". LINAC 2006, MOP002. http://accelconf.web.cern.ch/accelconf/l06/PAPERS/MOP002.PDF.

[46] CLIC-CTF3 Collaboration. "A Multi-TeV Linear Collider based on CLIC Technology, CLIC Conceptual Design Report". CERN-2012-007, p. 711. http://project-clic-cdr.web.cern.ch/project-CLIC-CDR/CDR_Volume1.pdf.

[47] A. Aksoy. "Drive Beam Linac Longitudinal Tolerances". August 11, 2010. http://indico.cern.ch/contributionDisplay.py?contribId=1&confId=103860.

[48] CLIC-CTF3 Collaboration. "A Multi-TeV Linear Collider based on CLIC Technology, CLIC Conceptual Design Report". CERN-2012-007, p. 370. http://project-clic-cdr.web.cern.ch/project-CLIC-CDR/CDR_Volume1.pdf.

[49] O. Kononenko et. al. "Compensation of Transient Beam-Loading in CLIC Main Linac". Proceedings of LINAC2010, MOP021. http://accelconf.web.cern.ch/accelconf/LINAC2010/papers/mop021.pdf.

[50] CLIC-CTF3 Collaboration. "A Multi-TeV Linear Collider based on CLIC Technology, CLIC Conceptual Design Report". CERN-2012-007, p. 45. http://project-clic-cdr.web.cern.ch/project-CLIC-CDR/CDR_Volume1.pdf.

[51] J. Rees et. al. "Limitations on Performance of e^+e^- Storage Rings and Linear Colliding Beam Systems at High Energy". eConf C781015, (1978) 009. http://www.slac.stanford.edu/econf/C781015/pdf/009.pdf.

[52] CLIC-CTF3 Collaboration. "Physics and Detectors at CLIC, CLIC Conceptual Design Report". CERN-2012-003. http://lcd.web.cern.ch/LCD/CDR/CDR.html.

[53] J. Resta Lopez, D. Schulte & R. Tomas et. al. "The Post-linac Collimation System of CLIC: Machine Protection Aspects". Machine Protection workshop, 6-8 June 2012. http://indico.cern.ch/contributionDisplay.py?contribId=29&sessionId=7&confId=185561.

[54] D. Schulte et al. "Status of the CLIC Phase and Amplitude Stabilisation Concept". Proceedings of LINAC2010, MOP024, CERN-ATS-2010-226.

[55] D. Schulte & R. Tomas. "Dynamic Effects in the New CLIC Main Linac". Proceedings of PAC09, TH6PFP046. http://epaper.kek.jp/PAC2009/papers/th6pfp046.pdf.

[56] A. Aksoy. "Simulations for CLIC Drive Beam Linac". 25 Feb 2012, arXiv:1202.5628v1.

[57] D.Schulte. "CLIC Phase Stabilisation". CERN-2012-007, p. 714. http://indico.cern.ch/getFile.py/access?contribId=0&resId=1&materialId=slides&confId=164428.

[58] D. Schulte et. al. "The Impact of Longitudinal Drive Beam Jitter on the CLIC Luminosity". Proceedings of LINAC 2004, MOP43. http://accelconf.web.cern.ch/accelconf/l04/PAPERS/MOP43.PDF.

[59] P. Skowronski. "Drive Beam phase feed-forward". CLIC Collaboration Working Meeting, 3-4 November 2011, CTF3-002. https://indico.cern.ch/contributionDisplay.py?contribId=29&confId=156004.

[60] A. Gerbershagen et. al. "Simulation of Phase Stability at the Flat Top of the CLIC Drive Beam". Proceedings of International Particle Accelerator Conference 2011, San Sebastian, Spain, TUPC013. http://accelconf.web.cern.ch/accelconf/IPAC2011/papers/tupc013.pdf.

[61] D. Schulte. "First CLIC Phase Stability Meeting". 24 November 2011. http://indico.cern.ch/conferenceDisplay.py?confId=164428.

[62] CLIC-CTF3 Collaboration. "A Multi-TeV Linear Collider based on CLIC Technology, CLIC Conceptual Design Report". CERN-2012-007, p. 56-58. http://project-clic-cdr.web.cern.ch/project-CLIC-CDR/CDR_Volume1.pdf.

[63] A. Andersson et. al. "Precision Beam Timing Measurement System for CLIC Synchronization". Proceedings of EPAC 2006, TUPCH086. http://accelconf.web.cern.ch/accelconf/e06/PAPERS/TUPCH086.PDF.

[64] F. Ömer Ilday. "Long-distance optical stabilization with femtosecond resolution". CLIC09 Workshop.

[65] M. Felber. "Achievements and challenges during the first implementation phase of an engineered version in the accelerator". CLIC09 Workshop.

[66] H. Schlarb. "Synchronization of Accelerator Sub-Systems with Ultimate Precision". Proceedings of LINAC12, TU3A01.

[67] A. Gerbershagen et. al. "Specifications of the Distributed Timing System for the CLIC Main Linac". Proceedings of LINAC12, MOPB045.

[68] G. Bienvenu et. al. "A Thermionic Electron Gun for the Preliminary Phase of CTF3". Proceedings of EPAC 2002, p. 1753-1755, TUPRI055. http://accelconf.web.cern.ch/accelconf/e02/PAPERS/TUPRI055.pdf.

[69] CLIC-CTF3 Collaboration. "A Multi-TeV Linear Collider based on CLIC Technology, CLIC Conceptual Design Report". CERN-2012-007, p. 714. http://project-clic-cdr.web.cern.ch/project-CLIC-CDR/CDR_Volume1.pdf.

[70] M. Csatari Divall. "High power laser development in the UV for accelerators and light sources". PhD thesis, University of Szeged (2012).

[71] A. Aksoy. "Drive Beam Linac Design Studies". CLIC Meeting (Drive Beam linac), 13 August 2010. http://indico.cern.ch/contributionDisplay.py?contribId=3&confId=103214.

[72] A. Chao. "Handbook of Accelerator Physics and Engineering". ISBN: 978-981-02-3858-2.

[73] A.E. Dabrowski et. al. "Measuring the Longitudinal Bunch Profile at CTF3". Proceedings of LINAC2010, TUP100. http://cds.cern.ch/record/1302735/files/tup100.pdf.

[74] The GdfidL Electromagnetic Field simulator. http://www.gdfidl.de/.

[75] R. Wegner et. al. "CLIC Drive Beam Accelerating Structures". CLIC-Note-945. http://cdsweb.cern.ch/record/1478398/files/CERN-OPEN-2012-024.pdf?subformat=pdfa.

[76] R. Wegner. Private communication.

[77] D. Schulte. "PLACET: A Program to Simulate Drive Beams". Proceedings of EPAC 2000, Vienna, Austria, TUP7B05. http://accelconf.web.cern.ch/accelconf/e00/PAPERS/TUP7B05.pdf.

[78] ANSYS HFSS. http://www.ansys.com/.

[79] Ben Constance. "Design and beam testing of a fast, digital intra-train feedback system and its potential for application at the International Linear Collider". D.Phil. thesis, University of Oxford (2011). http://www-pnp.physics.ox.ac.uk/~font/papers/bConstance_thesis.pdf.

[80] W. S. Levine. "The control handbook". CRC Press (1996), ISBN 0-8493-8570-9, p. 1548.

[81] CLIC-CTF3 Collaboration. "A Multi-TeV Linear Collider based on CLIC Technology, CLIC Conceptual Design Report". CERN-2012-007, Chapter 8. http://project-clic-cdr.web.cern.ch/project-CLIC-CDR/CDR_Volume1.pdf.

[82] A. Gerbershagen et. al. "CLIC Recombination Scheme for the Low Energy Operation Mode". Proceedings of International Particle Accelerator Conference 2012, New Orleans, USA, TUPPR024. http://accelconf.web.cern.ch/accelconf/IPAC2012/papers/tuppr024.pdf.

[83] CLIC-CTF3 Collaboration. "A Multi-TeV Linear Collider based on CLIC Technology, CLIC Conceptual Design Report". p. 713, CERN-2012-007. http://project-clic-cdr.web.cern.ch/project-CLIC-CDR/CDR_Volume1.pdf.

[84] R. Corsini. "Status of CTF3". CLIC/CTF3 Collaboration Board Meeting, 5/19/2011. http://indico.cern.ch/getFile.py/access?contribId=11&resId=1&materialId=slides&confId=134291.

[85] O. Mete et.al. "PHIN photo-injector as the CLIC Drive Beam source". J. Phys.: Conf. Ser. 347 012036 (2012). http://iopscience.iop.org/1742-6596/347/1/012036.

[86] F. Stulle. "Beam phase and energy tolerances in the CLIC RTML". CLIC Note 874.

[87] D. Schulte for the CLIC collaboration. "CLIC Re-baselining". CLIC Workshop, February 2013. http://indico.cern.ch/contributionDisplay.py?contribId=4&sessionId=0&confId=204269.

[88] D. Schulte et. al. "CLIC Energy Scans". Proceedings of International Particle Accelerator Conference 2010, Kyoto, Japan, WEPE022.

[89] CLIC-CTF3 Collaboration. "A Multi-TeV Linear Collider based on CLIC Technology, CLIC Conceptual Design Report". Chapter 8:"CLIC Operation at Low Energies", CERN-2012-007. http://project-clic-cdr.web.cern.ch/project-CLIC-CDR/CDR_Volume1.pdf.

[90] E. Ikarios. "Measurements and analysis of CTF3 Phase with different Bunch Compressor Factors, part 1". 30 Jan 2013, CLIC Workshop 2013. http://indico.cern.ch/contributionDisplay.py?contribId=139&confId=204269.

[91] H. Schmickler. "Introduction to Beam Instrumentation". LC School 2011. http://ilcagenda.linearcollider.org/getFile.py/access?contribId=7&resId=1&materialId=slides&confId=5636.

[92] F. Marcellini et. al. "The CLIC Drive Beam Phase Monitor". WEPEB035, Proceedings of International Particle Accelerator Conference 2010, Kyoto, Japan, WEPEB035. http://accelconf.web.cern.ch/accelconf/IPAC10/papers/wepeb035.pdf.

[93] E. Ikarios. "Precision Phase Measurements and Feedback of the CTF3 Drive Beam". PhD thesis, Technical Univeristy of Athens. To be published, exp. 2014.

[94] J. Barranco Garcia. "Low Momentum Compaction and Bunch Length". 30 Jan 2013, CLIC Workshop 2013. http://indico.cern.ch/contributionDisplay.py?contribId=164&sessionId=29&confId=204269.

[95] A. Gerbershagen et. al. "Performance simulations of a phase stabilization system prototype for CTF3". Proceedings of International Particle Accelerator Conference 2012, New Orleans, USA, WEPPP066.

[96] T. Persson. Doctoral thesis for Chalmers University of Technology, Gothenburg, Sweden, to be published in 2014.